SMART POLYMERIC NANOCOMPOSITES TAILORED FOR TARGETED DELIVERY, PROTEIN SEPARATION AND BIOFILM DISRUPTION

by

Yavuz Öz

B.S., Chemistry, Gazi University, 2010

M.S., Chemistry, Boğaziçi University, 2014

Submitted to the Institute for Graduate Studies in
Science and Engineering in partial fulfillment of
the requirements for the degree of
Doctor of Philosophy

Graduate Program in Chemistry

Boğaziçi University

2020

ACKNOWLEDGEMENTS

I would like to express my sincere gratitude to my thesis supervisor Prof. Amitav Sanyal for his endless support and scientific guidance during my graduate studies. I deeply appreciate his patience, valuable comments and discussions regarding all my research. I am very grateful for his excellent mentoring throughout my graduate studies.

I would like to extend my thanks to my thesis jury, Prof. Rana Sanyal, Assoc. Prof. Abdullah Aydogan, Assoc. Prof. Oktay Demircan and Assist. Prof. Ozgul Gok for their constructive review of the final manuscript.

I wish to express my thanks to our collaborators Prof. Rabah Boukherroub, Prof. Remzi C. Becer, Prof. Sabine Szunerits and Prof. Vincent M. Rotello for their contributions to my graduate studies.

Insulin related experiments were done under supervision of Prof. Sabine Szunertis. I also acknowledge all help in experiments by Dr. Florina Teodorescu for this project. It was a great experience to work together to meet goals of the project.

I wish to acknowledge Prof. Remzi Becer, Dr. Gokhan Yilmaz and Yamin Abdouni for supplying glycopolymers for lectin seperation and purification by magnetic glyconanoparticles project.

The last part of the thesis was done under supervision of Prof Vincent M. Rotello. Therefore, I would like to thank Prof. Vincent M. Rotello for giving me this opportunity. Also, I wish to express my thanks to Ahmed Nabawy for all help in bacteria and biofilm experiments in this project.

I would like to thank past and present Sanyal Group members for their companion and friendship. I would like to extend my thanks to all the members of the faculty in

the Chemistry Department

I wish to acknowledge Scientific and Technological Research Council of Turkey (TUBITAK) for 2228-B National PhD Scholarship Programme for MSc Students and 2214-A International Research Fellowship Programme for PhD Students. Financial support from the Marie Sklodowska-Curie action H2020-MSCA-RISE-2015, PANG-690836) is also acknowledged.

I would like to express my thanks to my family and friends for their support and love during my studies.

Finally, I deeply thank my dear wife Ezgi for her endless love, support and encouragement.

ABSTRACT

SMART POLYMERIC NANOCOMPOSITES TAILORED FOR TARGETED DELIVERY, PROTEIN SEPARATION AND BIOFILM DISRUPTION

Fabrication and biomedical applications of polymeric nanomaterials are described. In the first study, transdermal delivery of insulin via rGO confined hydrogels is reported. rGO impregnated PEG-based hydrogels were fabricated by photo-induced FRP of PEGDMA monomers. Hydrogels loaded with insulin were used for on-demand drug release exploiting photothermal heating ability of rGO in the hydrogel matrix upon exposure to NIR irradiation. In the second part, functionalization of rGO with clickable maleimide group is reported. Maleimide was conjugated with a thiol bearing targeting peptide, and a chemotherapy drug was loaded on the surface of rGO via non-covalent interactions. Targeted delivery and cancer cell killing ability of doxorubicin loaded rGO were then evaluated. In the third part, selective cell targeting and imaging with polymer coated MNPs are studied. The surface of MNPs was modified with clickable groups which were further conjugated with a targeting peptide and an imaging agent. Cell targeting and internalization were achieved with these MNPs. In the fourth part, lectin separation using polymer coated MNPs is investigated. The surface of these MNPs was modified with adamantane group, and supramolecular host-guest interactions were exploited for binding of β-CD-sugar conjugates. A specific lectin from a mixture was separated by sugar containing MNPs. Final work describes phytochemical containing polymer NCs for eradication of MDR biofilms. A biodegradable and clickable amphiphilic copolymer was used to stabilize carvacrol oil-in-water emulsion. Biofilm disruption ability of these NCs was evaluated on different MDR biofilms. In summary, potential bio-applications of various nano-constructs was evaluated.

ÖZET

HEDEFLİ TAŞIMA, PROTEİN AYIRMA VE BİYOFİLM BOZULMASI İÇİN TASARLANMIŞ AKILLI POLİMER NANOKOMPOZİTLER

Polimerik nanopartiküllerin üretimi ve biyomedikal uygulamaları çalışılmıştır. İlk calışmada, rGO içeren hidrojeller ile transdermal insülin taşınması incelenmiştir. rGO içeren PEG tabanlı hidrojeller, serbest radikal polimerleşme ile üretilmiştir. İnsülin yüklenen hidrojeller, rGO'in yakın IR ile ısınma özelliğinden faydalanarak, isteğe bağlı ilaç salımı için kullanılmışlardır. İkinci kısımda maleimit içeren rGO'in sentezi çalışıldı. rGO üzerinde bulunan maleimit gruplara, tiyol içeren hedefleyici peptid konjuge edildi ve kanser ilacı rGO'e kovalent olmayan etkileşimlerle yüklendi. Doksorubisin yüklenmiş rGO'in hedefli ilaç taşınması ile kanserli hücreleri öldürebilme becerisi değerlendirildi. Üçüncü kısımda polimer kaplı nanopartiküller ile hücre hedefleme ve görüntüleme üzerine çalışıldı. Nanopartiküllerin yüzeyi klik kimyasına uygun gruplar ile modifiye edilerek, hedefleyici peptid ve görüntüleme ajanı konjuge edilmiştir. Bu nanopartiküller ile tümor hücresi hedefleme ve internalizasyonu gerçekleştirilmiştir. Dördüncü projede polimer kaplı nanopartiküller kullanarak lektin ayrıştırılması incelenmiştir. Manyetik nanopartiküllerin yüzeyleri adamantin ile modifiye edilip, β-siklodekstrin içeren şekerler ile hidrofobik etkileşimleri sağlanmıştır. Lektin karışımı içerisinden belirli bir lektin, şeker içeren nanopartiküller ile ayrılmıştır. Son çalışmada çoklu ilaç dirençli bakterilerin fitokimyasal içeren polimer nanokompozitler ile öldürülmesi açıklanmıştır. Biyobozunur ve klik kimyasına uygun amfifilik kopolimerler, karvakrolun su içinde yağ emülsiyonunu stabilize etmek için kullanılmıştır. Bu nanokompozitlerin biyofilm bozma etkinliği, çoklu ilaç direnci olan biyofilmler üzerinde denendi. Özet olarak bu tezde çeşitli nano-yapıların potansiyel biyo-uygulamaları değerlendirilmiştir.

TABLE OF CONTENTS

ACKNOWLEDGEMENTS . . . iii
ABSTRACT . . . v
ÖZET . . . vi
LIST OF FIGURES . . . xii
LIST OF TABLES . . . xxviii
LIST OF SYMBOLS . . . xxix
LIST OF ACRONYMS/ABBREVIATIONS . . . xxx
1. INTRODUCTION . . . 1
1.1. Polymeric Materials for Biomedical Applications . . . 1
1.1.1. Hydrogels . . . 1
1.1.2. Polymeric Nanostructures . . . 6
1.1.2.1. Micelles . . . 6
1.1.2.2. Polymer Nanocapsules . . . 8
1.1.2.3. Nanogels . . . 10
1.1.2.4. Polymer Nanocomposites . . . 13
1.2. Polymer Coated Metal Nanoparticles for Biomedical Applications . . . 14
1.3. Graphene Based Materials for Biomedical Applications . . . 18
2. RESEARCH OVERVIEW . . . 23
3. PHOTOTHERMALLY TRIGGERED ON-DEMAND INSULIN RELEASE FROM REDUCED GRAPHENE OXIDE MODIFIED HYDROGELS . . . 24
3.1. Introduction . . . 24
3.2. Experimental . . . 27
3.2.1. Materials and Characterizations . . . 27
3.2.2. Synthesis of PEGDMA-rGO Hydrogels . . . 28
3.2.3. Insulin Loading . . . 28
3.2.4. Photothermal Release Studies . . . 29
3.2.5. Determination of Insulin Activity . . . 29
3.2.6. Cytotoxicity Assay . . . 30

3.2.7. Apoptosis Assay . . . 30
3.2.8. Skin Staining and Histology . . . 30
3.2.9. Skin Permeation Experiments . . . 31
3.3. Results and Discussion . . . 32
3.3.1. Formulation of rGO Loaded PEGDMA-rGO . . . 32
3.3.2. Insulin Loading . . . 34
3.3.3. Photothermal Release of Insulin . . . 36
3.3.4. Evaluation of Photothermally Released Insulin Activity . . . 40
3.3.5. Biocompatibility of Photothermally Activable PEGDMA-rGO Hydrogels . . . 42
3.3.6. Transdermal Insulin Delivery Through Pig Skin . . . 44
3.4. Conclusions . . . 45
4. FUNCTIONALIZATION OF REDUCED GRAPHENE OXIDE VIA THIOL -MALEIMIDE "CLICK" CHEMISTRY: FACILE FABRICATION OF TARGETED DRUG DELIVERY VEHICLE . . . 47
4.1. Introduction . . . 47
4.2. Experimental . . . 50
4.2.1. Materials and Characterizations . . . 50
4.2.2. Preparation of Reduced Graphene Oxide (rGO) . . . 51
4.2.3. Synthesis of Maleimide-Containing Dopamine (dopa-MAL) . . . 51
4.2.3.1. Protected Maleimide-Containing Dopamine (dopa-pMAL) 51
4.2.3.2. Maleimide Group Activation via Retro Diels-Alder Reaction (dopa-MAL) . . . 52
4.2.4. Preparation of rGO/dopa-MAL . . . 52
4.2.5. Functionalization of rGO/dopa-MAL via Thiol–Ene Michael Addition Reactions . . . 53
4.2.5.1. Glutathione and 6-(Ferrocenyl)hexanethiol Linking . . 53
4.2.5.2. c(RGDfC) Attachment to rGO/dopa-MAL . . . 53
4.2.6. Quantification of Peptide and DOX Loading . . . 53
4.2.6.1. Peptide Quantification Using Bicinchoninic Acid (BCA) Assay . . . 53

4.2.6.2. Drug Loading 53
4.2.7. Cell Viability and Internalization 54
4.2.8. Cell Viability upon Treatment with rGO/dopa-MAL-c(RGDfC) 54
4.2.9. Cell Viability of DOX-Loaded rGO/dopa-MAL-c(RGDfC) under Passive and Active Conditions 54
4.3. Results and Discussion 55
4.3.1. Synthesis of Dopamine-Maleimide Modified Reduced Graphene Oxide (rGO/dopa-MAL) 55
4.3.2. Thiol-ene Michael Addition Reaction on rGO/dopa-MAL 58
4.3.3. Fabrication of Multifunctional Scaffold: Doxorubicin-Loaded rGO/dopa-MAL-c(RGDfC) 60
4.3.4. Targeted Cell-Killing Ability of DOX-Loaded rGO/dopa-MAL-c(RGDfC) 62
4.3.5. Targeted Photothermal Cell-Killing Ability of DOX-Loaded rGO/dopa-MAL-c(RGDfC) 64
4.4. Conclusions 66
5. MODULAR FABRICATION OF POLYMER BRUSH COATED MAGNETIC NANOPARTICLES: ENGINEERING THE INTERFACE FOR TARGETED CELLULAR IMAGING 68
5.1. Introduction 68
5.2. Experimental 72
5.2.1. Materials and Characterizations 72
5.2.2. Simultaneous Conjugation of Maleimide-containing MNPs with Dye and cRGDfC via Thiol–ene Reaction 73
5.2.3. Bicinchoninic Acid Protein Quantification 74
5.2.4. Cell Internalization Experiment 74
5.2.5. Cytotoxicity Experiment 74
5.3. Results and Discussion 75
5.3.1. Synthesis of Polymer Brush Coated Parent MNPs 75
5.3.2. Installation and Functionalization of “Clickable” Functional Groups 78

5.4. Conclusions 83
6. MAGNETIC GLYCONANOPARTICLES FOR SELECTIVE LECTIN SEPARATION AND PURIFICATION 84
6.1. Introduction 84
6.2. Experimental 87
6.2.1. Materials and Characterizations 87
6.2.2. Synthesis of the Adamantane Modified Azo-initiator (azobis-AD) 89
6.2.3. End Group Modification of Polymer Coated Iron Oxide NPs with azobis-AD 89
6.2.4. Synthesis of Per-(6-deoxy-6-azido)-β-cyclodextrin (β-CD-$(N_3)_7$) 90
6.2.5. Synthesis of Mannose Conjugated Beta-cyclodextrin (β-CD-$(Man)_7$) 90
6.2.6. Synthesis of Per-6-deoxy-6-(thiopropyl-2-bromo-2-methyl propanoate)-β-cyclodextrin (β-CD initiator) 90
6.2.7. Synthesis of Poly(mannose) Conjugated Beta-cyclodextrin (β-CD-p$(Man)_{280}$) 91
6.2.8. Supramolecular Complexation Between Fe_3O_4@PEG@AD and β-CD-$(Man)_7$/β-CD-p$(Man)_{280}$ 91
6.2.9. Lectin Binding Studies to Mannose Decorated Fe_3O_4@PEG@AD MNPs 92
6.2.10. Selective Lectin Separation Assays 92
6.3. Results and Discussion 92
6.3.1. Polymer Coating on MNPs 92
6.3.2. Modification of Polymer Coated MNPs with Adamantane 96
6.3.3. Synthesis of Mannose/galactose-containing Beta-CD Constructs 97
6.3.4. Investigation of Host-guest Complexation of AD-containing MNPs with Mannose Appended CD-based Constructs 99
6.3.5. Lectin Binding to Mannose-containing CD-decorated MNPs . . 101
6.4. Conclusions 110
7. BIODEGRADABLE POLY(LACTIC ACID) STABILIZED NANOSPONGES FOR THE TREATMENT OF MULTIDRUG-RESISTANT BACTERIAL

BIOFILMS 112
7.1. Introduction 112
7.2. Experimental 114
7.2.1. Materials and Characterizations 114
7.2.2. Attachment of TTMA to MA-PLA Copolymers 114
7.2.3. Fabrication of Nanosponges 115
7.2.4. Determination of Minimum Inhibitory Concentration 115
7.2.5. Biofilm Formation 116
7.2.6. Biofilm-3T3 Fibroblast Cell Co-culture 116
7.3. Results and Discussion 117
7.3.1. Fabrication and Characterizations of Nanosponges 117
7.3.2. Stability and Degradability of X-NCs 119
7.3.3. Penetration of Nanosponges into Biofilms 121
7.3.4. Antimicrobial Activity of X-NS against Bacterial Biofilms . . . 122
7.3.5. Selective Killing of Biofilms in a Co-culture Model 123
7.4. Conclusions 125
8. CONCLUSION 126
REFERENCES 128
APPENDIX A: SUPPLEMENTARY DATA 169
APPENDIX B: COPYRIGHT NOTICES 184

LIST OF FIGURES

Figure 1.1. Polymeric materials used in biomedical applications. 2

Figure 1.2. (a) Synthesis of redox-responsive hydrogels and degradation upon treatment with thiol containing compounds, (b) photographs of UV-illuminated FITC-BSA impregnated hydrogels in the presence of DTT and in the absence of DTT, (c) release profile of FITC-BSA from hydrogels with varying crosslinking densities with and without DTT solution at 37 °C. Reproduced from Ref. [24] with permission from The Royal Society of Chemistry. 4

Figure 1.3. (a) The 3D macroporous pNIPAAm-co-pAAm/GO hydrogel for reversible loading and on-demand release of cells by turning on/off NIR laser, (b) the capture of cell into the macroporous hydrogels facilitated by RGD cell targeting peptide and NIR-induced cell release. Reproduced from Ref. [33] with permission from John Wiley and Sons. 5

Figure 1.4. Self-assembly of amphiphilic copolymers in water, yielding polymeric micelles. Adapted with permission from [35] Copyright (2017) American Chemical Society. 6

Figure 1.5. (a) Formation of polymer micelle in the presence of siRNA and tumor targeting, (b) modification of PEG-b-PLL with cRGD and 2-iminothiolane. Adapted with permission from [45] Copyright (2017) American Chemical Society. 8

Figure 1.6. Polymeric nanocapsules formed via (a) self-assembly of amphiphilic polymers and (b) LbL self-assembly of charged polymers. Reproduced from Ref. [48] with permission from The Royal Society of Chemistry. 9

Figure 1.7. (a) Schematic representation of a base catalyzed interfacial polymerization reaction between amine and carbonate monomers in an inverse mini-emulsion, (b) synthesis of polymer and (c) enzymatic degradation and cellular uptake of nanocapsules. Adapted with permission from [55] Copyright (2017) American Chemical Society. 10

Figure 1.8. Nanogel preparation by emulsion polymerization (a) with oil-in-water emulsion, (b) with water-in-oil emulsion and (c) by crosslinking of amphiphilic block copolymer at core or shell of the polymer micelles in water. Reproduced from Ref. [62] with permission from John Wiley and Sons. 11

Figure 1.9. Synthesis and reduction-induced degradation of S-propranolol molecularly imprinted polymers for drug delivery. Reproduced from Ref. [69] with permission from The Royal Society of Chemistry. 12

Figure 1.10. (a) Emulsification of p-MA-alt-OD containing carvacrol oil in PONI-GAT dissolved water, (b) TEM image of nanocomposites, (c) chemical structure of PONI-GAT, (d) chemical structure of p-MA-alt-OD, (e) size distribution of nanocomposites and (f) biofilm distribution with carvacrol loaded nanocomposites. Adapted with permission from [75] Copyright (2017) American Chemical Society. . . 14

Figure 1.11. Preparation of cRGD-uPIC-AuNPs. cRGD-PEG-PLL modified with LA (cRGD-PEG-PLL-LA) at the ω-end was mixed with a single pair of siRNA to form monodisperse uPICs. Then, the uPICs were conjugated onto a 20 nm AuNP core through double Au–S bonds, followed by grafting of short PEG for construction of monodispersed 40 nm-sized cRGD-uPIC-AuNP. Reproduced from Ref. [87] Copyright (2016) with permission from Elsevier. 16

Figure 1.12. Commonly used anchoring groups for the surface modification of iron oxide NPs for biomedical applications. 17

Figure 1.13. (a) Deprotection of the phosphonate groups, (b) surface ligand exchange of the oleic acid coated iron oxide NPs, (c) confocal images of polymer coated NPs and (d) confocal images of GRP78 peptide conjugated NPs incubated with MCF-7 cell line. Left to right: images under different channels including the nuclei stained by DRAQ5, PBM fluorescence, and the merged images. Scale bars = 10 μm. Adapted with permission from [105] Copyright (2018) American Chemical Society. 18

Figure 1.14. Fabrication of graphene by different methods. Reprinted by permission from [112] Copyright (2017) Springer Nature. 19

Figure 1.15. Targeted drug delivery via graphene oxide and reduced graphene oxide. Reproduced from Ref. [113] with permission from The Royal Society of Chemistry. 20

Figure 1.16. (a) Synthesis of PEGylated graphene oxide and (b) anti-tumor activity of doxorubicin loaded redox responsive nano-graphene oxide and GSH triggered drug release in tumor cells. Reproduced from Ref. [120] with permission from John Wiley and Sons. 21

Figure 3.1. PEG-based hydrogels impregnated with rGO that allow efficient loading and 'on-demand' photothermal release of insulin. 27

Figure 3.2. (a) Illustration of the fabrication of PEGDMA-rGO hydrogels, (b) photographs of free standing hydrogels without rGO and (c) with rGO (0.8 mg). 32

Figure 3.3. Characterization of rGO and rGO loaded PEGDMA hydrogels: (a) UV–Vis absorption spectra of rGO (black), PEGDMA (orange) and PEGDMA-rGO (0.1 mg, blue), (b) raman spectra of rGO (black), PEGDMA (orange) and PEGDMA-rGO (0.8 mg, blue), (c) SEM images of PEGDMA, PEGDMA-rGO (0.8 mg) and insulin loaded PEGDMA-rGO (0.8 mg). 33

Figure 3.4. Insulin loading of PEGDMA-rGO hydrogels: (a) Calibration curve used for the determination of loading capacity of PEGDMA-rGO hydrogels, inset: UV-Vis spectrum of human insulin solution, (b) human insulin (100 μg mL^{-1}) loading capacity of PEGDMA-rGO as a function of rGO content at pH 7, (c) human insulin loading capacity of PEGDMA-rGO (0.8 mg) hydrogel as a function of pH by adjusting the pH through the addition of NaOH or HCl, (d) swelling ratio of rGO-PEGDMA (0.8 mg rGO) hydrogels as a function of pH by adjusting the pH through the addition of NaOH or HCl. The results are expressed as the mean ± SEM of at least 5 independent samples for each group. 35

Figure 3.5. (a) Change in solution temperature during illumination of different insulin loaded PEGDMA-rGO hydrogels at 980 nm for 10 min as a function of laser power, (b) photothermal heating curves of rGO (black, 0.8 mg, drop casted onto glass), PEGDMA (orange), and PEGDMA-rGO (0.8 mg) (blue) under NIR illumination (980 nm) at 0.7 W cm^{-2} using a continuous wave laser. The results are expressed as the mean ± SEM of at least 5 independent samples for each group. 37

Figure 3.6. Insulin release: (a) Stability of insulin loaded PEGDMA-rGO hydrogels in water for a period of 1 day (black) and one week (green), (b) percentage of insulin released photothermally into water (37 °C) using a continuous wave laser at 980 nm, 0.7 W cm^{-2} with illumination time of 10 min, (c) influence of irradiation time on insulin release (980 nm, 0.7 W cm^{-2}), (d) reloading and release of insulin on PEGDMA-rGO (0.8 mg) hydrogels for 6 cycles, (e) repeated insulin release over 7 days using 10 min laser illumination at 980 nm, 0.7 W cm^{-2}. The results are expressed as the mean ± SEM of at least 5 independent samples for each group. 39

Figure 3.7. (a) Effects of photo-released insulin on cell viability. Measurement of apoptotic HepG2 cells that were cultured for 72 h in the absence (control, 1) and presence of a PEGDMA-rGO hydrogel (2), insulin loaded PEGDMA-rGO hydrogel (3) and photo-released insulin (4). The fraction of cells undergoing apoptosis was determined by scoring the percentage of cells displaying pyknotic nuclei. Data are the mean of ± SD, (b) insulin activity from insulin loaded PEGDMA hydrogels determined on HepG2 cells Western blot of p-Akt/Akt cell lysates from HEPG2 cells incubated under several conditions: without insulin, with native insulin or with photo-released insulin (insulin loaded PEGDMA-rGO hydrogels), (c) insulin activity shown by the ratio between p-Akt and Akt (A.U.) for all the samples in comparison to a negative control (CTL neg) (cells without insulin treatment). One-way ANOVA and multi comparisons test. The results are expressed as the mean ± SEM of at least 3 independent samples for each group, (*p <0.05, **p <0.01, ***p <0.001). 41

Figure 3.8. (a) Relative cell viability of Caco-2 epithelial cell lines in the absence (control) and presence of insulin loaded PEGDMA-rGO hydrogels with and without laser illumination for 10 min at 980 nm at 0.7 W cm^{-2}; (cell viability was evaluated using the CCK-8 assay, where the absorbance at 450 nm is measured using a microplate reader) without irradiation. The results are expressed as the mean ± SEM of at least 3 independent samples for each group, (b) representative photographs and histology of pig ear skin before and after treatment with a laser at 980 nm for 10 min with a laser power density of 0.7 W cm^{-2}. 43

Figure 3.9. (a) HPLC chromatogram of insulin (10 μg mL^{-1}) and the corresponding calibration curve, (b) in vitro permeation profiles of insulin through porcine skin from insulin loaded PEGDMA-rGO hydrogels upon light irradiation at 980 nm for 10 min at 0.7 W cm^{-2}. 45

Figure 4.1. Schematic illustration of the synthesis of thiol-ene "clickable" Mal-rGO and its subsequent functionalization. 49

Figure 4.2. Synthesis of dopa-MAL (4) and its conjugation onto rGO through π-π stacking interactions. 56

Figure 4.3. (a) FT-IR spectra of rGO/dopa-MAL (black) and dopa-MAL (gray), (b) C_{1s} wide-scan XPS spectrum of rGO/dopa-MAL, (c) N_{1s} wide-scan XPS spectrum of rGO/dopa-MAL, (d) UV–Vis of rGO/dopa-MAL. 57

Figure 4.4. (a) S_{2p} high resolution XPS spectra of rGO/dopa-MAL-glutathione (blue) and rGO/dopa-MAL-ferrocene (black), (b) Fe_{2p} high resolution XPS spectrum of rGO/dopa-MAL-ferrocene, (c) cyclic voltammogram of rGO/dopa-MAL-ferrocene in tetraethyl ammonium hexafluorophosphate ($TEAPF_6$)/DMF (0.1 M), scan rate 100 mV s^{-1}, (d) change in the current density as a function of scan rate. 59

Figure 4.5. Formulation of doxorubicin-loaded rGO/dopa-MAL-c(RGDfC): (a) schematic of the attachment of targeting peptide to rGO/dopa-MAL via Michael addition followed by the noncovalent integration of doxorubicin, (b) cell viability of different concentrations (μg mL^{-1}) of rGO/dopa-MAL-c(RGDfC) on HeLa and MDA-MB-231 cells after incubation for 48 h, (c) UV-Vis spectrum of the DOX-loaded rGO/dopa-MAL-c(RGDfC). 61

Figure 4.6. Dose-response curves of HeLa (black) and MDA-MB-231 (blue) cancer cells to various concentrations of (a) free DOX for 24 h and (b) DOX-loaded rGO/dopa-MAL-c(RGDfC) nanostructures for 48 h, (c) optical images showing the targeting effect of DOX-loaded rGO/dopa-MAL-c(RGDfC) at two different concentrations (50 and 100 μg mL^{-1}) after 6 h incubation before and after washing with PBS. 64

Figure 4.7. (a) Photothermal heating profiles of DOX-loaded rGO/dopa-MAL-cRGDfC (100 μg mL^{-1}) using a 980 nm laser at different laser power densities, (b) DOX amount released from the DOX-loaded rGO/dopa-MAL-cRGDfC (17 μg DOX for 100 μg rGO/dopa-MAL-cRGDfC) matrix, (c) cell viability of MDA-MB-231 cells after irradiation for 10 min at 980 nm with different laser power densities after 6 h incubation and then additional 18 h incubation, (d) cell viability of HeLa cells after irradiation at 980 nm for 10 min at different laser power densities after 6 h incubation and then additional 18 h incubation. 66

Figure 5.1. Illustration of a modular approach to fabricate a library of functional MNPs through diversification of parent polymer-coated MNPs. 69

Figure 5.2. Synthesis and modular post-modification of polymer-coated MNPs. 71

Figure 5.3. Synthetic route of p(PEGMEA)-coated iron oxide MNPs. 75

Figure 5.4. (a) TEM image of Fe_3O_4@PEGMEA MNPs and (b) Fe_3O_4@PEGMEA MNPs as aqueous dispersion and (c) after 12 h exposure to magnet. 76

Figure 5.5. (a) XPS wide-scan spectrum of Fe_3O_4@CTA, (b) C 1s core-level spectra and (c) S 2p core-level spectra of Fe_3O_4@CTA, (d) wide-scan spectra of Fe_3O_4@PEGMEA, (e) C 1s core-level spectra and (f) S 2p core-level spectra of Fe_3O_4@PEGMEA. 77

Figure 5.6. Diversification of reactive surface modification of MNPs by azide or furan-protected maleimide derivatives. 79

Figure 5.7. (a) XPS wide-scan spectrum of Fe_3O_4@PEGMEA@pMAL1, (b) S 2p core-level spectrum and (c) N 1s core-level spectrum of Fe_3O_4 @PEGMEA@pMAL1, (d) wide-scan spectrum of Fe_3O_4@PEGMEA@ pMAL2, (e) S 2p core-level spectrum and (f) N 1s core-level spectrum of Fe_3O_4@PEGMEA@pMAL2, (g) wide-scan spectrum of Fe_3O_4 @PEGMEA@pMAL3, (h) S 2p core-level spectrum and (i) N 1s core-level spectrum of Fe_3O_4@PEGMEA@pMAL3. 80

Figure 5.8. Attachment of targeting peptide (cRGDfC) and imaging dye (BODIPY-SH) onto the Fe_3O_4@PEGMEA@MAL3 MNPs. 81

Figure 5.9. Cell cytotoxicity evaluation of cRGD-attached Fe_3O_4@PEGMEA@ MAL3 MNPs with different concentrations over MDA-MB-231 cells. 82

Figure 5.10. Merged fluorescence images of MDA-MB-231 cells following treatment with (a) BODIPY-attached and (b) BODIPY- and cRGD-attached Fe_3O_4@PEGMEA@MAL3 NPs. 82

Figure 6.1. Incorporation of β-CD-sugar derivatives to MNPs via supramolecular host-guest interactions and representation of lectin binding with these MNPs. 87

Figure 6.2. RAFT polymerization from the MNP surface with the PEGMEA monomer and surface modification of polymer coated NPs with the azobis-ADA initiator. 93

Figure 6.3. (a) FT-IR spectrum of Fe_3O_4@OA, Fe_3O_4@CTA and Fe_3O_4@PEG MNPs, TEM images of (b) Fe_3O_4@OA, (c) Fe_3O_4@CTA, (d) Fe_3O_4@PEG and (e) Fe_3O_4@PEG@AD MNPs. 95

Figure 6.4. Synthetic route of the adamantane modified azo-initiator (azobis-ADA). 96

Figure 6.5. Synthesis of mannose containing β-CD constructs; (a) β-CD based $(mannose)_7$, (b) β-CD based $poly(mannose)_{280}$, (c) β-CD based $poly(galactose)_{280}$, (d) SEC traces of the synthesized β-CD-$(N_3)_7$ and β-CD-$(Man)_7$, (e) ^{1}H NMR spectra of β-CD-$(Man)_7$, (f) SEC traces of the synthesized β-CD-$(Br)_7$ initiator and CD-based mannose glycopolymer, (g) ^{1}H NMR spectra of β-CD-$p(Man)_{280}$. . . . 98

Figure 6.6. UV-Vis spectra of (a) 8 μM PP solutions at pH = 10.2 with 32 μM β-CD and different amount of Fe_3O_4PEG@AD MNP addition, (b) with 32 μM β-CD and different amount of Fe_3O_4@PEG MNP addition as control experiments, (c) with β-CD-$(Man)_7$ and (d) β-CD-$p(Man)_{280}$, followed by mixing with Fe_3O_4@PEG@AD MNPs. 100

Figure 6.7. Host-guest interactions between Fe_3O_4@PEG@AD MNPs and β-CD-$(Man)_7$, followed by the specific binding of ConA to mannose containing magnetic nanoparticles and release of ConA by the addition of competitive sugar, α-D-mannose; (a) fluorescence spectra of FITC-ConA solution (0.05 mg mL^{-1}) and supernatants from Fe_3O_4@PEG@AD/β-CD-$(Man)_7$ MNPs containing different amounts of β-CD-$(Man)_7$ (control experiment was carried out with Fe_3O_4@PEG@AD/β-CD MNPs), (b) fluorescence spectra of ConA release from ConA captured Fe_3O_4@PEG@AD/β-CD-$(Man)_7$ MNPs upon addition of D-(+)-mannose, (c) TEM images of Fe_3O_4@PEG@AD/β-CD-$(Man)_7$, (d) ConA bound clustered MNPs and (e) redispersed MNPs after the addition of free mannose. 103

Figure 6.8. Host-guest interactions between Fe_3O_4@PEG@AD MNPs and β-CD-p$(Man)_{280}$, followed by specific binding and subsequent release of ConA. (a) Fluorescence spectra of a FITC-ConA solution (0.05 mg mL^{-1}), and supernatants from Fe_3O_4@PEG@AD/β-CD-p$(Man)_{280}$ MNPs with different amounts of β-CD-p$(Man)_{280}$ (control experiment was carried out with Fe_3O_4@PEG@AD/β-CD MNPs), (b) ConA release from MNPs upon the addition of D-(+)-mannose and TEM images of (c) Fe_3O_4@PEG@AD/β-CD-p$(Man)_{280}$, (d) ConA bound clustered MNPs and (e) redispersed MNPs after the addition of free mannose. 105

Figure 6.9. Fluorescence spectra of supernatants of FITC-ConA, Rhd-PNA and FITC-PNA solutions before and after treatment with: (a) Fe_3O_4@PEG@AD/β-CD-$(Man)_7$ NPs, (b) Fe_3O_4@PEG@AD/β-CD-p$(Man)_{280}$ NPs and (c) and (d) Fe_3O_4@PEG@AD/β-CD-$(Gal)_{280}$. 107

Figure 6.10. (a) Illustration of the specific capture of ConA onto Fe_3O_4@PEG@AD/β-CD-p$(Man)_{280}$ MNPs from a Con A and PNA mixture. (b) The release of captured ConA was achieved by the addition of competitive sugar, α-D-mannose; relative amounts of captured lectin from ConA and the PNA mixture with Fe_3O_4@PEG@AD/β-CD-p$(Man)_{280}$ NPs and recovery of captured lectin upon the addition of α-D-mannose. 108

Figure 6.11. (a) MALDI-TOF mass spectra of ConA, PNA, and ConA/PNA mixture (1 : 1) and recovered ConA from MNPs, (b) PNA-spiked ConA solutions in comparison with recovered ConA from MNPs. . 110

Figure 7.1. Preparation of carvacrol oil-in-water crosslinked biodegradable PLA X-NS by emulsification and schematic representation of biofilm disruption upon delivery of essential oil payload. 114

Figure 7.2. (a) TEM picture of X-NS, (b) DLS histogram of X-NS in 150 mM PBS solution and (c) zeta potential of X-NS. 118

Figure 7.3. DLS size distributions of X-NS (a) stability evaluation in 10 % FBS solution for 6 h; (b) degradability in presence of physiologically relevant biomolecule (proteinase K enzyme) in PBS solution (24 h). 120

Figure 7.4. Confocal images of GFP expressing *K. pneumonia* biofilm after 1 h treatment with 5 % X-NS. Nile red was loaded into X-NCs for tracking biofilm penetration. The overlay demonstrated X-NS effectively penetrated into the biofilm, colocalizing with bacteria that express GFP. Scale bars are 30 μm. 121

Figure 7.5. Viability of *E. coli* (CD-2), *A. baumannii* (CD-575) and methicillin-resistant *S. aureus* (CD-6169) biofilms after 3 h of treatment with X-NS, carvacrol oil, and TTMA-MA-PLA at different emulsion concentrations (v/v % of emulsion). The results are an average of triplicate, and the error bars indicate the standard deviation. . . . 123

Figure 7.6. Viability of 3T3 fibroblast cells and *P. aeruginosa* biofilms in the co-culture model after 3 h treatment with different emulsion concentrations of X-NS. Line bars represent 3T3 fibroblast cell viability and bar plots are $\log_{10}$ of colony-forming units in biofilms. Results are given as an average of three experiments, and the error bars designate the standard deviations. 124

Figure A.1. FT-IR spectra of PEGDMA (red) and rGO-PEGDMA (green) hydrogels. 169

Figure A.2. Water uptake profile of rGO-PEGDMA hydrogel at pH 7.0. 169

Figure A.3. TGA curve of PEGDMA-rGO (0.8 mg) based hydrogel. 170

Figure A.4. (a) ^{1}H-NMR spectrum of Dopa-pMAL in $CDCl_3$, (b) ^{1}H-NMR spectrum of Dopa-MAL in $(CD_3)_2SO$ and (c) ^{13}C-NMR spectrum of Dopa-MAL in $(CD_3)_2SO$. 171

Figure A.5. Calibration curve of standard peptide solutions based on UV absorbance values at 562 nm and UV-Vis spectrum of rGO/dopa-MAL-c(RGDfC) (inset). 172

Figure A.6. Doxorubicin calibration curve and UV-Vis spectrum of diluted supernatant after doxorubicin loading onto rGO/dopa-MAL-c(RGDfC) (inset). 172

Figure A.7. Field dependent magnetization curve of Fe_3O_4@OA MNPs. 173

Figure A.8. Images of Fe_3O_4@PEGMEA MNPs in dilute water dispersion (a) without permanent magnet attraction, (b) with attraction <10 min and (c) 12 h magnet attraction. 173

Figure A.9. (a) UV-vis spectrum of BCA assay standards and cRGD conjugated MNPs (b) BCA assay calibration curve. 174

Figure A.10. DLS measurements of magnetic NPs (a) Fe_3O_4@OA, (b) Fe_3O_4@CTA, (c) Fe_3O_4@PEG and (d) Fe_3O_4@PEG@AD NPs. 174

Figure A.11. UV visible spectra of (a) Fe_3O_4@OA and Fe_3O_4@CTA, (b) Fe_3O_4@PEG and Fe_3O_4@PEG@AD. 175

Figure A.12. TGA measuremants of OA, CTA and PEG polymer coated MNPs. 175

Figure A.13. (a) ^{1}H-NMR and (b) ^{13}C-NMR spectrum of azobis-ADA initiator. 176

Figure A.14. UV-vis spectra of 8 μM PP solutions at pH = 10.2 after addition of varying amounts of Fe_3O_4@PEG MNPs. 176

Figure A.15. Calibration curve of FITC-labelled ConA using fluorescence spectroscopy. 177

Figure A.16. Fluorescence spectra of (a) FITC-ConA/BSA mixture solution and supernatant after treatment with Fe_3O_4@PEG@ADA/β-CD-p$(MAN)_{280}$ MNPs, and (b) released ConA. 177

Figure A.17. MALDI-TOF mass spectra of (a) the BSA/ConA mixture (9 : 1), (b) residual BSA in the supernatant after magnetic separation and (c) ConA recovered from MNPs ConA-BSA mixture. 178

Figure A.18. ^{1}H-NMR spectrum of protected maleimide containing PLA polymer (pMA-PLA). 178

Figure A.19. ^{1}H-NMR spectrum of maleimide containing PLA polymer (MA-PLA). 179

Figure A.20. ^{1}H-NMR spectrum of TTMA attached maleimide functional polymer (TT-MA-PLA). 180

Figure A.21. Stability evaluation of X-NS in 10 % FBS solution for 24 h. 180

Figure A.22. Stability evaluation of NX-NS in 10 % FBS solution for 6 h. . . . 181

Figure A.23. ^{1}H-NMR spectra of (a) TT-MA-PLA polymer in deuterated PBS with proteinase K enzyme (t = 0 h) and (b) biodegraded X-NS in deuterated PBS after proteinase K addition (t = 48 h). 182

Figure A.24. (a) Degradation of X-NS with proteinase K enzyme (6.9 μM) in PBS solution (t = 0, 24 and 48 h) and (b) stability of X-NS in the absence of proteinase K enzyme (t = 0, 24 and 48 h) as a control. 183

Figure B.1. Permission for Figure 1.2 from Ref. [24] 184

Figure B.2. Permission for Figure 1.3 from Ref. [33] 185

Figure B.3. Permission for Figure 1.4 from Ref. [35] 185

Figure B.4. Permission for Figure 1.5 from Ref. [45] 186

Figure B.5. Permission for Figure 1.6 from Ref. [48] 187

Figure B.6. Permission for Figure 1.7 from Ref. [55] 188

Figure B.7. Permission for Figure 1.8 from Ref. [62] 188

Figure B.8. Permission for Figure 1.10 from Ref. [75] 189

Figure B.9. Permission for Figure 1.11 from Ref. [87] 190

Figure B.10. Permission for Figure 1.13 from Ref. [105] 190

Figure B.11. Permission for Figure 1.14 from Ref. [112] 191

Figure B.12. Permission for Figure 1.16 from Ref. [120] 192

Figure B.13. Permission for Chapter 3 192

Figure B.14. Permission for Chapter 4 193

Figure B.15. Permission for Chapter 5 193

LIST OF TABLES

Table 4.1. Determination of the atomic percentages of elements by the XPS analysis. 58

Table 6.1. Characteristics of magnetic NPs by DLS, TEM and zeta potential. 94

LIST OF SYMBOLS

A	Surface area
F	Faraday constant
Q_A	Transferred anodic charge
Γ	Surface coverage
ζ	Zeta potential

LIST OF ACRONYMS/ABBREVIATIONS

Ada-TEG	2-(2-2-[2-(adamantan-1-ylmethoxy)-ethoxy]-ethoxy-ethoxy)-ethanol)
AIBN	2,2′-Azobis(2-methylpropionitrile)
ATRP	Atom Transfer Radical Polymerization
BCA	Bicinchoninic Acid
BSA	Bovine Serum Albumin
c(RGDfC)	Cyclo(Arg-Gly-Asp-D-Phe-Cys)
CMC	Critical Micelle Concentration
ConA	Concanavalin A
CTA	Chain Transfer Agent
CuAAC	Copper Catalyzed Azide-alkyne Cycloaddition Reaction
CV	Cyclic Voltammetry
DBM	Dibromomaleimide
DCC	*N,N*′-Dicyclohexylcarbodiimide
DBU	1,8-Diazabicyclo[5.4.0]undec-7-ene
DCM	Dichloromethane
DDMAT	2-(Dodecylthiocarbonothioylthio)-2-methyl Propionic Acid
DLS	Dynamic Light Scattering
DMAP	4-(Dimethylamino)pyridine
DMEM	Dulbecco's Modified Eagle's Medium
DMF	Dimethylformamide
DMPA	2,2-Dimethoxy-2-phenylacetophenone
DMSO	Dimethyl Sulfoxide
Dopa-CTA	Dopamine Functionalized Chain Transfer Agent
DOX	Doxorubicin
DTT	Dithiothreitol
ECM	Extracellular Matrix
EPR	Enhanced Permeability and Retention

EPS	Extracellular Polymeric Substances
EtOAc	Ethyl Acetate
FBS	Fetal Bovine Serum
FRP	Free Radical Polymerization
FITC	Fluorescein Isothiocyanate
FT-IR	Fourier-transform Infrared Spectroscopy
GelMA	Gelatin Methacryloyl
GO	Graphene Oxide
GPC	Gel Permeation Chromatography
GSH	Glutathione
HEPES	4-(2-hydroxyethyl)-1-piperazineethanesulfonic Acid
HPLC	High Performance Liquid Chromatography
LA	Lactic Acid
LB	Lysogeny Broth
LbL	Layer-by-layer
LCST	Lower Critical Solution Temperature
MALDI	Matrix-assisted Laser Desorption/Ionization
MDR	Multidrug Resistant
Me_6TREN	Tris[2-(dimethylamino)ethyl]amine
MNPs	Magnetic Nanoparticles
MRI	Magnetic Resonance Imaging
MTBE	Methyl tert-Butyl Ether
MWCO	Molecular Weight Cut-off
NGO	Nano-graphene Oxide
NHS	*N*-Hydroxysuccinimide
NIR	Near Infrared
NMR	Nuclear Magnetic Resonance
PBS	Phosphate-buffered Saline
PDA	Polydopamine
PEG	Poly(ethylene glycol)
PEGDMA	Poly(ethylene glycol) Dimethacrylate

PEGDMA-rGO	Reduced Graphene Oxide Containing Hydrogels
PEGMEA	Poly(ethylene glycol) Methyl Ether Acrylate
PEO	Poly(ethylene oxide)
PLA	Poly(lactic acid)
PLL	Poly(l-lysine)
p-MA-*alt*-OD	Poly(maleic anhydride-*alt*-1-octadecene)
PNA	Peanut Agglutinin
PNIPAM	Poly(N-isopropylacrylamide)
PONI-GAT	Guanidine Bearing Poly(oxanorborneneimide)
PP	Phenolphthalein
PS	Polystyrene
PVDF	Poly(vinylidene difluoride)
RAFT	Reversible Addition-fragmentation Chain-transfer Polymerization
rGO	Reduced Graphene Oxide
RID	Refractive Index Detector
ROP	Ring-opening Polymerization
SEC	Size-exclusion Chromatography
SEM	Scanning Electron Microscopy
SET-LRP	Single-electron Transfer Living Radical Polymerization
siRNA	Small Interfering Ribonucleic Acid
SPAAC	Strain Promoted Azide-Alkyne Cycloadditions
TEA	Triethylamine
TEM	Transmission Electron Microscopy
TFA	Trifluoroacetic Acid
TGA	Thermogravimetric Analysis
THF	Tetrahydrofuran
TLC	Thin Layer Chromatography
TTMA	Thioalkyl tetra(ethylene glycol)ated trimethylammonium
uPIC	Unimer Polyion Complex
UV-Vis	Ultraviolet-visible Spectroscopy

V-501	4,4′-Azobis(4-cyanovaleric acid)
XPS	X-ray Photoelectron Spectroscopy
VSM	Vibrating Sample Magnetometer
β-CD	Beta-cyclodextrin

1. INTRODUCTION

1.1. Polymeric Materials for Biomedical Applications

Polymeric materials have been extensively utilized in biomedical applications because of their unique physical and chemical properties and ease of bearing different functionalities for desired purposes [1–6]. Such polymeric materials should conform with some essential criteria for their use in biomedical applications. For instance, they should not have any non-specific interactions with biomolecules to ensure sustained stability in physiological conditions. Moreover, biocompatibility of polymeric materials is of utmost importance so as to perform without systematic toxicity in biological conditions. Functional polymers used in biomedical applications need to be bio-orthogonal so that any biochemical reactions occurring in the body are not interfered by these polymeric materials. Lastly, they should assure high drug loading capacity and sustained on-demand release for drug delivery applications.

Polymeric materials mainly used in biomedical applications include hydrogels, micelles, nanogels and nano-capsules/composites (Figure 1.1). These materials could be synthesized with various techniques that will be mentioned in the following sections. The properties of polymeric materials such as size, porosity, hydrophilicity and hydrophobicity, mechanical strength, shape, stability and surface charge are easily tuned either during their fabrication or by post-modification reactions. Moreover, post-modification of these polymeric constructs with functional groups or direct fabrication with functional monomers/polymers allows further conjugation of biomolecules, targeting groups and imaging agents.

1.1.1. Hydrogels

Hydrogels are defined as chemically or physically crosslinked three-dimensional hydrophilic polymer networks. They have attracted significant attention since the

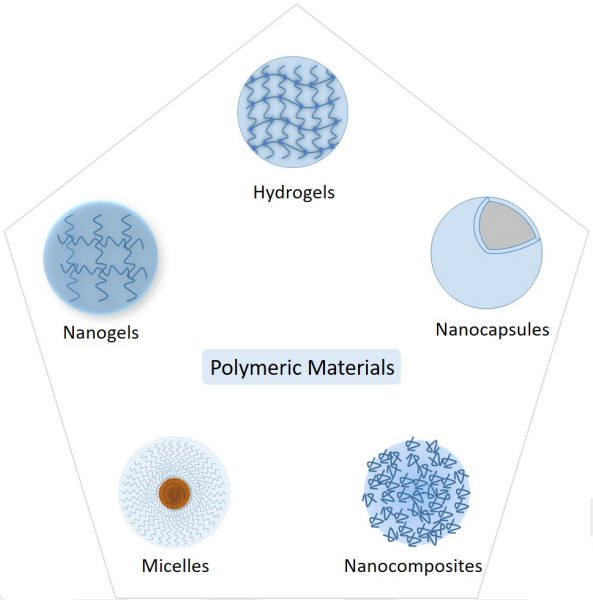

Figure 1.1. Polymeric materials used in biomedical applications.

pioneering work of Wichterle and Lim in 1960 was reported on crosslinking of 2-hydroxyethyl methacrylate monomer for biological use [7]. After that, hydrogels have exploited in various bio-applications such as drug delivery, wound healing, biosensors, tissue engineering and bioimmobilization [8–13]. They are not soluble in water due to the crosslinking between polymer chains but they can absorb large amount of water (up to 1000-times of their dry weight) while maintaining the polymer network structure. The amount of absorbed water in hydrogel network is mainly determined by crosslinking degree and hydrophilic character of polymers in the network structure.

Hydrogels are mainly divided into two categories according to crosslinking strategy: chemically crosslinked hydrogels and physically crosslinked hydrogels. The junction points in chemically crosslinked hydrogels are permanent while physically crosslinked hydrogels are composed of transient junctions that are formed by physical interactions such as polymer entanglement [14], hydrogen bonding [15], ionic [16,17] or hydrophobic interactions [18]. Covalently crosslinked hydrogels could be synthesized by free radical crosslinking strategy and various click type of chemistries such as azide-alkyne cycloaddition, thiol-ene and Diels-Alder reactions [19–22]. Since chemically crosslinked

hydrogels are obtained by the formation of covalent bonds, they are generally more stable compared to physically crosslinked hydrogels where the network structure arises from weak physical interactions. For some bio-applications of chemically crosslinked hydrogels, reversible covalent linkage formation could be also employed where the network structure is broken upon administration of external or internal stimuli such as heat, pH, reducing agents, etc.

Stimuli-responsive hydrogels, commonly called as smart hydrogels, have been widely used in drug delivery, protein release, antimicrobials and sensors [23–25]. These hydrogels are generally synthesized by the incorporation of dynamic covalent linkages that respond different stimuli or they are directly obtained from stimuli-responsive polymers such as PNIPAM. Incorporation of stimuli-responsive organic or inorganic materials such as graphene oxide and Au NPs into polymer network also yields stimuli-responsive hydrogels [26,27]. These smart hydrogels are mostly administered transdermally or direct in situ implementation and injection for drug delivery applications, reducing the systematic toxicity of drugs. Recently, pH responsive salecan/poly(methacrylic acid) polymer network hydrogels were used as anticancer drug delivery system by Bi, Dong and coworkers [28]. pH responsive hydrogels are widely exploited as a smart drug delivery and release system in cancer treatment because it is well-known that cancer cells are more acidic (pH 5.5) than the normal healthy cells (pH 7.4), which serves a suitable environment to trigger chemotherapy drug from the hydrogel network.

Redox responsive hydrogels can be fabricated using dynamic disulfide based crosslinkers that are cleaved by thiol bearing reducing agents such as DTT and GSH [29,30]. These reducing agents trigger the degradation of hydrogel and facilitate release of its cargo. In some cases, conjugation of drug molecules into hydrogel network via disulfide linkage also ends up with redox responsive hydrogels in which no degradation is required for drug release. In that case, thiol bearing stimuli trigger the release of drug cleaving the disulfide linkage between hydrogel and drug molecule. Recently, Sanyal and coworkers reported redox responsive degradable hydrogels for controlled protein release. The Diels-Alder chemistry was utilized to obtain stimuli responsive

hydrogels under benign reaction conditions using side-chain furan bearing water soluble polymers and bismaleimide crosslinker that contains a cleavable disulfide linker in the middle (Figure 1.2a) [24]. The protein (FITC-BSA) was encapsulated during the formation of hydrogel network. The release of BSA from the hydrogel was achieved by the addition of DTT, which stimulates the degradation of hydrogels cleaving the disulfide linkages (Figure 1.2b). They also showed that the higher release of protein was observed for the less crosslinked hydrogels as illustrated in Figure 1.2c (HG 1 contains the least amount of crosslinker whereas HG 3 contains the most one).

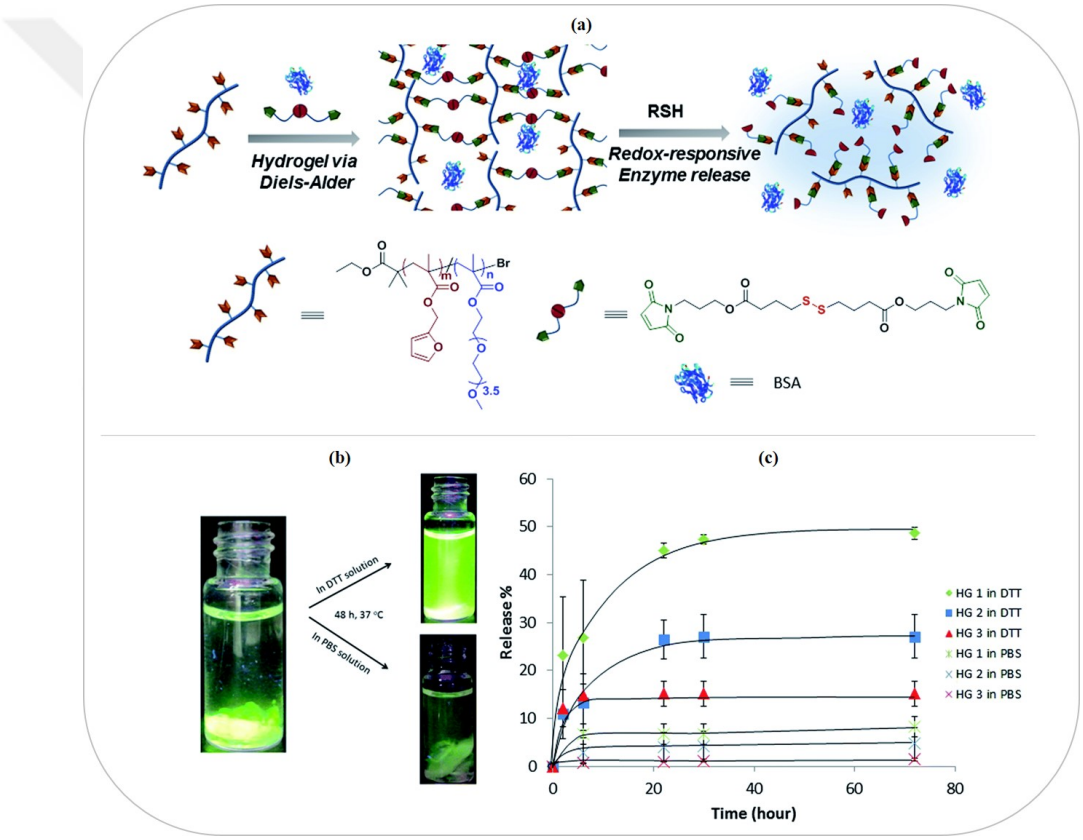

Figure 1.2. (a) Synthesis of redox-responsive hydrogels and degradation upon treatment with thiol containing compounds, (b) photographs of UV-illuminated FITC-BSA impregnated hydrogels in the presence of DTT and in the absence of DTT, (c) release profile of FITC-BSA from hydrogels with varying crosslinking densities with and without DTT solution at 37 °C. Reproduced from Ref. [24] with permission from The Royal Society of Chemistry.

Hydrogels have attracted a great deal of attention in tissue engineering owing to the fact that they mimic natural ECM [31]. Hydrogels synthesized by incorporation of stimuli responsive materials respond to external stimuli such as heat, light and magnetic field. In these systems, external trigger allows remote control over payload release [32]. For instance, Qu and coworkers reported therapeutic cell impregnated graphene oxide containing hydrogels that respond NIR light [33]. When NIR light is applied, GO absorbs the light and generates heat. PNIPAAM based hydrogels starts shrinking to release therapeutic cells when the temperature increases above its LCST (Figure 1.3a). RGD peptide was introduced into hydrogel network to increase cell uptake (Figure 1.3b). With this smart hydrogel system, they were able to release the cells on-demand switching NIR on/off.

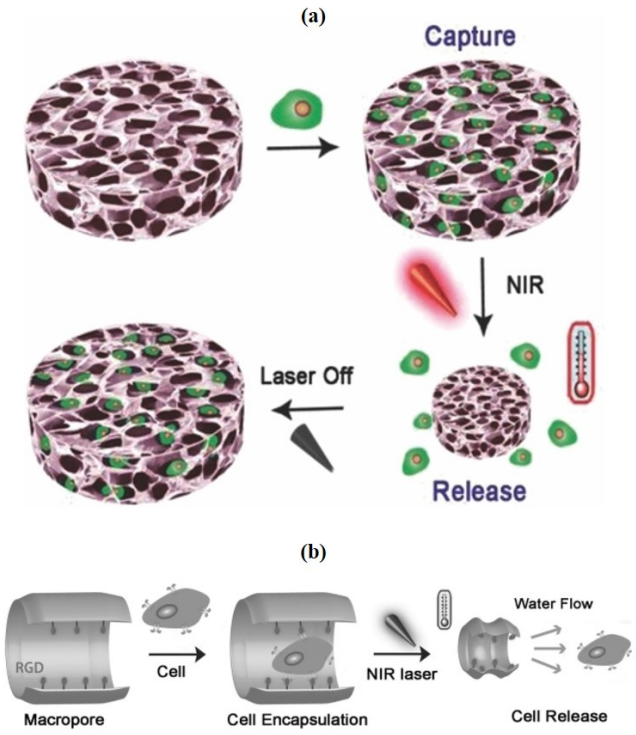

Figure 1.3. (a) The 3D macroporous pNIPAAm-co-pAAm/GO hydrogel for reversible loading and on-demand release of cells by turning on/off NIR laser, (b) the capture of cell into the macroporous hydrogels facilitated by RGD cell targeting peptide and NIR-induced cell release. Reproduced from Ref. [33] with permission from John Wiley and Sons.

1.1.2. Polymeric Nanostructures

1.1.2.1. Micelles. Micelles are aggregated polymeric colloidal dispersions in water. The formation of micellar structures is driven by different attractive interactions such as electrostatic and hydrophobic interactions [34, 35]. They are composed of hydrophobic inner core and hydrophilic outer shell originated upon self-assembly of amphiphilic copolymers (Figure 1.4). These polymers are able to self-assemble into micellar structures at above concentrations of CMC while they are soluble below CMC. The hydrophobic part of amphiphilic polymer comes together to avoid water contact and hydrophilic part stays contacted with water that surrounds the hydrophobic core of micelle.

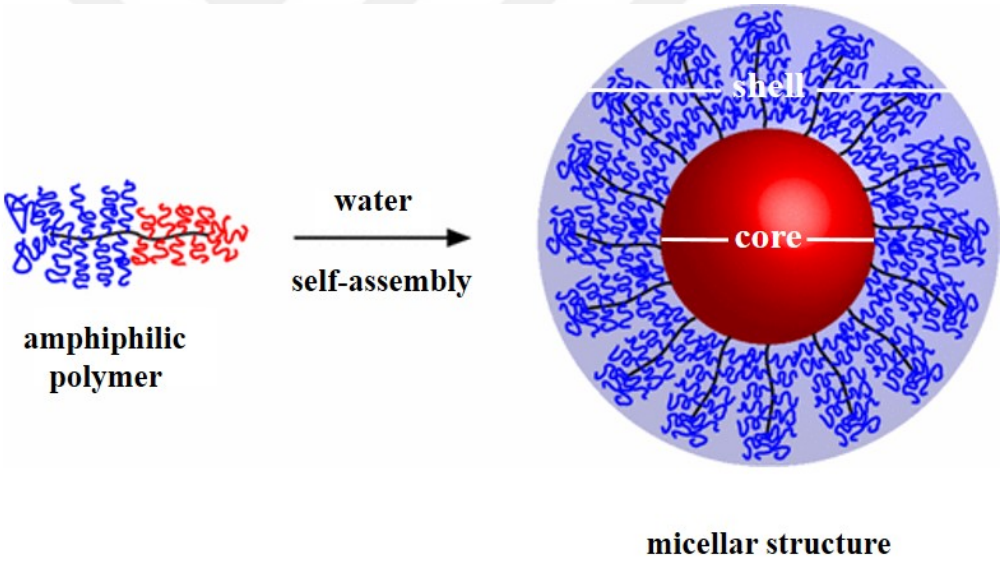

Figure 1.4. Self-assembly of amphiphilic copolymers in water, yielding polymeric micelles. Adapted with permission from [35] Copyright (2017) American Chemical Society.

Core-shell structure of polymeric micelles makes them indispensable delivery vehicles for hydrophobic drugs. Moreover, their composition and structure can be easily controlled depending on the desired applications. One of the mostly used amphiphilic polymers to obtain micelles for drug delivery applications is PLA-PEO copolymer be-

cause of their biodegradable nature [36–38]. This polymer could form highly stable drug loaded micelles through self-assembly. For example, Venkatraman and coworkers demonstrated micelle-like nanoparticles using PLA-b-PEO block copolymers for encapsulation and release of paclitaxel [39]. Similarly, Sanyal and coworkers utilized polyester dendron-polymer conjugates to obtain biodegradable micellar structures [4]. Targeting group conjugated micelles were loaded with an anti-cancer drug doxorubicin, and they showed successful targeted internalization and killing over MDA-MB-231 breast cancer cells.

Polymer micelles have been utilized in various bio-applications. Among them, delivery of siRNA using polymeric nanostructures has also gained much attention because it is used for the treatment of viral infections [40, 41], cancer [42, 43] and hereditary disorders [44]. siRNA generated by degradation of longer double-stranded RNA is a large and anionic water soluble molecule; therefore, the diffusion of siRNA into cell membrane is not easy (since the cell membrane surface is negatively charged). Cationic copolymers are able to bind siRNA, and form micellar structures for effective delivery. Recently, Kataoka and coworkers introduced an siRNA encapsulated micellar polymeric system for targeted delivery [45]. PEG-b-PLL block copolymer was exploited for the fabrication of micelles in the presence of siRNA (Figure 1.5a). To obtain targeting ability, the copolymer was conjugated with cyclic RGD peptide at the PEG chain end, which improves tumor targeting by obtained micelles (Figure 1.5b).

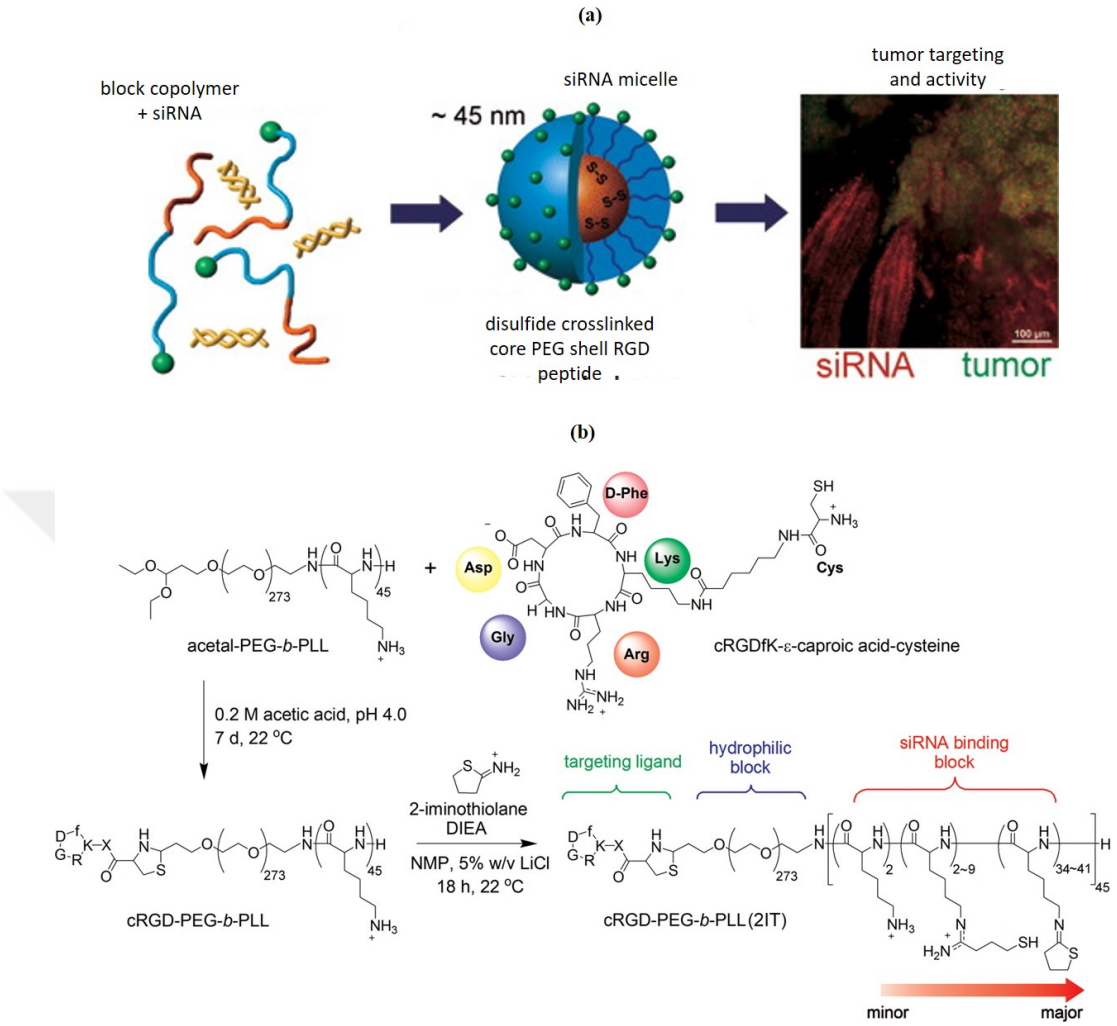

Figure 1.5. (a) Formation of polymer micelle in the presence of siRNA and tumor targeting, (b) modification of PEG-b-PLL with cRGD and 2-iminothiolane. Adapted with permission from [45] Copyright (2017) American Chemical Society.

1.1.2.2. Polymer Nanocapsules. Nanocapsules are one of widely used nanomaterials for biomedical applications. Since they are spherical hollow nanostructures, they allow introduction of various materials into their voids. The fabrication of nanocapsules can be achieved using numerous methods such as nanoprecipitation, emulsion polymerizations, LbL self-assembly and so forth [46, 47]. Nanocapsules formed by self-assembly of amphiphilic block copolymers are called as polymersomes (Figure 1.6a). Similarly, two oppositely charged polymers can self-assemble via LbL self-assembly to form nanocap-

sules (Figure 1.6b) [48]. However, formation of nanocapsules generally requires a solid template that can be removed after formation of the capsule. Such templates are called as sacrificial templates, and Au, PS and silica NPs are often used as sacrificial templates [49–52]. After removal of these solid templates, hollow nanocapsules that are able to load therapeutic molecules are readily formed. Size of nanocapsules can be modulated by varying the size of sacrificial template from 10 nanometers to several micrometers. Thickness and shell composition of nanocapsules mainly determine their chemical and mechanical properties [53].

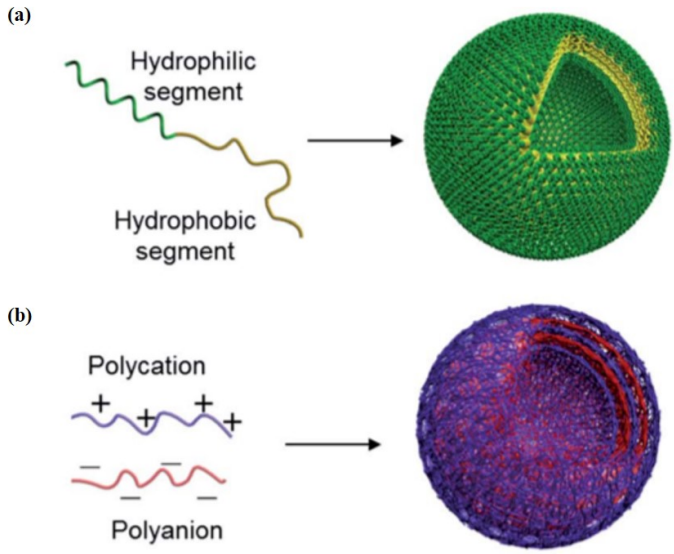

Figure 1.6. Polymeric nanocapsules formed via (a) self-assembly of amphiphilic polymers and (b) LbL self-assembly of charged polymers. Reproduced from Ref. [48] with permission from The Royal Society of Chemistry.

Due to their larger inner voids, nanocapsules have higher therapeutic loading capacity. Drugs stored in the void of nanocapsules are protected from external environment by the shell. Moreover, drug release can be well controlled if nanocapsules are made up of stimuli responsive polymers. Das, Swarnakar, Pramanik and coworkers studied melatonin-loaded pH-responsive biodegradable nanocapsules fabricated via an inverse mini-emulsion technique [54]. In acidic pH, hydrolysis of polymeric backbone stimulated degradation of nanocapsules and eventually the release of entrapped drug. Same research group also evaluated enzyme-triggered drug release from nanocapsules

obtained using the same methodology [55]. The voids of nanocapsules were used for the encapsulation of doxorubicin and a fluorescent dye (Figure 1.7). Repetitive ester groups of nanocapsules ensured drug release and its biodegradation in the presence of an ester hydrolysis enzyme. Moreover, alkylated triphenylphosphonium cation was conjugated onto the surface of nanocapsules to facilitate mitochondrial targeting (Figure 1.7).

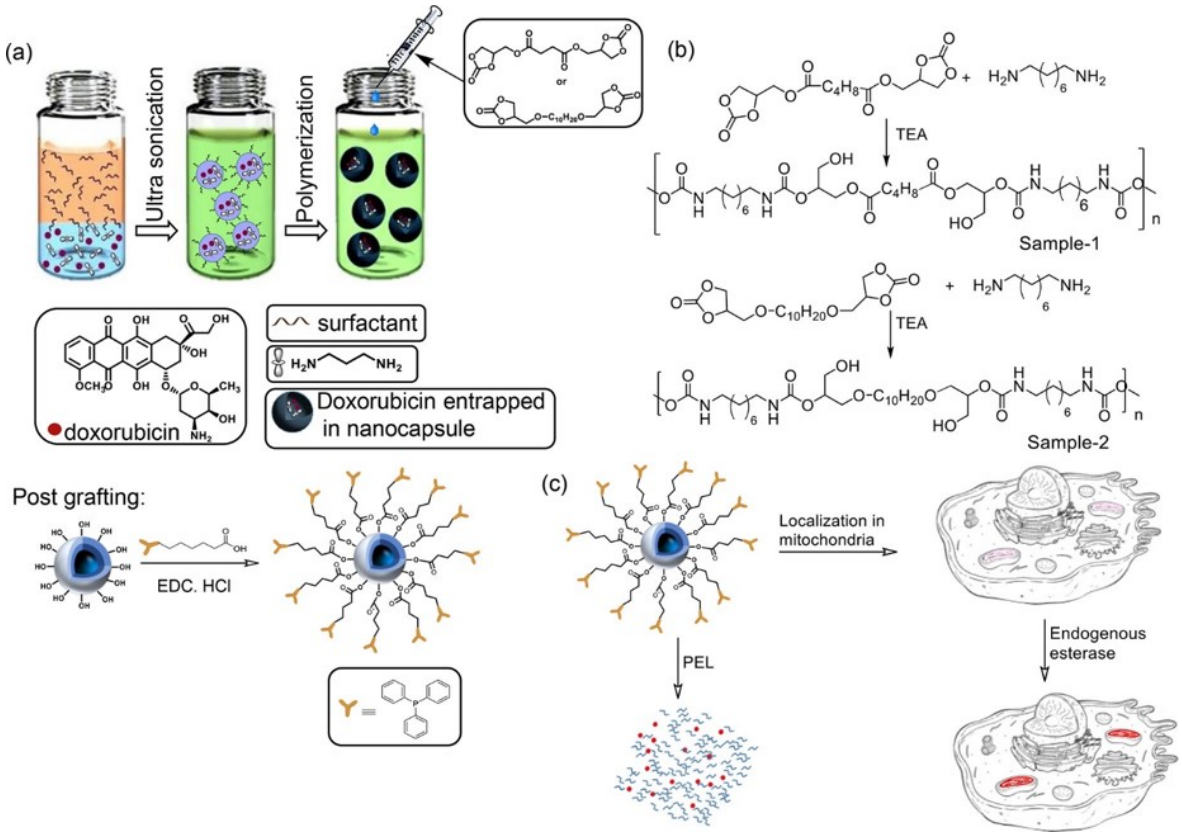

Figure 1.7. (a) Schematic representation of a base catalyzed interfacial polymerization reaction between amine and carbonate monomers in an inverse mini-emulsion, (b) synthesis of polymer and (c) enzymatic degradation and cellular uptake of nanocapsules. Adapted with permission from [55] Copyright (2017) American Chemical Society.

1.1.2.3. Nanogels. Nanogels are physically or chemically crosslinked polymer chains with the dimension of nanometer. The growing interest for nanogels is due to their potential in biomedical applications such as drug delivery, imaging, etc. [5, 56–58]. Characteristic properties of nanogels like size, surface charge and so on are dependent

on their chemical composition. They can host and deliver a plethora of hydrophilic or hydrophobic molecules with their tunable size and properties. Especially, nanogels are highly convenient delivery vehicles for proteins and biomolecules since they protect these biomolecules from degradation providing excellent host environment.

Synthesis of nanogels can be carried out using various techniques including self-assembly of amphiphilic polymer, emulsion polymerization and precipitation polymerization [59–61]. In emulsion polymerization, monomers confined in an emulsion are polymerized in the presence of a crosslinker (Figure 1.8a and b) [62]. One drawback of this polymerization is that it requires a surfactant for emulsion which can cause toxicity even if trace amount of surfactant remains after purification. In contrast, self-assembly of amphiphilic copolymers provides a surfactant free fabrication of nanogels after covalent crosslinking (Figure 1.8c). The crosslinking can be achieved via various approaches such as click chemistry, photo-induced radical crosslinking and so on [63–66].

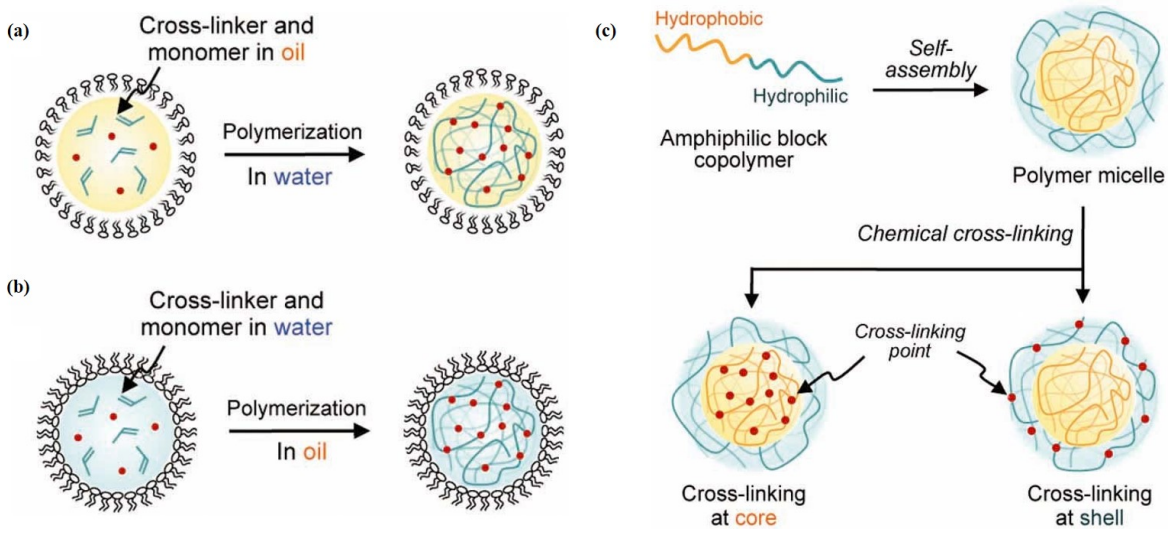

Figure 1.8. Nanogel preparation by emulsion polymerization (a) with oil-in-water emulsion, (b) with water-in-oil emulsion and (c) by crosslinking of amphiphilic block copolymer at core or shell of the polymer micelles in water. Reproduced from Ref. [62] with permission from John Wiley and Sons.

Nanogels obtained by stimuli responsive polymers could change their conformation and structure in response to stimuli. That triggers the release of entrapped molecules from the nanogels. For example, nanogels containing disulfide linker can deliver their cargo remaining stable in the blood but they readily release the cargo when internalized in the cell. Chen and coworkers reported hyaluronic acid nanogels with disulfide linker for the encapsulation of doxorubicin [67]. Glutathione induced release of doxorubicin was successfully shown. In another redox responsive nanogel work investigated by Matyjaszewski and coworkers, disulfide containing dimethacrylate crosslinker was used to fabricate biodegradable nanogels [68]. Similarly, glutathione facilitated the release of cargo upon cleavage of disulfide bonds in the crosslinker. Recently, Falcimaigne-Cordin, Haupt and coworkers reported molecularly imprinted redox responsive nanogels [69]. S-Propranolol was imprinted during the polymerization of methacrylic acid in the presence of two different disulfide containing crosslinkers (Figure 1.9). These nanogels were effectively release the template molecule in a reductive environment.

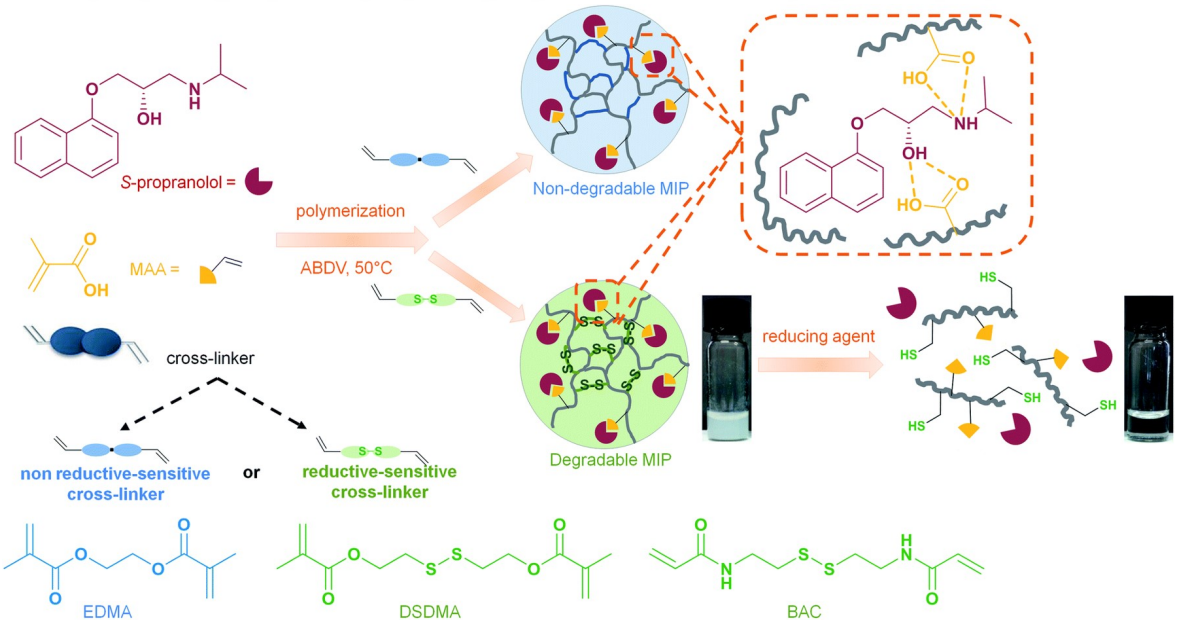

Figure 1.9. Synthesis and reduction-induced degradation of S-propranolol molecularly imprinted polymers for drug delivery. Reproduced from Ref. [69] with permission from The Royal Society of Chemistry.

1.1.2.4. Polymer Nanocomposites. Polymer nanocomposites are a mixture of polymers and non-polymeric organic or inorganic molecules in nanometer size. Inorganic components could be nanoparticles, graphene, nanotubes while organic molecules inside polymer dispersion are mostly composed of phytochemicals, biomolecules, etc [70–73]. Inorganic materials containing polymer nanocomposites will be discussed in the following section. Here, organic components dispersed in polymer matrix are outlined.

In nanocomposite formation, polymers are mostly used to stabilize nanofillers that are not stable or soluble in aqueous environment. These nanocomposites have unique physical and chemical properties due to the combined properties of fillers and polymers. For example, polypropylene suffers from its brittleness and high hydrophobicity in many applications. To circumvent these drawbacks of polypropylene, a polymer nanocomposite with polypropylene in the matrix structure can be utilized. Kessler and coworkers recently demonstrated PDA surface coating on polypropylene for polymer nanocomposite applications [74]. However, they did not show any biomedical applications with these nanocomposites.

Polymer nanocomposites for stabilization of phytochemicals for eradications of biofilm have been thoroughly investigated by Rotello and coworkers. Even though phytochemicals are known as natural antibacterial agents, their poor solubility and inability to penetrate into biofilms need to be addressed for biofilm related infections. Therefore, Rotello and coworkers proposed an oil-in-water emulsion system that contains a phytochemical as an oil phase stabilized by amphiphilic copolymers [75]. As shown in Figure 1.10, a phytochemical, carvacrol, that contains p-MA-alt-OD was initially emulsified in water using an amalgamator. PONI-GAT polymer was also dissolved in water before emulsification in order to stabilize carvacrol emulsions in water. Further stabilization was achieved via crosslinking of the polymer with p-MA-alt-OD. MDR bacterial biofilms were successfully eradicated using these nanocomposites (Figure 1.10).

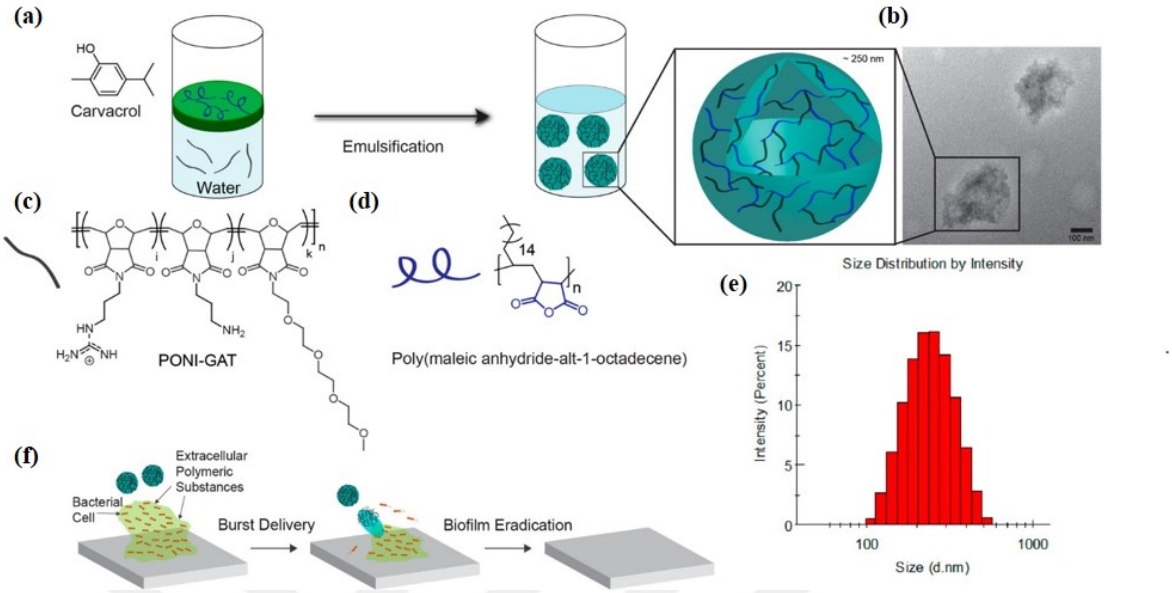

Figure 1.10. (a) Emulsification of p-MA-alt-OD containing carvacrol oil in PONI-GAT dissolved water, (b) TEM image of nanocomposites, (c) chemical structure of PONI-GAT, (d) chemical structure of p-MA-alt-OD, (e) size distribution of nanocomposites and (f) biofilm distribution with carvacrol loaded nanocomposites. Adapted with permission from [75] Copyright (2017) American Chemical Society.

1.2. Polymer Coated Metal Nanoparticles for Biomedical Applications

The commonly used nanoparticles in biomedical applications includes metal nano particles like gold, cobalt and iron, carbon based nanoparticles such as polymer nanoparticles, graphene, carbon nanotubes, and semiconductor nanoparticles like quantum dots. In this section, some important biomedical applications of metal based nanoparticles will be explained in details. Metal nanoparticles have been used in numerous biomedical applications such as drug delivery, imaging, photothermal therapy, protein separations, etc. due to their very high surface area to volume ratio, biocompatibility and easy surface modification [76–78].

Au NPs are easy to synthesize and show good stability in aqueous environment when their surface is modified with water soluble polymers. The surface of Au NPs is

mostly modified with thiol bearing small molecules or polymers exploiting the strong gold-thiol interactions. Surface modification of Au NPs allows the design of targeted imaging agents, biological sensors and drug delivery vehicles. To protect nanoparticles from surrounding biological invasion in biomedical applications, antibiofouling polymers should be coated onto the surface of Au nanoparticles [79–81]. For example, Sanson and coworkers recently evaluated the colloidal stability of Au NPs using thiol bearing antibiofouling zwitterionic polymers which have both positive and negative charges on the polymer chains [82]. It is well known that zwitterionic polymers show very good antibiofouling property due to their high hydration capacity [83, 84]. Beside zwitterionic polymers, PEG coatings also acquire antibiofouling behavior to Au NPs [85,86]. Therefore, PEGylated Au NPs are regarded as potential targeted delivery agents for cancer treatment. Recently, Kataoka and coworkers used PEG-PLL polymer for surface modification of Au NPs, and they utilized these particles for the delivery of siRNA to cervical cancer via targeted pathway [87]. PEG-PLL polymer was modified with cRGD for effective targeting and with LA at the ω-end for immobilization onto Au NP surface. Then, this copolymer was mixed with siRNA to obtain monodisperse uPICs (Figure 1.11). Immobilization of uPICs onto Au NPs was achieved by the conjugation of Au and LA at the polymer termini (Figure 1.11). They evaluated targeted siRNA delivery on HeLa-luc cells and demonstrated enhanced cellular internalization.

Polymer modified magnetic NPs are attractive for biomedical applications since they can be manipulated by external magnetic fields for desired applications. Magnetic properties of these nanoparticles are mainly determined by their size; thus, many attempts have focused on production of NPs with narrow size distribution to ensure uniform chemical and physical properties [88–90]. Magnetic iron oxide NPs can be synthesized by co-precipitation, thermal decomposition, sonochemical method and etc. [91–93]. Among these methods, thermal decomposition of ferric oleate complex in the presence of a high boiling solvent with surface capping agents like oleic acid provides a versatile method for the fabrication of highly monodispersed magnetic iron oxide NPs [94, 95]. However, thermal decomposition method generally ends up with organic solvent dispersible MNPs that are not suitable for biomedical applications.

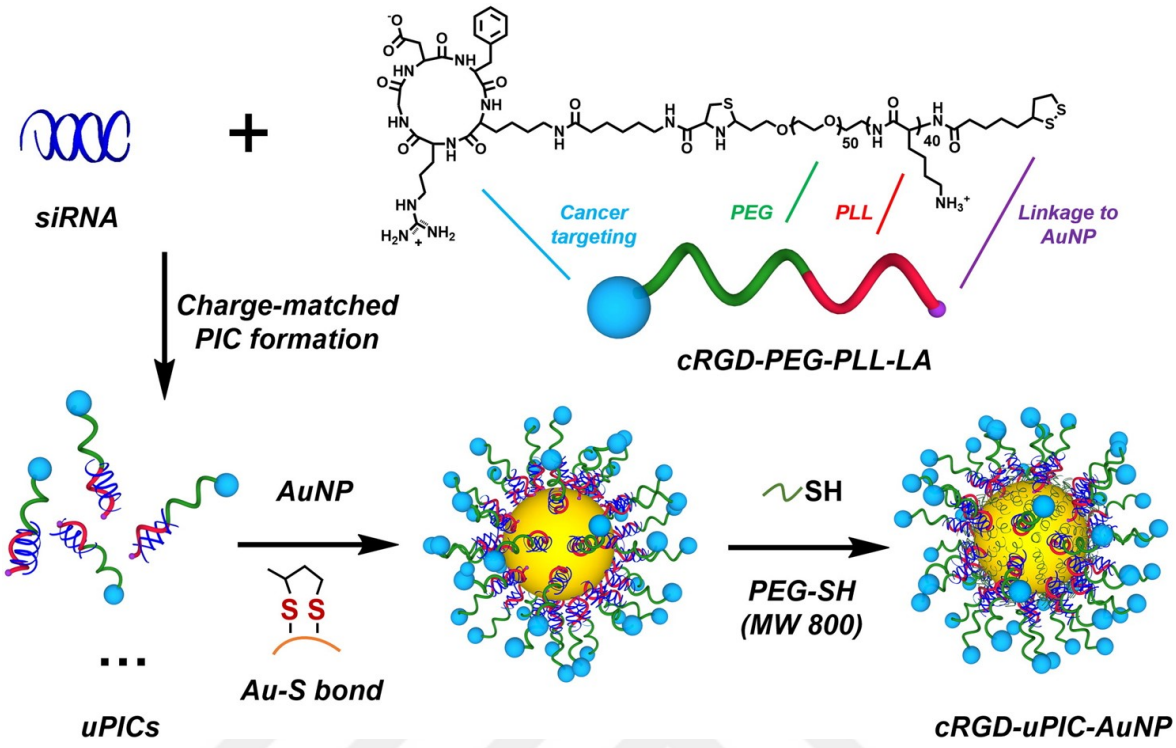

Figure 1.11. Preparation of cRGD-uPIC-AuNPs. cRGD-PEG-PLL modified with LA (cRGD-PEG-PLL-LA) at the ω-end was mixed with a single pair of siRNA to form monodisperse uPICs. Then, the uPICs were conjugated onto a 20 nm AuNP core through double Au–S bonds, followed by grafting of short PEG for construction of monodispersed 40 nm-sized cRGD-uPIC-AuNP. Reproduced from Ref. [87] Copyright (2016) with permission from Elsevier.

Therefore, water soluble capping agents are utilized for the coating of MNPs surface to render the particles water-dispersible. The most commonly used ligands which tether the iron oxide NP surface are the ones that contain catechol, carboxylic acids and phosphonates groups (Figure 1.12) [96–98]. Utilizing these anchoring groups, water soluble polymers can be immobilized onto iron oxide surface. Polymer coated MNPs have been exploited for drug delivery, MRI imaging, magnetic hyperthermia, protein separation and targeted cellular imaging [99–104].

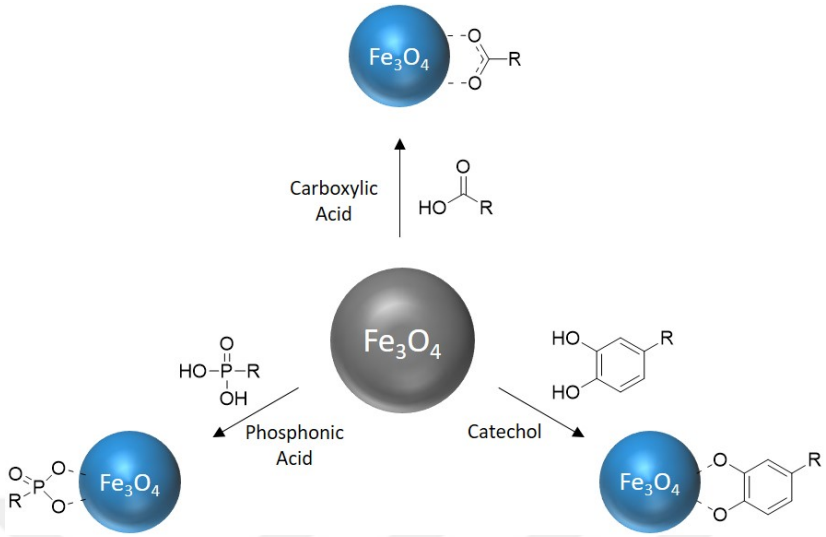

Figure 1.12. Commonly used anchoring groups for the surface modification of iron oxide NPs for biomedical applications.

Davis and coworkers recently described the surface modification of iron oxide NPs synthesized through thermal decomposition method with biocompatible PEG based polymers containing DBM to provide a new strategy for the development of selectively targeting nanoprobes [105]. Block co-polymerization was carried out using DBM containing RAFT agent in the presence of PEG acrylate and phosphonate monomers, respectively. Phosphonic ester group of the block co-polymer was dealkylated to yield phosphonic acid group that is a good anchoring group for iron oxide NPs (Figure 1.13a). Polymer grafting onto the surface was achieved via a place exchange reaction in THF removing the hydrophobic oleic acid coating (Figure 1.13b). The surface coating with synthesized block co-polymer would allow facile surface modification of the NPs since DBM group is reactive toward thiolated biomolecules under benign reaction conditions. Moreover, intrinsic fluorescent character of the DBM conjugates can be exploited for labelling and tracking. Therefore, tumor specific GRP78-binding peptide (CRLLDT-NRPFLPY) was conjugated to iron oxide NPs to investigate specific cellular targeting. Upon 2 h incubation with MCF-7 breast cancer cell line, iron oxide NPs conjugated with GRP78-peptide showed a fluorescence under confocal microscopy (Figure 1.13d) while iron oxide NPs devoid of binding peptide as control group demonstrated no emis-

sion (Figure 1.13c). Successful cell internalization of the NPs with GRP78-peptide was probed by colocalization confocal images.

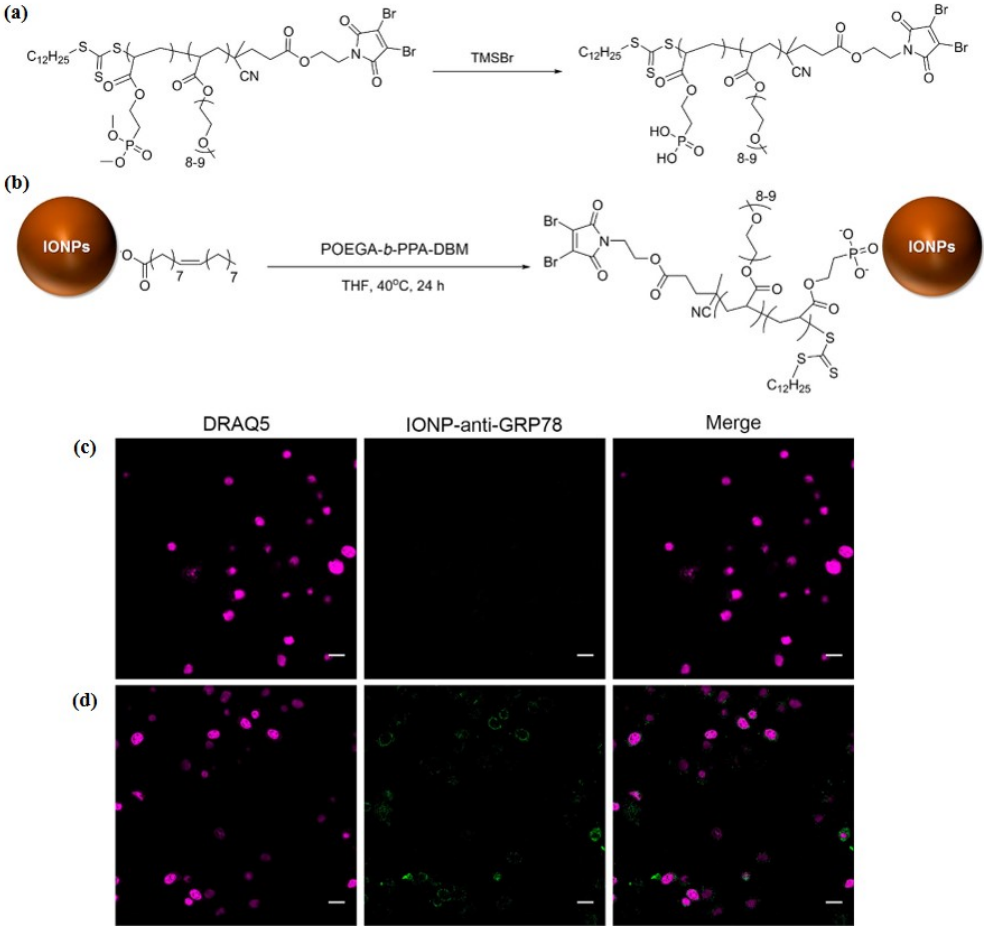

Figure 1.13. (a) Deprotection of the phosphonate groups, (b) surface ligand exchange of the oleic acid coated iron oxide NPs, (c) confocal images of polymer coated NPs and (d) confocal images of GRP78 peptide conjugated NPs incubated with MCF-7 cell line. Left to right: images under different channels including the nuclei stained by DRAQ5, PBM fluorescence, and the merged images. Scale bars = 10 μm. Adapted with permission from [105] Copyright (2018) American Chemical Society.

1.3. Graphene Based Materials for Biomedical Applications

Graphite, an allotrope of carbon, is formed by the multiple stacking of two dimensional (2D) carbon sheets arranged in a hexagonal lattice. Single sheets in graphite

are called as graphene, which was isolated by Novoselov and Geim for the first time in 2004 [106]. Since its first isolation, graphene has been used in various applications including drug delivery, sensors, cellular imaging, DNA detection, photodynamic therapy due to its electronic, thermal and optical properties [107–111]. Its hydrophobic nature limits some of the biomedical applications, and requires modification with oxygen containing functional groups. Therefore, oxidation of graphite helps not only for the fabrication of a water dispersible family member of graphene called as graphene oxide but also exfoliation of stacked layers. However, oxidation of graphite gives rise to some defects on graphene layer as well as destroyed π-conjugation, which affects most of the physical and chemical properties of graphene. To recover π-conjugation maintaining single layer structure, graphene oxide is generally reduced by suitable reducing agents, and obtained material is called as reduced graphene oxide (Figure 1.14). Along with oxidation-reduction process, liquid-phase exfoliation and micromechanical cleavage are in the class of top-down graphene fabrication methods while epitaxial growth on SiC and chemical vapor deposition are known as bottom-up approaches (Figure 1.14) [112].

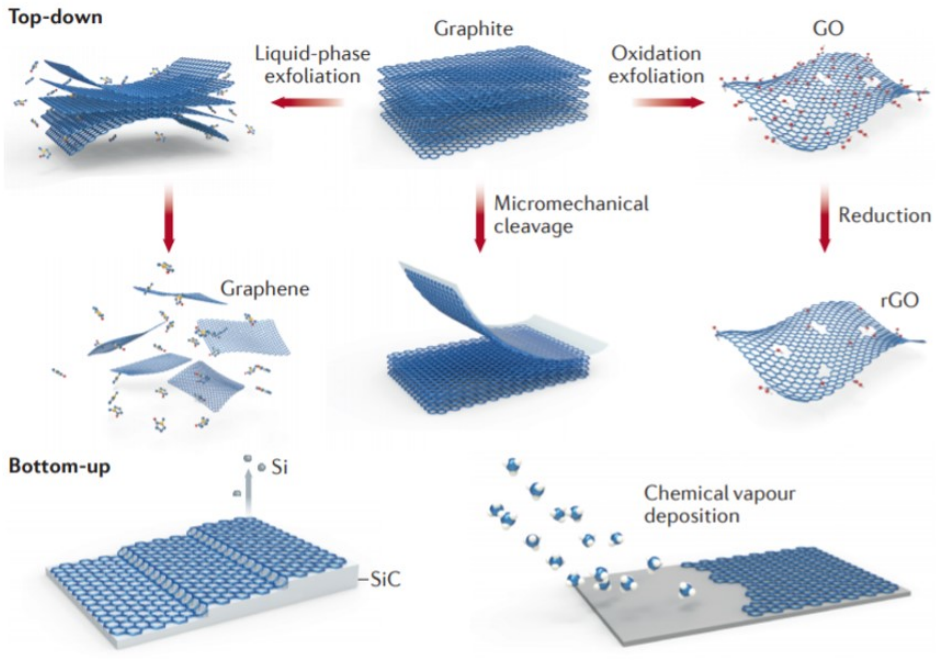

Figure 1.14. Fabrication of graphene by different methods. Reprinted by permission from [112] Copyright (2017) Springer Nature.

High surface area of 2D graphene oxide sheets allows loading of drug molecules via hydrophobic and π-π stacking interactions, and conjugation of different molecules exploiting functional groups on graphene oxide surface. For example, epoxide or carboxylic acid functional groups on graphene oxide could be used for the attachment of a targeting group. In that way, graphene oxide can deliver its payload in a targeted manner and release it in response to a stimulus such as pH and NIR light (Figure 1.15) [113]. Due to very efficient light to heat conversion ability of graphene oxide, NIR light induced drug release from graphene based materials has been widely utilized [114–116]. Also, pH difference between the cytoplasm and the extracellular matrix can trigger drug desorption from graphene oxide surface. pH triggered drug release is generally achieved by broken hydrophobic and π-π stacking interactions between drug molecules and graphene oxide.

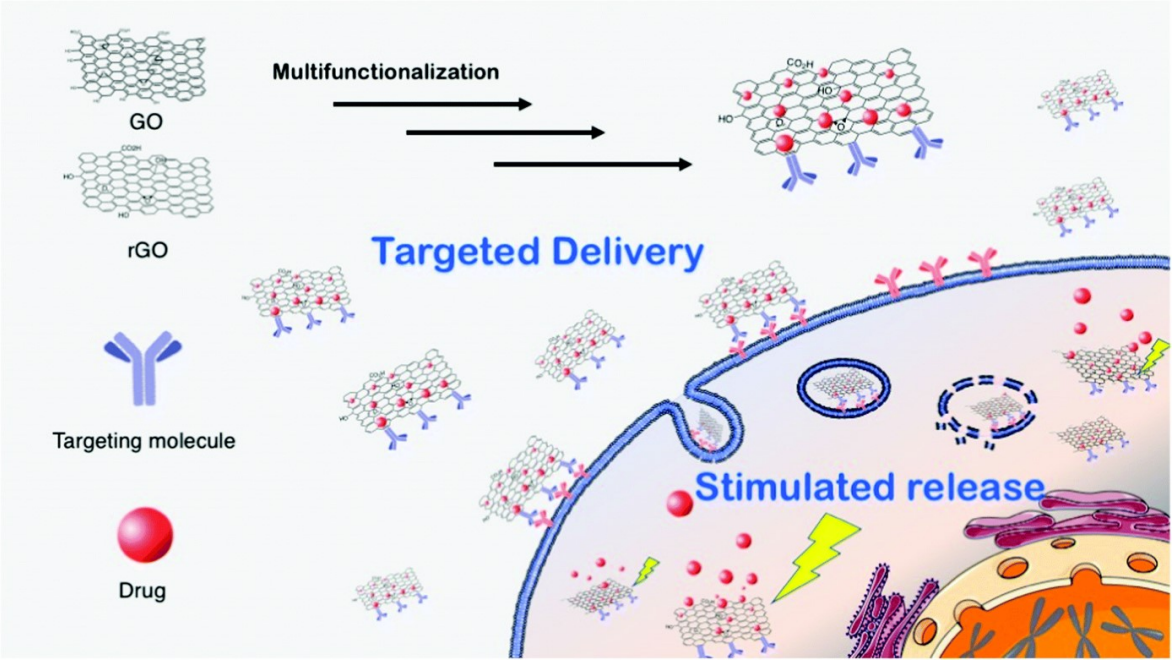

Figure 1.15. Targeted drug delivery via graphene oxide and reduced graphene oxide. Reproduced from Ref. [113] with permission from The Royal Society of Chemistry.

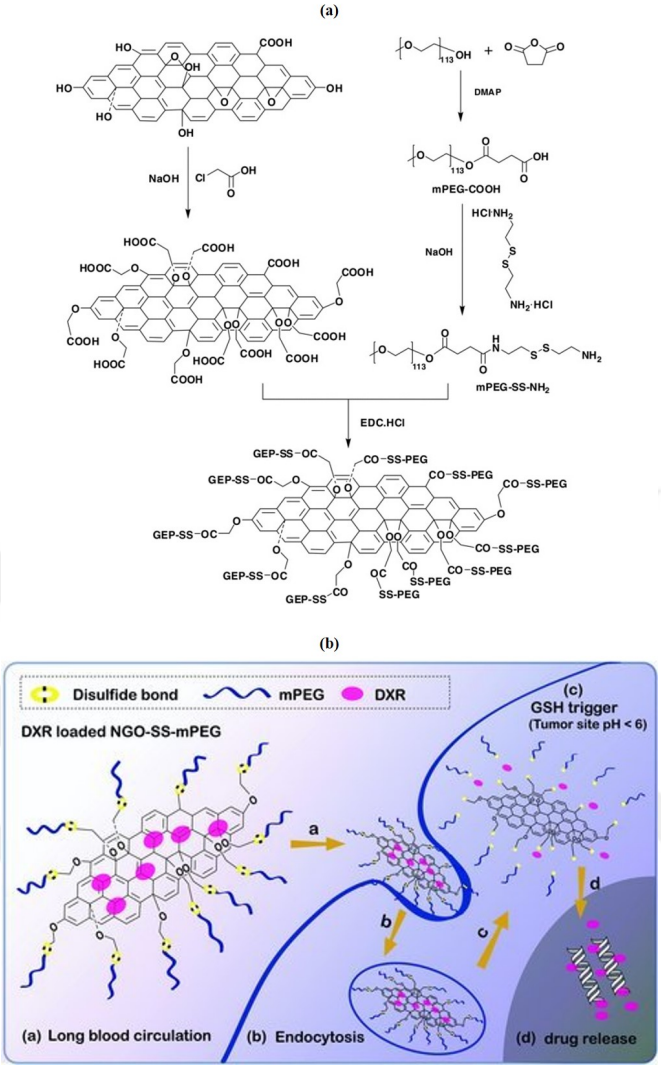

Figure 1.16. (a) Synthesis of PEGylated graphene oxide and (b) anti-tumor activity of doxorubicin loaded redox responsive nano-graphene oxide and GSH triggered drug release in tumor cells. Reproduced from Ref. [120] with permission from John Wiley and Sons.

The surface characteristics of graphene oxide can be tuned by the conjugation of functional groups such as clickable azide or maleimide. Furthermore, tunable surface modification of graphene oxide may improve its drug loading capacity and also reduce nonspecific drug release in the body. Utilizing functional groups on the graphene oxide surface, synthetic antibiofouling polymers are easily attached onto the GO, which mainly avoids fouling of biomolecules. PEGylation has been commonly used for the

fabrication of antibiofouling graphene oxide materials for drug delivery applications. PEGylated graphene oxide materials not only have a prolong circulation time in the body but also have ability to accumulate at the tumor site via EPR effect [117]. However, drug release from PEGylated delivery vehicles can be hindered by PEG's diffusion barrier [118,119]. Recent work by Shi, Li and coworkers focused on this dilemma caused by PEGylation of graphene oxide [120]. As shown in Figure 1.16a, disulfide containing amino-terminated PEG was conjugated to carboxylated NGO sheets. This design ensures stability of NGO in physiological conditions while enabling the release of loaded drug upon GSH trigger inside the tumor cells. Doxorubicin was loaded on NGO utilizing strong π-π and hydrophobic interactions. NGO releases its payload in the presence of GSH after internalization via endocytosis because it is well-known that GSH concentration is significantly higher inside cells. Redox responsive disulfide is readily broken by GSH and subsequently PEG is released, which facilitates the release of doxorubicin from NGO (Figure 1.16b).

2. RESEARCH OVERVIEW

The scope of this dissertation is fabrication of NPs, polymeric and rGO based materials for various biomedical applications. Therefore, several polymerization techniques such as ROP, RAFT and FRP were applied to synthesize hydrogels, NCs and polymer grafted MNPs. Desired functional groups on polymer side chain or end group were borne via post-polymerization modifications utilizing retro Diels-Alder chemistry and radical cross-coupling reactions.

The first two chapters cover rGO based materials for drug delivery applications. Graphene is considered as a wonder material due to its very efficient light to heat conversion ability as well as high surface area with a large number of pi-conjugation that allows its use in a wide range of applications. In this thesis, rGO containing hydrogels obtained by photo-induced FRP were utilized for on-demand release and transdermal delivery of insulin. Moreover, rGO was also used for the delivery of a chemotherapy drug in a targeted manner. A targeting agent was attached to rGO through maleimide-thiol click reaction. In the following chapters, thesis focuses on magnetic and polymeric NPs for targeted imaging, lectin separation and biofilm eradication applications. Surface of polymer coated MNPs was modified with clickable groups for the conjugation of a targeting peptide and imaging agent. In the following work, polymer end groups of MNPs were modified with a sugar that selectively binds a lectin in a lectin mixture. A sepecific lectin was separated by a magnetic attraction using these particles. Finally, maleimide functional biodegradable polymers were used for the fabrication of phytochemical loaded NCs. These NCs demonstrated a broad spectrum activity against bacterial biofilms. Maleimide groups were exploited for crosslinking of NCs to bear extended stability in physiological conditions. In summary, this dissertation is related to rGO based hydrogels and drug delivery systems, polymer coated MNPs for targeted cellular imaging, lectin separation and phytochemical loaded polymeric NCs for biofilm disruption.

3. PHOTOTHERMALLY TRIGGERED ON-DEMAND INSULIN RELEASE FROM REDUCED GRAPHENE OXIDE MODIFIED HYDROGELS[1]

3.1. Introduction

The controlled release of active principles over long-term periods has been recognized as one of the most promising biomedical technologies for the treatment of certain types of diseases. Medical conditions such as cancer, diabetes and chronic pain require medications that must be dosed intermittently on-demand and over a long period of time. To address these issues, intelligent drug delivery systems for on-demand release are highly desirable. These smart drug carriers offer important advantages over systematically administered drugs as they are able to overcome problems associated with drug solubility and stability and allow accumulation and release of the therapeutics at selected locations [122–127]. Among the different smart drug carriers such as liposomes, microspheres or hydrogels, graphene-based materials are emerging nanostructures for drug delivery [124, 127–132]. The high specific surface area of graphene combined with the various interactions offered by this material (π-π stacking, electrostatic, hydrophobic interactions, hydrogen bonding) is beneficial for achieving high drug loading of poorly soluble drugs without compromising potency or efficiency [117, 127, 133, 134].

Graphene-based drug carriers have also successfully been utilized to develop stimuli-responsive nanocarriers [124,135]. The effectiveness of rGO as an NIR-absorbing photothermal agent with excellent stability and rapid light-to-heat conversion under low-power NIR irradiation led to the development of photothermally triggered release systems [115, 131, 136–138]. Controlled release in response to illumination at a specific wavelength has the advantage of being non-invasive with the possibility of remote spatiotemporal control due to good heat confinement using optimized irradiation conditions [131]. Poly(N-isopropylacrylamide) functionalized graphene loaded

[1]Published in Journal of Controlled Release [121]. Reproduced by permission of Elsevier.

with anticancer drugs has been previously exploited for temperature dependent drug release with reported higher potency and efficiency than the free drug [138]. FeCo-graphene nanocomposite showed remarkable enhanced photothermally triggered drug release [136]. Photothermally-induced cytosolic doxorubicin delivery via endosomal disruption as well as photothermally-controlled gene delivery from functionalized rGO was recently demonstrated by the group of Kim and co-workers [137]. Chitosan-modified rGO loaded with doxorubicin was proposed by Wang *et al.* as thermosensitive nanogel, where upon NIR light action, rapid and repetitive doxorubicin release was observed [115]. Matteini *et al.* reported more recently the use of millisecond-long light pulses for the controlled release of different molecules from chitosan-modified rGO nanogels [131]. Using 8 repeated laser pulses of 200 ms and 40 - 42 J cm^{-2}, the delivery of insulin through the submicrometer pores of the chitosan-rGO film was demonstrated [131].

Indeed, the release of therapeutic proteins such as insulin is of high interest for treatment of diabetic patients. The oral administration of hydrophilic molecules such as insulin is encountered with many difficulties such as denaturation by the low pH of the gastric medium in the stomach as well as degradation by different digestive enzymes. Current treatment methods involve therefore regular injections of insulin, which can be both painful and inconvenient [139]. In order to overcome these hurdles, new insulin formulations as well as administration systems have been sought after. Kim *et al.* developed sugar-responsive delivery vehicles of insulin based on polymersomes [140]. Self-regulated insulin delivery was achieved by phenylboronic acid bearing hydrogels [141]. While electrically erodible polymer gels have been proposed by Kwon *et al.* [142], prolonged insulin delivery in diabetic rabbits was achieved using poly(lactide-ethylene-glycol) nanoparticles [143]. Insulin amidated pectin hydrogels were recently proposed as insulin delivery platforms by Hadebe *et al.* [144]. Teodorescu *et al.* have recently exploited the good electrical properties of rGO thin films for efficient electrochemical release of human insulin from rGO-modified electrodes [128]. Thermally modulated insulin release approaches have to be added to the list [130, 131, 145]. Poly(N-isopropylacrylamide-co-acrylic acid) microgel thin films [145] as well as poly-

meric microneedles [130] filled with insulin have been proposed as thermally activable delivery platforms.

Although desirable release profiles were obtained in these studies, extent of insulin loading and release 'on-demand' still remains a challenge to enable translation of these findings into the clinic and thus warrants the development and testing of alternative platforms. Burst release of the therapeutics is often encountered in many polymer and hydrogel based formulations [131, 146]. While the photothermal triggered release of insulin was demonstrated by Matteini [131], no details about loading/release capacity as well as on the insulin activity after photo-triggered release were given so far, crucial parameters when it comes to consider therapeutic applications.

In this work, we provide an in-depth study and evolution of the insulin loading capacity into rGO entrapped PEG hydrogels and laser-controlled, repetitive insulin release on demand (Figure 3.1). PEG-based hydrogels are investigated in this work as scaffold materials because they are widely utilized and are well established matrices for immobilization and encapsulation of biomolecules [129]. PEG molecules provide a non-interacting hydrophilic environment that preserves the biological activity of biomolecules by maintaining their structural conformation due to lack of denaturing interactions. Commercially available PEGDMA is utilized as hydrogel precursor and photo-polymerized in the presence of varying amounts of well-dispersed rGO to yield hydrogels in a single step. The hydrogel matrix is designed to induce a photothermal heating effect upon exposure to NIR irradiation, which results in a controlled release of insulin at therapeutic relevant concentrations in few minutes. It will be shown that, upon optimization of the insulin loaded scaffold, therapeutic levels of insulin can be released in short time. Most importantly, we demonstrated that the photothermal triggered insulin release has no bearing on the biological activity of insulin, nor on cell viability a necessity required for effective therapeutic treatment. The ability of the hydrogel matrix for the transdermal delivery of insulin across the skin is in addition evaluated.

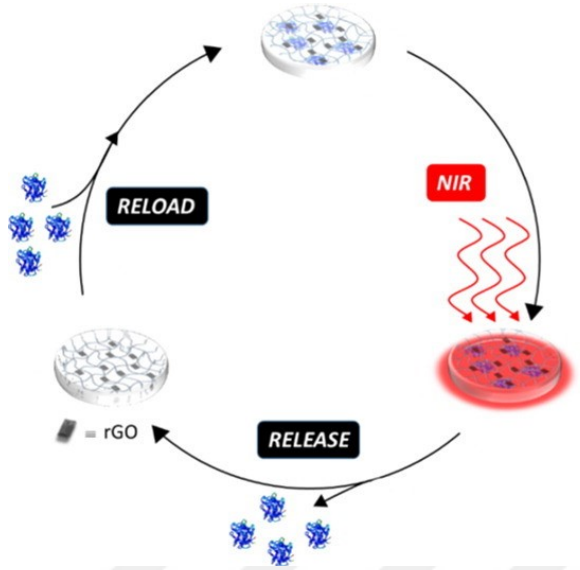

Figure 3.1. PEG-based hydrogels impregnated with rGO that allow efficient loading and 'on-demand' photothermal release of insulin.

3.2. Experimental

3.2.1. Materials and Characterizations

2-Hydroxy-4′-(2-hydroxyethoxy)-2-methylpropiophenone, human insulin, sodium hydroxide, PEGDMA M_n = 550 g mol^{-1}, acetic acid, hydrazine hydrate and chitosan were purchased from Sigma Aldrich. PEGDMA was purified by passing through an activated aluminum oxide column prior to use. GO powder was purchased from Graphenia, Spain.

SEM images were obtained by ESEM-FEG/EDAX Philips XL-30 (Philips, Eindhoven, The Netherlands) instrument using an accelerating voltage of 10 kV.; UV-Vis absorption spectra were recorded using SAFAS UV-Vis spectrophotometer in quartz cuvettes with an optical path of 10 mm. The wavelength range was 200 - 1100 nm; FT-IR analyses were performed on Thermo Fisher Scientific Inc, Nicolet 380. Micro-Raman spectroscopy measurements were performed on a LabRam HR Micro-Raman system (Horiba Jobin Yvon, France) combined with a 473-nm laser diode as excitation source.

Visible light is focused by a 100x objective. The scattered light is collected by the same objective in backscattering configuration, dispersed by an 1800 mm focal length monochromator and detected by a CCD. TGA was conducted on a TA instruments at a heating rate 10 °C/min under a nitrogen atmosphere.

3.2.2. Synthesis of PEGDMA-rGO Hydrogels

To 5 mL GO aqueous suspension (0.5 mg mL^{-1}) was added hydrazine hydrate (0.50 mL, 32.1 mM) and heated in an oil bath at 100 °C for 24 h over which the reduced GO gradually precipitated out the solution. The product was isolated by filtration over a PVDF membrane with a 0.45 μm pore size, washed copiously with water (5 x 20 mL) and methanol (5 x 20 mL), and dried overnight in an oven. For the preparation of PEGDMA-rGO hydrogels, rGO (0.1 - 1.2 mg) was dispersed in 130 μL of water under ultrasonication. PEGDMA (99.2 mg, 0.18 mmol) and 2-hydroxy-4′-hydroxyethoxy-2-methylpropiophenone (0.4 mg, 1.78 μmol) were added to the rGO dispersion and sonicated for 2 min to obtain a homogenous mixture. The mixture was irradiated using UV light (365 nm) for 15 min. Thereafter, the rGO containing hydrogel was washed copiously with water, and incubated in water for 12 h to remove all unreacted reagents. The hydrogel was lyophilized before further characterizations. All the other PEGDMA-rGO hydrogels with varying rGO loadings were synthesized using similar procedure.

3.2.3. Insulin Loading

Insulin loading into the hydrogels was achieved by immersion in human insulin (1 mL, 100 μg mL^{-1}) and shaking (150 rpm) at 4 °C overnight. The concentration of insulin loaded into the hydrogels was determined indirectly by measuring the absorption intensity of the remaining insulin in solution at 270 nm using UV-Vis spectrometry. Standard human insulin calibration curve was generated beforehand from a series of insulin solutions ranging from 5 to 200 μg mL^{-1}.

3.2.4. Photothermal Release Studies

Insulin release experiments were performed in 1 mL PBS (pH 7.4) at 37 °C. The hydrogels were irradiated with a continuous mode laser (Gbox model, Fournier Medical Solution) with an output light at 980 nm at various power densities (0.7 - 4 W cm^{-2}) for various time intervals (1 - 60 min). Thermal images were captured by an Infrared Camera (Thermovision A40) and treated using ThermaCam Researcher Pro 2.9 software. The quantity of insulin released was evaluated from the absorbance spectra of the solution collected after irradiation.

3.2.5. Determination of Insulin Activity

The activity of insulin released from the PEGDMA-rGO hydrogels (10 min, 980 nm, 0.7 W cm^{-2}) into water was evaluated, *in vitro*, on a human hepatic HepG2 cell line model using native insulin as a positive control and the same culture without insulin as a negative control. After overnight culture in a serum-free and glucose-free medium, HepG2 cells were incubated for 1 h without insulin (negative control), with native insulin (positive control) and with photothermally released insulin at a physiologically active concentration of 200 nM. After 1 h of incubation, cells were lysed and proteins were collected. Expression of p-Akt and Akt proteins was evaluated by Western blotting analysis. For western blotting experiments, 40 μg of total proteins of each condition was loaded and separated onto a polyacrylamide gel, then transferred on a nitrocellulose membrane. Immunoblotting for p-Akt and Akt was performed using anti p-Akt specific antibody (Thr-308, Cell signaling), anti Akt specific antibody (sc-8312, Santa Cruz) and fluorescence-coupled secondary antibodies against both mouse and rabbit primary antibodies. Analysis of the Western Blot was performed using Odyssey revelation process and Image J quantification technique.

3.2.6. Cytotoxicity Assay

Caco-2 human intestinal cells (Sigma-Aldrich, Steinheim, Germany) were cultured and maintained in Dulbecco's Modified Eagle's medium (DMEM, Gibco®) supplemented with 10 % fetal bovine serum (FBS, Gibco®) and 1 % penicillin-streptomycin (Gibco®) in a humidified incubator at 37 °C and 5 % CO_2. Cells were seeded at a density of 104 cells/well in a 96-well plate and grown for 24 h before assay. The culture medium was replaced with a fresh medium and the hydrogels added. After 24 h, the old medium was aspirated and cells were washed three times with PBS. The cell viability was evaluated using the Cell Counting Kit-8 (CCK-8, Sigma Aldrich) assay. Briefly, 10 μL of the CCK-8 solution was added to each well containing 100 μL of DMEM/10 % FBS, and the plates were incubated for 3 h in a humidified incubator. The absorbance of each well was measured at 450 nm using a microplate reader (PHERAstar FS, BMG LABTECH GmbH, Germany). Each condition was replicated five times and the mean absorbance value of non-exposed cells was taken as 100 % cellular viability.

3.2.7. Apoptosis Assay

Apoptosis was determined by scoring cells displaying pyknotic nuclei (visualized with Hoechst 33, 342). The counting was performed blind by three different experimenters.

3.2.8. Skin Staining and Histology

Before and after laser release studies, porcine skin was cleaned in water, dissected and placed in paraformaldehyde (4 % v/v) for 24 h in order to fix the tissue. The samples were paraffined, sectioned and stained with the Masson's trichrome dye.

3.2.9. Skin Permeation Experiments

Skin permeation studies were performed using fresh porcine ear skin purchased in a local slaughterhouse. After thorough rinsing the pig ear with distilled water, the cartilage and the adipose tissue layer were removed with the aid of a surgical scalpel. The skin was gently shaved and cut into 1.8 cm^2 circular pieces. After measurement of its thickness using a digimatic micrometer (Mitutoyo, France), the skin was used immediately thereafter for diffusion experiments. Insulin skin diffusion experiments were carried out using static Franz diffusion cells (SES GmbH, Analyse System, Bechenheim, Germany) exhibiting an effective area of 0.64 cm^2. After filling the receptor compartment with degassed PBS (1x, pH 7.4), the solution was maintained at 32 °C and stirred with a magnetic stirring bar at around 500 rpm. The porcine skin was carefully clamped between the donor and the receptor compartment (3.1 mL) and pre-incubation in distilled water (receptor compartment medium) for 1 h before the insulin-loaded hydrogel was applied to the skin previously wetted with 100 μL of water to insure contact between the patch and the skin. The diffusion experiment was started and followed for 6 h. The hydrogel was irradiated with a continuous wave laser at 980 nm for 10 min using 0.7 W cm^{-2}. At determined time intervals, 250 μL aliquots of diffused solution were removed from the receptor compartment and analyzed by HPLC. After each sampling, an equal volume of fresh diffusion medium was added to the receptor compartment to maintain a constant volume. All experiments were performed in triplicates. The flux of insulin was determined according to Eq. 3.1:

$$J = \frac{A}{S} \tag{3.1}$$

J Flux of insulin through the skin (μg cm^{-2} h^{-1})

A Linear slope of the cumulative amount versus time curves in equilibrium conditions (μg h^{-1})

S Surface of the membrane of the Franz cell (0.64 cm^2)

HPLC analysis was performed as following:

Kinetex C18 (100 x 4.60 mm i.d., 2.6 μm) column (Phenomenex, Le Pecq, France) preceded by a guard C18 column (1 x 4.60 mm). Gradient elution mode at 1 mL min^{-1} using H_2O (A) and acetonitrile (B), both containing 0.1 % formic acid: linear increase in B from 20 % to 90 % in 5 min; 25 °C; UV detection at 210 nm.

3.3. Results and Discussion

3.3.1. Formulation of rGO Loaded PEGDMA-rGO

Reduced graphene oxide containing hydrogels (PEGDMA-rGO) were prepared through photopolymerization of an aqueous dispersion of rGO, PEGDMA and a photoinitiator under UV irradiation at 365 nm (Figure 3.2a). A free-standing and robust hydrogel was obtained and its chemical composition was confirmed using FT-IR spectroscopy (Figure A.1). The photographs of the hydrogel formulated in the absence and presence of rGO indicated further the successful integration of rGO, as the colorless PEGDMA hydrogel turned grey-black upon rGO loading (Figure 3.2b).

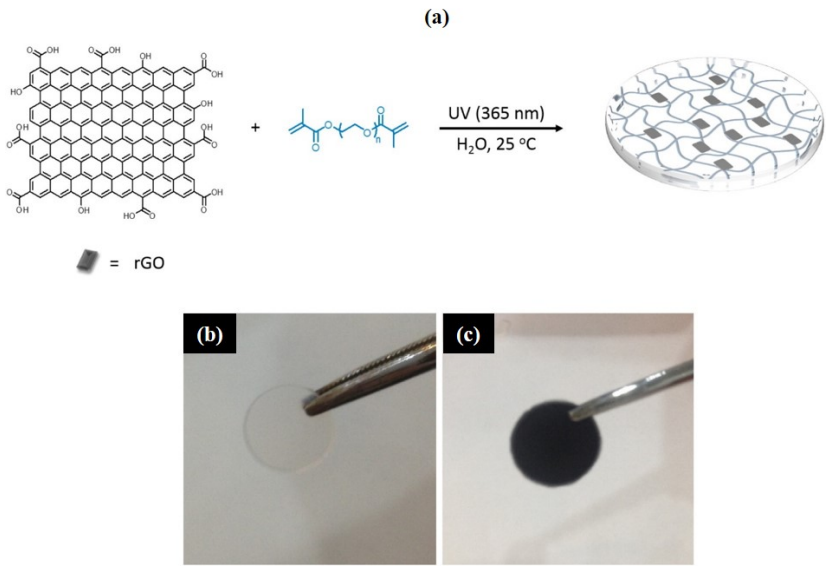

Figure 3.2. (a) Illustration of the fabrication of PEGDMA-rGO hydrogels, (b) photographs of free standing hydrogels without rGO and (c) with rGO (0.8 mg).

The rGO modified hydrogel was further characterized by UV-Vis (Figure 3.3a) spectrophotometry and Raman spectroscopy (Figure 3.3b). The UV-Vis spectrum of GO after reaction with hydrazine at 100 °C displayed an optical absorption peak at 273 nm with an absorption tail in the NIR characteristic of rGO (Figure 3.3a). The PEGDMA hydrogel alone shows strong absorption between 206 and 280 nm. The rGO loaded PEGDMA hydrogel shows a broad absorption in the UV-Vis with a maximum at 273 nm. The significant increase of the absorption tail in the NIR is in accordance of the integration of rGO into the PEGDMA hydrogels.

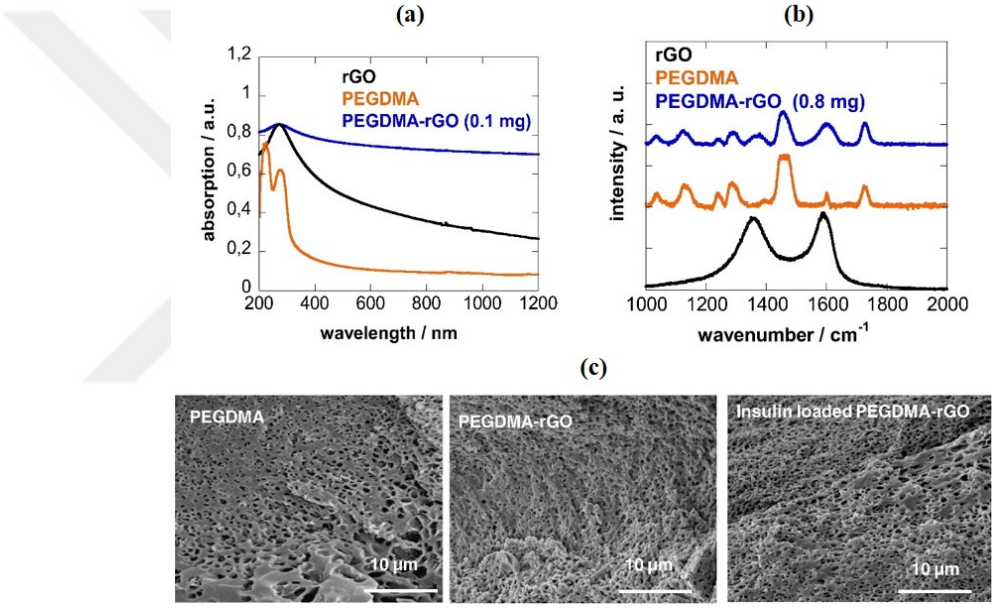

Figure 3.3. Characterization of rGO and rGO loaded PEGDMA hydrogels: (a) UV–Vis absorption spectra of rGO (black), PEGDMA (orange) and PEGDMA-rGO (0.1 mg, blue), (b) raman spectra of rGO (black), PEGDMA (orange) and PEGDMA-rGO (0.8 mg, blue), (c) SEM images of PEGDMA, PEGDMA-rGO (0.8 mg) and insulin loaded PEGDMA-rGO (0.8 mg).

The successful integration of rGO into the hydrogel is validated by Raman spectroscopy. The Raman spectrum of rGO displays bands at ≈ 1350 cm^{-1} (D-band) and ≈ 1580 cm^{-1} (G-band) due to the local defects/disorder and the sp^2 graphitized structure of rGO, respectively (Figure 3.3b). The I_D/I_G intensity ratio was determined to be 0.93 for rGO. The Raman spectrum of PEGDMA hydrogel exhibits several bands

between 1000 and 1800 cm^{-1}. The bands at 1728 cm^{-1} and 1032 cm^{-1} are assigned to C=O and C-O functions on PEGDMA respectively, while the bands at 1235 and 1285 cm^{-1} are due to -CH_2- bonds [147]. While the Raman signatures of the hydrogel prevail, the presence of rGO is clearly identified by the bands at 1359 and 1600 cm^{-1}. The morphology of the PEGDMA-rGO was investigated using SEM, showing a homogenous microporous structure for lyophilized samples after immersion in liquid nitrogen before analysis (Figure 3.3c).

3.3.2. Insulin Loading

Insulin was integrated into PEGDMA-rGO hydrogels through simple immersion of the hydrogel into a human insulin solution (100 μg mL^{-1}) in water for 4 h at room temperature. The hydrogels possess limited swelling since the used PEG chains are short. These hydrogels absorb water equal to their weight as evidenced from the water uptake profile (Figure A.2). Loading the PEGDMA-rGO hydrogels with insulin did not alter the morphology of the patch as evidenced in Figure 3.3c by comparison with the PEGDMA-rGO hydrogels before and after insulin loading.

The loading capacity of PEGDMA-rGO hydrogels for human insulin was evaluated by determining the concentration of insulin in solution before and after loading using UV-Vis spectrometric measurements at 270 nm. At this wavelength, insulin displays a characteristic absorption maximum (inset Figure 3.4a), which scales linearly with its concentration in solution (Figure 3.4a). As seen in Figure 3.4b, insulin loading increases upon the increase of rGO in the hydrogel and saturates at 80 % loading for hydrogels with rGO contents higher than 0.8 mg. These loadings are higher as compared to that obtained by mixing rGO (1 mg mL^{-1}) with human insulin (0.1 mg mL^{-1}) where a loading of 55 % was reached [128]. The 3D structure of the hydrogel seems to be favorable for the integration of insulin. Indeed, the major adsorption of insulin is due to interaction with the porous hydrophilic network of the PEG-based hydrogel network as suggested by Figure 3.4b.

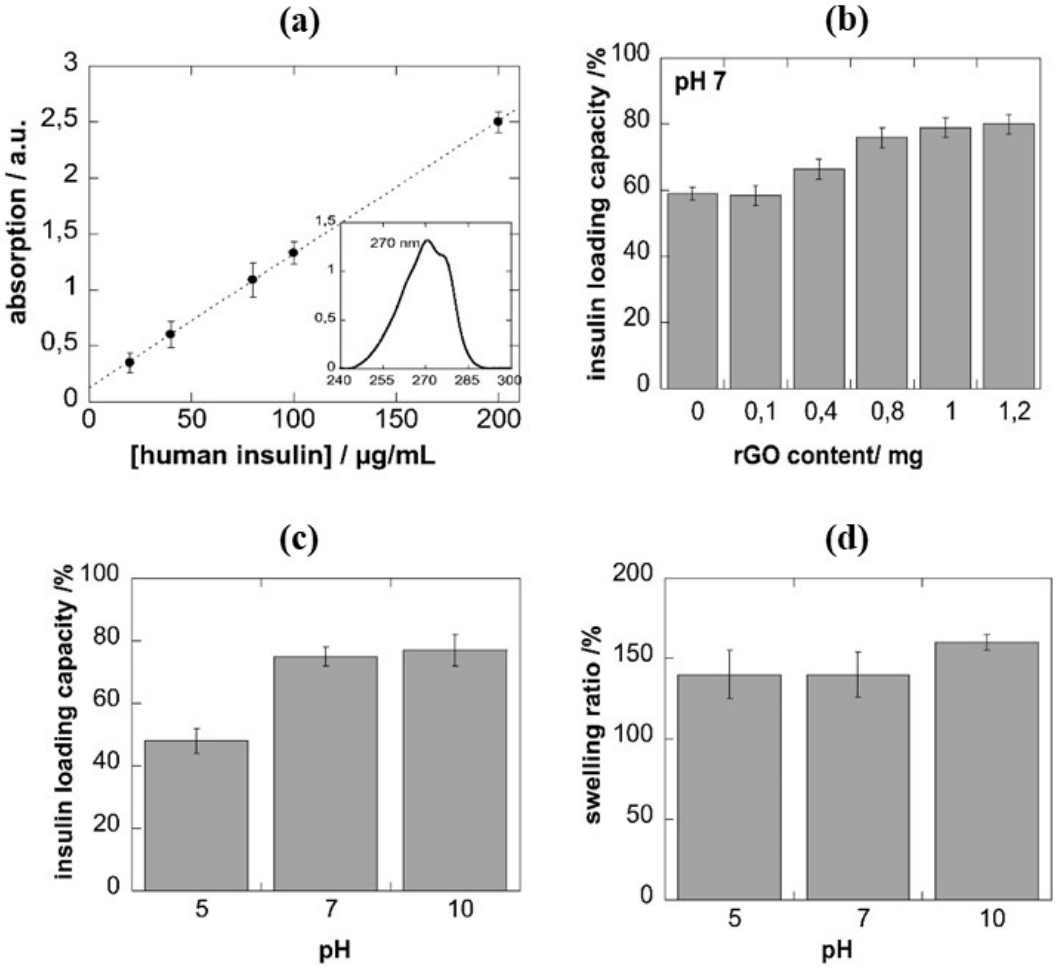

Figure 3.4. Insulin loading of PEGDMA-rGO hydrogels: (a) Calibration curve used for the determination of loading capacity of PEGDMA-rGO hydrogels, inset: UV-Vis spectrum of human insulin solution, (b) human insulin (100 μg mL^{-1}) loading capacity of PEGDMA-rGO as a function of rGO content at pH 7, (c) human insulin loading capacity of PEGDMA-rGO (0.8 mg) hydrogel as a function of pH by adjusting the pH through the addition of NaOH or HCl, (d) swelling ratio of rGO-PEGDMA (0.8 mg rGO) hydrogels as a function of pH by adjusting the pH through the addition of NaOH or HCl. The results are expressed as the mean ± SEM of at least 5 independent samples for each group.

The loading capacity was found to be pH dependent, with a higher insulin loading at pH >7 (Figure 3.4c). This is in contrast to insulin loading onto GO where higher insulin loading was achieved at pH <5, as below pH 5.4, insulin is positively charged and interacts more strongly with the negatively charged GO [127]. This is also different from the case of rGO where no pH dependent loading was observed [128] as π-π stacking interactions, being pH independent, were believed to prevail between insulin and rGO. In addition, no significant influence of the pH on the swelling ratio of the hydrogel was observed (Figure 3.4d). The increase in loading at pH 7 is correlated with the better water solubility of insulin above pH 6 [148]. Indeed, insulin is highly soluble at high and low pH conditions but is poorly dissolved at pH 5 (near the pKa value of insulin). At pH 7, the solubility of insulin is high enough to promote an effective diffusion through the gel resulting in increased loading capacity when compared to pH 5 (Figure 3.4c).

3.3.3. Photothermal Release of Insulin

The photothermal heating ability of PEGDMA and insulin loaded PEGDMA-rGO hydrogels were investigated under NIR irradiation (Figure 3.5a). The size of the hydrogels used in these experiments was 1 x 1 cm^2 and had a thickness of approximately 1 mm. As expected, PEGDMA hydrogels exhibit no photothermal heating ability even under high laser power. On the contrary, the rGO loaded PEGDMA hydrogels exhibited good photothermal properties. Using a laser power of 0.7 W cm^{-2}, a temperature of $\approx$ 70 °C can be achieved within 10 min for insulin loaded PEGDMA-rGO hydrogels with rGO loading of 0.8 mg and higher (Figure 3.5b). Such temperatures are believed to be high enough to interfere with the affinity between human insulin and rGO. Importantly, the hydrogels remained stable at this temperature since no thermal decomposition of the hydrogels was observed, as evidenced from the thermogravimetric analysis (Figure A.3). Additionally, no weight loss of hydrogel was observed upon such a photothermal irradiation in water. Under the same conditions, an equivalent amount of rGO (0.8 mg) drop-casted onto a glass interface reached a final temperature of only 60 °C, which is 10 °C lower than that recorded with PEGDMA-rGO hydrogel (Fig-

ure 3.5b). The confinement of rGO into the hydrogel seems to have a positive effect on the photothermal properties of the matrix; temperatures around 100 °C can be even reached upon increasing the laser power to 4 W cm^{-2}. The local confinement of the water molecules present within the hydrogel matrix in close proximity to the irradiated rGO allows effective localized temperature increase through slow heat dissipation into the surrounding medium.

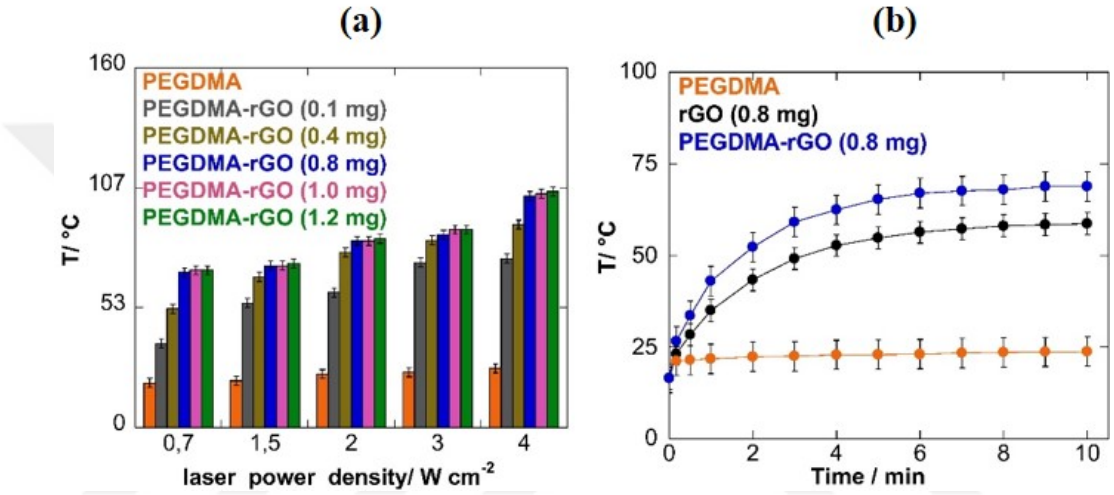

Figure 3.5. (a) Change in solution temperature during illumination of different insulin loaded PEGDMA-rGO hydrogels at 980 nm for 10 min as a function of laser power, (b) photothermal heating curves of rGO (black, 0.8 mg, drop casted onto glass), PEGDMA (orange), and PEGDMA-rGO (0.8 mg) (blue) under NIR illumination (980 nm) at 0.7 W cm^{-2} using a continuous wave laser. The results are expressed as the mean ± SEM of at least 5 independent samples for each group.

Before determining the amount of insulin released during photothermal activation, the long-term stability of the insulin impregnated PEGDMA-rGO hydrogels was established. The PEGDMA-rGO hydrogels with rGO loading of 0.8 mg were used for the following experiments, as a further increase of rGO loading did not alter the photothermal characteristics of the hydrogel.

Figure 3.6a indicates that around 10 % of insulin was desorbed from the hydrogel after 1 day when left immersed in PBS of pH 7 at 37 °C. Thereafter, no further decrease

was observed. This probably comes from a burst effect due to insulin present on the surface of the hydrogel.

Figure 3.6b depicts the amount of photothermally released insulin upon illumination of the hydrogels at 980 nm for 10 min with a laser power of 0.7 W cm^{-2}. In the absence of rGO in the PEGDMA hydrogel, the insulin release was small due to the inefficiency of the matrix to heat (Figure 3.5a). The good heating capacity of PEGDMA-rGO patches with a rGO content of >0.4 mg results on the other hand on an efficient insulin release from the patch between 38 and 51 % (corresponding to a solution concentrations reaching 6.5 - 8.7 μM). The photothermal triggered release is comparable to the electrochemical release of $\approx$ 7 μM insulin [128]. To decrease diabetic blood glucose concentrations to normal levels, 250 - 330 nM of insulin is needed [149]. The photothermal triggered release approach is thus well adapted for on-demand insulin release from the rGO loaded hydrogels. To investigate, if the system is working robustly, the influence of the irradiation time on the amount of insulin released was determined. Figure 3.6c shows that for the first 10 min the release of insulin scales linearly with the irradiation time with a release rate of about 5 % insulin per min. Thereafter, increase in irradiation time results in nonlinear insulin release, with a maximum ($\approx$ 80 $\pm$ 3 %) of released insulin after 40 min.

An important feature of the hydrogels is their reusability. Reloading of insulin into the hydrogels where insulin was photothermally released could be performed with the same efficiency for six cycles (Figure 3.6d), making these hydrogels of particular interest for the development of on-demand delivery platforms of diabetic patients. The insulin loaded PEGDMA-rGO hydrogels also provide sustained drug release upon NIR trigger. Figure 3.6e shows the amount of insulin released from the hydrogel over a week when activated once a day for 10 min by laser illumination at 980 nm (0.7 W cm^{-2}). The insulin release is constant after 3 days with an insulin dose of 2.6 μg mL^{-1}.

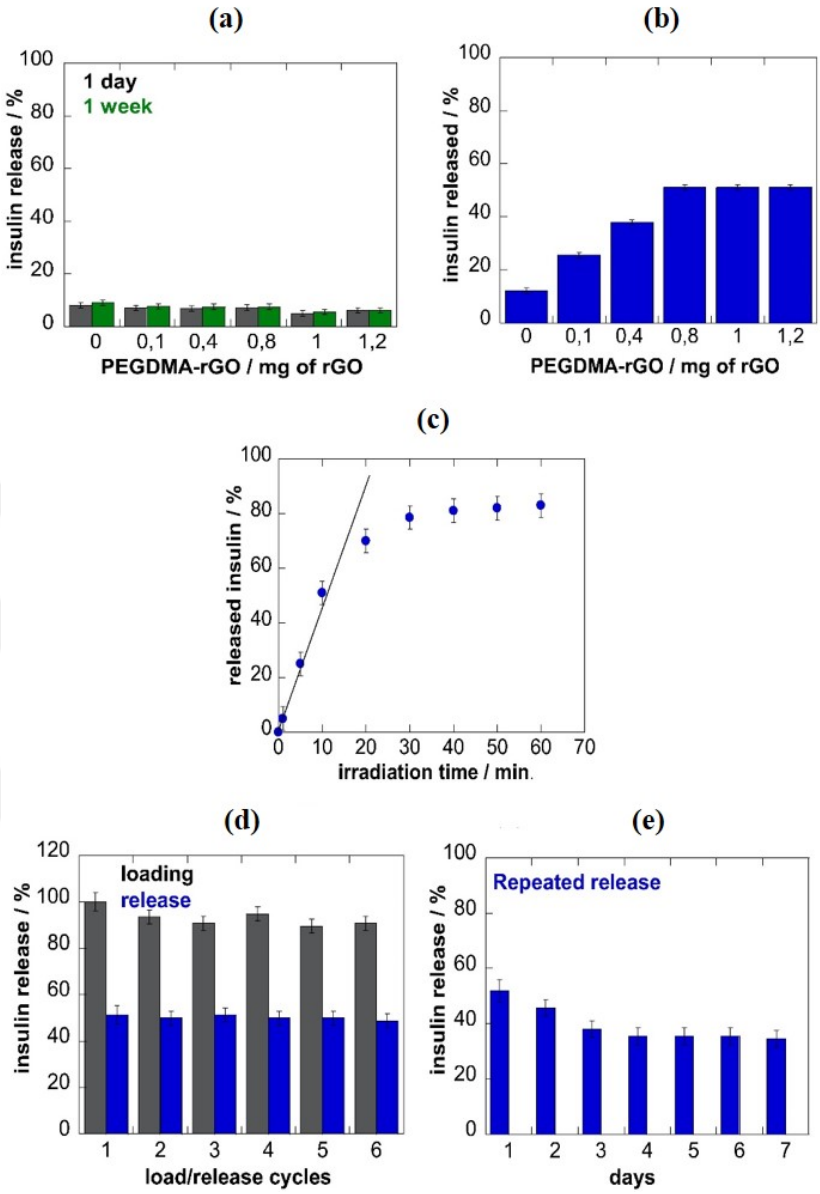

Figure 3.6. Insulin release: (a) Stability of insulin loaded PEGDMA-rGO hydrogels in water for a period of 1 day (black) and one week (green), (b) percentage of insulin released photothermally into water (37 °C) using a continuous wave laser at 980 nm, 0.7 W cm^{-2} with illumination time of 10 min, (c) influence of irradiation time on insulin release (980 nm, 0.7 W cm^{-2}), (d) reloading and release of insulin on PEGDMA-rGO (0.8 mg) hydrogels for 6 cycles, (e) repeated insulin release over 7 days using 10 min laser illumination at 980 nm, 0.7 W cm^{-2}. The results are expressed as the mean ± SEM of at least 5 independent samples for each group.

3.3.4. Evaluation of Photothermally Released Insulin Activity

To evaluate if the photothermal release of insulin from the PEGDMA-rGO hydrogels does not impact negatively the physiological and metabolic action of insulin, human hepatic HepG2 cells were cultivated in the presence of native or photothermally released insulin. Before this, we checked the potential toxicity of the patch itself and that of photo-released insulin in HepG2 cells. Cells viability was similar in cells cultured with different photo-released insulin preparations for 72 h (Figure 3.7a). No toxicity was found in addition when cells were cultured with the different preparations at various times (1 h, 24 h or 48 h).

Insulin acts on HepG2 cells through its receptor, which after binding induces a signaling cascade leading to protein kinase B phosphorylation (p-Akt). This well-characterized key regulator of glucose metabolism in the liver will be used here as a marker for the determination of the metabolic activity of insulin. Figure 3.7b indicates that the insulin activity (Akt phosphorylation, pAkt/Akt ratio) increased when HepG2 cells were treated with native insulin in comparison to non-treated cells (p-Akt /Akt ratio of 4.82 versus 1.0 for the negative control). A significant increase of Akt phosphorylation on HepG2 cells treated with the photothermally released insulin was observed (p-Akt/Akt ratio of 6.14 versus 1.0 for the negative control). It is important to notice that native insulin was less efficient to increase Akt phosphorylation than insulin released from the PEGDMA-rGO loaded hydrogels (p-Akt/Akt ratio of 6.14 versus 4.82 for cells treated with native insulin) (Figure 3.7c). The reasons for this statistically greater activity in comparison to native insulin are currently unclear. However, it underlines insulin release under the used conditions has no negative effect on its activity.

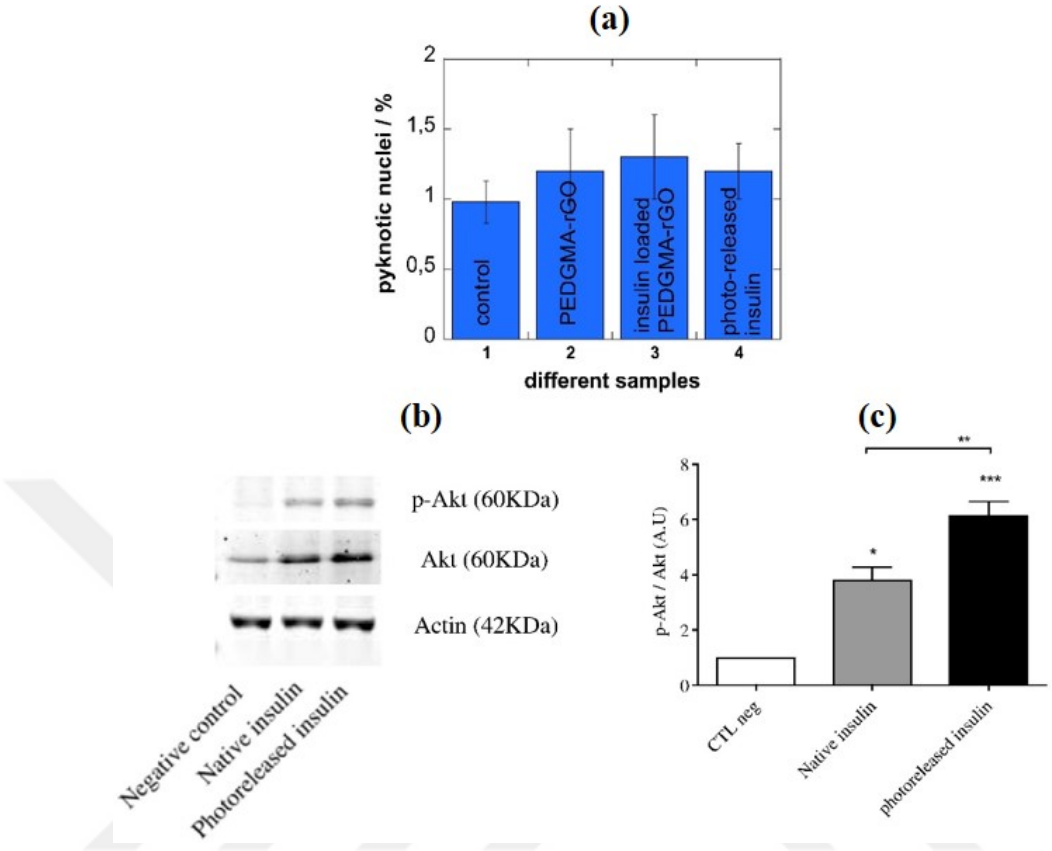

Figure 3.7. (a) Effects of photo-released insulin on cell viability. Measurement of apoptotic HepG2 cells that were cultured for 72 h in the absence (control, 1) and presence of a PEGDMA-rGO hydrogel (2), insulin loaded PEGDMA-rGO hydrogel (3) and photo-released insulin (4). The fraction of cells undergoing apoptosis was determined by scoring the percentage of cells displaying pyknotic nuclei. Data are the mean of ± SD, (b) insulin activity from insulin loaded PEGDMA hydrogels determined on HepG2 cells Western blot of p-Akt/Akt cell lysates from HEPG2 cells incubated under several conditions: without insulin, with native insulin or with photo-released insulin (insulin loaded PEGDMA-rGO hydrogels), (c) insulin activity shown by the ratio between p-Akt and Akt (A.U.) for all the samples in comparison to a negative control (CTL neg) (cells without insulin treatment). One-way ANOVA and multi comparisons test. The results are expressed as the mean ± SEM of at least 3 independent samples for each group, (*p <0.05, **p <0.01, ***p <0.001).

3.3.5. Biocompatibility of Photothermally Activable PEGDMA-rGO Hydrogels

To demonstrate further the feasibility of the laser-activated hydrogel, the eventual photothermal damage to cells was investigated. As can be seen in Figure 3.8a, the presence of the hydrogel did not induce any cytotoxicity to Caco-2 epithelial cells. Most importantly, the cell viability did not decrease even after illumination at 980 nm for 10 min at 0.7 W cm^{-2} pointing towards the absence of any photothermal damage to cells.

The impact of the laser irradiation on the skin structure was in addition taken into account by performing some histological investigations. Porcine ear skin was used since its stratum corneum is very similar to that of human stratum corneum [150]. The thickness of the skin was determined as being 1.6 $\pm$ 0.4 mm. Masson's trichrome dye was used for staining as keratin and muscle fibers are colored red, collagen and bone blue/green, cytoplasm red/pink, and cell nuclei brown/black. As seen in Figure 3.8b, using a laser power density of 0.7 W cm^{-2} shows no histological changes. These results are encouraging for using the developed patch for transdermal insulin delivery.

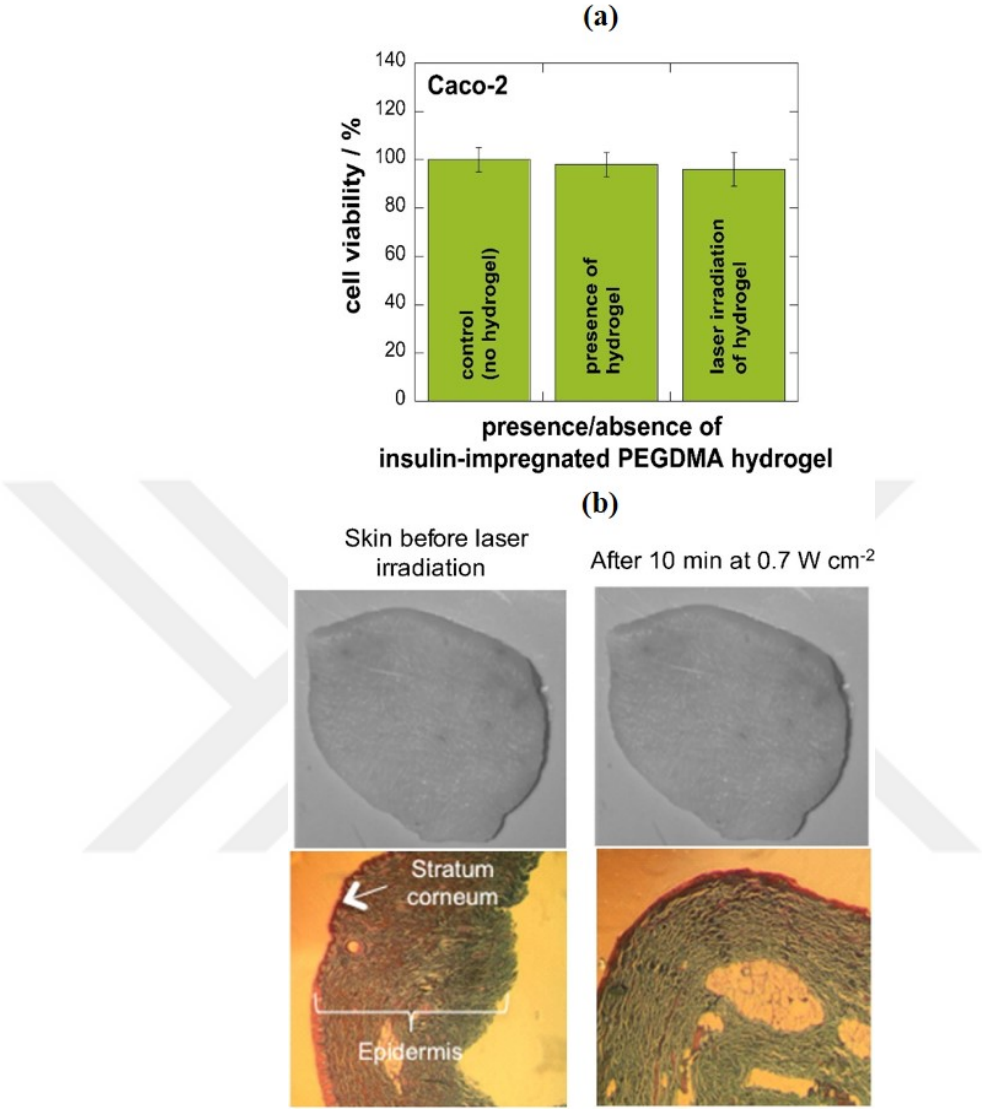

Figure 3.8. (a) Relative cell viability of Caco-2 epithelial cell lines in the absence (control) and presence of insulin loaded PEGDMA-rGO hydrogels with and without laser illumination for 10 min at 980 nm at 0.7 W cm^{-2}; (cell viability was evaluated using the CCK-8 assay, where the absorbance at 450 nm is measured using a microplate reader) without irradiation. The results are expressed as the mean ± SEM of at least 3 independent samples for each group, (b) representative photographs and histology of pig ear skin before and after treatment with a laser at 980 nm for 10 min with a laser power density of 0.7 W cm^{-2}.

3.3.6. Transdermal Insulin Delivery Through Pig Skin

To determine the possibility of NIR laser heating of insulin impregnated PEGDMA-rGO hydrogels to delivery insulin transdermally, the transdermal flux of insulin through the skin was determined using a Franzen diffusion cell. Porcine ear skin of about 1.1 ± 0.8 mm in thickness was used since its stratum corneum is believed to be very similar to that of human stratum corneum [150]. After wetting the insulin impregnated PEGDMA hydrogels to insure good contact with the skin, it was irradiated for 10 min at 980 nm at 0.7 W cm^{-2} and the passage of insulin through the skin was followed over 6 h. Skin permeability was determined by measuring the transdermal flux of insulin using HPLC/UV (Figure 3.9a), which allowed the detection of insulin as low as about 1 μg mL^{-1}. Figure 3.9b represents the permeation profile of insulin across the skin. No passive insulin permeation is observed due to the high molecular weight of insulin, preventing insulin from penetrating intact skin. Irradiation at 0.7 W cm^{-2} resulted in a remarkable increase in the quantity of permeated insulin with a lag time of around 1 h. This is comparable and even faster than the lag time reported by Prausnitz using ITC-labeled bovine insulin [151]. The increase in insulin permeation is believed to be correlated to the increase in temperature in the vicinity of the skin due to the photothermal heating effect of the PEGDMA-rGO hydrogel (Figure 3.5a). At 0.7 W cm^{-2} irradiation, the insulin flux across the skin was estimated as J = 0.8 ± 0.2 μg cm^{-2} h^{-1} for 3 h. The skin permeability to insulin after laser irradiation using the PEGDMA-rGO hydrogels is significantly higher when compared to intact skin.

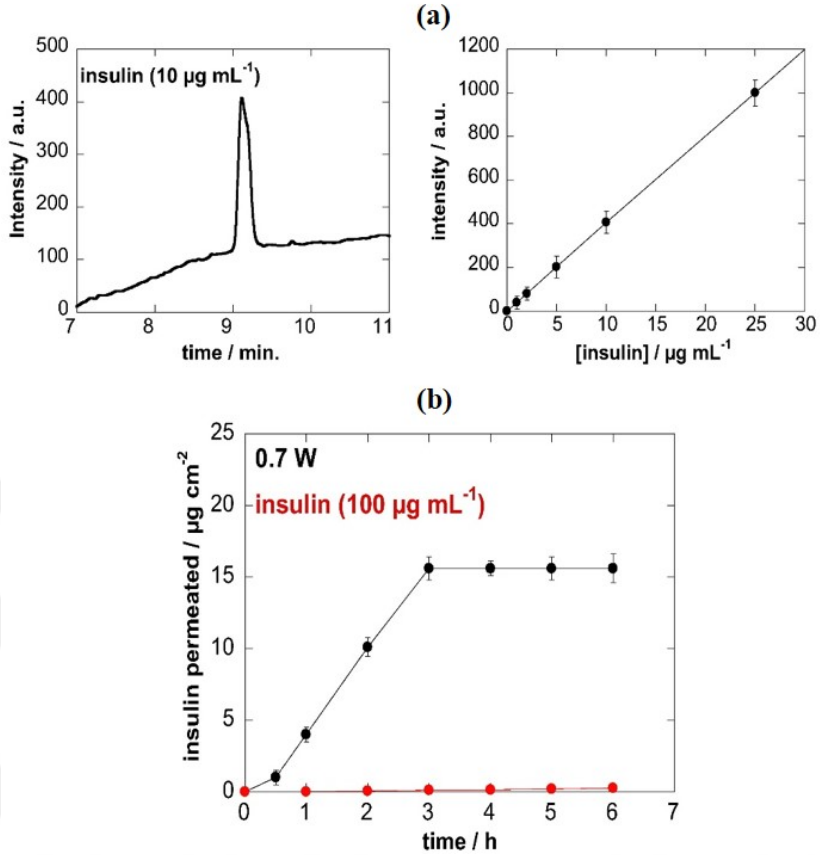

Figure 3.9. (a) HPLC chromatogram of insulin (10 μg mL^{-1}) and the corresponding calibration curve, (b) in vitro permeation profiles of insulin through porcine skin from insulin loaded PEGDMA-rGO hydrogels upon light irradiation at 980 nm for 10 min at 0.7 W cm^{-2}.

3.4. Conclusions

In conclusion, the potential of reduced graphene oxide impregnated poly(ethylene glycol) dimethacrylate hydrogels (PEGDMA-rGO) to act as an efficient carrier of therapeutic relevant quantities of insulin is demonstrated. We describe further the ability to deliver insulin in a controlled manner using laser-induced photothermal activation. It is based on the use of NIR laser irradiation at 980 nm with a laser power density of 0.7 W cm^{-2}, which results in heating of the hydrogel and modulating the affinity of insulin in the PEGDMA-rGO hydrogel. We show for the first time, that the accounted

temperature rise during the photothermal release does not have a negative consequence on the biological and metabolic activity of insulin as validated by an *in vitro* assay, and has no cytotoxic effect on cells. We further validated that the photothermal conditions used have no negative impact on the skin morphology with no skin inflammation being observed after insulin delivery.

Due to the ease of insulin loading and reloading as well as on the possibility to control the release kinetics by changing irradiation time and laser power, this insulin hydrogel should be of potential interest for the treatment of diabetic patients. The biocompatible nature of the rGO-PEGDMA hydrogels would allow its implantation under the skin of diabetic patients, where refilling of the hydrogel could be envisaged using micro valves as used already in insulin pumps. Moreover, the use of such an intrinsically soft martial such as rGO-PEGDMA enhances the possible integration of the patch with the human skin and its use as topical insulin patch. The possibility of such a strategy to deliver insulin through the skin has been validated by using porcine skin as a model. These first experiments, which are extremely encouraging, show that permeation of insulin is taking place in a relatively short time scale (0-3 h). Further studies in this direction are underway and will hopefully provide new opportunities for the treatment of diseases such as diabetes mellitus.

4. FUNCTIONALIZATION OF REDUCED GRAPHENE OXIDE VIA THIOL-MALEIMIDE "CLICK" CHEMISTRY: FACILE FABRICATION OF TARGETED DRUG DELIVERY VEHICLE[2]

4.1. Introduction

Nanosystems that release cancer drugs and induce toxicity in response to an external stimulus offer unique advantages over the commonly employed conventional carriers that release their payload in a passive fashion. rGO nanosheets with restored sp^2 network have most lately shown to be ideally suited for drug-loading- and drug-release-based applications using electrical [128, 153, 154] as well as thermal induced triggers [115, 121, 124, 131, 155–157]. Although the majority of the aromatic scaffold of rGO is devoid of any functional groups, a few carboxylic acid and alcohol groups are present at the edges and other defect points. This limits the effective functionalization of the rGO through covalent transformations. To circumvent this limitation, the noncovalent π-π stacking-based functionalization route of the rGO scaffold has been extensively exploited [158–163]. This approach is effective for hydrophobic/aromatic molecules that are able to undergo efficient noncovalent interactions. Conjugation of molecules unable to undergo such an association with the rGO, however, becomes challenging. An approach that would allow facile and effective covalent attachment in a modular manner to the rGO would be rather useful.

Aromatic anchoring groups like pyrene [159, 164], tetrathiafulvalene [160, 162] and dopamine derivatives [161, 163] have shown to be of high interest for rGO functionalization. Some of us have reported surface functionalization of the rGO with dopamine containing clickable alkyne and azide groups [161, 163]. The azide containing rGO could be further modified with alkynyl terminated molecules such as ferrocene

[2]Published in ACS Applied Materials & Interfaces [152]. Reproduced by permission of American Chemical Society.

via the Cu(I)-catalyzed azide-alkyne Huisgen-type click reaction. Although the azide-alkyne-based rGO functionalization was effective, the requirement to use copper as a catalyst can be a concern for the biomedical applications because any trace of copper adds to the overall cytotoxicity of the nanostructures. This necessitates the expansion of the tool box to include click reactions that do not need metal catalysts, like the SPAAC [165] and the nucleophilic or radical thiol-ene reactions [163, 166]. Although approaches based on SPAAC have gained interest lately [167], the multistep synthesis or high cost of the cyclooctyne-based materials limits the widespread utilization of this approach. Nucleophilic thiol-ene-based reactions have been extensively employed in the bio-conjugations using the thiol-maleimide functional group dyad and seem advantageous [168–171]. The maleimide-thiol addition reaction is a facile process that does not require any catalyst and can be carried out under mild conditions. Although thiol groups can be readily incorporated in various molecules, they are also present in the cysteine residue of various peptides and biomolecules, or can be installed using standard protocols during or after synthesis.

Herein, we report the synthesis of a maleimide functional group containing the rGO, which is amenable to facile functionalization by thiol group containing molecules (Figure 4.1). The conjugation of thiol-bearing molecules proceeds through the thiol-ene click-type conjugation reaction, under metal-free conditions. Maleimide functionalized rGO was easily prepared through π-π interactions under ultrasonication of the rGO with a maleimide-containing dopamine (dopa-MAL) ligand. To demonstrate the utility of this clickable rGO, we took the advantage of the covalent conjugation of a thiol bearing targeting peptide, c(RGDfC), and the noncovalent loading of the rGO-c(RGDfC) nanostructures with the anticancer drug DOX. The two-dimensional structure of graphene sheets serves as an excellent drug carrier due to its high drug loading capacity arising from the π-π stacking and other hydrophobic interactions. Attachment of a targeting group on the rGO through covalent conjugation further expands its application to the targeted drug delivery. Selective delivery of anticancer agents to the tumor site has become important for efficient cancer therapy by minimizing the negative side effects. Synthetic cyclic peptides with arginine-glycine-aspartic acid sequences

(RGDs) are known to possess high affinity to integrin α_v β_3, a cell adhesion domain highly expressed on the tumor cells [172,173]. Their integration into the nanostructures and polymers for targeted drug delivery has thus found growing interest [174, 175].

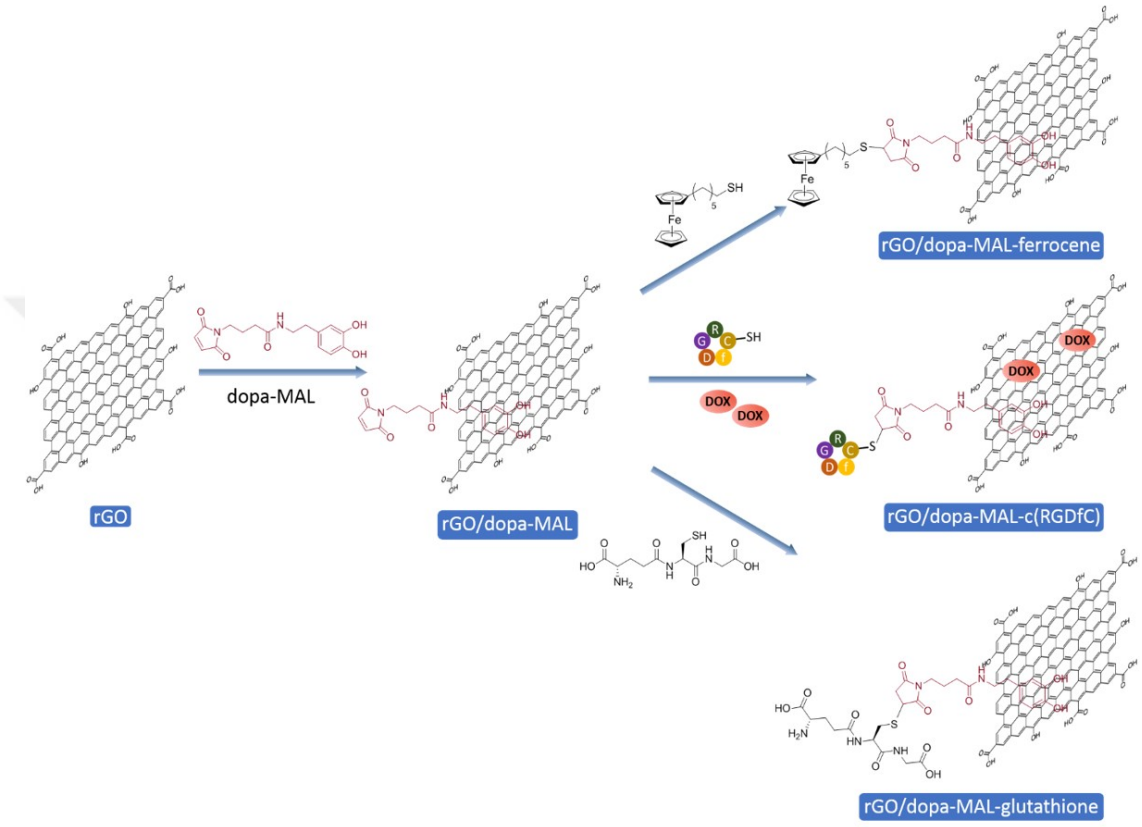

Figure 4.1. Schematic illustration of the synthesis of thiol-ene "clickable" Mal-rGO and its subsequent functionalization.

Finally, the excellent photothermal properties of DOX loaded rGO/dopa-MAL-c(RGDfC) allow for chemophototherapy; the combination of photothermal therapy with chemotherapeutic release of DOX is often beneficial specifically for solid tumors [176]. The cytotoxicity of targeted and non-targeted rGO under normal and photothermal conditions was assessed on two cancer cell lines, human breast MDA-MB-231 and human cervical cancer cells (HeLa), to highlight the advantages of the construct. Overall, facile fabrication and functionalization of a maleimide group containing rGO-based functional material with potential for applications in many areas is outlined.

4.2. Experimental

4.2.1. Materials and Characterizations

NHS was purchased from Alfa Aeser. DCC, DMAP, dopamine hydrochloride, TEA, γ-aminobutyric acid, l-glutathione reduced, 6-(ferrocenyl)hexanethiol, graphite powder (<20 μm) and hydrazine monohydrate were purchased from Sigma-Aldrich. 4-(exo-3,5-Dioxo-10-oxa-4-aza-tricyclo[5.2.1.0]dec-8-en-4-yl)-butyric acid (furan-protected maleimide containing acid) was synthesized according to a previous report [177]. Bags with regenerated cellulose dialysis membranes (Spectra/Por Biotech, molecular weight cut-offs 10 kDa) were obtained from Spectrum Laboratories. Purification by silica gel column was done using silica gel 60 (Merck). Purity of the compounds was determined using thin-layer chromatography on the silica-coated aluminum plates (Kieselgel 60 F254, Merck). Methanol, THF, and DMF were bought from Merck. Anhydrous toluene from SciMatCo system was used, and other solvents were stored on the molecular sieves when needed. Graphene oxide was bought from Graphenea, Spain.

UV-Vis absorption spectra were recorded using SAFAS UV-Vis spectrophotometer in quartz cuvettes with an optical path of 10 mm. The wavelength range was 200-1100 nm. FT-IR analyses were performed on a Thermo Fisher Scientific Inc, Nicolet 3700. ^{1}H NMR and ^{13}C NMR spectra were obtained using a Bruker 400 MHz spectrometer. Micro-Raman spectroscopy measurements were performed on a LabRam HR Micro-Raman system (Horiba Jobin Yvon, France) using a 473-nm laser diode as excitation source. Visible light is focused by a 100x objective. The scattered light is collected by the same objective in backscattering configuration, dispersed by an 1800 mm focal length monochromator and detected by a CCD camera. Zeta-potential measurements were performed using a Zetasizer Nano-ZS (Malvern Instruments Inc. Worcestershire, UK). Samples were diluted to 10 μg mL^{-1} and measured in Milli-Q water at different pH. XPS experiments were performed using a PHl 5000 VersaProbe - Scanning ESCA Microprobe (ULVAC-PHI, Japan/USA) instrument at a base pressure below 5 x 10^{-9} mbar. Core-level spectra were acquired at pass energy of 23.5 eV with

a 0.1 eV energy step. All spectra were acquired with 90° between X-ray source and analyzer and with the use of low energy electrons and low energy argon ions for charge neutralization. After subtraction of the Shirley-type background, the core-level spectra were decomposed into their components with mixed Gaussian-Lorentzian (30:70) shape lines using the CasaXPS software. Quantification calculations were conducted using sensitivity factors supplied by PHI. Electrochemical measurements were performed with a potentiostat/galvanostat (Autolab, The Netherlands). A conventional three-electrode configuration was employed using a silver wire and a platinum mesh as reference and auxiliary electrodes, respectively. Thermal images were taken with an IR Camera (Thermovision A40) and images were processed with ThermaCam Researcher Pro 2.9 software. A Gbox model continuous laser (Fournier Medical Solution) S-3 was used. PHERAstar FS (BMG LABTECH GmbH, Germany) was used as a plate reader. Optical images of cell lines were recorded using a 10x magnification inverted microscope (Nikon Eclipse TS100, Japan).

4.2.2. Preparation of Reduced Graphene Oxide (rGO)

GO aqueous suspension (150 mg, 3 mg mL^{-1}) was sonicated and hydrazine hydrate (50 μL, 1.03 mmol) added to this suspension. The mixture was heated for 24 h at 100 °C and rGO slowly precipitated out. The desired material was obtained by filtering with a PVDF membrane (0.45 μm pore size), rinsed with water (20 mL × 5) and methanol (20 mL × 5), followed by drying in an oven.

4.2.3. Synthesis of Maleimide-Containing Dopamine (dopa-MAL)

4.2.3.1. Protected Maleimide-Containing Dopamine (dopa-pMAL). Furan protected maleimide containing acid (2.45 g, 9.76 mmol), NHS (1.18 g, 10.25 mmol), and DMAP (0.24 g, 1.95 mmol) were dissolved in DMF (15 mL) in a round-bottom flask at 0 °C. DCC dissolved in 5 mL of DMF was subsequently added to this solution dropwise. After stirring at 0 °C for 15 min, the reaction was left to proceed at room temperature for 16 h. The solvent was removed in vacuo and the product (NHS ester of the acid)

was extracted with $NaHCO_3$. This activated ester was used without further purification. Dopamine.HCl (1.43 g, 7.54 mmol), and TEA (1.09 g, 10.8 mmol) were mixed in 10 mL of DMF with magnetic stirring for 15 min. The DMF solution of the activated ester (2.5 g, 7.18 mmol) was added to the mixture and stirred at room temperature for 24 h. The solvent was partially evaporated (≈ 1-2 mL) and 1 M HCl solution (50 mL) was added to the concentrated solution. It was extracted with EtOAc. The organic phase was collected and dried over Na_2SO_4. Column chromatography using CH_2Cl_2/methanol (10:1) was employed to obtain the pure product (1.28 g, yield: 82 %). ^{1}H NMR ($CDCl_3$) δ (ppm): 6.79 (d, 1H, CH-C*H*=C-OH), 6.72 (d, 1H, C-C*H*=C-OH), 6.58 (dd, 1H, C=C*H*-CH), 6.51 (s, 2H, C*H*=CH), 5.23 (s, 2H, bridgehead protons), 3.46 (m, 4H, NH-CH_2-CH_2, N-CH_2-CH_2), 2.84 (s, 2H, C*H*-CH bridge protons), 2.70 (t, 2H, NH-CH_2-CH_2-C), 2.08 (t, 2H, O=C-CH_2-CH_2), 1.87 (m, 2H, CH_2-CH_2-CH_2).

4.2.3.2. Maleimide Group Activation via Retro Diels-Alder Reaction (dopa-MAL). Furan maleimide adduct-containing dopamine (1.0 g) in anhydrous toluene (150 mL) was heated under nitrogen protection at 110 °C for 10 h. The solution was then cooled down to ambient temperature and toluene was removed via rotary evaporation, yielding maleimide-appended dopamine (dopa-MAL) (0.80 g, yield: 97 %). ^{1}H NMR (DMSO-d_6) δ (ppm): 8.69 (s, 2H, C-O*H*), 7.81 (t, 1H, N*H*), 7.0 (s, 2H, C*H*=CH), 6.61 (d, 1H, CH-C*H*=C-OH), 6.55 (s, 1H, C-C*H*=C-OH), 6.41 (d, 1H, C=C*H*-CH), 3.38 (t, 2H, N-CH_2-CH_2), 3.13 (dd, 2H NH-CH_2-CH_2), 2.02 (t, 2H, O=C-CH_2-CH_2), 1.70 (m, 2H, CH_2-CH_2-CH_2). ^{13}C NMR (DMSO-d_6) δ (ppm): 171.1, 145.0, 143.0, 134.5, 130.2, 119.2, 115.9, 115.5, 40.6, 36.9, 34.7, 32.6, 24.2. LC-MS expected [M + H] m/z = 318 and observed [M + H] m/z = 318.

4.2.4. Preparation of rGO/dopa-MAL

To a solution of rGO in DMF (1 mg mL^{-1}), dopa-MAL (6.3 mM) was added and the mixture ultrasonicated for 3 h at room temperature. Maleimide-functionalized rGO was collected by centrifugation at 13 000 rpm for 30 min and washed with DMF to remove all of the unbound dopa-MAL compounds. The functionalized rGO was

then dried under vacuum.

4.2.5. Functionalization of rGO/dopa-MAL via Thiol–Ene Michael Addition Reactions

4.2.5.1. Glutathione and 6-(Ferrocenyl)hexanethiol Linking. Dispersion of rGO/dopa-MAL in DMF (1 mg mL^{-1}) was mixed with glutathione (10 mM) and sonicated for 6 h at room temperature. The product rGO/dopa-Mal-glutathione was collected by centrifugation at 13 000 rpm for 30 min. Similarly, 6-(ferrocenyl)hexanethiol (10 mM) was attached to rGO/dopa-MAL (1 mg mL^{-1} DMF solution) under ultrasonication for 6 h at room temperature. Purified rGO/dopa-MAL-ferrocene was obtained by centrifugation at 13 000 rpm for 30 min.

4.2.5.2. c(RGDfC) Attachment to rGO/dopa-MAL. c(RGDfC) (4 mM) was added to 1 mg mL^{-1} DMF dispersion of rGO/dopa-MAL and the mixture sonicated for 12 h at room temperature. The non-conjugated peptide was removed by dialyzing (using MWCO 10 000 Da membrane) against water for 48 h to yield rGO/dopa-MAL-c(RGDfC).

4.2.6. Quantification of Peptide and DOX Loading

4.2.6.1. Peptide Quantification Using Bicinchoninic Acid (BCA) Assay. The amount of peptide c(RGDfC) in rGO/dopa-MAL-c(RGDfC) was measured using a BCA kit (ThermoScientific) using a protocol provided by the manufacturer.

4.2.6.2. Drug Loading. Peptide-modified rGO was dispersed in water at 0.5 mg mL^{-1}. Doxorubicin hydrochloride (4.2 mM) was added to the dispersion and left to stir for 12 h at ambient temperature. The solution was centrifuged to remove free DOX from the DOX-loaded rGO/dopa-MAL-c(RGDfC) nanoconjugate.

4.2.7. Cell Viability and Internalization

The HeLa cell line derived from cervical carcinoma (ATCC CCL-2, ECACC, Sigma-Aldrich, Saint-Quentin Fallavier, France) and the MDA-MB-231 cell line derived from human breast adenocarcinoma (ATCC HTB-26, ECACC, Sigma-Aldrich, Saint-Quentin Fallavier, France) were used. DMEM (Gibco) containing 10 % FBS (Gibco) and 1 % penicillin-streptomycin (Gibco) were used to culture and maintain the cells in a humidified incubator at 37 °C and 5 % CO_2.

4.2.8. Cell Viability upon Treatment with rGO/dopa-MAL-c(RGDfC)

A 96-well plate was used to seed cells at a density of 10^4 cells/well and grown for 24 h prior to assay. A fresh medium containing rGO/dopa-MAL-c(RGDfC) was used to replace the culture medium. After 48 h, the old medium was aspirated, washed with PBS, and replaced with new medium. Cellular viability was measured using Uptiblue (Interchim) method. Briefly, 10 μL of the Uptiblue solution were added to the wells containing 100 μL of DMEM with 10 % FBS and the plate was incubated for 4 h in the incubator. The fluorescence of each well (exc. 540 nm / em. 590 nm) was obtained with a plate reader. Experimental runs were repeated five times. The average absorbance of the untreated cells was considered as 100 % viability.

4.2.9. Cell Viability of DOX-Loaded rGO/dopa-MAL-c(RGDfC) under Passive and Active Conditions

Cells were seeded in a 24-well plate (10^5 cells/well) and grown for 24 h prior to assay. For passive release of DOX, the cell culture medium was renewed with a fresh medium that contains DOX-loaded rGO/dopa-MAL-c(RGDfC) at pH 7.4. After 48 h, the old medium was removed, washed with PBS, and replaced with a fresh medium. The cell viability was measured using Uptiblue method as described above. For active release of DOX, the culture medium was replaced with the medium containing DOX-loaded rGO/dopa-MAL-c(RGDfC). After 6 h, each well was illuminated with a

continuous laser at 980 nm at various power densities (1 - 4 W cm^{-2}) for 10 min. During the same time, thermal images were taken with an IR camera. The cell viability was evaluated after additional 18 h using Uptiblue method as described above.

4.3. Results and Discussion

4.3.1. Synthesis of Dopamine-Maleimide Modified Reduced Graphene Oxide (rGO/dopa-MAL)

The aromatic structure of catechol units allows dopamine to develop strong π-stacking interactions with other aromatic bearing units such as rGO. Additionally, dopamine can be easily functionalized by exploiting its amine terminal functions as used here for the synthesis of dopa-MAL (Figure 4.2). 4-(exo-3,5-Dioxo-10-oxa-4-aza-tricyclo[5.2.1.0]dec-8-en-4-yl)-butyric acid (1) was obtained according to a previously reported literature procedure [177]. Dopamine group conjugation was achieved through the reaction between NHS-activated acid of maleimide derivative (2) and dopamine. The ^{1}H NMR spectroscopy of dopa-pMAL (3) is seen in Figure A.4a. Furan deprotection was achieved by heating dopa-pMAL in toluene followed by NMR spectroscopy (Figure A.4b). Loss of proton resonances at 2.84, 5.23, and 6.51 ppm belonging to the bicyclic core and emergence of a new proton resonance at 7.0 ppm belonging to the proton on maleimide ring were indicative of effective furan deprotection. The ^{13}C NMR spectrum for unmasked maleimide-containing dopamine (dopa-MAL, 4) showed the expected resonances, particularly those from the two distinct carbonyl groups, one from the amide and the other from the imide group (Figure A.4c).

Maleimide-functionalized rGO was obtained by mixing DMF dispersion of the rGO with dopa-MAL at room temperature for 3 h using a mass ratio of 2:1 (dopa-MAL/rGO). FT-IR spectroscopy (Figure 4.3a) and XPS (Figure 4.3b) were performed for establishing the successful formation of rGO/dopa-MAL. The FT-IR spectrum of rGO/dopa-MAL shows a broad band at $\sim$3400 cm^{-1} due to the vibration of hydroxyl groups of the dopamine ligand and the remaining OH groups on the rGO. The char-

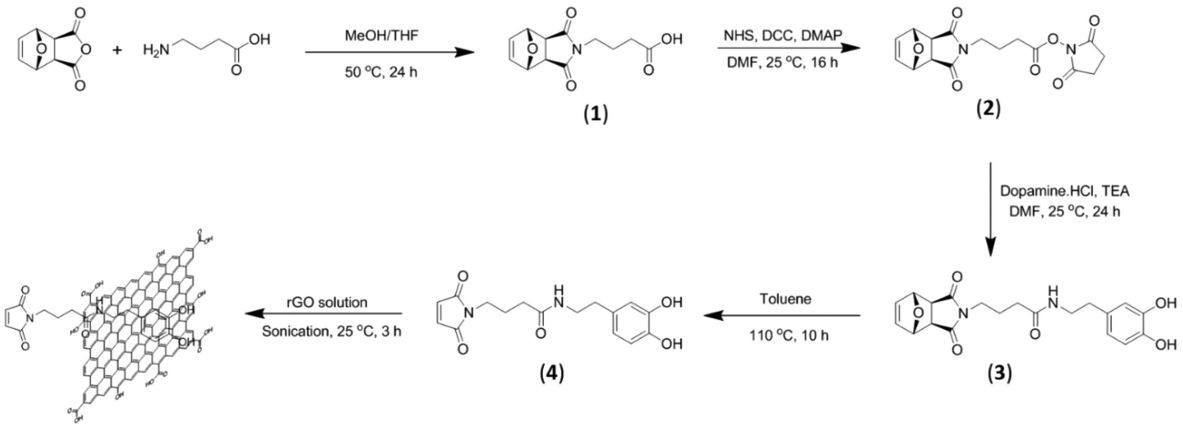

Figure 4.2. Synthesis of dopa-MAL (4) and its conjugation onto rGO through π-π stacking interactions.

acteristic vibration band of the maleimide carbonyl group at 1696 cm^{-1} is clearly observed. The band at ∼1570 cm^{-1} is due to the C=C stretching modes of the aromatic network, whereas the band at 1223 cm^{-1} is due to the C–O (alkoxy) stretching modes of the rGO and the ligand. The absorption bands at 2922 and 2859 cm^{-1} correspond to the CH and CH_2 stretching vibrations, respectively.

XPS analysis was performed in addition to gain additional information on the rGO/dopa-MAL chemical composition (Figure 4.3b). The XPS survey spectrum displays bands due to C_{1s}, O_{1s}, and N_{1s} (Table 4.1), in good agreement with the composition of the functionalized rGO. The C_{1s} high-resolution spectrum can be deconvoluted into bands at 284.5 eV (C-C sp^2), 285.0 eV (C-H/C-C), 286.1 eV (C-O), 288.2 eV (N-C=O, C=O), and 290.3 eV (COOH). The presence of N_{1s} is attributed to the incorporation of maleimide onto the rGO sheets. The band at 400.2 eV in the N_{1s} high resolution (Figure 4.3c) corresponds to the N-C=O bonds in the rGO/dopa-MAL nanocomposite. The UV-Vis spectrum of a water dispersion of rGO/dopa-MAL (Figure 4.3d) exhibits an absorption maximum at 269 nm, characteristic of the sp^2 hybridized structure together with a prolonged absorption tail in the NIR.

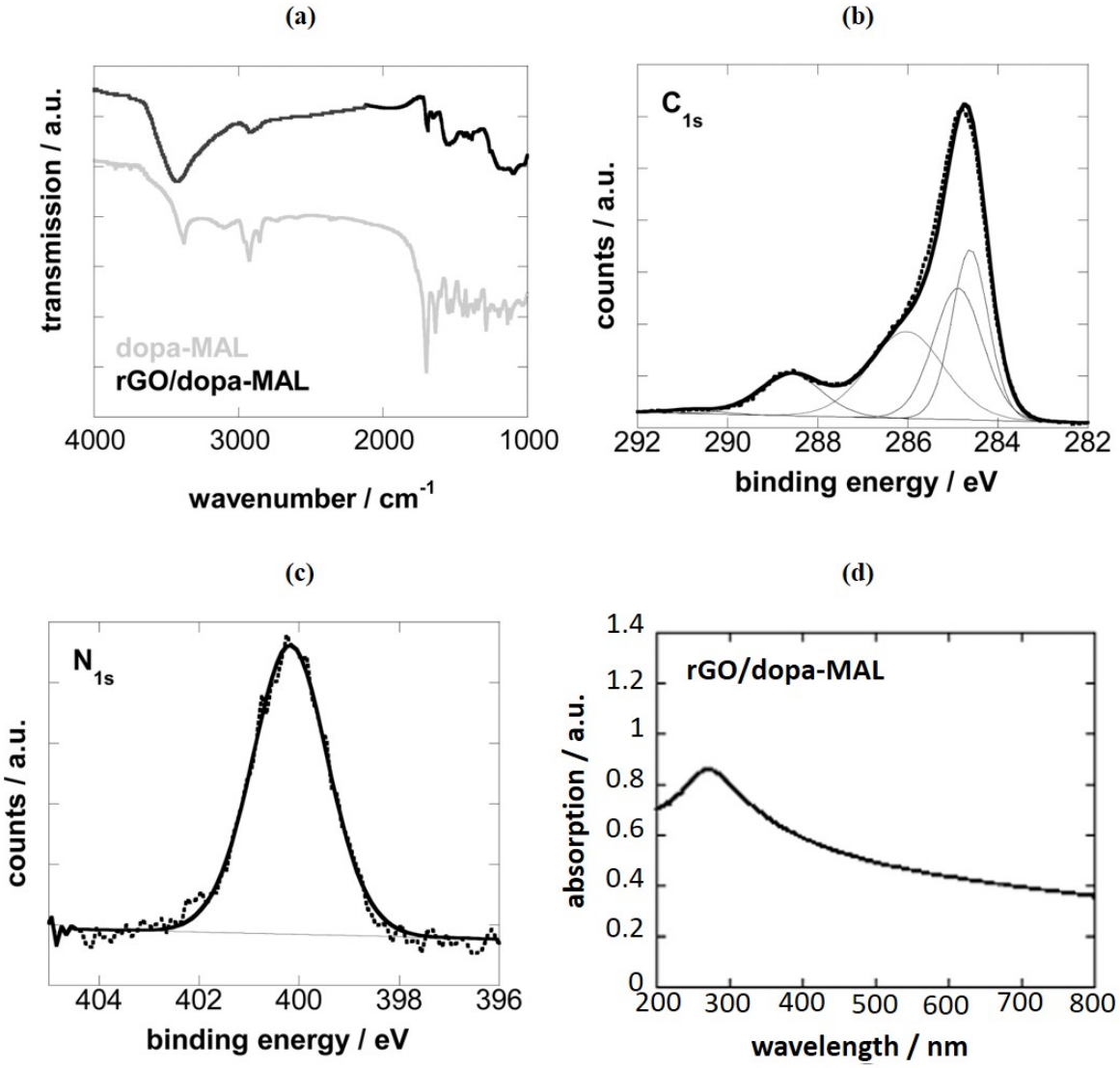

Figure 4.3. (a) FT-IR spectra of rGO/dopa-MAL (black) and dopa-MAL (gray), (b) C_{1s} wide-scan XPS spectrum of rGO/dopa-MAL, (c) N_{1s} wide-scan XPS spectrum of rGO/dopa-MAL, (d) UV–Vis of rGO/dopa-MAL.

Table 4.1. Determination of the atomic percentages of elements by the XPS analysis.

	C_{1s} atom %	**O_{1s} atom %**	**N_{1s} atom %**	**S_{2p} atom %**	**Fe_{2p} atom %**
rGO/dopa-MAL	81.84	14.86	3.3	0	0
rGO/dopa-MAL-glutathione	81.03	11.17	6.6	1.2	0
rGO/dopa-MAL-ferrocene	81.6	12.00	3.3	1.5	1.6

4.3.2. Thiol-ene Michael Addition Reaction on rGO/dopa-MAL

The possibility to integrate thiol-containing ligands onto rGO/dopa-MAL was investigated by the conjugation of glutathione and 6-(ferrocenyl)hexanethiol via Michael addition reaction (Figure 4.1). Both conjugations were carried out in DMF at room temperature for 6 h, and the attachment was confirmed by XPS and FT-IR spectroscopy. The presence of S_{2p} indicates the successful linking of glutathione or ferrocene onto the rGO/dopa-MAL nanocomposite (Table 4.1). The exact binding constant is not determined for the rGO/dopa-MAL system due to its heterogeneous nature. No significant decrease in nitrogen atom content was observed in the XPS analysis of the product obtained after conjugation with ferrocene thiol, thus indicating that the maleimide-containing ligands do not detach from the rGO surface during these steps (Table 4.1). Figure 4.4a depicts the high-resolution XPS spectrum of the S_{2p} core-level spectra of rGO/dopa-MAL-glutathione and rGO/dopa-MAL-ferrocene. Both spectra can be fitted with two peaks at 164.2 eV ($S_{2p3/2}$) and 165.3 eV ($S_{2p1/2}$) due to S-C bond formation with no oxidized sulfur being present, underlining the covalent integration of the thiol-bearing ligands. As a control experiment, the rGO was reacted with glutathione under the same conditions and the product was analyzed by XPS.

The absence of S_{2p} component in the XPS spectrum clearly indicates that glutathione physisorption does not take place (or very limited) under our experimental conditions. The same is true for 6-(ferrocenyl)hexanethiol-modified rGO/dopa-MAL. The presence of Fe_{2p} at ≈ 710 eV shows in addition the integration of ferrocene units onto the matrix (Figure 4.4b). The Fe_{2p} high-resolution XPS spectrum comprises two bands at 711.7 and 725.6 eV due to $Fe_{2p3/2}$ and $Fe_{2p1/2}$, respectively, of the Fe moiety in the (III) oxidation state [178].

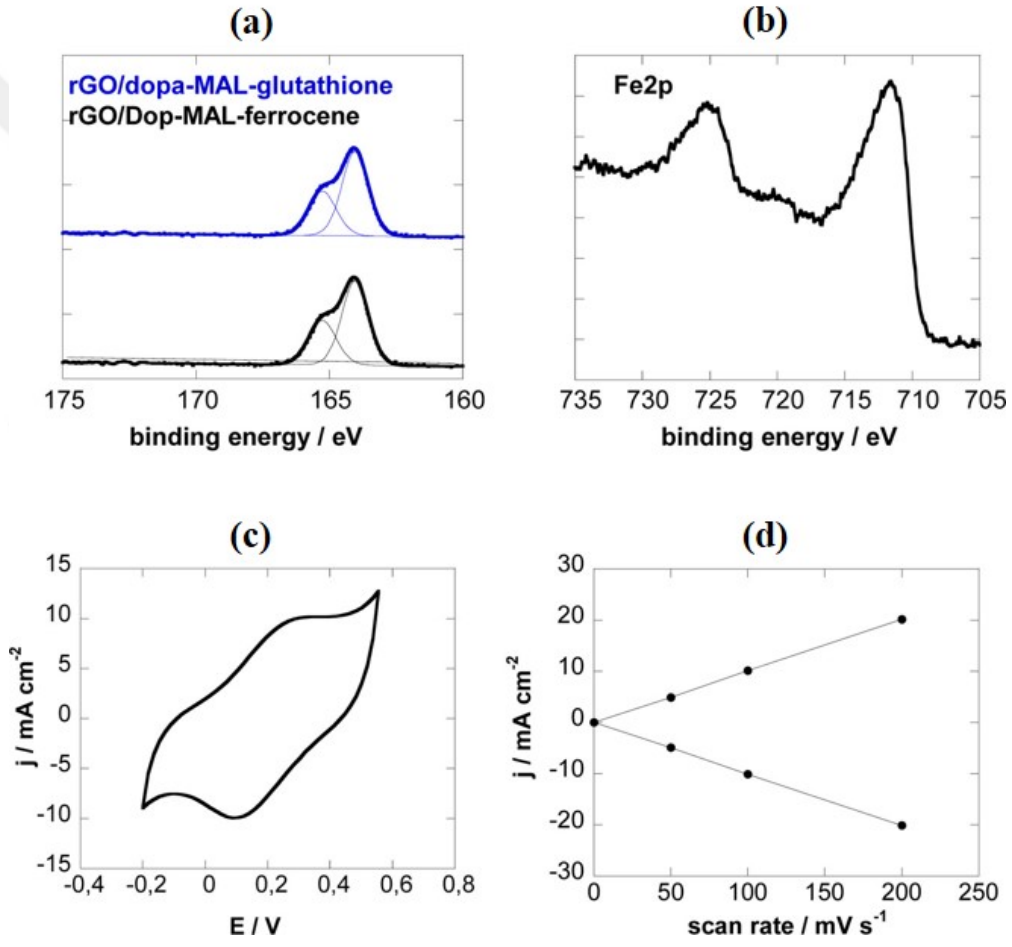

Figure 4.4. (a) S_{2p} high resolution XPS spectra of rGO/dopa-MAL-glutathione (blue) and rGO/dopa-MAL-ferrocene (black), (b) Fe_{2p} high resolution XPS spectrum of rGO/dopa-MAL-ferrocene, (c) cyclic voltammogram of rGO/dopa-MAL-ferrocene in tetraethyl ammonium hexafluorophosphate ($TEAPF_6$)/DMF (0.1 M), scan rate 100 mV s^{-1}, (d) change in the current density as a function of scan rate.

In addition, the ferrocene-modified rGO/dopa-MAL was probed by CV in 0.1 M tetraethyl ammonium hexafluorophosphate ($TEAPF_6$) in DMF (Figure 4.4c). The presence of the redox peak with a peak separation of 164 mV and $E_0 \approx 0.18$ V versus Ag/AgCl evidences the incorporation of ferrocene groups on the rGO/dopa-MAL. The peak current change recorded as a function of the scan rate suggests that the ferrocene units are immobilized on the surface rather than being adsorbed. Figure 4.4d shows that the anodic and cathodic peak currents scale linearly with the scan rate, indicating a surface redox process. The loading of attached ferrocene onto the rGO surface via thiol-ene reaction was calculated according to Eq. 4.1:

$$\Gamma = \frac{Q_A}{nFA} \tag{4.1}$$

Q_A	Transferred anodic charge
n	Number of exchanged electrons (n = 1)
F	Faraday constant
A	Surface area (A = 0.12 cm^2)

A surface coverage of $\Gamma = 4.5 \times 10^{-10}$ mol cm^{-2} (2.71×10^{14} molecules cm^{-2}) is determined, being similar to that determined for the ferrocene "clicked" to diamond interfaces [178] and 6-(ferrocenyl)hexanethiol immobilized on rGO/alkynyl-dopamine through thiol-yne reaction [163].

4.3.3. Fabrication of Multifunctional Scaffold: Doxorubicin-Loaded rGO/dopa-MAL-c(RGDfC)

After the successful demonstration of facile covalent functionalization of the maleimide-containing rGO, this scaffold was investigated for its potential to target cancer cells by covalently linking to the maleimide-functionalized rGO a cyclic peptide containing the sequence c(RGDfC), known to target the integrin receptors that are often overexpressed in various types of cancer (Figure 4.5a).

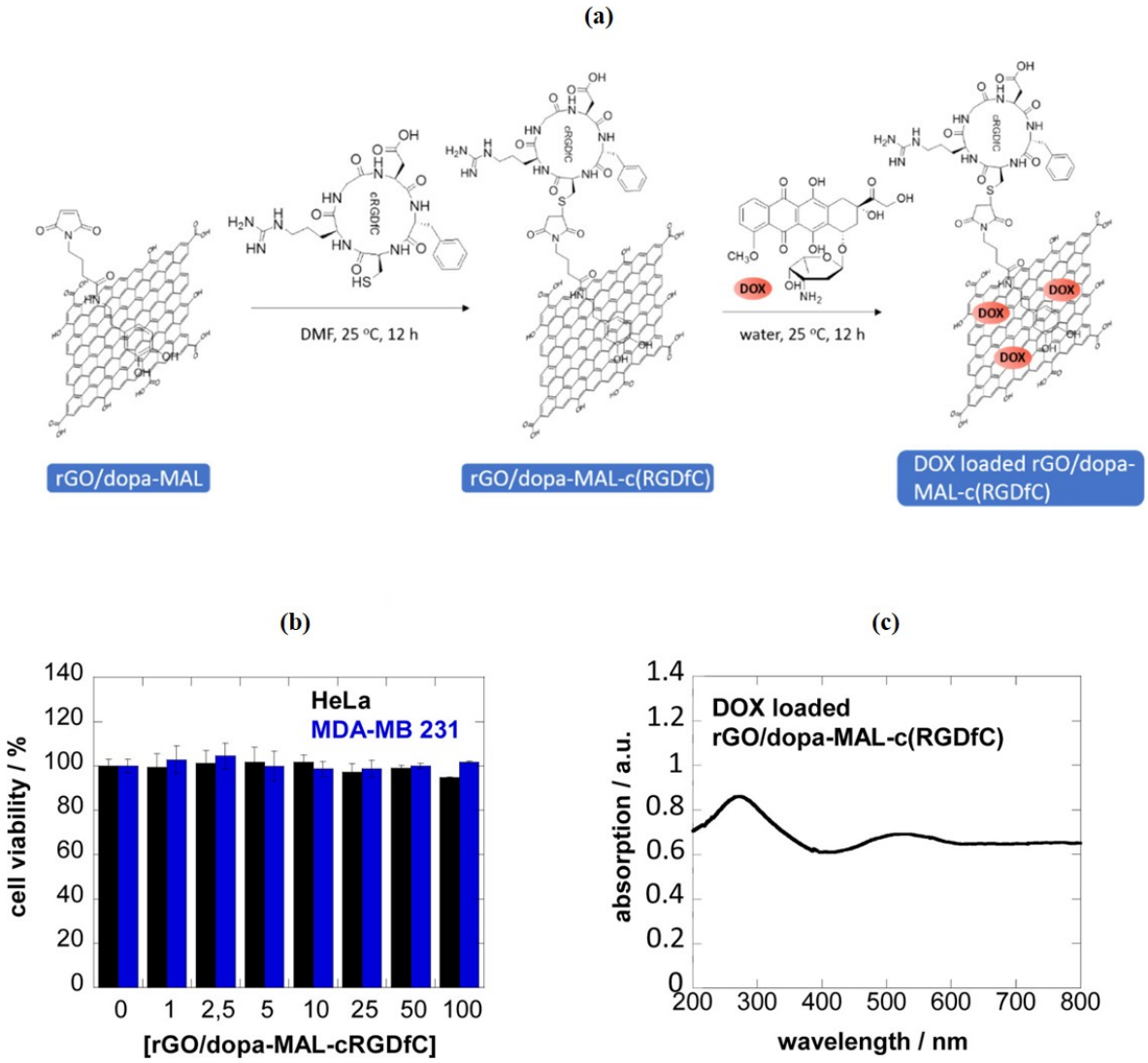

Figure 4.5. Formulation of doxorubicin-loaded rGO/dopa-MAL-c(RGDfC): (a) schematic of the attachment of targeting peptide to rGO/dopa-MAL via Michael addition followed by the noncovalent integration of doxorubicin, (b) cell viability of different concentrations (μg mL^{-1}) of rGO/dopa-MAL-c(RGDfC) on HeLa and MDA-MB-231 cells after incubation for 48 h, (c) UV-Vis spectrum of the DOX-loaded rGO/dopa-MAL-c(RGDfC).

Attachment of the thiol-containing peptide was undertaken in DMF under ambient conditions, followed by dialysis against water to remove any unbound peptide. The peptide attachment was confirmed by using the BCA protein assay kit. The amount of attached peptide on rGO/dopa-MAL was determined to be 263 μg mg^{-1} by using the calibration plot obtained from the UV absorbance data of the peptide solution standards at 562 nm (see Figure A.5). The cytotoxicity of rGO/dopa-MAL-c(RGDfC) was assessed using the Uptiblue assay on the human breast MDA-MB-231 and human cervical HeLa cancer cells (Figure 4.5b). The rGO/dopa-MAL-c(RGDfC) material does not show damage to the two cell lines at the concentration of 0-100 μg mL^{-1} after 48 h incubation, illustrating the suitability of the material as a drug delivery platform.

The chemotherapy drug DOX was next loaded onto the rGO/dopa-MAL-c(RGDfC) nanosheets by exploiting the various interactions (π-stacking, H-bonding, hydrophobic) between DOX and rGO. The loading was carried out in water in the dark, and the unbound drug was removed through centrifugation of the dispersion at 13 000 rpm (Figure 4.5a). The successful loading of DOX on rGO/dopa-MAL-c(RGDfC) was evidenced by the reddish color of the solution attributed to DOX showing an absorption peak at 480 nm (Figure 4.5c). The amount of DOX loaded on the matrix was determined by monitoring the UV-Vis absorbance of the supernatant (Figure A.6) and determined to be as 170 μg DOX loaded onto 1 mg of rGO/dopa-MAL-c(RGDfC).

4.3.4. Targeted Cell-Killing Ability of DOX-Loaded rGO/dopa-MAL-c(RGDfC)

We next evaluated the cell-killing ability of DOX-loaded rGO/dopa-MAL-c(RGDfC) on the human cervical HeLa and the human breast MDA-MB-231 cancer cells at pH 7.4. The HeLa cells were used as a negative control, as the nanostructures are designed to target essentially the MDA-MB-231 cancer cell line. The dose-response curves of the free DOX for HeLa and MDA-MB-231 cancer cells (Figure 4.6a) allow to determine the IC_{50} values of 2.35 and 10.5 μM for HeLa and MDA-MB-231 lines, respectively. It is, thus, clear that DOX is much less effective on the MDA-MB-231 cell line than on

the HeLa and will preferentially kill HeLa cells.

We next evaluated the viability of HeLa and MDA-MB-231 cells upon the incubation with DOX-loaded rGO/dopa-MAL-c(RGDfC) nanostructure for 48 h. Figure 4.6b suggests that under physiological pH, the nanostructure does not show any cell-killing ability for the HeLa cells. However, 100 μg mL^{-1} of rGO/dopa-MAL-c(RGDfC) (corresponding to 17 μg DOX) induced cell killing with an estimated IC_{50} = 58 μg mL^{-1} for DOX-loaded rGO/dopa-MAL-c(RGDfC). Considering that 17 μg DOX is integrated onto 100 μg of the rGO nanosheets, this corresponds to an IC_{50} = 9.9 μg mL^{-1} for DOX in the matrix, comparable to the IC_{50} = 10.5 μM of free DOX for the same cell line (Figure 4.6a). The targeting effect is even more clearly pronounced, as HeLa cells are more sensitive to DOX with free DOX showing a $\approx$ 4 times lower IC_{50} value when compared with the MDA-MB-231 cells. The optical images of both cell lines after treatment with DOX-loaded rGO/dopa-MAL-c(RGDfC) (100 μg mL^{-1}) (Figure 4.6c) demonstrate in addition the targeting effect of DOX-loaded rGO/dopa-MAL-c(RGDfC). The cell morphology of HeLa cells is preserved, whereas that of MDA-MB-231 cells is compromised. Interestingly, most DOX molecules remained attached to the rGO/dopa-MAL-c(RGDfC) nanostructure and only <1 % of DOX was released from the structures after 24 h incubation in the physiological solution with the same ionic strength but different pH values. We were thus intrigued to see if the photothermal properties of the rGO/dopa-MAL-c(RGDfC) nanosheets can further improve the cell-killing ability without losing its targeting benefit.

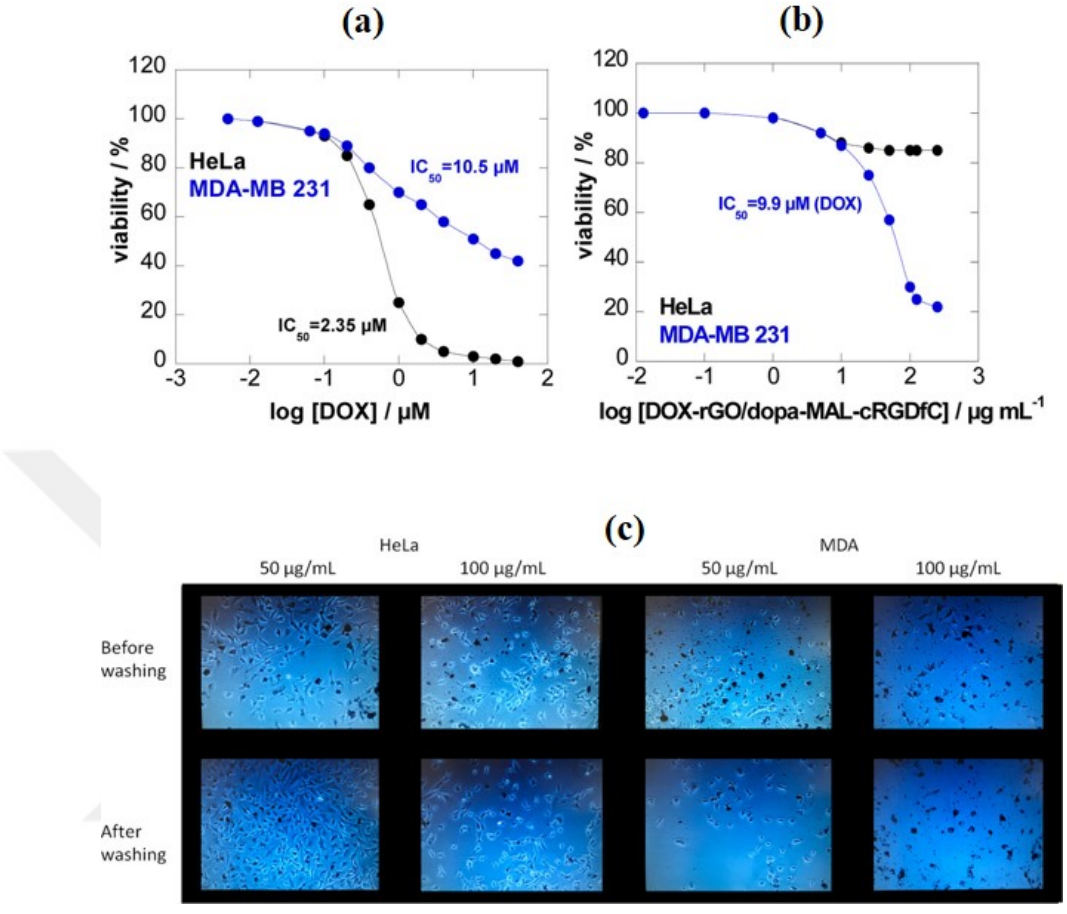

Figure 4.6. Dose-response curves of HeLa (black) and MDA-MB-231 (blue) cancer cells to various concentrations of (a) free DOX for 24 h and (b) DOX-loaded rGO/dopa-MAL-c(RGDfC) nanostructures for 48 h, (c) optical images showing the targeting effect of DOX-loaded rGO/dopa-MAL-c(RGDfC) at two different concentrations (50 and 100 μg mL^{-1}) after 6 h incubation before and after washing with PBS.

4.3.5. Targeted Photothermal Cell-Killing Ability of DOX-Loaded rGO/ dopa-MAL-c(RGDfC)

Graphene nanosheets, due to their good photothermal properties together with excellent loading capacity of water-insoluble cancer drugs [157] and drugs with aromatic structures [156] such as DOX, are considered as an ideal nanomaterial for the devel-

opment of combined therapeutic approaches [179, 180]. Particularly, the photothermal properties are appealing, as the generated heat will result in the photothermal ablation of cancer cells, which is known to increase the sensitivity of chemotherapy [181]. Figure 4.7a depicts the heat profiles of different concentrations of DOX-loaded rGO/dopa-MAL-c(RGDfC) solutions upon irradiation for 10 min with a continuous NIR laser at 980 nm at various laser power densities. The temperature increase is dependent on concentration and laser power, with a 100 μg mL^{-1} DOX-loaded rGO/dopa-MAL-c(RGDfC) heating from 22 to 45 °C in 10 min using a laser power of 4 W cm^{-2}, being sufficient to induce cancer cell death. In addition, the generated heat gradient changes the affinity of DOX to rGO/dopa-MAL-c(RGDfC). As seen from Figure 4.7b, a pH- and laser-power-dependent DOX release takes place. The release is rather moderate from 0.17 μg mL^{-1} DOX (no light) to 2.1 μg mL^{-1} upon illumination at 4 W cm^{-2}. Looking at cell viability upon light irradiation (Figure 4.7c and d), it becomes additionally clear that the laser power densities of 4 W cm^{-2} override the targeting approach, resulting in nontargeted cell killing. With a laser power of 2 W cm^{-2}, the DOX-loaded rGO/dopa-MAL-c(RGDfC) shows a somewhat improved IC_{50} = 48 μg mL^{-1} for MDA-MB-231 cells, corresponding to DOX IC_{50} = 8.2 μg mL^{-1} and keeping a complete targeting capability.

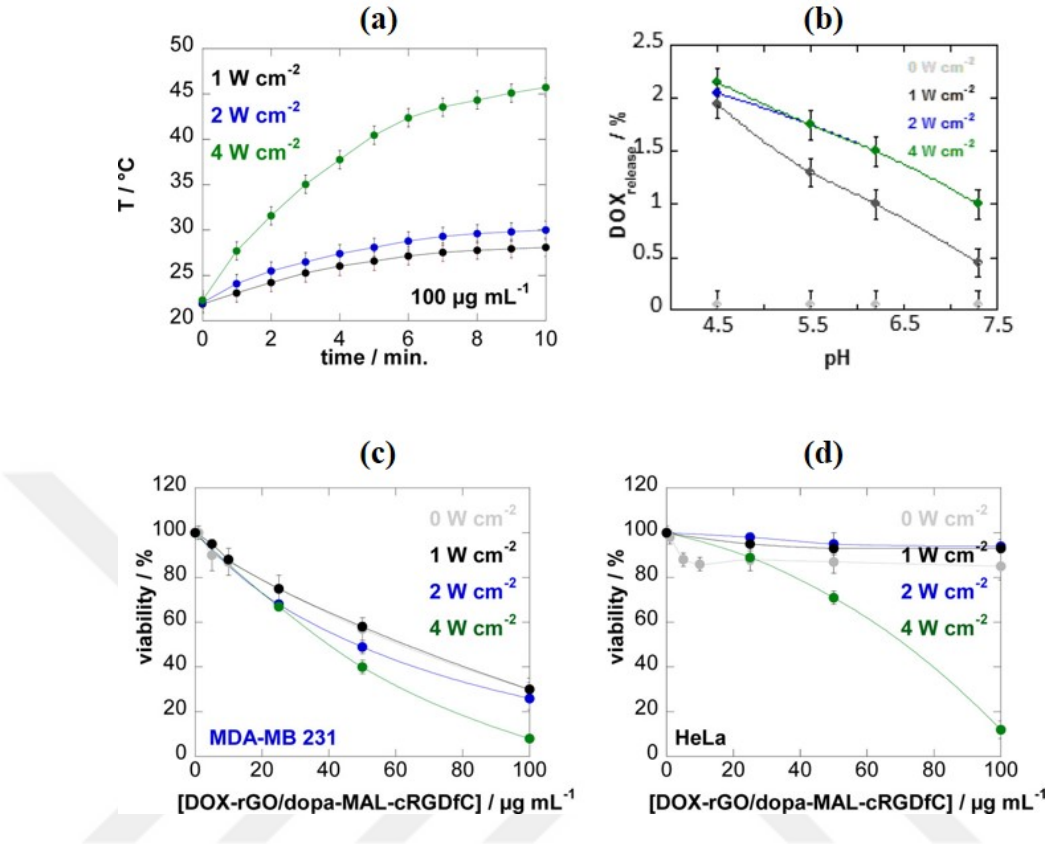

Figure 4.7. (a) Photothermal heating profiles of DOX-loaded rGO/dopa-MAL-cRGDfC (100 μg mL^{-1}) using a 980 nm laser at different laser power densities, (b) DOX amount released from the DOX-loaded rGO/dopa-MAL-cRGDfC (17 μg DOX for 100 μg rGO/dopa-MAL-cRGDfC) matrix, (c) cell viability of MDA-MB-231 cells after irradiation for 10 min at 980 nm with different laser power densities after 6 h incubation and then additional 18 h incubation, (d) cell viability of HeLa cells after irradiation at 980 nm for 10 min at different laser power densities after 6 h incubation and then additional 18 h incubation.

4.4. Conclusions

In conclusion, we have demonstrated the interest of a maleimide-containing catechol (dopa-MAL) ligand as a versatile surface anchor onto the rGO nanosheets. The rGO/dopa-MAL-modified nanosheets can be easily modified with the thiol-containing molecules under ambient metal-free conditions. We could show that this approach

is not only effective for model molecules such as glutathione and ferrocene containing a thiol group, but it is also adaptable to the covalent linking of thiol-containing tripeptides, such as the cancer cell targeting peptide c(RGDfC). The specific cell targeting and ablation properties of DOX-loaded rGO/dopa-MAL-c(RGDfC) nanosheets was confirmed through the cell viability of human breast MDA-MB-231 adenocarcinoma cells after 48 h incubation with the nanostructures and of the human cervical HeLa cancer cells as the negative control. The HeLa cells remained unaffected by even high concentrations of DOX-loaded rGO/dopa-MAL-c(RGDfC). The nanostructures were, however, effective on MDA-MB-231 cells with an $IC_{50} = 58$ μg mL^{-1} for the DOX-loaded rGO/dopa-MAL-c(RGDfC), corresponding to an $IC_{50} = 9.9$ μg mL^{-1} for DOX in the matrix. Slight improvements were achieved upon 980 nm irradiation of the DOX-loaded rGO/dopa-MAL-c(RGDfC) in the presence of MDA-MB-231 cells for 10 min at 2 W cm^{-2}, whereas high laser power densities proved detrimental for the targeting ability of the c(RGDfC) peptide-containing construct.

5. MODULAR FABRICATION OF POLYMER BRUSH COATED MAGNETIC NANOPARTICLES: ENGINEERING THE INTERFACE FOR TARGETED CELLULAR IMAGING[3]

5.1. Introduction

MNPs have emerged as indispensable building blocks for a broad range of functional materials for biomedical applications [182–186]. Oftentimes, these nanoparticles are coated with a layer of polymeric material to impart properties that enable and enhance their utility. Today, polymeric coatings on MNPs play a role beyond just simple prevention of their agglomeration. They impart these magnetic nanomaterials with functional attributes for various applications such as targeted drug delivery and MRI contrast agent. A judicious choice of biocompatible polymeric coating also provides the much needed resistance to biofouling under physiological conditions [101]. For many applications, the surface coating on MNPs needs to be engineered in a manner that would allow attachment of specific ligands and biomolecules while exhibiting resistance toward undesired protein adsorption in the biological media [187]. A variety of polymeric coatings ranging from ultrathin coatings of amphiphilic copolymers to block copolymers, as well as surface-tethered polymer brushes, have been utilized toward fabrication of functional MNPs [188, 189]. While there have been several advances in coating of MNPs with biocompatible polymeric brushes, only a few reports have focused on functionalizable polymer brushes [190–192]. Furthermore, depending on the application, it may be desirable as well as sufficient to effectively modify only the surface of the polymeric brush, as it is this interface that is presented to the surroundings. Traditionally, end-functionalizable brushes have been obtained by chain-end modification of polymers produced using controlled radical polymerizations such as ATRP and RAFT polymerization. In spite of advantages like control over coating thickness and

[3]Published in ACS Applied Materials & Interfaces [170]. Reproduced by permission of American Chemical Society.

their uniformity, this approach limits the types of conjugation chemistries that can be utilized to obtain a diversely functionalized collection of nanoparticles from a particular batch of polymer coated MNPs. Strategies to extend the methods of functionalization of the nanoparticle interface while minimizing batch-to-batch variability will be highly desirable. This can be accomplished through an approach that would entail fabrication of parent nanoparticles where the end group on the polymer can be converted into a variety of different "clickable" functional groups that undergo effective reaction under mild and benign conditions (Figure 5.1). Thus, availability of a library of reactive polymer-coated nanoparticles that can be modified using a variety of different "click" chemistries can be utilized to obtain a diverse library of functional nanoparticles.

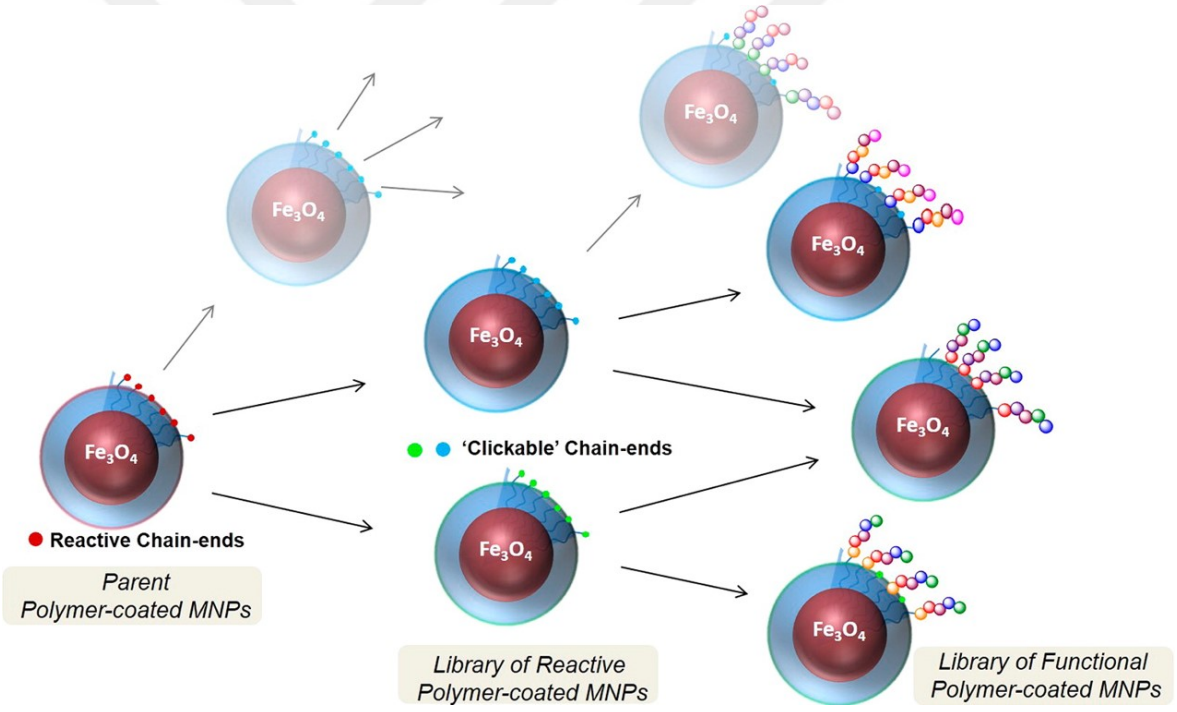

Figure 5.1. Illustration of a modular approach to fabricate a library of functional MNPs through diversification of parent polymer-coated MNPs.

A functional polymer brush based coating must satisfy some basic criteria: (a) robust tethering onto the nanoparticle surface to provide stability in challenging biological milieu, (b) an antibiofouling nature to minimize nonspecific attachment of proteins, and (c) stable reactive groups for facile and efficient attachment of functional moieties such as imaging agents, drugs, and targeting groups. Robustness of polymeric shell on the MNPs' surface is determined by the affinity of anchor group for iron oxide. While traditionally some common anchor groups such as carboxylic acids [193], phosphonates [194], and silanes [195] have been employed, recent interest has focused on catechol-based bioinspired anchoring because of its high affinity for iron oxide and resistance to thermal and hydrolytic decomposition [196, 197]. In addition, the catechol unit can be readily introduced into a polymer or a polymerization initiator that bears an activated carboxylic acid [198, 199]. A "graft-from" or a "graft-to" approach can be utilized for obtaining polymer brush coating. In a recent work, we reported modification of MNPs through a "graft-to" approach using side-chain thiol-reactive copolymers containing a catechol moiety at the chain end [171]. Although the "graft-to" approach provides a well-defined polymeric coating, obtaining dense polymeric coating is challenging due to steric hindrance. A "graft-from" technique, where all polymer chains simultaneously grow from the nanoparticle surface, provides a more robust and dense coating. The choice of polymeric material largely depends on the intended application. Polymer brushes composed of PEG-based hydrophilic polymer have been extensively studied because it reduces nonspecific protein adsorption to the NP surface, which prolongs circulation of iron oxide NPs in the biological systems [200]. PEG-coated NPs can be easily obtained using various controlled radical polymerization techniques [201, 202]. Surface-initiated RAFT (SI-RAFT) polymerization is one of the most widely used controlled polymerization techniques because it is compatible with a wide range of functional monomers and the polymerization proceeds under mild reaction conditions without the need of any metal catalyst. Importantly, the resulting polymer chains possess a thiocarbonylthio groups at the chain ω-end, which can be modified by a variety of methods to obtain desirable end groups or grow another block of polymer [203–205].

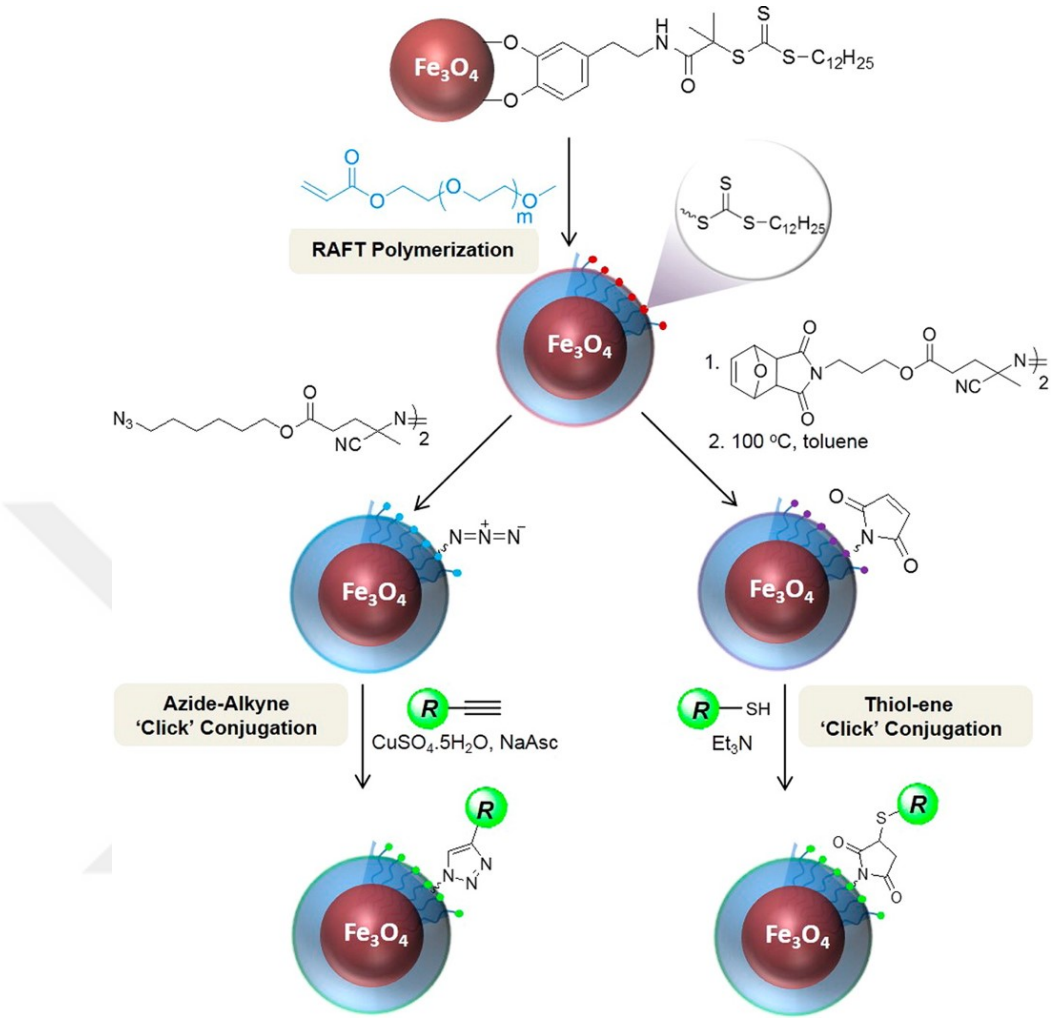

Figure 5.2. Synthesis and modular post-modification of polymer-coated MNPs.

In this study, we outline a modular approach toward generating a library of surface-functionalized MNPs coated with chain-end "clickable" polymer brushes that are produced using the "graft-from" approach (Figure 5.2). Diversification of chain-end reactive groups on the parent nanoparticles is achieved through modification of the trithiocarbonate functional groups on the polymer chain ends using a radical cross-coupling reaction with appropriately functionalized azo-based compounds to install reactive "clickable" groups such as azide and maleimide. This approach leads to facile fabrication of water-dispersible MNPs that can be functionalized with (i) alkyne- or (ii) thiol-containing molecules. The azide functional end group enables the conjugation of an alkyne-containing compound via copper-catalyzed Huisgen-type click re-

action. Likewise, functionalization of maleimide end groups on the polymer can be accomplished with thiol-bearing molecules via nucleophilic Michael addition reaction. Importantly, this approach also allows tailoring of the amount of "clickable" reactive functional group on the surface by using a mixture of "clickable" bisazo-compound along with a nonreactive bisazo-compound such as AIBN during surface modification. Surface-reactive MNPs thus generated provide flexibility with desirable modifications using different types of conjugation chemistries.

5.2. Experimental

5.2.1. Materials and Characterizations

Column chromatography was performed using silica gel 60 (43–60 nm, Merck). TLC was performed using silica gel plates (Kieselgel 60 F254, 0.2 mm, Merck). Furan-protected maleimide-containing alcohol [206], BODIPY-thiol [207], BODIPY alkyne [208], 6-azido-1-hexanol [209], 4-(3-hydroxypropyl)-10-oxa-4-azatricyclo[5,2,1,02,6]dec-8-ene-3,5-dione (azobis-pMAL) [210], cRGDfC [211], DDMAT [212], and DDMAT succinimide ester (DDMAT-NHS) [213] were synthesized according to previous literature examples.

Zeta potential and DLS measurements were performed at 20 °C using a Malvern Zetasizer Nano ZS analyzer. TEM observations were carried out on a LVEM5 microscope operated at 5 kV. XPS was carried out using a K-Alpha instrument (Thermo Scientific). Fourier transform infrared (FT-IR) spectroscopy analyses were performed on a Nicolet 380 (Thermo Fisher Scientific, Inc.) instrument. Magnetization measurement was carried out using a VSM on dry samples at room temperature. UV studies were performed with a Varian Cary 50 Scan UV/vis spectrophotometer. Fluorescent spectra were taken using a Varian Cary Eclipse Fluorescence spectrometer (Varian, Agilent, U.S.A.). The dialysis bags (Spectra/Por Biotech Regenerated Cellulose Dialysis Membranes, MWCO 3500 Da) were purchased from Spectrum Laboratories. Cell internalization studies were performed with Zeiss Observer Z1 fluorescence microscope

connected to Axiocam MRc5 using a Zeiss Filter set 38 (excitation band-pass (BP) 470/40, emission BP 525/50) for imaging the functionalized MNPs. A Zeiss Filter set 49 (excitation G365, emission BP 445/50) was used for imaging DAPI stained nuclei. Images were obtained to visualize cell nuclei and morphology using Zeiss AxioVision software. Cell viability (CV) values for the cytotoxicity experiments were determined by measuring the absorbance of 96-well plates in use at 450 nm by Multiscan FC Microplate Photometer from Thermo Scientific equipped with a quartz halogen light source of a precision CV $\leq$ 0.2 % (0.3–3.0 Abs). It has an excitation wavelength range of 340 - 850 nm with excitation filters installed at 405, 450, and 620 nm.

Cells. Human breast adenocarcinoma MDA-MB-231 cell line was obtained from ATCC (Wessel, Germany). Cells were kept in the logarithmic phase of cell growth for the duration of the experiments. MDA-MB-231 cells were maintained in RPMI-1640 culture medium (Roswell Park Memorial Institute) (Gibco, Invitrogen) supplemented with 10 % FBS (Lonza), 100 U mL^{-1} penicillin, 100 g mL^{-1} streptomycin, and 0.25 g mL^{-1} amphotericin B at 37 °C, under 5 % CO_2 atmosphere and 95 % relative humidity. 2-(4-Aminophenyl)-6-indolecarbamidine dihydrochloride (DAPI) was obtained from Sigma-Aldrich.

5.2.2. Simultaneous Conjugation of Maleimide-containing MNPs with Dye and cRGDfC via Thiol–ene Reaction

End-group maleimide-modified magnetic NPs (Fe_3O_4@PEGMA-MAL3) MNPs (5 mg), cRGDfC (0.22 mg, 0.38 μmol), and BODIPY-SH (0.16 mg, 0.38 μmol) were dissolved in 300 μL of DMF under nitrogen atmosphere. Then, TEA (0.56 μL, 4 μmol) was added into the reaction mixture. The reaction mixture was stirred at 37 °C for 16 h. MNPs were precipitated from diethyl ether and centrifuged at 4000 rpm to remove unreacted dye. After dye purification, MNPs were dispersed in water and unreacted peptide was removed from the dispersion by dialyzing against water for 48 h (MWCO 3500 Da).

5.2.3. Bicinchoninic Acid Protein Quantification

The peptide (cRGD) conjugated onto the MNPs' surface was quantified using a BCA kit (ThermoScientific, U.S.A.) according to manufacturer's instructions. In brief, 100 μL of each standard and MNPs (as unknown sample) were pipetted to glass tubes and 2.0 mL of working reagent prepared as described in the manufacturer's instructions was added to each tube. Tubes were incubated in a water bath at 60 °C for 30 minutes and then cooled to room temperature. The absorbance of each sample was measured by UV-vis at 562 nm within 10 minutes. Finally, total peptide amount was calculated from calibration curve plotted from the protein standards.

5.2.4. Cell Internalization Experiment

Adenocarcinoma MDA-MB-231 human breast cells (50 000 cells/well) were seeded in a 12-well plate as triplicate in 1000 μL of appropriate culture medium. Cells were incubated at 37 °C for 24 h for complete adhesion. Then the culture medium was aspirated and replaced with fresh medium containing imaging agent functionalized NPs at a concentration of 1×10^{-5} M. The experiments were completed in triplicate. After incubation at 37 °C for several time points (3, 6, and 24 h), sample solutions were removed. Wells were washed with 100 μL of PBS three times, and cells were mounted with PBS containing DAPI (5 mg mL^{-1}) at 37 °C for 30 min. After being washed with PBS three times, cells were fixed with 4 % formaline solution at 37 °C for 5 min. Images were collected using Zeiss Observer Z1 fluorescence microscope at room temperature.

5.2.5. Cytotoxicity Experiment

Cytotoxic activity of cRGD-attached Fe_3O_4@PEGMA-MAL3 MNPs was investigated by CCK-8 viability assay against MDA-MB-231 human breast adenocarcinoma. Cells were seeded in 96-well plates and treated with the MNPs at 37 °C for 48 h. Seven different concentrations (from 1 μg mL^{-1} to 1 mg mL^{-1}) of MNPs were pre-

pared by diluting the stock concentration. Cells were incubated after treatment with these samples. Wells were washed with 100 μL of PBS solution twice. Cell viability was evaluated by CCK-8 assay by adding 10 μL of CCK-8 reagent in 100 μL of fresh medium onto wells.

5.3. Results and Discussion

5.3.1. Synthesis of Polymer Brush Coated Parent MNPs

MNPs with narrow size distribution were obtained by thermal decomposition of iron oleate complex in the presence of oleic acid in 1-octadecene, a high-boiling hydrocarbon solvent, using literature protocols [214, 215]. Nanoparticles were superparamagnetic as deduced from their field-depended magnetization curve obtained using VSM (Figure A.7). The coating of MNPs with poly(PEGMEA) was carried out by a two-step procedure. First, a trithiocarbonate-based CTA bearing catechol functionality was utilized to anchor MNP surface (Figure 5.3). The catechol group is a well-known anchor for various metal and metal oxides surfaces [216], and the strong binding ability of the catechol group on various surfaces has been exploited in modification of MNPs and planar surfaces with polymeric materials [217–219]. In the second step, surface-initiated RAFT polymerization was used to obtain polymer brushes on the MNPs.

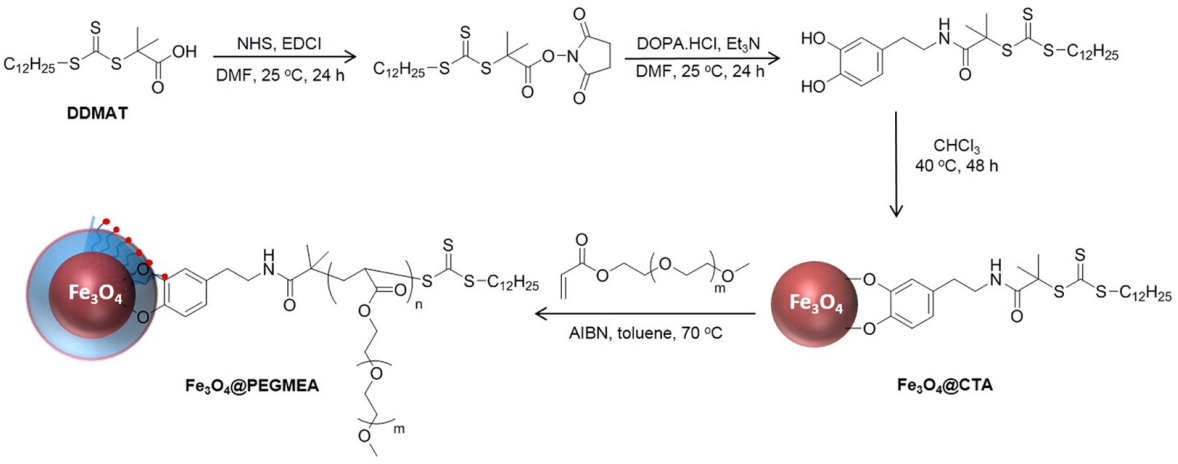

Figure 5.3. Synthetic route of p(PEGMEA)-coated iron oxide MNPs.

Albeit having a dense polymer coating on the surface, MNPs showed good magnetic behavior by being attracted within <10 min in the presence of an external magnet (Figure A.8). The dispersion solution became almost clear after 12 h magnet attraction, which indicates that one can exploit the magnetic behavior of Fe_3O_4@PEGMEA MNPs even after polymer coating (Figure 5.4c). Zeta potential was measured as − 8.7 mV (data not shown), low enough to consider the particles as neutral. Furthermore, TEM analysis of polymer-coated nanoparticles dispersed in water indicates that MNPs did not form any aggregates during the polymerization (Figure 5.4a).

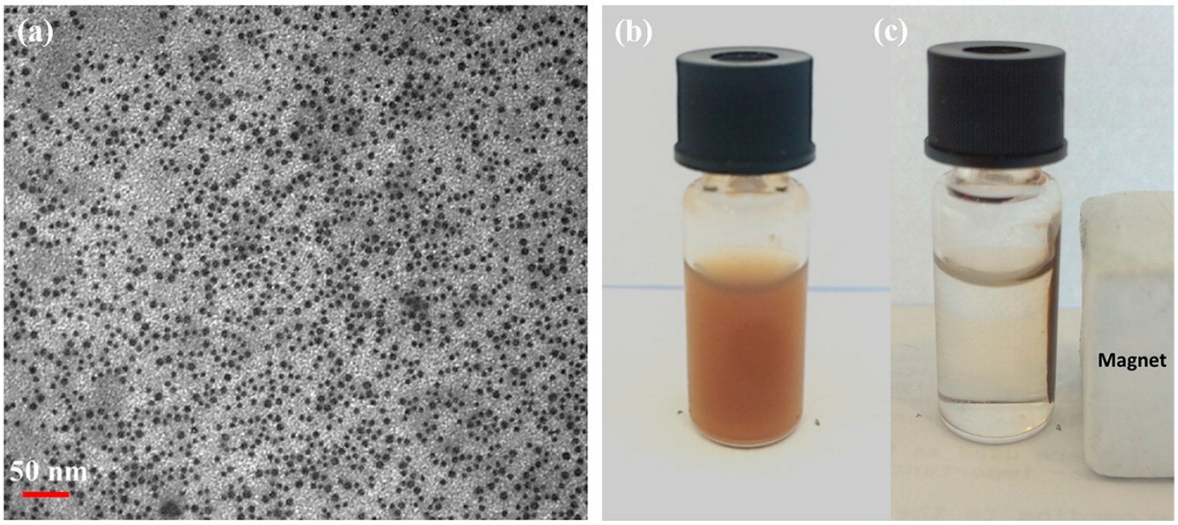

Figure 5.4. (a) TEM image of Fe_3O_4@PEGMEA MNPs and (b) Fe_3O_4@PEGMEA MNPs as aqueous dispersion and (c) after 12 h exposure to magnet.

The nanoparticle surface modification using the catechol-bearing CTA and grafted polymer chains was also characterized using XPS. For the CTA-derived MNPs, the peaks with binding energies (BEs) of 56 (Fe 3p), 164 (S 2p), 285 (C 1s), 400 (N 1s), 532 (O 1s), and 711 (Fe 2p) were observed from wide-scan spectrum (Figure 5.5a). In the core-level spectrum of C (1s), the peaks at 285.0, 286.6, and 288.9 eV were attributed to C–C/C–H, C–O, and C=O, respectively (Figure 5.5b). The S (2p) peak belonging to sulfur in the trithiocarbonate groups was observed at 164 eV (Figure 5.5c). As expected, the area ratio of N to S peaks was observed to be 1:3. The chemical composition of Fe_3O_4@PEGMEA MNPs was also characterized using XPS (Figure 5.5d),

with characteristic peaks of Fe (3p), S (2p), C (1s), N (1s), O (1s), and Fe (2p) observed at 56, 163, 285, 400, 532, and 710 eV, respectively. In the core-level spectra of C (1s) and S (2p), binding energies of 285.0, 286.5, 288.9, and 164.2 eV are attributed to C–C/C–H, C–O, C=O, and S (2p), respectively (Figure 5.5e and f).

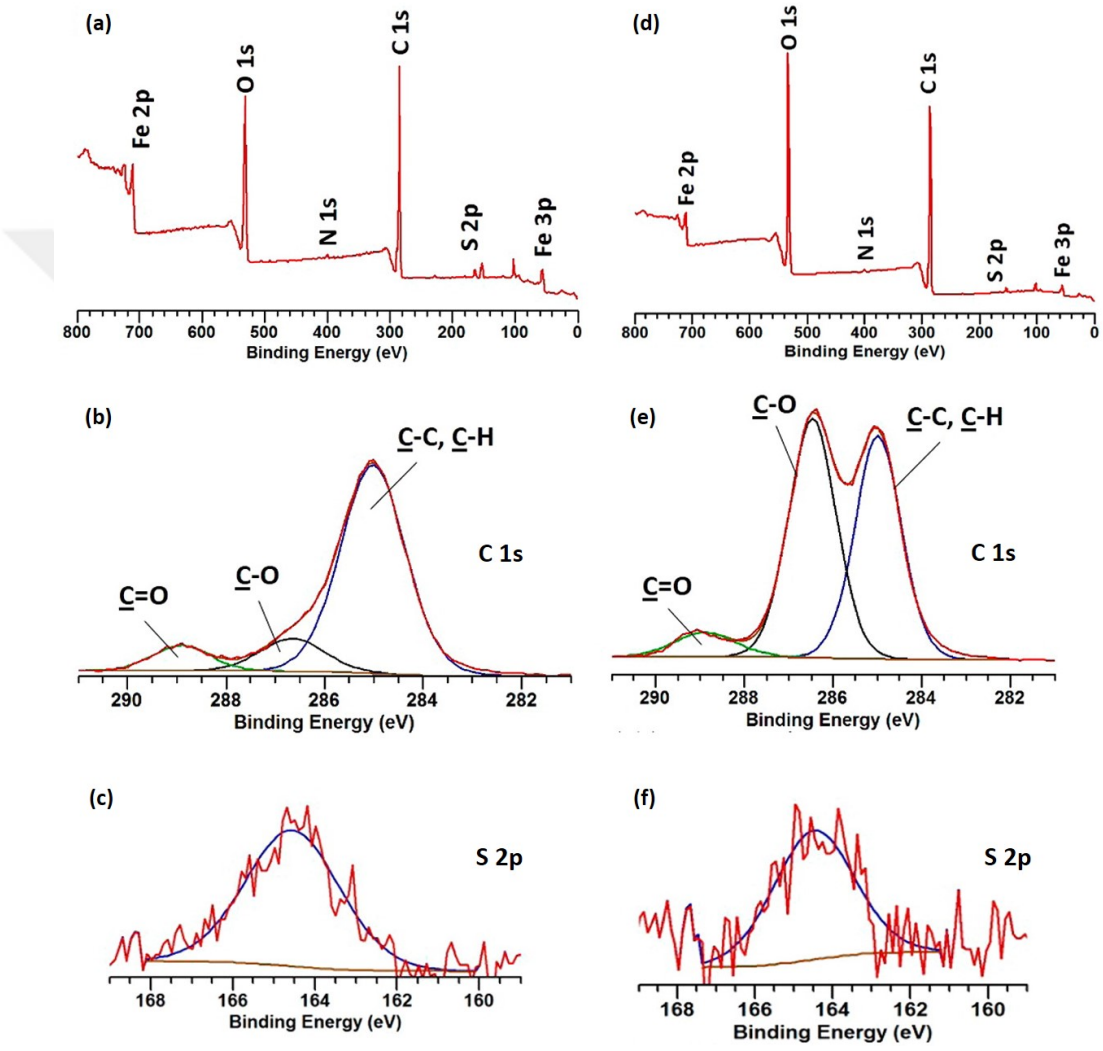

Figure 5.5. (a) XPS wide-scan spectrum of Fe_3O_4@CTA, (b) C 1s core-level spectra and (c) S 2p core-level spectra of Fe_3O_4@CTA, (d) wide-scan spectra of Fe_3O_4@PEGMEA, (e) C 1s core-level spectra and (f) S 2p core-level spectra of Fe_3O_4@PEGMEA.

5.3.2. Installation and Functionalization of "Clickable" Functional Groups

Post-polymerization chain-end modification was accomplished in a modular approach using radical exchange reactions in the presence of appropriately modified bisazo-based compounds bearing "clickable" reactive groups. To introduce the azide groups, an azo-based azide-containing compound azobis-N_3 was synthesized and used for end-group modification of polymer brush coated iron oxide MNPs. Using radical cross-coupling approach, polymer-coated MNPs decorated with azide groups at the polymer chain termini (Fe_3O_4@PEGMEA@N_3) were synthesized (Figure 5.6). Polymer brush coated MNPs with protected maleimide end groups (Fe_3O_4@PEGMEA@pMAL) were synthesized using azobis-pMAL (Figure 5.6). Attachment of furan-protected maleimide groups at the chain ends of grafted polymers was investigated using the radical cross-coupling modification with varying ratios of azobis-pMAL and AIBN to show the efficiency of controlling the end-group density. Three sets of surface-modified MNPs with increasing maleimide content were obtained using 25, 50, and 100 % of the masked maleimide azobis-pMAL to yield Fe_3O_4@PEGMEA@pMAL1, Fe_3O_4@PEGMEA@pMAL2, and Fe_3O_4@PEGMEA@pMAL3, respectively. During the modification reaction, the temperature was kept at 65 °C to avoid any deprotection of maleimide groups.

Surface compositions and maleimide ratio of the NPs were also analyzed via XPS (Figure 5.7). The photoelectron lines at binding energies (BEs) of about 286 eV (C 1s), 399 eV (N 1s), and 531 eV (O 1s) were observed from wide-scan spectrum. After end-group modification of the MNPs, the S (2p) peak coming from the trithiocarbonate end groups of RAFT polymers completely disappeared and a new N (1s) peak appeared. As expected, the XPS results clearly indicate an increase in the N atom content (from 0.31 % to 0.44 %) upon increasing the maleimide content.

Fe_3O_4@PEGMEA@pMAL3 MNPs were activated by retro-Diels–Alder reaction by removing furan groups by heating MNPs to 110 °C. Then, cRGDfC, a cyclic peptide targeting the overexpressed integrin receptors in several types of cancer, and the fluores-

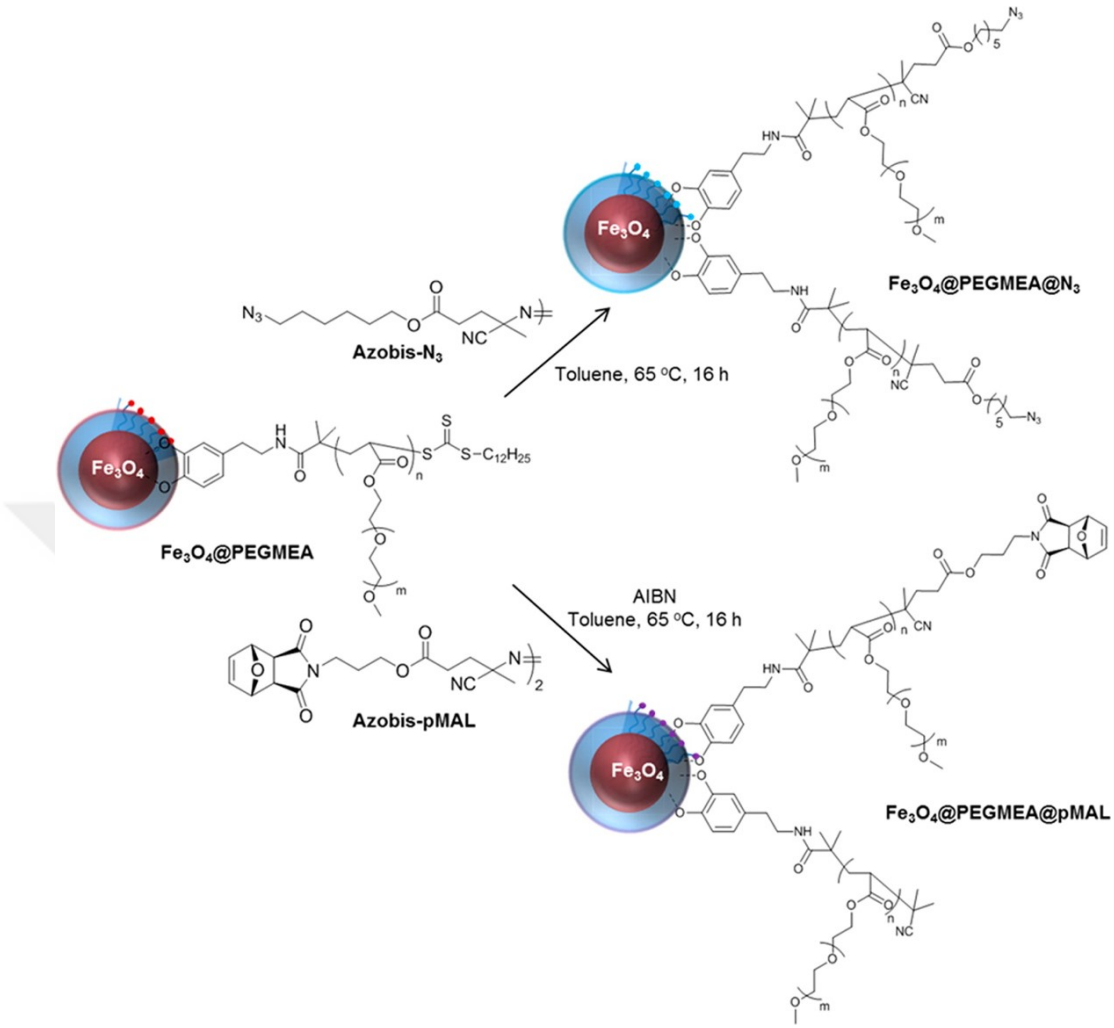

Figure 5.6. Diversification of reactive surface modification of MNPs by azide or furan-protected maleimide derivatives.

cent dye, BODIPY, were conjugated onto the MNP surface (Fe_3O_4@PEGMEA@MAL3) via Michael addition reaction to evaluate these multifunctional constructs for targeted cellular imaging (Figure 5.8). Conjugation onto the nanoparticle surface was carried out using cRGDfC and BODIPY-SH simultaneously. The attachment of the cRGDfC peptide onto the nanoparticle surface was confirmed by BCA analysis (Figure A.9). The amount attached onto the MNP surface was calculated as 9.78 μg mg^{-1} nanoparticle by using a calibration curve using UV absorbance values for standard peptide solutions at 562 nm. Cytotoxicity of cRGD-attached MNPs was evaluated on MDA-MB-231 human breast cancer cell lines. The results showed that cRGD-conjugated

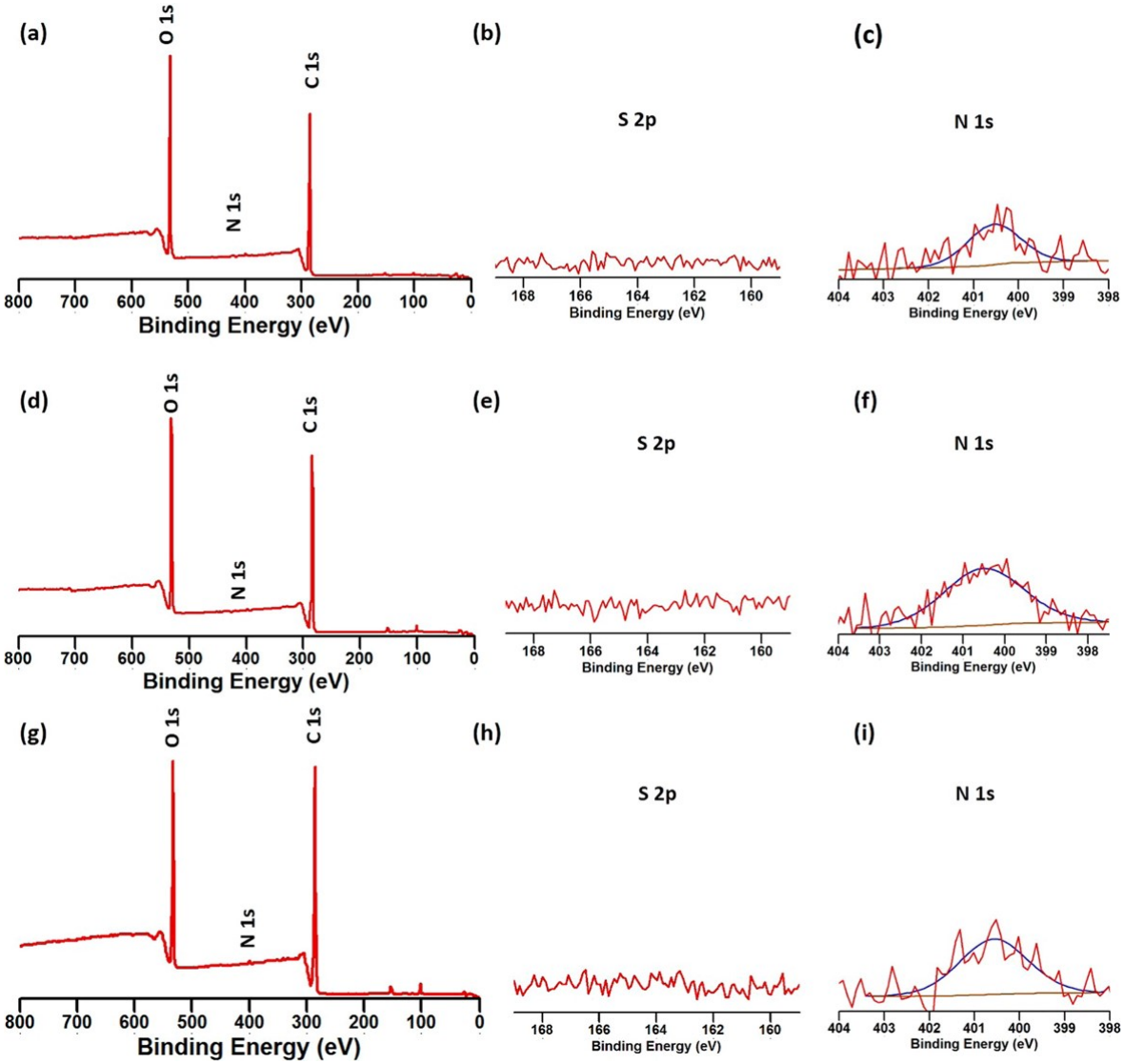

Figure 5.7. (a) XPS wide-scan spectrum of Fe_3O_4@PEGMEA@pMAL1, (b) S 2p core-level spectrum and (c) N 1s core-level spectrum of Fe_3O_4@PEGMEA@pMAL1, (d) wide-scan spectrum of Fe_3O_4@PEGMEA@pMAL2, (e) S 2p core-level spectrum and (f) N 1s core-level spectrum of Fe_3O_4@PEGMEA@pMAL2, (g) wide-scan spectrum of Fe_3O_4@PEGMEA@pMAL3, (h) S 2p core-level spectrum and (i) N 1s core-level spectrum of Fe_3O_4@PEGMEA@pMAL3.

MNPs did not have cytotoxic effect on the cell lines, as indicated in Figure 5.9. This safe aspect of the peptide-functionalized polymer-coated MNPs suggests them to be appropriate for biological applications.

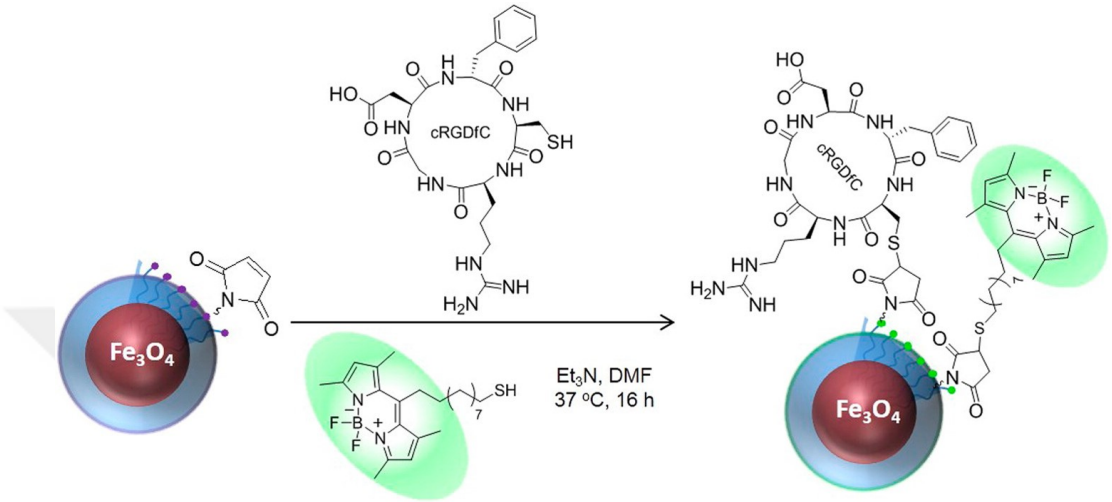

Figure 5.8. Attachment of targeting peptide (cRGDfC) and imaging dye (BODIPY-SH) onto the Fe_3O_4@PEGMEA@MAL3 MNPs.

The uptake of cRGDfC-conjugated MNPs was examined over integrin overpressing adenocarcinoma MDA-MB-231 human breast cell line. Cellular uptake of fluorescent MNPs was investigated using fluorescence microscopy. Cultured cells were treated with dye-conjugated Fe_3O_4@PEGMEA@MAL3 MNPs and incubated at 37 °C. Cell-internalization experiments were investigated at 3, 6, and 24 h. Cell nuclei were detected by staining with DAPI, which can be visualized by its blue fluorescence. As expected, it was observed that the cellular internalization increased upon increasing the time of incubation for both MNPs. However, it can be seen that, after 6 and 24 h, the green fluorescence was remarkably higher for cells treated with cRGD- and BODIPY-conjugated MNPs when compared to the cells treated with MNPs conjugated with only BODIPY (Figure 5.10). Thus, MDA-MB-231 cells with overexpressed integrin receptors could be targeted and visualized using the targeting ligand and imaging agent containing MNPs that were readily obtained using the polymer-coated MNPs.

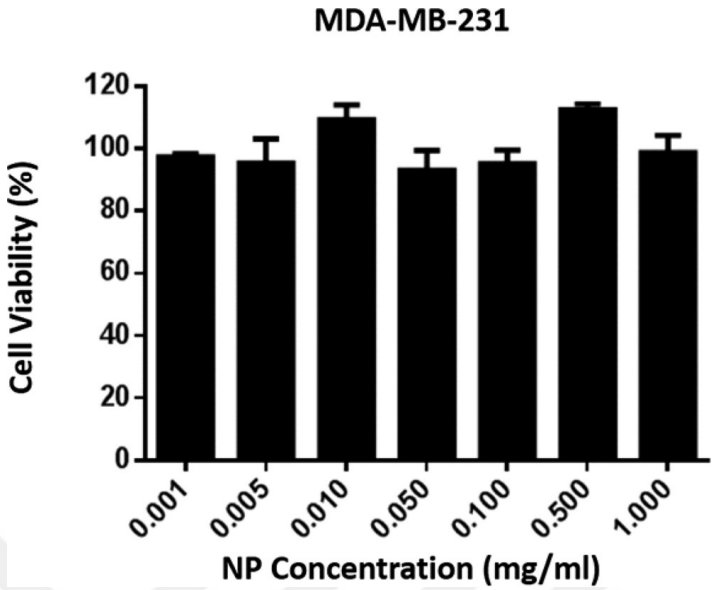

Figure 5.9. Cell cytotoxicity evaluation of cRGD-attached Fe_3O_4@PEGMEA@MAL3 MNPs with different concentrations over MDA-MB-231 cells.

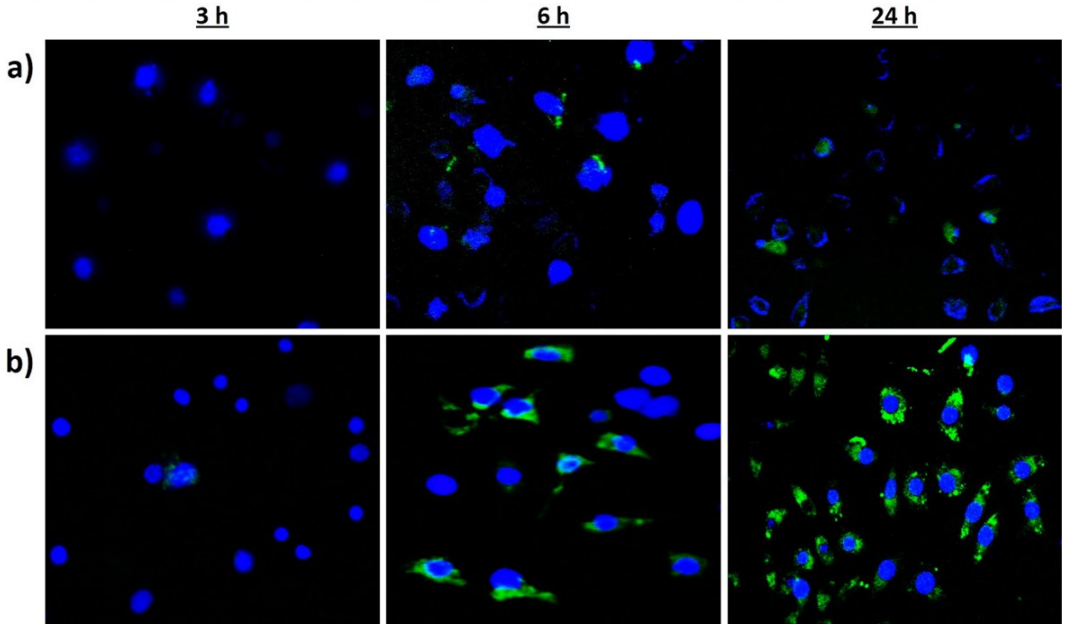

Figure 5.10. Merged fluorescence images of MDA-MB-231 cells following treatment with (a) BODIPY-attached and (b) BODIPY- and cRGD-attached Fe_3O_4@PEGMEA@MAL3 NPs.

5.4. Conclusions

The approach to obtain a library of "clickable" polymer-coated magnetic nanoparticles reported here expands the tool box of building blocks for rapid fabrication of multifunctional nanoparticles. Polymer brush coated parent MNPs were modified to obtain different types of surface-reactive "clickable" nanoparticles. This expands the availability of various conjugation strategies, thus allowing facile generation of a diverse library of materials originating from the same batch of nanoparticles. In particular, polymeric brushes synthesized using RAFT can be modified with clickable functional groups like azides and maleimides. Thus, modified MNPs can be decorated with alkyne-containing and thiol-containing functional moieties like peptides and dyes. The approach outlined here is not limited to the installation of azides and maleimides but can be expanded to a variety of "clickable" groups. Multifunctional materials fabricated here benefit from the magnetic nature of the metal-oxide core, which can enable localization as well as imaging, and the polymeric shell, which enhances dispersibility in biological media, as well as surface functionalities that enable targeting and optical imaging. Development of such efficient and rapid protocols for diversification of functional nanomaterials promises to enable identification of lead candidates for various applications such as imaging and delivery using high-throughput protocols.

6. MAGNETIC GLYCONANOPARTICLES FOR SELECTIVE LECTIN SEPARATION AND PURIFICATION[4]

6.1. Introduction

Lectins are carbohydrate binding proteins that can specifically and reversibly bind specific carbohydrates without any chemical transformations and play the role of reading the sugar code in biology [221, 222]. Due to the nature of their selective and specific interaction, the lectin-carbohydrate interactions play a vital role in the development of diagnostics and therapy platforms. In general, lectins are mainly obtained from plants and are mostly purified using relevant carbohydrate conjugated affinity chromatography or membrane sorbents that only capture relevant lectins from a mixture. Even though conventional affinity chromatography is widely utilized for lectin separation [223–225], especially for tight-binding lectins, it requires multiple washing steps resulting in a loss of weak-affinity lectins and a decrease in the purification yield. Therefore, the fabrication of an effective and facile system for lectin separation with a high purity and recovery yield has been sought by researchers. This separation system should have: (i) a high carbohydrate density to accumulate even weak-binding lectins, (ii) good stability in aqueous media and (iii) a high selectivity toward desired lectins preventing unspecific binding.

Recently, MNPs have been exploited for biomedical applications, such as drug delivery, MRI contrast agent, hyperthermia, etc, because of their biocompatibility and chemical and physical stability under physiological conditions [186, 226–228]. In addition, these nanoparticles have been utilized for the magnetic separation of biomarkers and biomolecules (lectins, proteins, etc.) [229–233] which is a powerful alternative to conventional separation techniques because they have a very high surface area to vol-

[4]Published in Polymer Chemistry [220]. Reproduced by permission of the Royal Society of Chemistry.

ume ratio and the surface of nanoparticles can be easily tuned with specific carbohydrates for selective lectin separation. These MNPs are often coated with hydrophilic and biocompatible materials such as silicon oxide and polymers to endow MNPs with good water dispersibility [171, 234–236]. Beyond water dispersibility, a polymeric coating on the nanoparticle surface allows one to modify the surface according to the desired application [237].

In our previous work, we reported a modular approach for the surface functionalization of nanoparticles via the modification of polymer chain ends originating from RAFT polymerization with modified azo-based compounds [170]. This approach allows the facile installation of a desired functional group to the polymer chain end. While any desired end group can be installed, we envisioned that a modular construct can be obtained by installation of an end group that is amenable for modification through host-guest chemistry. An adamantane based end group offers an attractive choice since it can readily undergo non-covalent host-guest inclusion complex formation with β-CDs [238–244]. Seminal contribution in this area was very recently reported by Ravoo and Samanta, where they investigated β-CD capped MNPs to separate a desired lectin from a lectin mixture in a magnetic field utilizing a supramolecular system [231]. MNPs were decorated with specific carbohydrates, namely mannose and galactose, exploiting an inclusion complex with adamantane carbohydrate conjugates and β-CD capped MNPs. Lectin separation from a mixture was successfully demonstrated by using two orthogonal supramolecular interactions which are adamantane/β-CD and carbohydrate/lectin. In order to suppress the non-specific interaction of the nanoparticle surface with the protein, an ethylene glycol repeat unit containing the adamantane ligand was also added to the CD-coated nanoparticle surface. A nanoparticle based system possessing an inherently protein repellant coating would be an attractive construct. Furthermore, these interactions between carbohydrates and lectins can be considerably enhanced by multivalent carbohydrate ligands. Along similar lines, a multivalent sugar β-CD derivative for the fabrication of MNPs with desired biofunctionality was recently reported by Chen and coworkers, while our work was in progress but they have not studied the selective separation of lectins [230]. They synthesized adamantane function-

alized core-shell structured magnetic composite nanoparticles (MNP@SiO_2-Ada) and β-CD derivatives were incorporated onto these MNPs via host-guest interactions. A β-CD derivative conjugated with seven mannose units (CD-M) was evaluated for ConA binding capacity. They reported that multivalent mannose containing MNPs showed higher binding capacity compared to pristine particles, but particles also showed non-specific binding to some extent. It is well known that the interactions between sugars and target lectins can be dramatically increased by using multivalent glycopolymers where sugar units are in close proximity to each other resulting in a cluster glycoside effect. Along these lines, work reported to date consists of sugar unit containing polymeric brushes grafted-from MNP surfaces [245–247]. We envisioned that as an attractive alternative, a 'plug and play' type modular platform based on host-guest chemistry can be used to obtain sugar containing MNPs for lectin isolation and purification.

In this work, we evaluated supramolecular host-guest interactions between surface adamantane modified MNPs coated with PEGMEA and β-CD-sugar conjugates for the separation of lectins. The surface of MNPs was modified with adamantane via a radical cross-coupling reaction in the presence of an adamantane modified azo-initiator. The incorporation of two β-CD-sugar conjugates to MNPs, which are β-CD conjugated with hepta-mannose (β-CD-$(Man)_7$) and conjugated with poly(mannose) (β-CD-p$(Man)_{280}$) was achieved via supramolecular interactions. Lectin binding efficiencies of these MNPs were evaluated in the presence of ConA. Furthermore, lectin separation from a mixture was shown using β-CD-p$(Man)_{280}$ incorporated MNPs (Figure 6.1). Also, by using a galactose-containing polymer, it is demonstrated that PNA can be specifically targeted. So the system is highly modular and specific lectins can be captured by appropriate choice of glycopolymer.

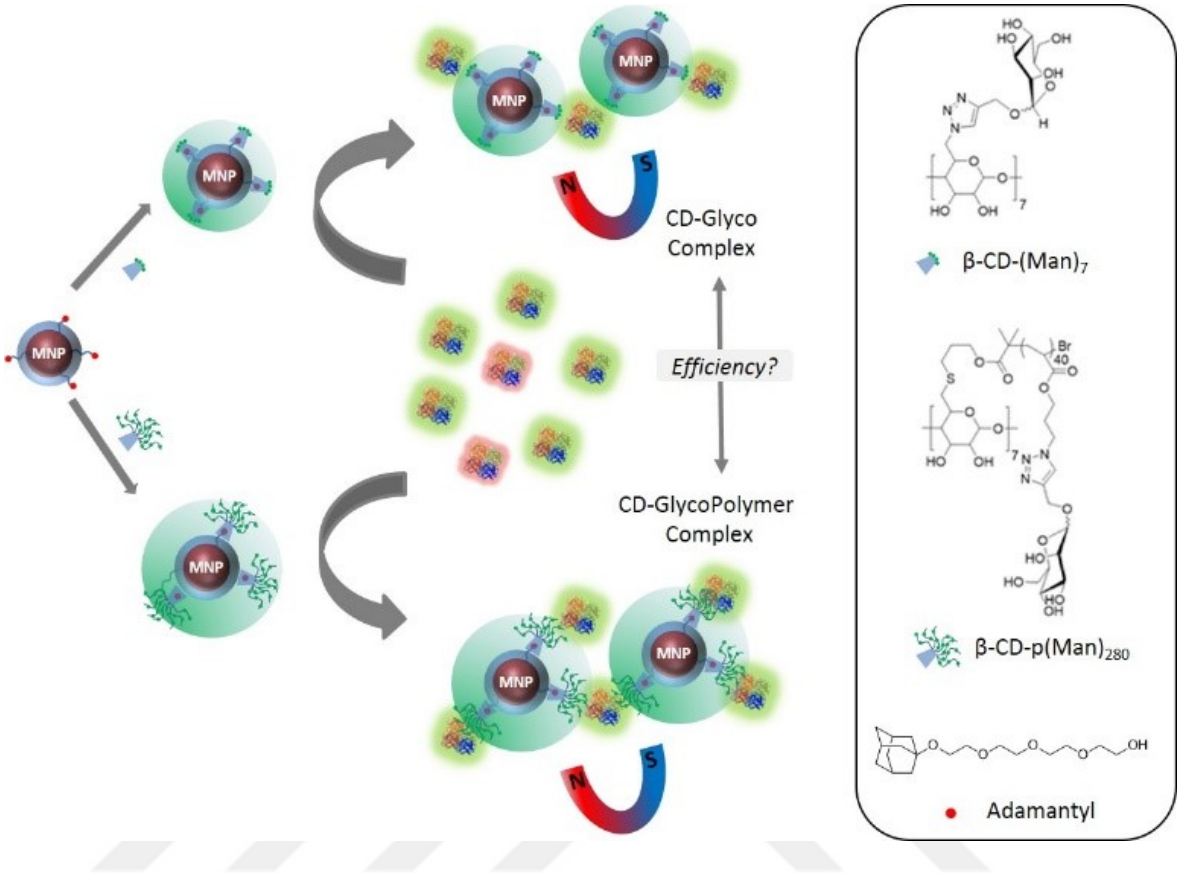

Figure 6.1. Incorporation of β-CD-sugar derivatives to MNPs via supramolecular host-guest interactions and representation of lectin binding with these MNPs.

6.2. Experimental

6.2.1. Materials and Characterizations

Iron (III) chloride hexahydrate ($FeCl_3.6H_2O$), dopamine hydrochloride, oleic acid, Aliquat 336, 1-dodecanethiol, DMAP, tetraethylene glycol, 1-bromoadamantane, calcium chloride ($CaCl_2$), manganese chloride ($MnCl_2$) and TEA were purchased from Sigma-Aldrich and used without further purification. Concanavalin A (FITC conjugate) was purchased from ThermoFisher. PEGMEA (Mn = 480 g mol^{-1}) was purchased from Sigma-Aldrich and purified over neutral aluminum oxide before use. AIBN (Sigma) was recrystallized from methanol and dried at room temperature under vacuum prior to use. V-501 and carbon disulfide (CS_2) were purchased from Fluka.

1-Octadecene, N-hydroxysuccinimide (NHS), beta-cyclodextrin (β-CD) and D-(+)-mannose were purchased from Alfa-Aesar. Sodium oleate was purchased from TCI. Thin layer chromatography was performed using silica gel plates (Kieselgel 60 F254, 0.2 mm, Merck). Column chromatography was performed using silica gel 60 (43–60 nm, Merck). DDMAT [212], DDMAT succinimide ester (DDMAT-NHS) [213], Ada-TEG [248], iron oxide nanoparticles [214], Dopa-CTA, Dopa-CTA immobilized MNPs (Fe_3O_4@CTA), polymer coated MNPs (Fe_3O_4@PEG) [170] and mannose acrylate [249] were synthesized according to previous literature examples. DCM, chloroform, ethanol, DMF, THF and *n*-hexane were purchased from Merck. Anhydrous THF and DCM were obtained from the SciMatCo purification system, and other solvents were dried over molecular sieves. All other reagents and solvents were obtained at the highest purity available from Sigma Aldrich Chemical Company (Dorset, UK) and used as received unless stated otherwise. A dialysis tube (1 and 3.5 kDa MWCO) was purchased from Spectrum Laboratories (California, USA).

DLS and ζ-potential measurements were performed using a Malvern Zetasizer Nano ZS analyzer. TEM observations were carried out on a LVEM5 microscope operated at 5 kV. FT-IR analyses were performed on Thermo Fisher Scientific Inc.; Nicolet 380. ^{1}H NMR and ^{13}C NMR spectra were recorded using a Bruker 400 MHz spectrometer. UV-Vis studies were performed using a Varian Cary 100 Scan UV-Vis spectrophotometer and a PerkinElmer UV-Vis Spectrometer Lambda 35. Fluorescence spectra were recorded on a Varian Cary Eclipse spectrophotometer (Varian, Agilent, USA). The MALDI-TOF MS spectrum acquisitions were conducted on a Shimadzu AXIMA Performance Instrument (Shimadzu Biotech, Manchester, U.K.) equipped with a 337 nm N_2-laser, calibrated using TOF-mixed from Laser BioLabs (Sophia-Antipolis Cedex, France). All spectra were recorded in the positive ion reflection mode. Sinapic acid (10 mg mL^{-1}) solution in acetonitrile/water (1:1 v/v) with 0.1 % TFA was used as the matrix. The obtain spectra were analyzed using MALDI-MS software (Shimadzu Biotech, Manchester, U.K.). SEC measurements were conducted on an Agilent 1260 infinity system operating in DMF with 5.0 mM NH_4BF_4 and equipped with an RID and variable wavelength detector (VWD), 2PLgel 5 μm mixed-C columns (300 x 7.5

mm), a PLgel 5 mm guard column (50 × 7.5 mm) and an autosampler. The instrument was calibrated with linear narrow poly(styrene) standards in range of 575 to 281 700 g mol^{-1}. All samples were passed through 0.2 μm PTFE filter before analysis. TGA was conducted on a TA Instruments TGA Q500 under a nitrogen atmosphere using approximately 7.0 mg of the respective sample by heating from 25 to 500 °C at a rate of 5 °C min^{-1}.

6.2.2. Synthesis of the Adamantane Modified Azo-initiator (azobis-AD)

4,4′-Azobis(4-cyanovaleric acid) (V-501) (0.2 g, 0.71 mmol), Ada-TEG (0.61 g, 1.85 mmol) and DMAP (35 mg, 0.29 mmol) were dissolved in 4 mL of DCM at room temperature. The mixture was cooled to 0 °C in an ice bath and allowed to stir for 15 min. DCC in 1 mL of DCM was added into this mixture dropwise. The mixture was stirred at 0 °C for 30 min, then allowed to warm to room temperature. After stirring for 24 h, the precipitated byproduct was filtered off. The solvent was removed under reduced pressure to obtain a crude product, followed by column purification with ethyl acetate as the eluent (452 mg, 71 % yield). ^{1}H NMR ($CDCl_3$) δ (ppm): 4.27 (m, 4H, OCH_2CH_2OOC), 3.71 (t, 4H, $AdOCH_2CH_2$), 3.69-3.63 (m, 16H, OCH_2CH_2O), 3.67-3.56 (m, 8H, $AdOCH_2CH_2$ + OCH_2CH_2OOC), 2.64-2.32 (m, 8H, $COCH_2CH_2C$), 2.13 (s, 6H, $Ad[CH_2CHCH_2]$), 1.74 (d, 15H, $Ad[CHCH_2CH]$ + CH_3), 1.68-1.57 (m, 12H, $CHCH_2CH[Ad]$). ^{13}C NMR ($CDCl_3$) δ (ppm): 171.4, 117.5, 72.3, 72.0, 71.8, 71.3, 70.7, 70.6, 69.0, 64.2, 59.3, 41.5, 36.5, 33.1, 30.6, 29.1, 24.0.

6.2.3. End Group Modification of Polymer Coated Iron Oxide NPs with azobis-AD

Azobis-AD (61 mg, 68 μmol) and Fe_3O_4@PEG NPs (50 mg) were dispersed in 3 mL of toluene and purged with nitrogen for 20 min. The mixture was stirred in an oil bath at 70 °C for 24 h. End group modified polymer coated MNPs (Fe_3O_4@PEG@AD) were subsequently purified by dialyzing against acetonitrile using a dialysis membrane (MWCO 3500 Da) for 24 h.

6.2.4. Synthesis of Per-(6-deoxy-6-azido)-β-cyclodextrin (β-CD-$(N_3)_7$)

β-CD-$(N_3)_7$ was prepared according to the previous published report [244]. Heptakis (6-deoxy-6-bromo)-β-cyclodextrin (10 g, 6.3 mmol) was dissolved in anhydrous DMF (80 mL) and NaN_3 (5.78 g, 88.8 mmol). The resulting suspension was stirred at 70 °C under Ar for 36 h. The suspension was then allowed to cool down and precipitated in 2 L of stirred ice-water. The precipitate was filtered, washed with water and redissolved in DMF (20 mL) and precipitated in 1 L of stirred ice-water. The precipitate was filtered and washed with water and with little acetone. The resulting product was a white solid (yield: 7.2 g, 86.5 %) and was dried under vacuum overnight. ^{1}H NMR (400 MHz, DMSO-d_6, 298 K, ppm): $\delta = 5.90$ (d, 7H, 6.8 Hz), 5.75 (d, 7H, 2 Hz), 4.91 (d, 7H, 3.4 Hz), 3.74 (m, 14H), 3.59 (m, 14H), 3.36 (m, 14H, overlap with H_2O). MALDI-TOF MS m/z: calculated for $C_{42}H_{63}N_{21}O_{28}K^+$: 1348.37; found, 1348.27.

6.2.5. Synthesis of Mannose Conjugated Beta-cyclodextrin (β-CD-$(Man)_7$)

β-CD-$(N_3)_7$ (1.96 g, 1.5 mmol) and (2′-propargyl)-beta-d-mannopyranoside (2.61 g, 12 mmol) were dissolved in DMSO (20 mL) in a Schlenk tube. Bipyridine (0.37 g, 0.0024 mmol) and CuBr (0.17 g, 0.0012 mmol) were added. The resulting mixture was evacuated and filled with argon and 3 freeze-pump-thaw cycles were performed to eliminate oxygen from the reaction mixture. The mixture was then allowed to stir at 50 °C for 24 h. After the reaction, water was added to the reaction medium and the resulting mixture was dialyzed against water. After dialysis, the resulting clear solution was freeze dried.

6.2.6. Synthesis of Per-6-deoxy-6-(thiopropyl-2-bromo-2-methyl propanoate)-β-cyclodextrin (β-CD initiator)

Per-6-thio-β-cyclodextrin (2.5 g, 2 mmol), and DTT (618 mg, 4 mmol) were dissolved in 40 mL anhydrous DMF under argon and heated to 60 °C. After 60 h, the reaction mixture was allowed to cool down to room temperature and allyl 2-

bromoisobutyrate (14.53 g, 70 mmol) and DMPA (179 mg, 7 mmol) were added to the reaction mixture and stirring was continued for 5 h under UV irradiation (365 nm). The solution was precipitated in 500 mL of MTBE in 50 mL centrifuge tubes and centrifuged at 8000 rpm for 5 min. The solvent was decanted and all precipitated fractions collected in two 50 mL centrifuge tubes and fresh MTBE was added, mixed and centrifuged again. This procedure was repeated 4 times in order to remove DMF and allyl 2-bromoisobutyrate. Subsequently the product was dried under vacuum, yielding a fine beige solid. (3.7 g, yield: 68 %). ^{1}H NMR (400 MHz, DMSO-d_6, 298 K, ppm): δ = 5.90 (d, 7H, 5.6 Hz), 5.8 (m, 7H), 4.85 (m, 7H), 4.22 (t, 14H, 5.2 Hz), 3.85 (m, 7H), 3.57 (m, 7H), 3.33 (m, 14H), 3.09 (d, 7H, 10.6 Hz), 2.82 (m, 7H), 2.69 (m, 14H), 1.90 (s, 56H). MALDI-TOF MS m/z: calculated for $C_{91}H_{147}Br_7O_{42}S_7K^+$: 2733.12; found: 2733.36.

6.2.7. Synthesis of Poly(mannose) Conjugated Beta-cyclodextrin (β-CD-p(Man)$_{280}$)

A Schlenk tube was charged with the mannose acrylate monomer (580.22 mg, 280 eq.), pre-activated Cu(0) wire (5 cm), $CuBr_2$ (0.35 mg, 0.28 eq.) and Me_6TREN (1.70 mg, 1.33 eq.) in DMSO (2 ml) and then the mixture was degassed by gentle bubbling of argon gas for 30 min. The pre-degassed CD initiator in 1 ml DMSO (15 mg, 1 eq.) was then added via a gas tight syringe sequentially. The Schlenk tube was sealed and the reaction mixture was allowed to polymerize at 25 °C. Sampling was carried out using a degassed syringe to check the conversion of the monomer. After it reached full conversion, the polymerization solution was directly dialyzed against water for 3 days. The CD initiated glycopolymer was recovered as a powder by freeze drying.

6.2.8. Supramolecular Complexation Between Fe_3O_4@PEG@AD and β-CD-(Man)$_7$/β-CD-p(Man)$_{280}$

β-CD-(Man)$_7$ or β-CD-p(Man)$_{280}$ was added to 1.67 mg mL^{-1} dispersion of Fe_3O_4@PEG@AD MNPs in Milli-Q water. The mixture was incubated for 15 min, fol-

lowed by the collection of MNPs via a permanent magnet yielding Fe_3O_4@PEG@AD/β-CD-$(Man)_7$ and Fe_3O_4@PEG@AD/β-CD-p$(Man)_{280}$ supramolecular complexes.

6.2.9. Lectin Binding Studies to Mannose Decorated Fe_3O_4@PEG@AD MNPs

Mannose attached MNPs (1.67 mg mL^{-1}) were mixed with 0.05 mg mL^{-1} FTIC labelled ConA in an aqueous buffer solution (20 mM HEPES, 1.0 mM $MnCl_2$, 1.0 mM $CaCl_2$ and 0.15 M NaCl, adjusted to pH 7.4). The mixture was subjected to a magnet for 10 min to collect MNPs. The fluorescence spectrum of the supernatant was taken at an excitation wavelength of 490 nm.

6.2.10. Selective Lectin Separation Assays

A mixture of lectins (FITC-ConA and rhodamine-PNA) was prepared in a HEPES buffered saline and mannose decorated MNPs (1.67 mg mL^{-1}) were subsequently added to this mixture to selectively capture ConA. The mixture was subjected to a magnet for the separation of lectins. The fluorescence spectrum of the supernatant was recorded at an excitation wavelength for FITC-ConA at 490 nm and Rhd-PNA at 520 nm.

6.3. Results and Discussion

6.3.1. Polymer Coating on MNPs

Iron oxide nanoparticles have been extensively exploited for the magnetic separation and detection of biomolecules [250–252]. Oleic acid stabilized iron oxide nanoparticles (Fe_3O_4@OA) were synthesized via a thermal decomposition method according to the previously reported literature [170], and characterized by FT-IR (Figure 6.2). Asymmetric and symmetric CH_2 peaks of oleic acid capped onto the MNP surface appeared at 2916 and 2848 cm^{-1}, respectively (Figure 6.3a). The size distribution of Fe_3O_4@OA NPs was found as an average diameter of 20 nm from DLS analysis (Table 6.1 and Figure A.10) and TEM (Figure 6.3b-e), revealing spherical particles.

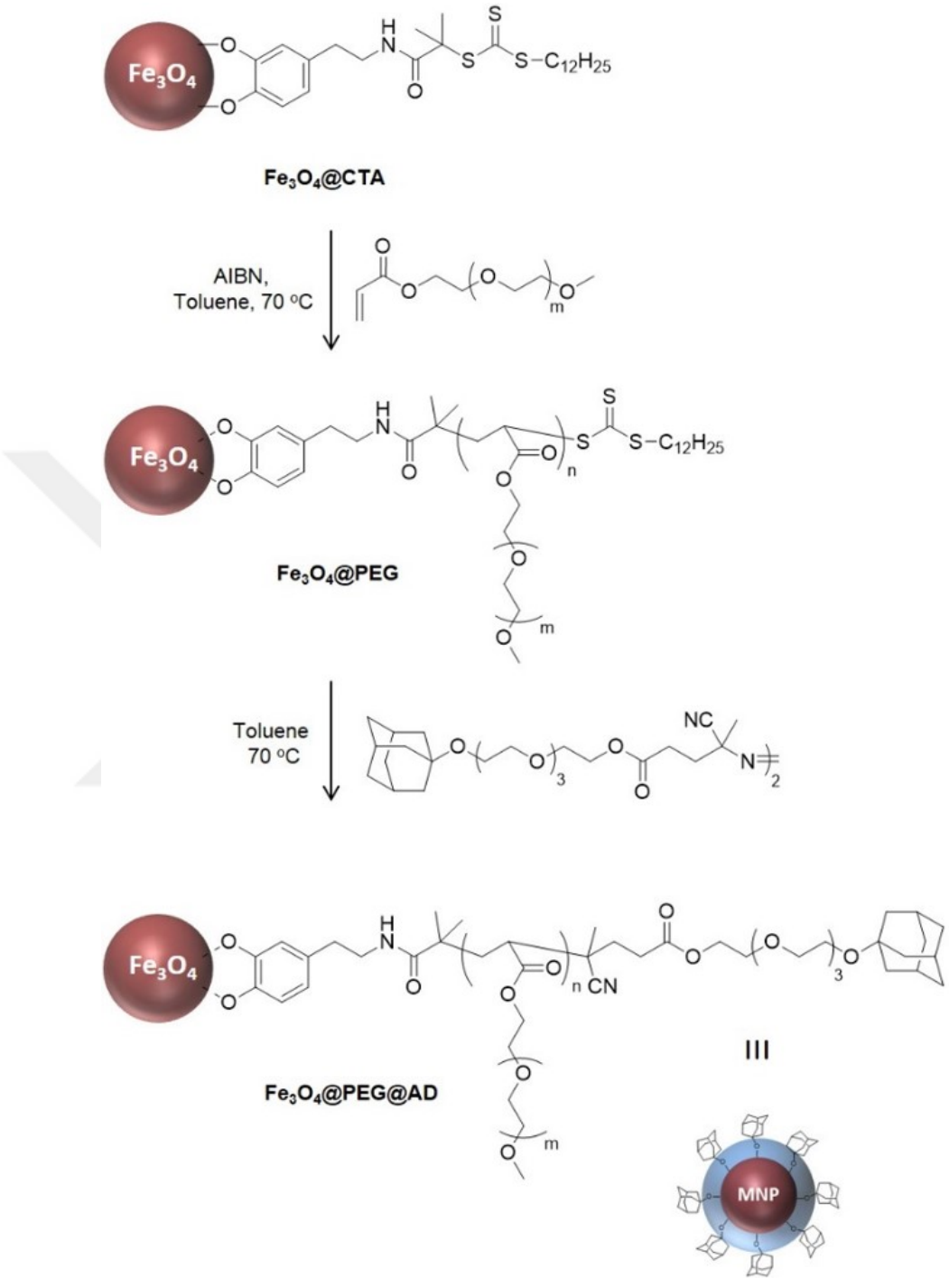

Figure 6.2. RAFT polymerization from the MNP surface with the PEGMEA monomer and surface modification of polymer coated NPs with the azobis-ADA initiator.

Table 6.1. Characteristics of magnetic NPs by DLS, TEM and zeta potential.

	D_{DLS}/PDI	D_{TEM} (nm)	ζ (mV)
Fe_3O_4@OA	20 (0.46)	19 ± 1.7	-
Fe_3O_4@CTA	17 (0.47)	19 ± 2.0	-
Fe_3O_4@PEG	24 (0.46)	19 ± 1.5	-4.5 ± 4.5
Fe_3O_4@PEG@AD	22 (0.23)	19 ± 2.1	-3.2 ± 4.1

The strategy to grow polymer brushes on the MNP surface begins with immobilization of the RAFT agent (dopa-CTA) on the surface because the catechol unit is known to possess high affinity for a variety of surfaces [152,253,254]. A place exchange reaction was carried out in the presence of excess dopa-CTA to immobilize the RAFT agent onto the MNP surface [170]. The surface coating of the MNPs with this modified RAFT agent via a place exchange reaction was confirmed by FT-IR spectroscopy from the presence of a small band at 1645 cm^{-1} belonging to the amide carbonyl group of dopa-CTA (Figure 6.3a). UV-Vis spectroscopy also confirmed the presence of the trithiocarbonate based RAFT agent from its characteristic absorption band around 308 nm that was not present in Fe_3O_4@OA MNPs (Figure A.11a). MNPs did not show any aggregation during the place exchange reaction as indicated in the TEM image of Fe_3O_4@CTA (Figure 6.3c). The hydrodynamic size of the RAFT agent immobilized MNPs was measured as 17 nm from DLS, which was similar to the size of oleic acid coated NPs (Figure A.10).

The polymer brush coating on the MNP surface was obtained via RAFT polymerization with the help of dopa-CTA immobilized onto the surface. The PEGMEA monomer was used to obtain a dense and hydrophilic anti-biofouling polymer shell on the MNP surface using the "graft-from" approach (Figure 6.2). The coating of the hydrophilic PEG polymer on the NP surface was confirmed by FT-IR. The carbonyl stretching of PEG at 1732 cm^{-1} and ether (CH_2-O-CH_2) stretching at 1093 cm^{-1} were observed from FT-IR analysis, which confirms a successful polymer growth from the surface (Figure 6.3a). The hydrodynamic size of Fe_3O_4@PEG MNPs was determined

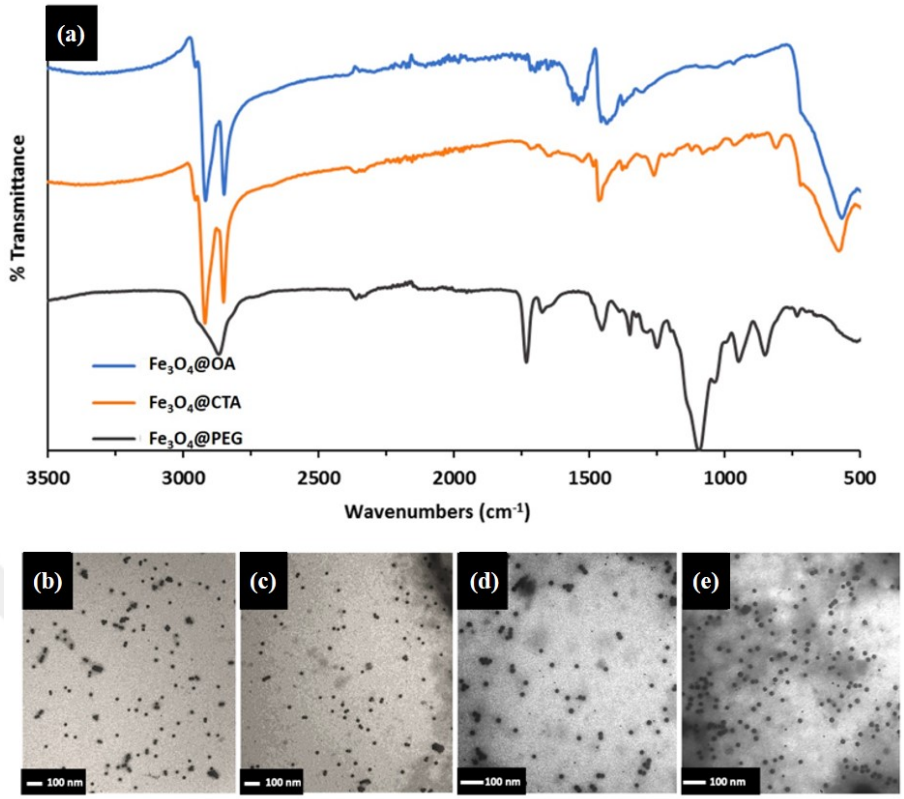

Figure 6.3. (a) FT-IR spectrum of Fe_3O_4@OA, Fe_3O_4@CTA and Fe_3O_4@PEG MNPs, TEM images of (b) Fe_3O_4@OA, (c) Fe_3O_4@CTA, (d) Fe_3O_4@ PEG and (e) Fe_3O_4@PEG@AD MNPs.

by DLS measurements, revealing an average diameter of 24 nm. The zeta potential of polymer coated MNPs was measured as -4.5 mV (Table 6.1). The increase in the hydrodynamic size of the MNPs results from the grafting of a hydrophilic PEG based polymer on the surface. TEM analysis of Fe_3O_4@PEG NPs revealed that they did not undergo any aggregation during polymerization (Figure 6.3d). Furthermore, all these immobilization steps for OA, CTA and PEG polymer respectively on MNPs were confirmed by TGA, as well. As seen in Figure A.12, the amount of mass loss exhibited an increase after each immobilization step. Each coated MNPs showed mass loss until approximately 450 °C due to the decomposition of the material on it, and the remaining fraction was the Fe_3O_4 core that was unaffected at high temperature. It was observed that PEG polymer coated MNPs contained 94.5 % of the polymer.

6.3.2. Modification of Polymer Coated MNPs with Adamantane

Radical-induced transformation of trithiocarbonate (or thiobenzoate, dithiobenzoate and so on) based end group of the RAFT polymers is a versatile process to obtain desired chain end functionality. Exploiting this methodology, an adamantane group was installed onto the polymer coated nanoparticle surface using the azobis-ADA initiator. The initiator was synthesized from Ada-TEG and 4,4′-azobis(4-cyanovaleric acid) in the presence of DCC and DMAP (Figure 6.4). The structure of the azobis-ADA terminating agent was confirmed using ^{1}H-NMR spectroscopy (Figure A.13). End group adamantane modified MNPs (Fe_3O_4@PEG@AD) were synthesized via a radical cross-coupling modification reaction at 70 °C with an excess amount of the azobis-ADA initiator (Figure 6.2). The modification of the trithiocarbonate end group of the polymer chain on the MNP surface was monitored by UV-Vis spectroscopy. A small absorption shoulder around 308 nm belonging to the trithiocarbonate group disappeared after the cross-coupling modification of the RAFT polymer chain-end on the MNP surface (Figure A.11b). The size distribution of Fe_3O_4@PEG@AD MNPs obtained from the DLS measurements indicated an average diameter of 22 nm. The zeta potential of adamantane end group modified MNPs was found as -3.2 mV (Table 6.1). Moreover, the adamantane modified MNPs were characterized by TEM and the presence of discrete MNPs suggested that no aggregation occurred during the radical coupling based end group modification step (Figure 6.3).

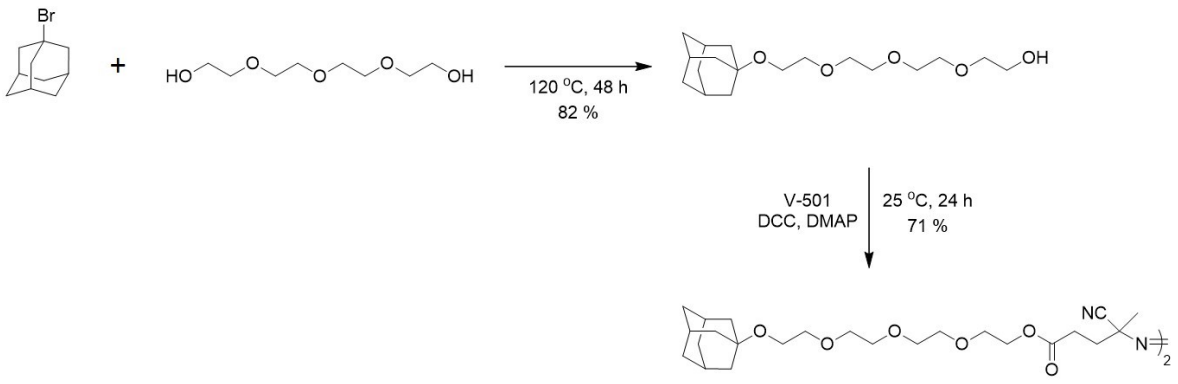

Figure 6.4. Synthetic route of the adamantane modified azo-initiator (azobis-ADA).

6.3.3. Synthesis of Mannose/galactose-containing Beta-CD Constructs

Two types of mannose-containing beta-CD constructs were synthesized to tailor the NP interface for effective targeting of ConA lectin. As depicted in Figure 6.5a and Figure 6.5b, a β-CD derivative (β-CD-$(Man)_7$) containing seven mannose groups at the lower rim and a star-shaped macromolecular construct (β-CD-p$(Man)_{280}$) containing polymeric arms bearing mannose groups as side chain moieties exuding from the lower rim of CD were synthesized. The β-CD-$(Man)_7$ was synthesized according to a previously reported procedure [244]. Briefly, a beta-CD derivative containing hepta-azide groups at the lower rim was clicked with an alkyne-containing mannose derivative using CuAAC. As seen in Figure 6.5d and Figure 6.5c, this successful click reaction was followed by ^{1}H-NMR and DMF GPC analysis. ^{1}H-NMR spectra represented the presence of a new triazole ring peak at approximately 8.0 ppm and also DMF GPC traces showed a significant shift to a lower retention time after the click of mannose alkyne due to the change of hydrodynamic volume.

The polymeric construct that consisted of mannose-containing polymers appended to the bottom rim was synthesized via SET-LRP. The homopolymerization of mannose acrylate was carried out using the synthesized beta-CD initiator (β-CD-$(Br)_7$) under high dilution conditions to avoid a radical-radical coupling side reaction according to previously published report [255]. Briefly, a Schlenk tube was charged with mannose acrylate, preactivated Cu(0) wire, Cu(II)Br_2 and Me_6Tren in DMSO. The pre-degassed β-CD initiator was then added into the Schlenk tube to start the polymerization at 25 °C. After reaching approximately full conversion according to ^{1}H-NMR, the star-shaped macromolecular construct (β-CD-p$(Man)_{280}$) was obtained in the pure form after dialysis. The elution profile revealed a complete shift to a higher molecular weight without any coupling and tailing peaks, strongly indicating a successful synthesis of the polymers (Figure 6.5f and Figure 6.5g). Furthermore, β-CD-p$(Gal)_{280}$ was synthesized using the same approach to target PNA lectins (Figure 6.5c), thus demonstrating that binding to a specific protein can be achieved by choosing the appropriate sugar based ligand.

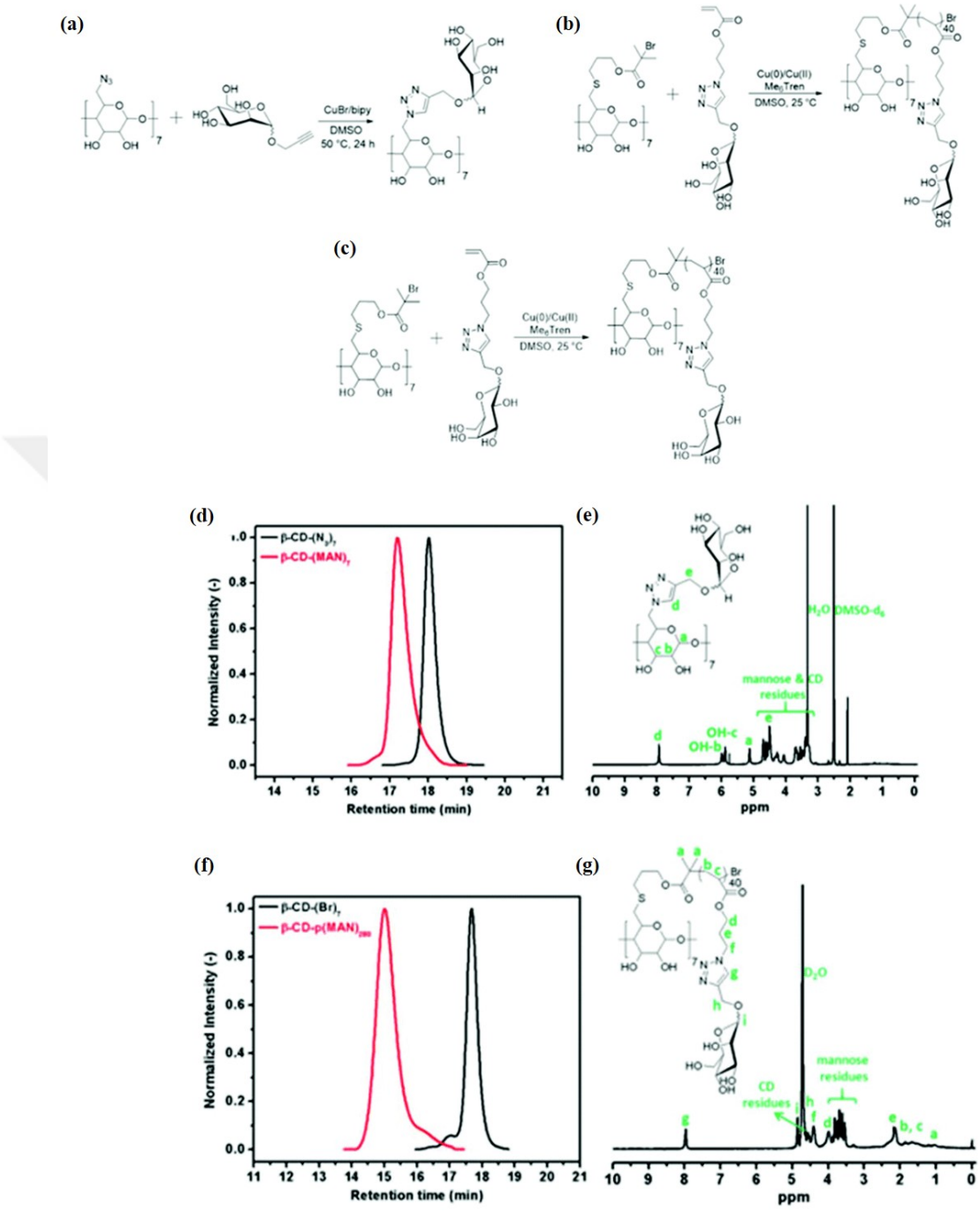

Figure 6.5. Synthesis of mannose containing β-CD constructs; (a) β-CD based $(\text{mannose})_7$, (b) β-CD based $\text{poly(mannose)}_{280}$, (c) β-CD based $\text{poly(galactose)}_{280}$, (d) SEC traces of the synthesized β-CD-$(N_3)_7$ and β-CD-$(\text{Man})_7$, (e) ^{1}H NMR spectra of β-CD-$(\text{Man})_7$, (f) SEC traces of the synthesized β-CD-$(\text{Br})_7$ initiator and CD-based mannose glycopolymer, (g) ^{1}H NMR spectra of β-CD-p(Man)_{280}.

6.3.4. Investigation of Host-guest Complexation of AD-containing MNPs with Mannose Appended CD-based Constructs

Installation of the adamantane group on the surface of polymer coated magnetic nanoparticles provides them with the ability to undergo non-covalent functionalization through host-guest interactions with β-CDs. Hence, the ability of the adamantyl moiety on the NP surface to undergo a successful host-guest type complexation with β-CD was examined. A basic PP solution was treated with β-CD and the decrease in absorbance of the dye due to its complexation with the CD cavity was recorded using UV-Vis spectroscopy. Recovery of the absorbance from the dye upon addition of an adamantyl group containing material indicates its complexation with β-CD to liberate the dye from the CD cavity. For the complexation experiments, β-CD (32 μM) was added to a PP solution which is pink in color at pH >8.2. The decrease in absorbance arising from the inclusion of PP into the β-CD cavity was followed by UV-Vis measurements (Figure 6.6). The addition of different amounts of Fe_3O_4@PEG@AD MNPs (from 1 to 2 mg) triggered the release of PP from β-CD cavity within a few seconds because adamantane has a higher binding affinity for β-CD compared to PP. A recovery of absorbance ascribed to the release of PP from the cavity was observed upon addition of Fe_3O_4@PEG@AD NPs (Figure 6.6). As a control experiment, no recovery of absorbance occurs upon the addition of MNPs devoid of adamantyl groups (1.0 and 1.5 mg). A minimal increase in absorbance was observed upon the addition of more MNPs (2.0 mg), which probably arises from complex formation between the hydrophobic undecane group at the end of polymer brush and β-CD. Background scattering of magnetic NPs in UV analysis did not affect the intensity of the dye because it was found that the UV intensity of PP upon the addition of polymer coated MNPs (from 1 mg to 2 mg) to PP solution showed no intensity increase while MNPs' background scattering was still observable (Figure A.14). Overall, the results indicated that adamantyl groups were successfully installed onto the polymeric shell on the nanoparticle, and were capable of undergoing specific complexation through host-guest interaction with β-CD.

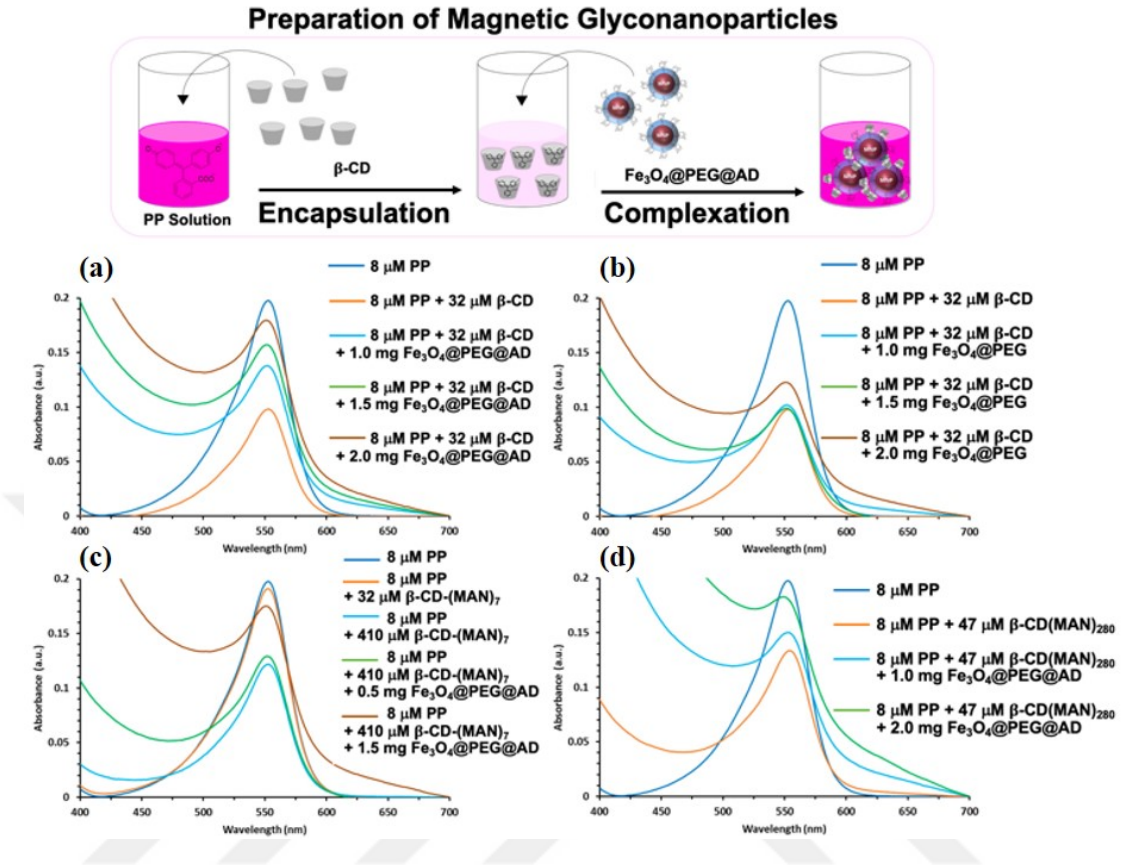

Figure 6.6. UV-Vis spectra of (a) 8 μM PP solutions at pH = 10.2 with 32 μM β-CD and different amount of Fe_3O_4PEG@AD MNP addition, (b) with 32 μM β-CD and different amount of Fe_3O_4@PEG MNP addition as control experiments, (c) with β-CD-$(Man)_7$ and (d) β-CD-p$(Man)_{280}$, followed by mixing with Fe_3O_4@PEG@AD MNPs.

After these initial complexation studies, adamantane functionalized MNPs were investigated toward the formation of supramolecular host-guest complexes with the mannose containing β-CD derivatives β-CD-$(Man)_7$ and β-CD-p$(Man)_{280}$. As expected, UV-Vis absorbance of the PP solution at 552 nm decreased upon the addition of either β-CD-$(Man)_7$ or β-CD-p$(Man)_{280}$ with increasing concentrations. Fe_3O_4@PEG @AD MNPs were subsequently added to these solutions for complexation with these mannose modified CDs. Recovery of the absorbance in the UV-Vis spectra indicated the occurrence of binding between the adamantane groups on the NPs and β-CD derivatives (Figure 6.6), thus suggesting that the surface of MNPs could be decorated with

these mannose containing CD constructs through host-guest interactions.

6.3.5. Lectin Binding to Mannose-containing CD-decorated MNPs

First, the MNPs capped with heptamannose were evaluated for binding with fluorescein-containing ConA (FITC-ConA). Fe_3O_4@PEG@AD MNPs were mixed with different concentrations of β-CD-$(Man)_7$ (from 18.7 μM to 800 μM) in Milli-Q water to obtain a Fe_3O_4@PEG@AD/β-CD-$(Man)_7$ complex. Unbound β-CD-$(Man)_7$ was easily removed from the solution by decantation of the supernatant after subjecting the solution to a permanent magnet for 15 min to collect the MNPs. In this manner, surface α-D-mannose decorated Fe_3O_4@PEG@AD/β-CD-$(Man)_7$ MNPs were collected and these MNPs were subsequently used to evaluate Con A binding efficiency. As a control experiment, Fe_3O_4@PEG@AD MNPs were mixed with 410 μM of parent β-CD devoid of mannose groups. These MNPs were also collected using a magnet to obtain the Fe_3O_4@PEG@AD/β-CD inclusion complex. Afterwards, these surface modified MNPs were added to a FITC-ConA containing solution to probe their binding. Fe_3O_4@PEG@AD/β-CD-$(Man)_7$ (1.67 mg mL^{-1}) was added to 0.05 mg mL^{-1} of FITC-ConA solution in HEPES buffered saline (pH 7.4). Binding studies were monitored using fluorescence spectroscopy through excitation of FITC-ConA at 480 nm. After the addition of Fe_3O_4@PEG@AD/β-CD-$(Man)_7$ MNPs (1.67 mg mL^{-1}) to the ConA solution, the MNPs were collected using a magnet (Figure 6.7). As expected, a decrease in the fluorescence intensity of the supernatant solution was observed suggesting the binding of ConA to mannose containing MNPs. It was deduced that while Fe_3O_4@PEG@AD MNPs treated with 18.7 μM of β-CD-$(Man)_7$ captured 14.5 % ConA from the solution, 50.6 % of ConA was captured by MNPs treated with 600 μM of β-CD-$(Man)_7$ based on the decrease in fluorescence intensity of FITC (Figure 6.7a). The captured lectin amount was determined as 11.2 μg mg^{-1} of Fe_3O_4@PEG@AD/β-CD-$(Man)_7$ MNPs, which was calculated from a calibration curve of FITC-ConA solution (Figure A.15). It was observed that a saturation was reached where further increase in the concentration of β-CD-$(Man)_7$ from 600 μM to 800 μM did not increase ConA binding (Figure 6.7a). In a control experiment, no significant fluorescence intensity de-

crease was observed when the FITC-ConA solution was treated with a similar amount of Fe_3O_4@PEG@AD/β-CD MNPs (1.67 mg mL^{-1}), a construct devoid of any mannose units on the surface of the NPs. These experiments demonstrate that the supramolecular complex of β-CD-$(Man)_7$ is able to capture ConA from solution.

After the demonstration of the effective capture of ConA from solution, we investigated if they can be released from MNPs. In the presence of high concentrations of a competitive ligand i.e. free sugar in the solution, interactions between MNPs and surface bound ConA should diminish leading to the release of bound protein into solution. To this end, the magnetically isolated lectin bound MNPs were redispersed in a HEPES buffered saline and D-(+)-mannose was added to this solution to release captured ConA from MNPs. Upon the addition of sugar, MNPs were separated using a magnet and fluorescence measurements were undertaken on the supernatants to estimate the amount of protein released (Figure 6.7b). As expected, the highest amount of protein release was observed for 600 μM of β-CD-$(Man)_7$ immobilized magnetic NPs. The interaction of MNPs with ConA and the subsequent protein release could be followed through TEM analysis (Figure 6.7c-e). While the Fe_3O_4@PEG@AD/β-CD-$(Man)_7$ MNPs were non-aggregated, their treatment with ConA led to the formation of large aggregates due to the bridging interaction between the MNPs and proteins. Furthermore, upon addition of free sugar as a competitive ligand, the complexation between MNPs and ConA was disrupted and discrete MNPs were redispersed in the solution. Although lectin binding using β-CD-$(Man)_7$ provided an efficient method for the separation of lectins through multivalent non-covalent interactions, nearly 50 % percent of the lectin remained in the solution even upon using a high concentration of the Fe_3O_4@PEG@AD/β-CD-$(Man)_7$ complex (1.67 mg mL^{-1}). It was observed that an increase in the amount of β-CD-$(Man)_7$ for the decoration of the MNP surface beyond a certain concentration did not lead to an increase the amount of captured lectin. As an alternative approach, increased concentrations of magnetic NPs can be used, but this strategy is not pragmatic due to the usage of large amounts of magnetic nanoparticles, since apart from cost effectiveness, now more effort will be required to ensure removal of all NPs.

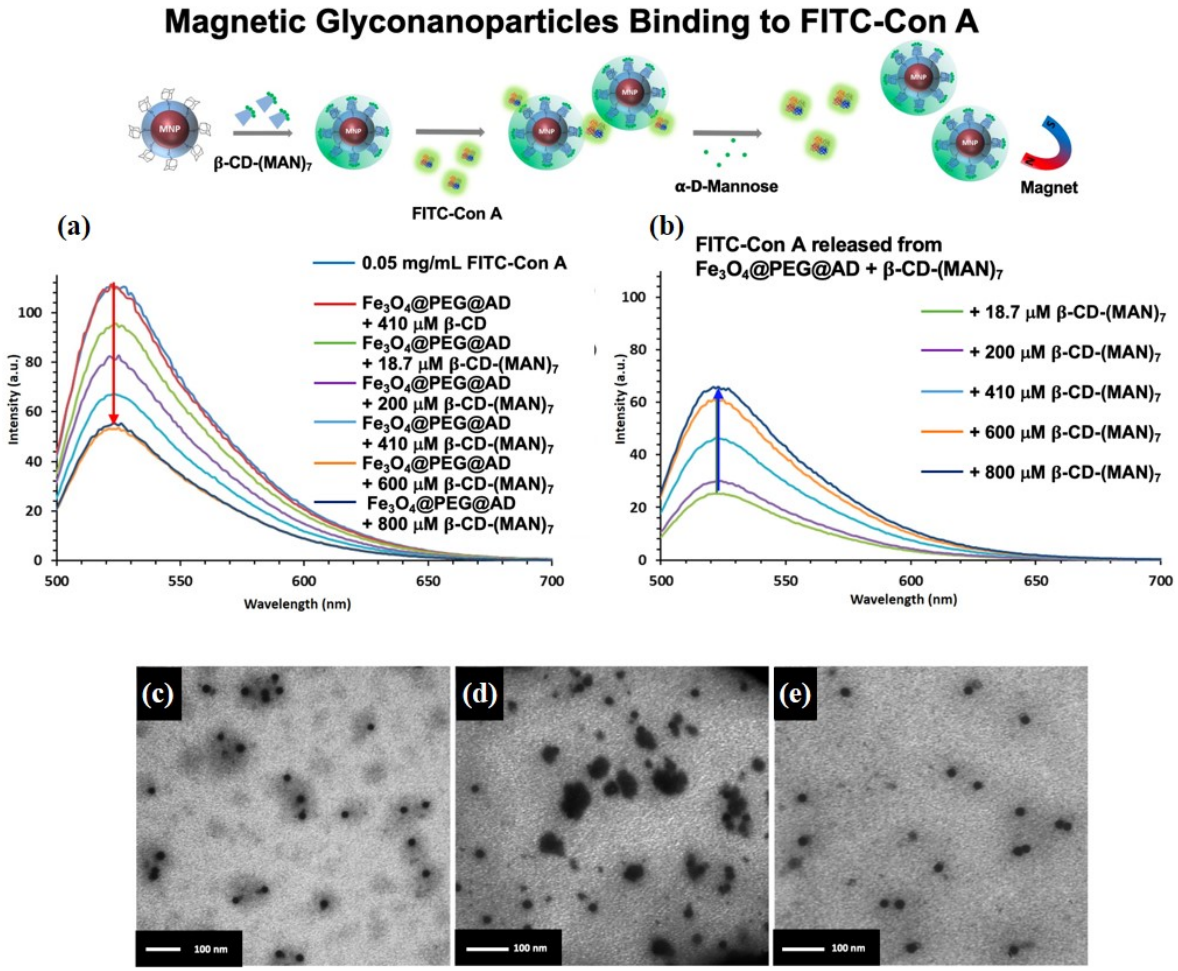

Figure 6.7. Host-guest interactions between Fe_3O_4@PEG@AD MNPs and β-CD-$(Man)_7$, followed by the specific binding of ConA to mannose containing magnetic nanoparticles and release of ConA by the addition of competitive sugar, α-D-mannose; (a) fluorescence spectra of FITC-ConA solution (0.05 mg mL^{-1}) and supernatants from Fe_3O_4@PEG@AD/β-CD-$(Man)_7$ MNPs containing different amounts of β-CD-$(Man)_7$ (control experiment was carried out with Fe_3O_4@PEG@AD/β-CD MNPs), (b) fluorescence spectra of ConA release from ConA captured Fe_3O_4@PEG@AD/β-CD-$(Man)_7$ MNPs upon addition of D-(+)-mannose, (c) TEM images of Fe_3O_4@PEG@ AD/β-CD-$(Man)_7$, (d) ConA bound clustered MNPs and (e) redispersed MNPs after the addition of free mannose.

As an alternative, we envisioned that better protein recovery can be achieved and binding efficiency could be perhaps increased using a β-CD-based star glycopolymer since a polymeric construct can be appended with a large number of mannose units for binding to ConA, and the multivalent presentation of ligands on nanoparticle surfaces has been shown to result in increased protein binding [256]. As a first step, β-CD-p$(Man)_{280}$ was immobilized onto the magnetic NP surface via host-guest interactions. Surface adamantane decorated MNPs were mixed with different concentrations of β-CD-p$(Man)_{280}$ (from 2 μM to 18.7 μM) in Milli-Q water to obtain the Fe_3O_4@PEG@AD/β-CD-p$(Man)_{280}$ supramolecular inclusion complex. Similar to the first approach, 1.67 mg mL^{-1} of poly(mannose) containing magnetic NPs were incubated with 0.05 mg mL^{-1} FITC-ConA solution in HEPES buffered saline at pH 7.4 for 10 min (Figure 6.8). After collection of MNPs via an external magnetic field, fluorescence spectroscopy measurements were performed for the supernatant. The fluorescence intensity of the FITC labelled ConA dramatically decreased compared to that of the supernatant purified from β-CD-$(Man)_7$ attached MNPs. MNPs treated with 2 μM of β-CD-p$(Man)_{280}$ were able to collect 26.8 % of the lectin while MNPs treated with 18.7 μM of β-CD-p$(Man)_{280}$ captured 86.7 % of ConA from the solution that is significantly higher than that of hepta mannose modified β-CD containing NPs (Figure 6.8a). The lectin capture capacity of poly(mannose) decorated MNPs was determined as 21.8 μg mg^{-1} of Fe_3O_4@PEG@AD/β-CD-p$(Man)_{280}$ MNPs, using a calibration curve of the FITC-ConA solution. As a control experiment, 1.67 mg mL^{-1} of the Fe_3O_4@PEG@AD/β-CD MNP dispersion was added to ConA solution and fluorescence spectrum of the supernatant was recorded after the removal of MNPs. As expected, it was deduced that ConA did not interact with these MNPs since there was no decrease in fluorescence intensity.

Recovery of ConA from MNPs was investigated by adding an excess amount of the free sugar D-(+)-mannose as a competitive binder to the protein nanoparticle complex. This resulted in the loss of interaction between ConA and MNPs. MNPs were removed from the solution applying a magnetic field, and the protein content in the supernatant was analyzed using fluorescence spectroscopy. From the measurements, it

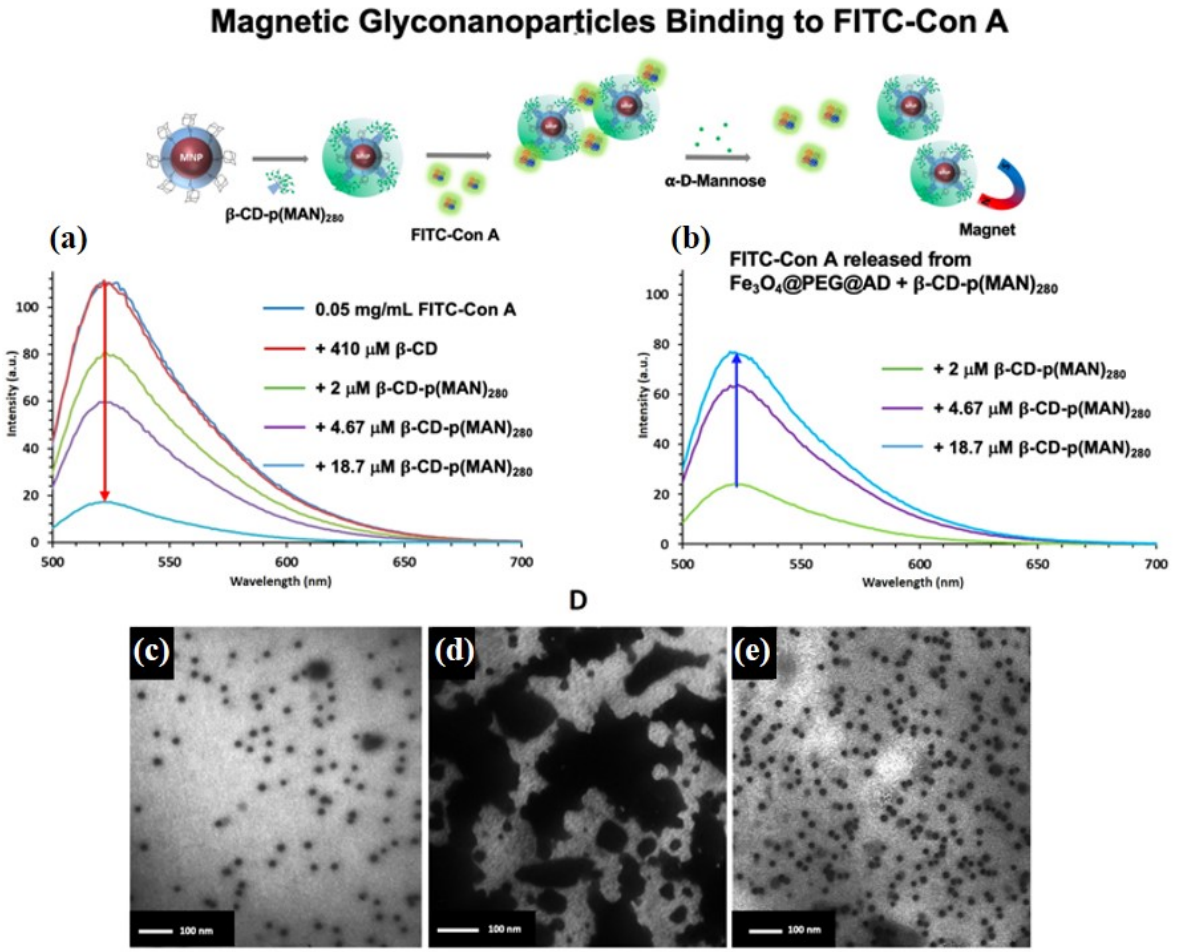

Figure 6.8. Host-guest interactions between Fe_3O_4@PEG@AD MNPs and β-CD-p(Man)$_{280}$, followed by specific binding and subsequent release of ConA. (a) Fluorescence spectra of a FITC-ConA solution (0.05 mg mL^{-1}), and supernatants from Fe_3O_4@PEG@AD/β-CD-p(Man)$_{280}$ MNPs with different amounts of β-CD-p(Man)$_{280}$ (control experiment was carried out with Fe_3O_4@PEG@AD/β-CD MNPs), (b) ConA release from MNPs upon the addition of D-(+)-mannose and TEM images of (c) Fe_3O_4@PEG@AD/β-CD-p(Man)$_{280}$, (d) ConA bound clustered MNPs and (e) redispersed MNPs after the addition of free mannose.

was deduced that about 83 % of ConA captured onto the nanoparticle was released (Figure 6.8b). Analysis of the protein binding and release process using TEM revealed that discrete Fe_3O_4@PEG@AD/β-CD-p$(Man)_{280}$ MNPs aggregated into large extended clusters after treatment with ConA (Figure 6.8c-e). In general, the clusters formed with the polymeric mannose coated MNPs were larger and extended when compared with the aggregates obtained with the hepta(mannose) coated MNPs. Disintegration of these clusters to release discrete MNPs due to disruption of their interactions with ConA upon the addition of free mannose to the solution was also clearly evident.

Selective lectin binding experiments were carried out using CD-conjugated MNPs with ConA and PNA. ConA selectively binds to mannose while no interactions occur between mannose and PNA. MNPs (1.67 mg mL^{-1}) were separately dispersed in 0.05 mg mL^{-1} of ConA and PNA solutions. ConA bound to mannose containing MNPs whereas PNA did not bind to β-CD-$(Man)_7$ and β-CD-p$(Man)_{280}$ decorated MNPs, as deduced from the fluorescence spectroscopy measurements of the supernatant after the removal of NPs through magnetic separation. The fluorescence intensity of rhodamine-PNA solution ($\lambda_{ext} = 550$ nm) did not change, while the fluorescence intensity of ConA decreased significantly (Figure 6.9a and b). Specificity towards a particular lectin can be tailored with the appropriate choice of the sugar based ligand. In order to test this, we synthesized a β-CD-based star glycopolymer using a galactose based monomer. Galactose based ligands are known to have high affinity towards PNA and a lack of affinity for ConA. Using similar procedures as above, MNPs were decorated with β-CD-p$(Gal)_{280}$ to show the selective binding to PNA. A significant decrease in fluorescence of FITC-PNA was observed upon treatment with galactose coated MNPs (Figure 6.9d). As a control experiment, when these nanoparticles were dispersed in FITC-ConA solution and collected with a magnet, no change in fluorescence was observed (Figure 6.9c), due to the lack of affinity.

After demonstrating that the engineered MNPs can selectively bind to ConA and they do not show any non-specific binding with PNA, we probed the efficiency of these MNPs for lectin separation from a mixture. A mixture of ConA (0.05 mg

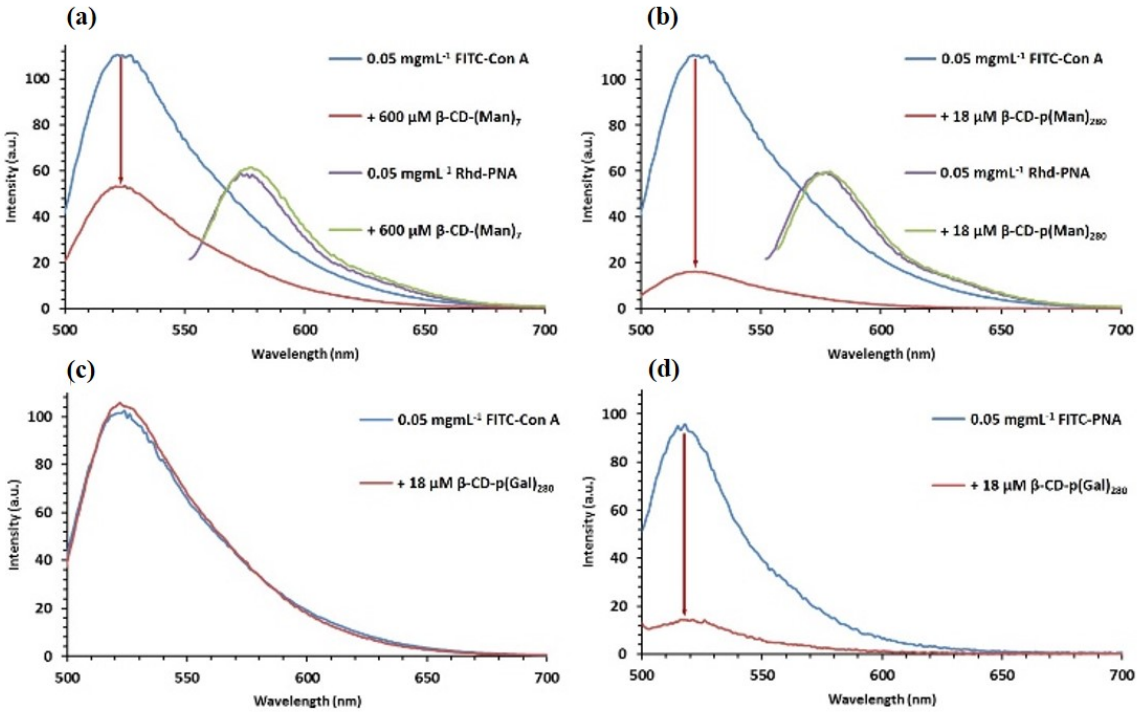

Figure 6.9. Fluorescence spectra of supernatants of FITC-ConA, Rhd-PNA and FITC-PNA solutions before and after treatment with: (a) Fe_3O_4@PEG@AD/β-CD-$(Man)_7$ NPs, (b) Fe_3O_4@PEG@AD/β-CD-p$(Man)_{280}$ NPs and (c) and (d) Fe_3O_4@PEG@AD/β-CD-$(Gal)_{280}$.

mL^{-1}) and PNA (0.05 mg mL^{-1}) was prepared in HEPES buffered saline at pH 7.4 and 1.67 mg mL^{-1} of poly(mannose) decorated MNPs were subsequently added to this solution. MNPs were collected via an external magnetic field and fluorescence intensities of supernatants were determined using a fluorescence spectrophotometer. It was deduced that about 86 % of ConA in the solution was captured by mannose-containing polymeric CD coated MNPs, based on the decrease in intensity at 518 nm. No non-specific binding of PNA lectin onto MNPs was deduced from no loss of fluorescence intensity at 575 nm (Figure 6.10b). The ConA bound MNPs were isolated by using a magnet and redispersed in HEPES buffer followed by the addition of 20-fold excess of α-D-mannose. Using this approach, ConA was quantitatively recovered from MNPs as determined by fluorescence measurements. As expected, there was

no corresponding fluorescence emission peak suggesting PNA release into the solution during these experiments.

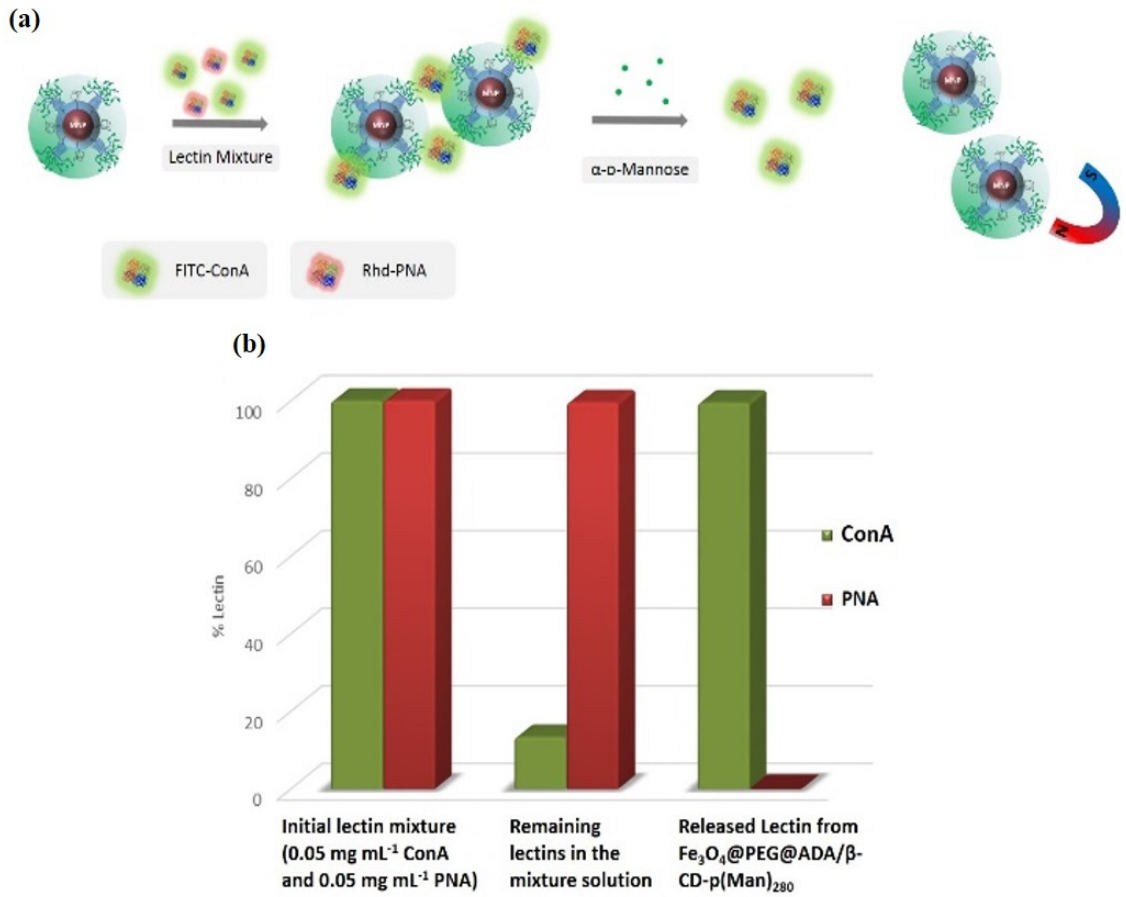

Figure 6.10. (a) Illustration of the specific capture of ConA onto Fe_3O_4@PEG@AD/β-CD-p$(Man)_{280}$ MNPs from a Con A and PNA mixture. (b) The release of captured ConA was achieved by the addition of competitive sugar, α-D-mannose; relative amounts of captured lectin from ConA and the PNA mixture with Fe_3O_4@PEG@AD/β-CD-p$(Man)_{280}$ NPs and recovery of captured lectin upon the addition of α-D-mannose.

Additional verification of the purity of the captured ConA lectin was performed through MALDI analysis of the protein isolated from the mixture of lectins (Fig-

ure 6.11). First, it was verified that distinct peaks could be obtained for the two lectins in MALDI analysis. While the peak for ConA was observed at 26.4 kDa, PNA could be observed as a non-overlapping peak at 25.4 kDa. Analysis of the mixture of lectins produced an overlap of the two peaks for individual lectins. Analysis of the ConA recovered from the mixture of the two lectins showed a peak that could be unequivocally assigned to the specific lectin. As a control, PNA was spiked in ConA solutions from 2 % to 10 % to find out detection limit of PNA in ConA solution. As shown in Figure 6.11b, even 2 % of spiked-PNA was detectable in ConA solution according to the MALDI spectrum. MALDI-TOF mass spectra of isolated ConA from the mixture of lectins indicated that recovered ConA was of high purity with no shoulder peak at 25.4 kDa corresponding to PNA. These results encouraged us to investigate if the lectin of choice can be isolated in the presence of an excess amount of another protein like albumin which is abundant in most biological samples. A mixture of FITC-ConA : BSA (1 : 9) was treated with Fe_3O_4@PEG@AD/β-CD-p$(Man)_{280}$ NPs. After collection of NPs using a magnet, a decrease of fluorescence intensity due to the depletion of ConA from solution was observed similar to that observed for the ConA solution without BSA (Figure A.16). This implied that the presence of excess does not interfere with the specific binding to the targeted protein. MALDI analysis of the supernatant solution indicated that all of FITC-ConA was isolated from the solution (Figure A.17). FITC-ConA bound to the nanoparticle was released by treatment with excess mannose and was analyzed by MALDI to confirm its high purity.

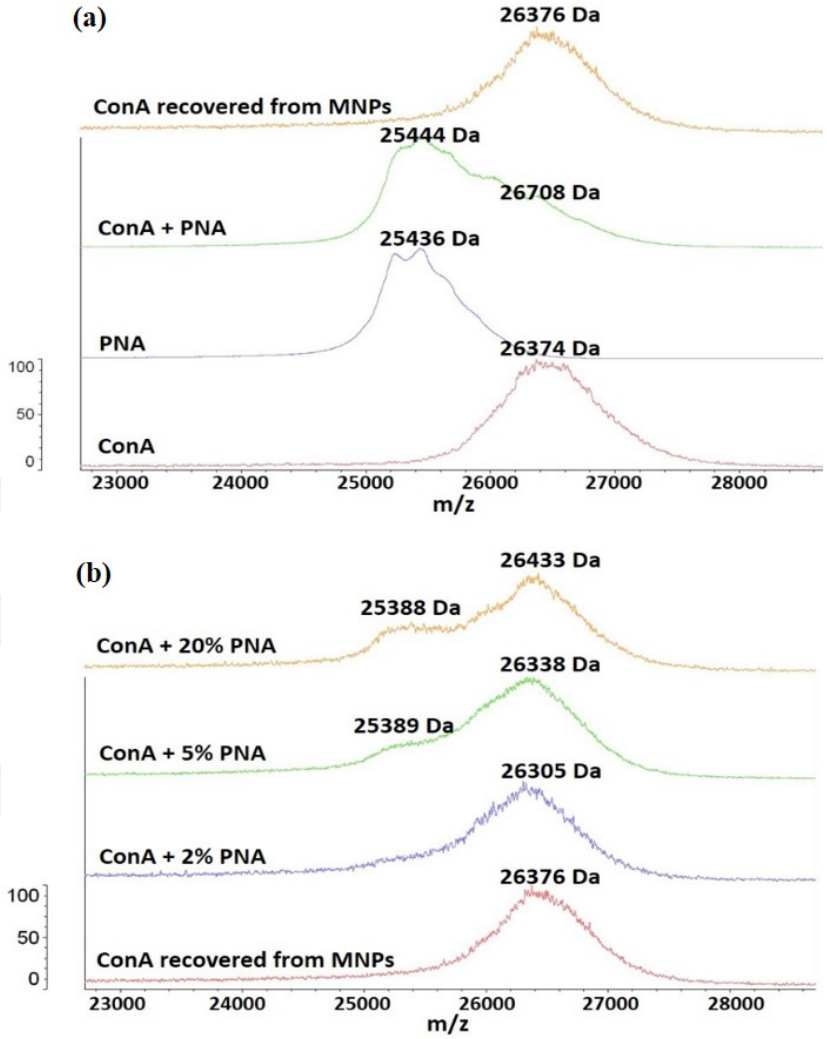

Figure 6.11. (a) MALDI-TOF mass spectra of ConA, PNA, and ConA/PNA mixture (1 : 1) and recovered ConA from MNPs, (b) PNA-spiked ConA solutions in comparison with recovered ConA from MNPs.

6.4. Conclusions

Polymer coated iron oxide nanoparticles appended with adamantane units on the surface allow modular functionalization with sugar containing cyclodextrin based constructs, which provides a modular platform for the separation and purification of lectins. Supramolecular host-guest interactions based on an adamantane/β-CD are utilized to modify the polymeric interface. Poly(ethylene glycol) based hydrophilic polymer-

coated magnetic iron oxide nanoparticles were fabricated using reversible addition-fragmentation chain transfer polymerization, followed by their chain-end modification to install adamantane groups. Polymer-coated magnetic nanoparticle interfaces bearing adamantane groups were amenable for the modification with mannose-containing β-CD constructs. Two different constructs, monomeric and polymeric mannose conjugated CDs were evaluated for selective binding toward ConA. It was deduced that the polymeric CD construct provided a more effective system separation and purification of ConA from a mixture of ConA and PNA. The surface bound isolated protein could be easily recovered by the addition of mannose, a competitive ligand. Importantly, such selective binding to ConA in a mixture containing excess BSA was also shown. Furthermore, selective binding to PNA is demonstrated using a polygalactose based star glycopolymer. Hence through the appropriate choice of sugar-containing CD-polymers, lectins of choice can be targeted. Thus, it can be envisioned that the nanoparticle interface can be tuned through host-guest chemistry to provide a modular system that can be easily tailored for the purification of specific proteins from mixtures.

7. BIODEGRADABLE POLY(LACTIC ACID) STABILIZED NANOSPONGES FOR THE TREATMENT OF MULTIDRUG-RESISTANT BACTERIAL BIOFILMS

7.1. Introduction

The escalating incidence of MDR bacterial infections poses an urgent threat to public health [257]. The World Health Organization predict that -if no interventions are made- MDR infections may cause 10 million deaths, and an economic loss up to $100 trillion worldwide [258]. The threat of MDR bacteria is further aggravated by the onset of biofilm infections [259,260]. Biofilm is an assemblage of bacteria within a self-secreted EPS matrix forming on biotic or abiotic surfaces [261]. Biofilm infections around wounds and indwelling devices are difficult to treat because the EPS matrix hinders the penetration of several antimicrobial agents and shields the residing bacteria from host immune response [262, 263]. Thus, biofilm infections are highly resistant (10- to 1000-fold) to conventional antibiotics that were developed to eliminate planktonic cells [264]. Current strategies to treat biofilm-associated infections focus on aggressive antibiotic therapy coupled with infected tissue removal [265]. However, these invasive procedures have considerable limitations including increased patient suffering, healthcare costs, and can even contribute to drug resistance development [266, 267]. Therefore, there is an urgent need to develop innovative therapeutic platforms that can eliminate these refractory infections.

Essential oils (EOs) are plant-derived natural products that have emerged as promising tools to combat MDR bacterial biofilm [268–270]. These natural antimicrobial agents feature broad-spectrum activity, low cost, and are generally recognized as safe (GRAS) [271]. However, poor aqueous solubility and limited biofilm penetration of EOs have limited their therapeutic potential as antibiofilm agents [272]. A range of delivery platforms has been identified to solubilize and deliver phytochemicals by forming oil-in-water nanoemulsions [273–275]. Among them, polymers have gained

wide interest due to high loading capacity, scalability and design flexibility [75]. Furthermore, covalent crosslinking of these emulsions improves their stability in complex environments such as serum [276]. The resulting polymer-stabilized nanosponges can efficiently penetrate the biofilm and eradicate the bacteria within. However, these polymers are mainly non-biodegradable and might accumulate inside the body causing unwanted side effects [277, 278].

PLA-based polymers are ubiquitous in biomedical applications owing to their biodegradability, biocompatibility and tailorable properties [279–281]. PLA is degraded by endogenous esterase enzymes to innocuous lactic acid LA that is further metabolized and converted to carbon dioxide and water [282]. Herein, we report the design and therapeutic applications of crosslinked PLA stabilized nanosponge (X-NS). X-NS fabrication is based on crosslinking of maleimide-functionalized polymers in the presence of a dithiol crosslinker via in situ maleimide-thiol Michael addition reaction that provides stability in biological environment [283, 284]. We demonstrate loading of these nanosponges with essential oil to provide a therapeutic strategy to combat bacterial biofilms (Figure 7.1). These nanosponges are stable in serum-containing media, but degrades rapidly in the presence of proteinase K [285]. Importantly, the therapeutic potential of X-NS was demonstrated in an *in vitro* biofilm-fibroblast co-culture model where we observed a 4-fold log reduction in biofilm colonies while maintaining high fibroblast cell viability. Overall, the biodegradability, stability, and antimicrobial efficacy of these nanosponges make them promising candidates to treat wound biofilm infections.

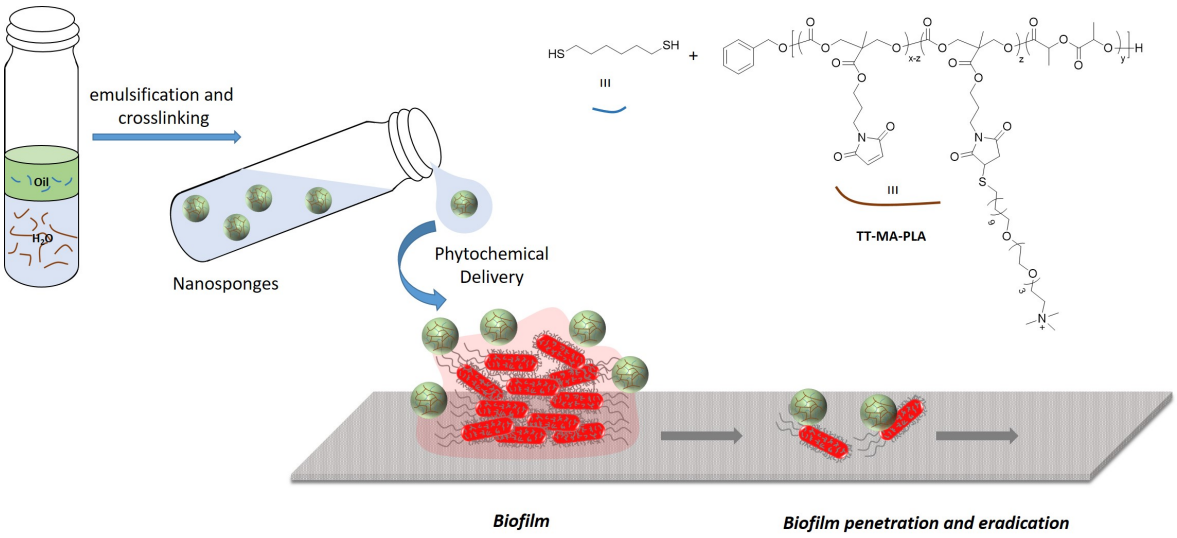

Figure 7.1. Preparation of carvacrol oil-in-water crosslinked biodegradable PLA X-NS by emulsification and schematic representation of biofilm disruption upon delivery of essential oil payload.

7.2. Experimental

7.2.1. Materials and Characterizations

All reagents and materials were purchased from Fisher Scientific and used as received. NIH-3T3 cells (ATCC CRL-1658) were purchased from ATCC. Dulbecco's Modified Eagle's Medium (DMEM) (DMEM; ATCC 30-2002) and fetal bovine serum (Fisher Scientific, SH3007103) were used in cell culture. Pierce LDH Cytotoxicity Assay Kit was purchased from Fisher Scientific. TTMA [286] and maleimide functional poly(lactic acid) (MA-PLA) [287] were synthesized according to previous literature examples.

7.2.2. Attachment of TTMA to MA-PLA Copolymers

MA-PLA polymer (20 mg, 7.66 x 10^{-4} mmol), TTMA (8.1 mg, 19.2 x 10^{-3} mmol) and triethylamine (1.94 mg, 19.2 x 10^{-3} mmol) were dissolved in 2 mL anhydrous DCM.

The reaction mixture was left to stir at 25 °C for 24 h under nitrogen atmosphere. The resultant polymer was purified by precipitation from diethyl ether (30 mL) (M_n, NMR= 33.8 kg/mol). ^{1}H NMR ($CDCl_3$,), δ (ppm) 7.37 – 7.31 (m, aromatic C*H*=C*H*), 6.71 (s, C*H*=C*H*), 5.17 (m, C*H* protons of lactide), 4.31 (d, CH_2 ester protons), 4.10 (t, O=C-OC*H*$_2$CH$_2$), 3.98 (t, OC*H*$_2$-CH$_2$N), 3.87 (t, (CH$_2$)$_9$-C*H*$_2$O), 3.69 – 3.54 (m, N-C*H*$_2$ + -C*H*$_2$O-), 3.43 (t, C*H*$_2$-N(CH$_3$)$_3$), 3.38 (s, -N(C*H*$_3$)$_3$), 2.80 (s, C*H*$_3$SO$_3$-), 2.68 (t, -C*H*$_2$-S), 1.94 (m, N-CH$_2$C*H*$_2$CH$_2$-O), 1.56 (m, C*H*$_3$ protons of lactide), 1.42 – 1.22 (m, C-C*H*$_3$ + -(C*H*$_2$)$_9$-).

7.2.3. Fabrication of Nanosponges

Stock nanocomposite solutions were prepared in 600 μL Eppendorf tubes. 3 μL of carvacrol oil (containing 10 wt. % 1,6-hexanedithiol) was added to 497 μL of Milli-Q water containing 12 μM of TTMA-conjugated PLA-MA copolymer (TT-MA-PLA). Then, it was emulsified using an amalgamator for 50 s. The emulsions were allowed to rest overnight before use.

7.2.4. Determination of Minimum Inhibitory Concentration

Bacteria were inoculated in LB solution at 37 °C, 275 rpm until their stationary phase. Bacteria culture was collected by centrifugation (5000 rpm, 5 min) and washed with 0.85 % sodium chloride solution three times. The optical density of the culture was measured at 600 nm to determine the concentration of resuspended culture in PBS. The solution was then diluted with M9 minimal medium to obtain a final concentration of 1 x 10^6 CFU mL^{-1}. 50 μL of bacteria solution was added into a 96-well plate and mixed with 50 μL of serially diluted X-NS solutions in M9 minimal media (0 – 32 v/v %). A growth control group was prepared using bacterial solution only and M9 media, and negative control was carried out only with growth medium. 96-well plate containing bacterial solutions was incubated in a shaker at 37 °C, 275 rpm for overnight. The cultures were done in triplicates and the lowest inhibitory concentrations of X-NS that prevent visible growth of the bacteria were observed with the unaided eye.

7.2.5. Biofilm Formation

Bacteria were cultured in LB solution at 37 °C until stationary phase and resuspended in M9 minimal medium to reach an OD_{600} of 0.1 as described above. 100 μL of the seeding solutions were added to each well of the microplate. The microplate was covered and incubated at 25 °C under static conditions for overnight. Then, planktonic bacteria were removed by washing biofilms with PBS solution.

Varied concentrations of X-NS solutions were prepared in M9 media (1 – 8 v/v %) and 100 μL of X-NS solutions were incubated with biofilms at 37 °C for 3 h under static conditions. Then, biofilms were washed with PBS three times and viability was determined using an Alamar Blue assay. M9 medium without bacteria was used as a negative control.

7.2.6. Biofilm-3T3 Fibroblast Cell Co-culture

3T3 Fibroblast co-culture was performed using the previously reported protocol [275]. A total of 20000 NIH-3T3 cells were cultured in DMEM with 10 % bovine calf serum and 1 % antibiotics at 37 °C in a humidified atmosphere of 5 % CO_2. Cells were kept for 24 h to reach a confluent monolayer. Bacteria (P. aeruginosa) were inoculated and harvested as mentioned above. Afterward, seeding solutions 108 cells/mL were inoculated in buffered DMEM supplemented with glucose. Old medium was removed from 3T3 cells followed by addition of 100 μL of seeding solution. The co-cultures were then stored in a box humidified with damp paper towels at 37 °C overnight without shaking. Nanosponges and other control solutions were diluted in DMEM media before use to obtain the desired testing concentrations. Media was removed from co-culture, replaced with testing solutions, and incubated for 3 hours at 37 °C. Co-cultures were then analyzed using an LDH S3 cytotoxicity assay to determine mammalian cell viability. To determine the bacteria viability in biofilms, the testing solutions were removed, and co-cultures were washed with PBS. Fresh PBS was then added to disperse remaining bacteria from biofilms in co-culture by sonication for 20

min and mixing with pipet. The solutions containing dispersed bacteria were then plated onto agar plates and colony forming units were counted after incubation at 37 °C overnight.

7.3. Results and Discussion

7.3.1. Fabrication and Characterizations of Nanosponges

PLA polymers were used to stabilize and crosslink the essential oil nanosponges. PLA based polymers were generated using ROP. Briefly, protected maleimide-containing poly(lactic acid) (pMA-PLA) copolymers were synthesized from L-lactide and furan-protected maleimide functionalized carbonate monomer (pMA) in the presence of DBU catalyst and benzyl alcohol initiator. Incorporation of maleimide moieties onto the polymer would allow fast reaction with thiol crosslinkers loaded into the essential oil core as MA-PLA polymers assemble at oil-water interface. Activation of maleimide groups was achieved via a retro Diels-Alder reaction in which furan protected group was quantitatively removed yielding thiol-reactive MA-PLA copolymer. Subsequently, maleimide groups of the copolymer were partially functionalized with TTMA ligand. The cationic quaternary ammonium head groups enable preferential interaction with negatively charged bacterial membrane [288, 289]. Furthermore, the oligo(ethylene glycol) segment of TTMA confers further amphiphilicity on the polymer allowing stable nanosponge assembly. Furan-protected MA-PLA (pMA-PLA) polymers, MA-PLA polymers, and TTMA-functionalized MA-PLA (TTMA-MA-PLA) polymers were characterized by proton nuclear magnetic resonance (^{1}H NMR) (Figure A.18, A.19 and A.20).

X-NS were formulated by dissolving the crosslinker 1,6-hexanedithiol in carvacrol (the major component of oregano oil) and emulsifying the oil phase into an aqueous solution of TTMA-MA-PLA copolymer. The emulsion of carvacrol oil in water was initially stabilized by the partition of polymer into the oil-water interface. In the presence of 1,6-hexanedithiol, crosslinking further stabilizes the assembly (Figure 7.1).

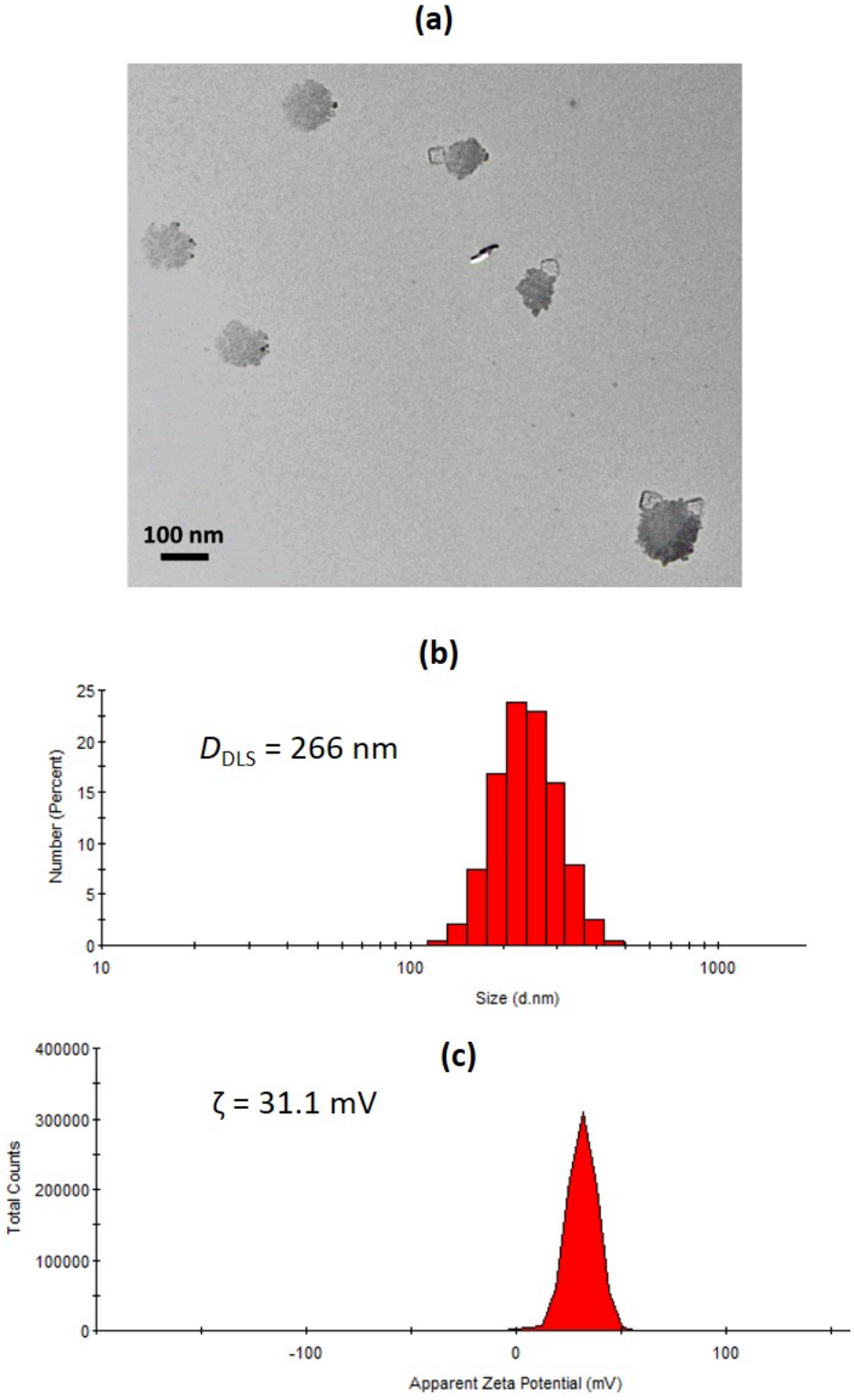

Figure 7.2. (a) TEM picture of X-NS, (b) DLS histogram of X-NS in 150 mM PBS solution and (c) zeta potential of X-NS.

Next, we prepared a series of samples containing different amounts of TTMA-MA-PLA and 1,6-hexanedithiol to find the optimal amount of crosslinker to obtain the most stable formulation. Nanosponges with a final TTMA-MA-PLA concentration of 12 μM and 10 wt. % 1,6-hexanedithiol were fabricated with an average diameter of 260 nm as shown by DLS and TEM (Figure 7.2a and b). ζ potential measurement was done to determine surface charge of X-NS. As expected, X-NS demonstrated an overall positive charge attributed to the trimethylammonium groups of TTMA ligand (Figure 7.2c).

7.3.2. Stability and Degradability of X-NCs

The stability of nanosponges in physiological conditions is a vital requirement for therapeutic applications [290]. Delivery vehicles should be stable enough to preserve and deliver its cargo yet degrade over time to prevent vehicle accumulation in the body [291]. Therefore, colloidal stability of X-NS was investigated through monitoring particle size by DLS. X-NS (prepared as 10 v/v % in 150 mM PBS) were incubated with 10 % FBS for 6 h. As shown in Figure 7.3a, DLS measurements indicated that there was no aggregation or destabilization of nanosponges. Importantly, X-NS maintained its stability even after 24 h incubation (Figure A.21). As a control experiment, non-crosslinked nanosponges (NX-NS) with the same formulation but lacking 1,6-hexanedithiol crosslinker had no stability in serum (Figure A.22).

Since the PLA backbone of the copolymer is biodegradable, we monitored the degradability of X-NS in the presence of proteinase K enzyme, an endogenous protease known to degrade PLA. X-NS were incubated for 24 h with 6.9 μM of proteinase K ($\geq$ 3 U mL^{-1}) in PBS (pH 7.4) at 37 °C. The particle size of X-NS (before and after degradation) and freshly prepared carvacrol oil emulsion (without polymer) in PBS were monitored by DLS. As shown in Figure 7.3b, X-NS maintain its stability after 24 h incubation in PBS. However, the size of X-NS significantly increased in proteinase K solution, indicating degradation of the nanosponges scaffold and subsequent aggregation of oil droplets (734 nm with PDI = 1.0, similar size to carvacrol emulsion in PBS)

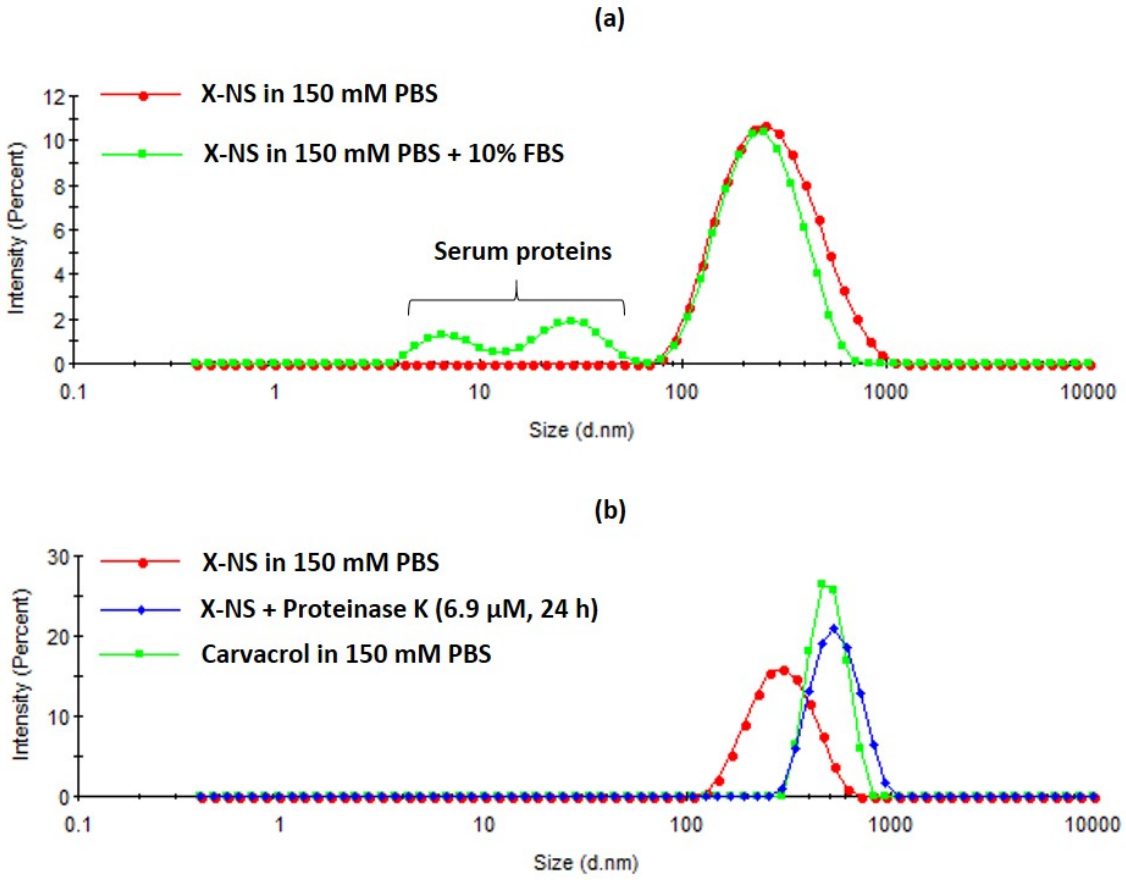

Figure 7.3. DLS size distributions of X-NS (a) stability evaluation in 10 % FBS solution for 6 h; (b) degradability in presence of physiologically relevant biomolecule (proteinase K enzyme) in PBS solution (24 h).

via an Ostwald ripening-like process. Freshly prepared carvacrol oil-in-water emulsion without polymer was measured as 876 nm (PDI = 1.0) while the size of X-NS in PBS remained the same after 24 h (Figure 7.3b). Additionally, enzymatic degradation of X-NS was analyzed by ^{1}H NMR spectroscopy. Degradation of X-NS was confirmed by appearance of methyl protons signals of oligo(lactic acid) and lactic acid at 1.46 and 1.34 ppm in deuterated PBS (Figure A.23) [292]. Moreover, physical signs of destabilization of X-NS upon degradation with proteinase K enzyme were also observed as the milky appearance of the X-NS became more transparent after 48 h (Figure A.24).

7.3.3. Penetration of Nanosponges into Biofilms

Penetration of antimicrobial agents into biofilms is crucial for effective biofilm eradication [293]. Hydrophobic essential oils such as carvacrol are insoluble in water and hence have limited capacity to penetrate biofilms [294]. Loading these oils into nanocarriers provides a promising strategy for efficient biofilm penetration [295]. Therefore, we investigated the ability of our nanosponges to penetrate biofilms via confocal microscopy. X-NS loaded with Nile Red dye (red fluorescence) within the oil core were incubated with a 4-day old biofilm of green fluorescent protein (GFP)-expressing Klebsiella pneumonia for 1 h to track their penetration into biofilms. As shown in Figure 7.4, X-NS actively penetrated and distributed throughout the biofilm while colocalizing with the embedded bacteria. These results indicated that X-NS could efficiently penetrate the biofilm and deliver their essential oil payload.

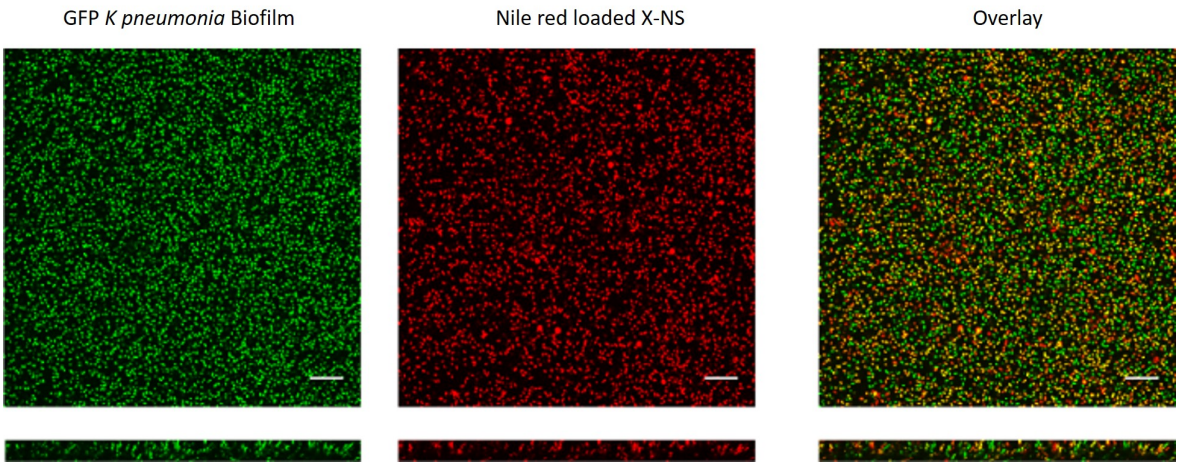

Figure 7.4. Confocal images of GFP expressing *K. pneumonia* biofilm after 1 h treatment with 5 % X-NS. Nile red was loaded into X-NCs for tracking biofilm penetration. The overlay demonstrated X-NS effectively penetrated into the biofilm, colocalizing with bacteria that express GFP. Scale bars are 30 μm.

7.3.4. Antimicrobial Activity of X-NS against Bacterial Biofilms

Next, we investigated the antimicrobial activity of X-NS against multiple gram-pathogenic gram-negative and gram-positive bacterial biofilms using Alamar Blue assay. Three pathogenic bacterial strains of clinical isolates, *E. coli* (CD-2), *A. baumannii* (CD-575), and methicillin-resistant *S. aureus* (CD-6169) were chosen to evaluate the antimicrobial activity of our system [296–298]. As shown in Figure 7.5, X-NS were able to eradicate all bacterial biofilms at concentrations of 6 – 8 v/v% (2.34 – 4.68 mM carvacrol oil) within 3 h while individual components of nanosponges showed minimal or no efficacy against bacterial biofilms. Therefore, combination of all nanosponge components is essential for maximum therapeutic efficacy. Notably, X-NS could be used to treat both gram-negative and gram-positive bacterial biofilms, indicating broad-spectrum activity of X-NS.

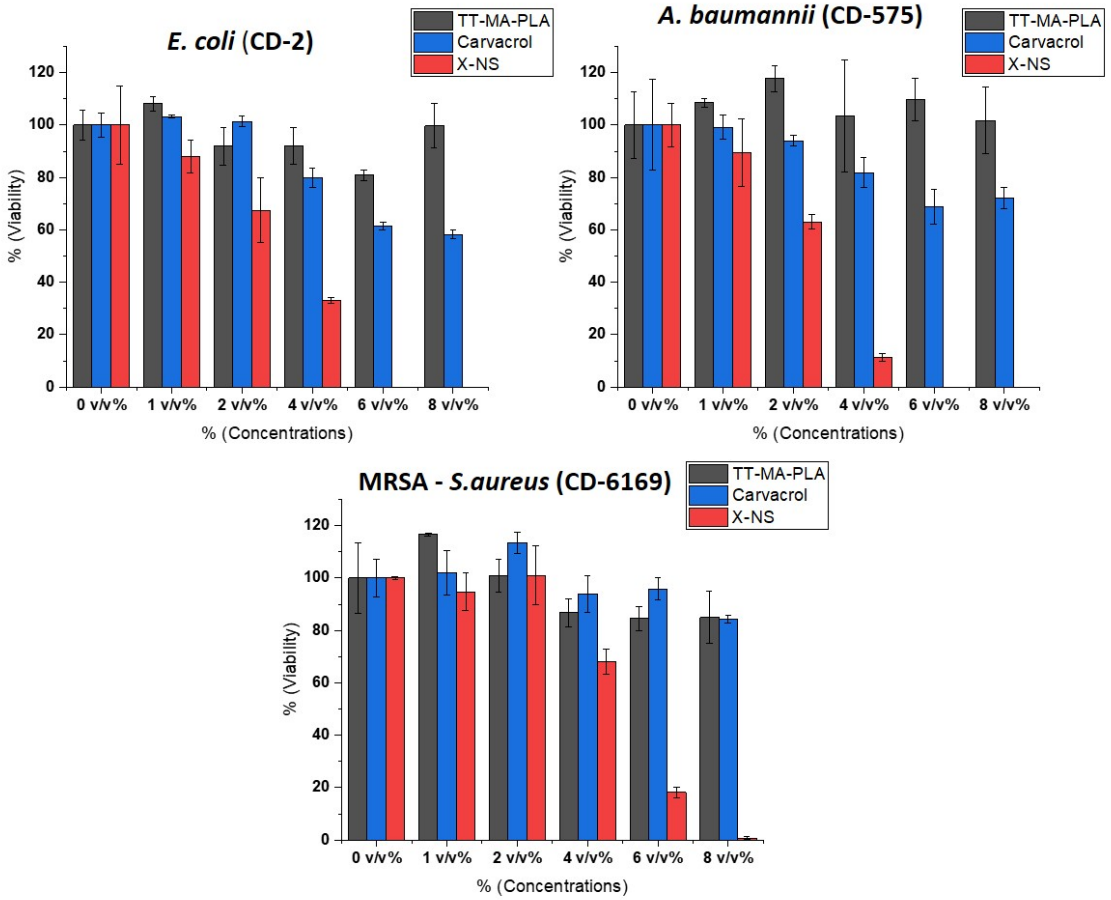

Figure 7.5. Viability of *E. coli* (CD-2), *A. baumannii* (CD-575) and methicillin-resistant *S. aureus* (CD-6169) biofilms after 3 h of treatment with X-NS, carvacrol oil, and TTMA-MA-PLA at different emulsion concentrations (v/v % of emulsion). The results are an average of triplicate, and the error bars indicate the standard deviation.

7.3.5. Selective Killing of Biofilms in a Co-culture Model

Biofilm infections on damaged skin tissues impair immune response and wound healing cascades, resulting in chronic non-healing wounds that are difficult to treat [299]. An ideal antimicrobial agent should eliminate bacteria without harming mammalian cells. In particular, fibroblasts play an important role in wound closure and formation of new extracellular matrix [300]. To assess the potential of our system to

treat wound biofilms, we designed an *in vitro* co-culture model comprised of a biofilm grown with mammalian fibroblasts cells. *P. aeruginosa* biofilm was allowed to grow on top of NIH 3T3 fibroblast cells overnight. The co-cultures were treated with different concentrations of carvacrol-loaded X-NS for 3 h. After carefully washing the co-cultures, the viabilities of bacterial biofilms and mammalian cells were determined. As shown Figure 7.6, X-NS effectively treated biofilms while fibroblast cells remained healthy. We observed a 4-fold log reduction ($\sim$ 99.5 %) in biofilm colonies at 16 v/v % emulsion concentration. Overall, the selectivity of X-NS towards eradicating bacterial biofilm suggests that this platform is a promising candidate for wound biofilms treatment.

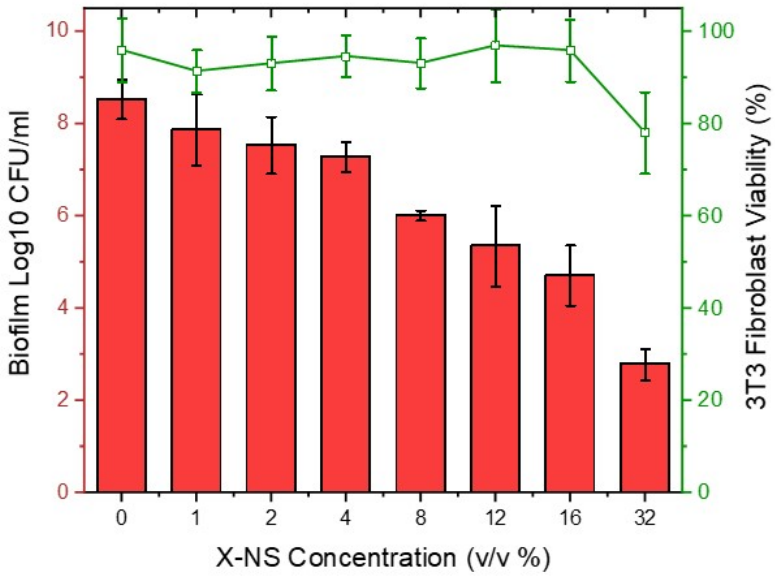

Figure 7.6. Viability of 3T3 fibroblast cells and *P. aeruginosa* biofilms in the co-culture model after 3 h treatment with different emulsion concentrations of X-NS. Line bars represent 3T3 fibroblast cell viability and bar plots are $\log_{10}$ of colony-forming units in biofilms. Results are given as an average of three experiments, and the error bars designate the standard deviations.

7.4. Conclusions

In conclusion, we have developed effective antimicrobial agents through combination of biodegradable polymeric scaffold and natural antibacterial essential oils into a translatable delivery platform. These X-NS fabricated from functionalized PLA copolymers and carvacrol showed good stability in serum while degrading in the presence of an ester hydrolyzing enzyme. X-NS effectively penetrated into biofilms and eliminated embedded gram-negative or gram-positive bacteria. Moreover, X-NS demonstrated selective killing of biofilms grown on fibroblast while retaining the mammalian cells viability. Taken together, these biodegradable polymer-based essential oils nanosponges offer a promising platform for the treatment of wound biofilms and other life-threatening infections.

8. CONCLUSION

In this dissertation, smart polymeric nanostructures that could be used in various biomedical applications were evaluated. A variety of polymerization techniques such as RAFT, ROP were applied to obtain these smart nanostructures. They were utilized in drug delivery, protein separation, targeted imaging and biofilm eradication.

The first chapter of thesis gives a brief introduction to smart polymeric nanostructures and synthetic approaches. It also covers some important literature examples related to polymeric smart nanostructures and their use in biomedical applications. The third and fourth sections thoroughly investigate drug delivery applications of rGO based materials. In the third chapter, stimuli-responsive hydrogels were obtained by confinement of rGO into the hydrogel network. The hydrogels had ability to heat under NIR light irradiation due to rGO that is capable of converting light to heat. After loading of insulin in hydrogels, these patches were utilized for transdermal delivery of insulin upon NIR exposure. It was shown that insulin was released from hydrogels when light is on while there was no release without light. That enables on-demand drug release from the patches by ease of the NIR light. In the fourth chapter, targeted drug delivery via rGO nanosheets was studied for the treatment of cancer. rGO was exploited as drug delivery agent owing to its very high surface area which is suitable for drug loading. A targeting peptide was conjugated to rGO via a thiol-ene Michael addition reaction utilizing the maleimide groups on the rGO. Specific targeting and killing of human breast MDA-MB-231 adenocarcinoma cells were achieved by drug loaded rGO nanosheets.

The fifth and sixth sections of the thesis are related to polymer coated MNPs for targeted cellular imaging and lectin separation. In the fifth chapter, end groups of polymer coated MNPs were modified with maleimide functional groups. Similar to rGO work, a targeting peptide and imaging agent were conjugated onto the surface of MNPs via thiol-maleimide addition reaction. Targeting and imaging were evaluated on human

breast MDA-MB-231 adenocarcinoma cells. After this work, we used polymer coated MNPs for lectin separation exploiting host-guest supramolecular interactions between adamantane and cyclodextrin in the sixth chapter. End group of polymer on MNP surface was modified with adamantane which allows interaction of mannose modified cyclodextrin. We demonstrated mannose modified MNPs were able to specifically catch ConA from a lectin mixture.

The final part of the thesis deals with MDR-resistant bacterial biofilms using phytochemical loaded nanosponges. A biodegradable and maleimide functional polymer was used to stabilize an oil-in-water nano-emulsion of carvacrol. Further stabilization was achieved by crosslinking maleimide functional polymer with dithiol containing crosslinker. These nanosponges showed a good therapeutic efficacy against MDR-resistant biofilms. Moreover, biodegradable nature of the polymer prevents undesired toxicity arising from accumulation of the nanomaterials in the body. In summary, smart polymeric nanostructures were prepared for various biomedical applications. Post-polymerization modifications were carried out to render polymeric nanostructures suitable for desired applications.

REFERENCES

1. Xu, X., L. He, B. Zhu, J. Li and J. Li, "Advances in polymeric materials for dental applications", *Polymer Chemistry*, Vol. 8, No. 5, pp. 807–823, 2017.

2. Fenton, O. S., K. N. Olafson, P. S. Pillai, M. J. Mitchell and R. Langer, "Advances in biomaterials for drug delivery", *Advanced Materials*, Vol. 30, No. 29, p. 1705328, 2018.

3. Bordat, A., T. Boissenot, J. Nicolas and N. Tsapis, "Thermoresponsive polymer nanocarriers for biomedical applications", *Advanced Drug Delivery Reviews*, Vol. 138, pp. 167–192, 2019.

4. Calik, F., A. Degirmenci, M. Eceoglu, A. Sanyal and R. Sanyal, "Dendron–polymer conjugate based cross-linked micelles: A robust and versatile nanosystem for targeted delivery", *Bioconjugate Chemistry*, Vol. 30, No. 4, pp. 1087–1097, 2019.

5. Chambre, L., W. S. Saw, G. Ekineker, L. V. Kiew, W. Y. Chong, H. B. Lee, L. Y. Chung, Y. Bretonniere, F. Dumoulin and A. Sanyal, "Surfactant-free direct access to porphyrin-cross-linked nanogels for photodynamic and photothermal therapy", *Bioconjugate Chemistry*, Vol. 29, No. 12, pp. 4149–4159, 2018.

6. Bolu, B. S., R. Sanyal and A. Sanyal, "Drug delivery systems from self-assembly of dendron-polymer conjugates", *Molecules*, Vol. 23, No. 7, p. 1570, 2018.

7. Wichterle, O. and D. Lim, "Hydrophilic gels for biological use", *Nature*, Vol. 185, No. 4706, pp. 117–118, 1960.

8. Singh, N. K. and D. S. Lee, "In situ gelling pH- and temperature-sensitive biodegradable block copolymer hydrogels for drug delivery", *Journal of Controlled Release*, Vol. 193, pp. 214–227, 2014.

9. Mehrali, M., A. Thakur, C. P. Pennisi, S. Talebian, A. Arpanaei, M. Nikkhah and A. Dolatshahi-Pirouz, "Nanoreinforced hydrogels for tissue engineering: Biomaterials that are compatible with load-bearing and electroactive tissues", *Advanced Materials*, Vol. 29, No. 8, p. 1603612, 2017.

10. Narayanaswamy, R. and V. P. Torchilin, "Hydrogels and their applications in targeted drug delivery", *Molecules*, Vol. 24, No. 3, p. 603, 2019.

11. Spicer, C. D., "Hydrogel scaffolds for tissue engineering: The importance of polymer choice", *Polymer Chemistry*, Vol. 11, pp. 184–219, 2020.

12. Li, Z., C. Tang, D. Huang, W. Qin, F. Luo, J. Wang, L. Guo, B. Qiu and Z. Lin, "Sensitive hyaluronidase biosensor based on target-responsive hydrogel using electronic balance as readout", *Analytical Chemistry*, Vol. 91, No. 18, pp. 11821–11826, 2019.

13. Park, E. J., T. N. Gevrek, R. Sanyal and A. Sanyal, "Indispensable platforms for bioimmobilization: Maleimide-based thiol reactive hydrogels", *Bioconjugate Chemistry*, Vol. 25, No. 11, pp. 2004–2011, 2014.

14. Edwards, C. E., D. J. Mai, S. Tang and B. D. Olsen, "Molecular anisotropy and rearrangement as mechanisms of toughness and extensibility in entangled physical gels", *Physical Review Materials*, Vol. 4, No. 1, p. 015602, 2020.

15. Song, G., L. Zhang, C. He, D. C. Fang, P. G. Whitten and H. Wang, "Facile fabrication of tough hydrogels physically cross-linked by strong cooperative hydrogen bonding", *Macromolecules*, Vol. 46, No. 18, pp. 7423–7435, 2013.

16. Hu, Y., Z. Du, X. Deng, T. Wang, Z. Yang, W. Zhou and C. Wang, "Dual physically cross-linked hydrogels with high stretchability, toughness, and good self-recoverability", *Macromolecules*, Vol. 49, No. 15, pp. 5660–5668, 2016.

17. Lin, P., S. Ma, X. Wang and F. Zhou, "Molecularly engineered dual-crosslinked

hydrogel with ultrahigh mechanical strength, toughness, and good self-recovery", *Advanced Materials*, Vol. 27, No. 12, pp. 2054–2059, 2015.

18. Tuncaboylu, D. C., M. Sari, W. Oppermann and O. Okay, "Tough and self-healing hydrogels formed via hydrophobic interactions", *Macromolecules*, Vol. 44, No. 12, pp. 4997–5005, 2011.

19. Altin, H., I. Kosif and R. Sanyal, "Fabrication of "clickable" hydrogels via dendron-polymer conjugates", *Macromolecules*, Vol. 43, No. 8, pp. 3801–3808, 2010.

20. Aimetti, A. A., A. J. Machen and K. S. Anseth, "Poly(ethylene glycol) hydrogels formed by thiol-ene photopolymerization for enzyme-responsive protein delivery", *Biomaterials*, Vol. 30, No. 30, pp. 6048–6054, 2009.

21. Tan, H., J. P. Rubin and K. G. Marra, "Direct synthesis of biodegradable polysaccharide derivative hydrogels through aqueous diels-alder chemistry", *Macromolecular Rapid Communications*, Vol. 32, No. 12, pp. 905–911, 2011.

22. Kosif, I., E.-J. Park, R. Sanyal and A. Sanyal, "Fabrication of maleimide containing thiol reactive hydrogels via Diels-Alder/retro-Diels-Alder strategy", *Macromolecules*, Vol. 43, No. 9, pp. 4140–4148, 2010.

23. Wang, X., C. Wang, X. Wang, Y. Wang, Q. Zhang and Y. Cheng, "A polydopamine nanoparticle-knotted poly(ethylene glycol) hydrogel for on-demand drug delivery and chemo-photothermal therapy", *Chemistry of Materials*, Vol. 29, No. 3, pp. 1370–1376, 2017.

24. Altinbasak, I., R. Sanyal and A. Sanyal, "Best of both worlds: Diels–Alder chemistry towards fabrication of redox-responsive degradable hydrogels for protein release", *RSC Advances*, Vol. 6, No. 78, pp. 74757–74764, 2016.

25. Dai, T., C. Wang, Y. Wang, W. Xu, J. Hu and Y. Cheng, "A nanocomposite

hydrogel with potent and broad-spectrum antibacterial activity", *ACS Applied Materials & Interfaces*, Vol. 10, No. 17, pp. 15163–15173, 2018.

26. Sun, S. and P. Wu, "A one-step strategy for thermal- and pH-responsive graphene oxide interpenetrating polymer hydrogel networks", *Journal of Materials Chemistry*, Vol. 21, No. 12, pp. 4095–4097, 2011.

27. Cong, H.-P., J.-H. Qiu and S.-H. Yu, "Thermoresponsive poly (N-isopropylacrylamide)/graphene/Au nanocomposite hydrogel for water treatment by a laser-assisted approach", *Small*, Vol. 11, No. 9-10, pp. 1165–1170, 2015.

28. Qi, X., W. Wei, J. Li, Y. Liu, X. Hu, J. Zhang, L. Bi and W. Dong, "Fabrication and characterization of a novel anticancer drug delivery system: Salecan/poly(methacrylic acid) semi-interpenetrating polymer network hydrogel", *ACS Biomaterials Science & Engineering*, Vol. 1, No. 12, pp. 1287–1299, 2015.

29. Gao, Y., S. Zong, Y. Huang, N. Yang, H. Wen, J. Jiang and J. Duan, "Preparation and properties of a highly elastic galactomannan-poly (acrylamide-N, N-bis (acryloyl) cysteamine) hydrogel with reductive stimuli-responsive degradable properties", *Carbohydrate Polymers*, Vol. 231, p. 115690, 2020.

30. Su, R. S.-C., R. J. Galas Jr, C.-Y. Lin and J. C. Liu, "Redox-responsive resilin-like hydrogels for tissue engineering and drug delivery applications", *Macromolecular Bioscience*, Vol. 19, No. 8, p. 1900122, 2019.

31. Slaughter, B. V., S. S. Khurshid, O. Z. Fisher, A. Khademhosseini and N. A. Peppas, "Hydrogels in regenerative medicine", *Advanced Materials*, Vol. 21, No. 32-33, pp. 3307–3329, 2009.

32. Bacelar, A. H., I. F. Cengiz, J. Silva-Correia, R. A. Sousa, J. M. Oliveira and R. L. Reisa, "Smart hydrogels in tissue engineering and regenerative medicine applications", *Handbook of Intelligent Scaffolds for Tissue Engineering and Regenerative*

Medicine, Vol. 2, pp. 327–361, 2017.

33. Li, W., J. Wang, J. Ren and X. Qu, "3D graphene oxide–polymer hydrogel: Near-infrared light-triggered active scaffold for reversible cell capture and on-demand release", *Advanced Materials*, Vol. 25, No. 46, pp. 6737–6743, 2013.

34. Mourya, V., N. Inamdar, R. Nawale and S. Kulthe, "Polymeric micelles: General considerations and their applications", *Indian Journal of Pharmaceutical Education and Research*, Vol. 45, No. 2, pp. 128–38, 2011.

35. Unsal, H., S. Onbulak, F. Calik, M. Er-Rafik, M. Schmutz, A. Sanyal and J. Rzayev, "Interplay between molecular packing, drug loading, and core crosslinking in bottlebrush copolymer micelles", *Macromolecules*, Vol. 50, No. 4, pp. 1342–1352, 2017.

36. Xiao, R. Z., Z. W. Zeng, G. L. Zhou, J. J. Wang, F. Z. Li and A. M. Wang, "Recent advances in PEG–PLA block copolymer nanoparticles", *International Journal of Nanomedicine*, Vol. 5, p. 1057, 2010.

37. M Saffer, E., G. N Tew and S. R Bhatia, "Poly (lactic acid)-poly (ethylene oxide) block copolymers: new directions in self-assembly and biomedical applications", *Current Medicinal Chemistry*, Vol. 18, No. 36, pp. 5676–5686, 2011.

38. Cohn, D. and H. Younes, "Biodegradable PEO/PLA block copolymers", *Journal of Biomedical Materials Research*, Vol. 22, No. 11, pp. 993–1009, 1988.

39. Jie, P., S. S. Venkatraman, F. Min, B. Y. C. Freddy and G. L. Huat, "Micelle-like nanoparticles of star-branched PEO–PLA copolymers as chemotherapeutic carrier", *Journal of Controlled Release*, Vol. 110, No. 1, pp. 20–33, 2005.

40. Morrissey, D. V., J. A. Lockridge, L. Shaw, K. Blanchard, K. Jensen, W. Breen, K. Hartsough, L. Machemer, S. Radka, V. Jadhav *et al.*, "Potent and persistent in vivo anti-HBV activity of chemically modified siRNAs", *Nature Biotechnology*,

Vol. 23, No. 8, pp. 1002–1007, 2005.

41. Okumura, A., P. M. Pitha and R. N. Harty, "ISG15 inhibits Ebola VP40 VLP budding in an L-domain-dependent manner by blocking Nedd4 ligase activity", *Proceedings of the National Academy of Sciences*, Vol. 105, No. 10, pp. 3974–3979, 2008.

42. Shen, H., T. Sun and M. Ferrari, "Nanovector delivery of siRNA for cancer therapy", *Cancer Gene Therapy*, Vol. 19, No. 6, pp. 367–373, 2012.

43. Davis, M. E., J. E. Zuckerman, C. H. J. Choi, D. Seligson, A. Tolcher, C. A. Alabi, Y. Yen, J. D. Heidel and A. Ribas, "Evidence of RNAi in humans from systemically administered siRNA via targeted nanoparticles", *Nature*, Vol. 464, No. 7291, pp. 1067–1070, 2010.

44. Leachman, S. A., R. P. Hickerson, P. R. Hull, F. J. Smith, L. M. Milstone, E. B. Lane, S. J. Bale, D. R. Roop, W. I. McLean and R. L. Kaspar, "Therapeutic siRNAs for dominant genetic skin disorders including pachyonychia congenita", *Journal of Dermatological Science*, Vol. 51, No. 3, pp. 151–157, 2008.

45. Christie, R. J., Y. Matsumoto, K. Miyata, T. Nomoto, S. Fukushima, K. Osada, J. Halnaut, F. Pittella, H. J. Kim, N. Nishiyama *et al.*, "Targeted polymeric micelles for siRNA treatment of experimental cancer by intravenous injection", *Acs Nano*, Vol. 6, No. 6, pp. 5174–5189, 2012.

46. Landfester, K., "Miniemulsion polymerization and the structure of polymer and hybrid nanoparticles", *Angewandte Chemie International Edition*, Vol. 48, No. 25, pp. 4488–4507, 2009.

47. Ramasamy, T., Z. S. Haidar, T. H. Tran, J. Y. Choi, J.-H. Jeong, B. S. Shin, H.-G. Choi, C. S. Yong and J. O. Kim, "Layer-by-layer assembly of liposomal nanoparticles with PEGylated polyelectrolytes enhances systemic delivery of mul-

tiple anticancer drugs", *Acta Biomaterialia*, Vol. 10, No. 12, pp. 5116–5127, 2014.

48. Jang, W.-D., D. Yim and I.-H. Hwang, "Photofunctional hollow nanocapsules for biomedical applications", *Journal of Materials Chemistry B*, Vol. 2, No. 16, pp. 2202–2211, 2014.

49. Boyer, C., M. R. Whittaker, C. Nouvel and T. P. Davis, "Synthesis of hollow polymer nanocapsules exploiting gold nanoparticles as sacrificial templates", *Macromolecules*, Vol. 43, No. 4, pp. 1792–1799, 2010.

50. Sun, L., R. M. Crooks and V. Chechik, "Preparation of polycyclodextrin hollow spheres by templating gold nanoparticles", *Chemical Communications*, , No. 4, pp. 359–360, 2001.

51. Son, K. J., H.-J. Yoon, J.-H. Kim, W.-D. Jang, Y. Lee and W.-G. Koh, "Photosensitizing hollow nanocapsules for combination cancer therapy", *Angewandte Chemie International Edition*, Vol. 50, No. 50, pp. 11968–11971, 2011.

52. Itoh, Y., M. Matsusaki, T. Kida and M. Akashi, "Locally controlled release of basic fibroblast growth factor from multilayered capsules", *Biomacromolecules*, Vol. 9, No. 8, pp. 2202–2206, 2008.

53. Wang, Y., A. S. Angelatos and F. Caruso, "Template synthesis of nanostructured materials via layer-by-layer assembly", *Chemistry of Materials*, Vol. 20, No. 3, pp. 848–858, 2008.

54. Pramanik, S. K., U. Pal, P. Choudhary, H. Singh, R. J. Reiter, A. Ethirajan, S. Swarnakar and A. Das, "Stimuli-responsive nanocapsules for the spatiotemporal release of melatonin: Protection against gastric inflammation", *ACS Applied Bio Materials*, Vol. 2, No. 12, pp. 5218–5226, 2019.

55. Pramanik, S. K., S. Sreedharan, H. Singh, M. Khan, K. Tiwari, A. Shiras, C. Smythe, J. A. Thomas and A. Das, "Mitochondria targeting non-isocyanate-

based polyurethane nanocapsules for enzyme-triggered drug release", *Bioconjugate Chemistry*, Vol. 29, No. 11, pp. 3532–3543, 2018.

56. Chambre, L., A. Degirmenci, R. Sanyal and A. Sanyal, "Multi-functional nanogels as theranostic platforms: Exploiting reversible and nonreversible linkages for targeting, imaging, and drug delivery", *Bioconjugate Chemistry*, Vol. 29, No. 6, pp. 1885–1896, 2018.

57. Aktan, B., L. Chambre, R. Sanyal and A. Sanyal, "Clickable nanogels via thermally driven self-assembly of polymers: Facile access to targeted imaging platforms using thiol–maleimide conjugation", *Biomacromolecules*, Vol. 18, No. 2, pp. 490–497, 2017.

58. Pinelli, F., G. Perale and F. Rossi, "Coating and functionalization strategies for nanogels and nanoparticles for selective drug delivery", *Gels*, Vol. 6, No. 1, p. 6, 2020.

59. Liu, C., Z. Zhang, Q. Kong, R. Zhang and X. Yang, "Enhancing the antitumor activity of tea polyphenols encapsulated in biodegradable nanogels by macromolecular self-assembly", *RSC Advances*, Vol. 9, No. 18, pp. 10004–10016, 2019.

60. Peng, S., Y. Men, R. Xie, Y. Tian and W. Yang, "Biodegradable phosphorylcholine-based zwitterionic polymer nanogels with smart charge-conversion ability for efficient inhibition of tumor cells", *Journal of Colloid and Interface Science*, Vol. 539, pp. 19–29, 2019.

61. Hajebi, S., A. Abdollahi, H. Roghani-Mamaqani and M. Salami-Kalajahi, "Hybrid and hollow poly(N,N-dimethylaminoethyl methacrylate) nanogels as stimuli-responsive carriers for controlled release of doxorubicin", *Polymer*, Vol. 180, p. 121716, 2019.

62. Sasaki, Y. and K. Akiyoshi, "Nanogel engineering for new nanobiomaterials:

From chaperoning engineering to biomedical applications", *The Chemical Record*, Vol. 10, No. 6, pp. 366–376, 2010.

63. Bhattacharya, K., S. L. Banerjee, S. Das, S. Samanta, M. Mandal and N. K. Singha, "REDOX responsive fluorescence active glycopolymer based nanogel: A potential material for targeted anticancer drug delivery", *ACS Applied Bio Materials*, Vol. 2, No. 6, pp. 2587–2599, 2019.

64. Gruber, A., L. Navarro and D. Klinger, "Reactive precursor particles as synthetic platform for the generation of functional nanoparticles, nanogels, and microgels", *Advanced Materials Interfaces*, Vol. 7, No. 5, p. 1901676, 2020.

65. Tiwari, R., D. Honders, S. Schipmann, B. Schulte, P. Das, C. W. Pester, U. Klemradt and A. Walther, "A versatile synthesis platform to prepare uniform, highly functional microgels via click-type functionalization of latex particles", *Macromolecules*, Vol. 47, No. 7, pp. 2257–2267, 2014.

66. Jiang, S., K. Wang, Y. Dai, X. Zhang and F. Xia, "Near-infrared light-triggered dual drug release using gold nanorod-embedded thermosensitive nanogel-crosslinked hydrogels", *Macromolecular Materials and Engineering*, Vol. 304, No. 7, p. 1900087, 2019.

67. Tian, Y., R. Tian, L. Chen, R. Jin, Y. Feng, Y. Bai and X. Chen, "Redox-responsive nanogel with intracellular reconstruction and programmable drug release for targeted tumor therapy", *Macromolecular Rapid Communications*, Vol. 40, No. 8, p. 1800824, 2019.

68. Oh, J. K., D. J. Siegwart, H.-I. Lee, G. Sherwood, L. Peteanu, J. O. Hollinger, K. Kataoka and K. Matyjaszewski, "Biodegradable nanogels prepared by atom transfer radical polymerization as potential drug delivery carriers: Synthesis, biodegradation, in vitro release, and bioconjugation", *Journal of the American Chemical Society*, Vol. 129, No. 18, pp. 5939–5945, 2007.

69. Zhao, Y., C. Simon, M. D. Attieh, K. Haupt and A. Falcimaigne-Cordin, "Reduction-responsive molecularly imprinted nanogels for drug delivery applications", *RSC Advances*, Vol. 10, No. 10, pp. 5978–5987, 2020.

70. Sahoo, N. G., S. Rana, J. W. Cho, L. Li and S. H. Chan, "Polymer nanocomposites based on functionalized carbon nanotubes", *Progress in Polymer Science*, Vol. 35, No. 7, pp. 837–867, 2010.

71. Rahman, I. A. and V. Padavettan, "Synthesis of silica nanoparticles by sol-gel: size-dependent properties, surface modification, and applications in silica-polymer nanocomposites - A review", *Journal of Nanomaterials*, Vol. 2012, 2012.

72. Kim, H., A. A. Abdala and C. W. Macosko, "Graphene/polymer nanocomposites", *Macromolecules*, Vol. 43, No. 16, pp. 6515–6530, 2010.

73. Li, C.-H., X. Chen, R. F. Landis, Y. Geng, J. M. Makabenta, W. Lemnios, A. Gupta and V. M. Rotello, "Phytochemical-based nanocomposites for the treatment of bacterial biofilms", *ACS Infectious Diseases*, Vol. 5, No. 9, pp. 1590–1596, 2019.

74. Thakur, V. K., D. Vennerberg and M. R. Kessler, "Green aqueous surface modification of polypropylene for novel polymer nanocomposites", *ACS Applied Materials & Interfaces*, Vol. 6, No. 12, pp. 9349–9356, 2014.

75. Landis, R. F., A. Gupta, Y.-W. Lee, L.-S. Wang, B. Golba, B. Couillaud, R. Ridolfo, R. Das and V. M. Rotello, "Cross-linked polymer-stabilized nanocomposites for the treatment of bacterial biofilms", *ACS Nano*, Vol. 11, No. 1, pp. 946–952, 2017.

76. Anderson, S. D., V. V. Gwenin and C. D. Gwenin, "Magnetic functionalized nanoparticles for biomedical, drug delivery and imaging applications", *Nanoscale Research Letters*, Vol. 14, No. 1, pp. 1–16, 2019.

77. Zheng, T., W. Wang, F. Wu, M. Zhang, J. Shen and Y. Sun, "Zwitterionic polymer-gated Au@TiO2 core-shell nanoparticles for imaging-guided combined cancer therapy", *Theranostics*, Vol. 9, No. 17, p. 5035, 2019.

78. Tavakoli, Z., B. Rasekh, F. Yazdian, A. Maghsoudi, M. Soleimani and J. Mohammadnejad, "One-step separation of the recombinant protein by using the amine-functionalized magnetic mesoporous silica nanoparticles; an efficient and facile approach", *International Journal of Biological Macromolecules*, Vol. 135, pp. 600–608, 2019.

79. Kim, D., S. Park, J. H. Lee, Y. Y. Jeong and S. Jon, "Antibiofouling polymer-coated gold nanoparticles as a contrast agent for in vivo X-ray computed tomography imaging", *Journal of the American Chemical Society*, Vol. 129, No. 24, pp. 7661–7665, 2007.

80. Boyer, C., M. R. Whittaker, M. Luzon and T. P. Davis, "Design and synthesis of dual thermoresponsive and antifouling hybrid polymer/gold nanoparticles", *Macromolecules*, Vol. 42, No. 18, pp. 6917–6926, 2009.

81. Yi, S., W. K. Lee, J.-H. Park, J.-S. Lee and J.-H. Seo, "One-pot synthesis of a zwitterionic small molecule bearing disulfide moiety for antibiofouling macro- and nanoscale gold surfaces", *Langmuir*, Vol. 35, No. 5, pp. 1768–1777, 2018.

82. Durand-Gasselin, C., R. Koerin, J. Rieger, N. Lequeux and N. Sanson, "Colloidal stability of zwitterionic polymer-grafted gold nanoparticles in water", *Journal of Colloid and Interface Science*, Vol. 434, pp. 188–194, 2014.

83. Chen, S., L. Li, C. Zhao and J. Zheng, "Surface hydration: Principles and applications toward low-fouling/nonfouling biomaterials", *Polymer*, Vol. 51, No. 23, pp. 5283–5293, 2010.

84. Leng, C., S. Sun, K. Zhang, S. Jiang and Z. Chen, "Molecular level studies on

interfacial hydration of zwitterionic and other antifouling polymers in situ", *Acta Biomaterialia*, Vol. 40, pp. 6–15, 2016.

85. Manson, J., D. Kumar, B. J. Meenan and D. Dixon, "Polyethylene glycol functionalized gold nanoparticles: The influence of capping density on stability in various media", *Gold Bulletin*, Vol. 44, No. 2, pp. 99–105, 2011.

86. Liu, Y., M. K. Shipton, J. Ryan, E. D. Kaufman, S. Franzen and D. L. Feldheim, "Synthesis, stability, and cellular internalization of gold nanoparticles containing mixed peptide- poly (ethylene glycol) monolayers", *Analytical Chemistry*, Vol. 79, No. 6, pp. 2221–2229, 2007.

87. Yi, Y., H. J. Kim, P. Mi, M. Zheng, H. Takemoto, K. Toh, B. S. Kim, K. Hayashi, M. Naito, Y. Matsumoto *et al.*, "Targeted systemic delivery of siRNA to cervical cancer model using cyclic RGD-installed unimer polyion complex-assembled gold nanoparticles", *Journal of Controlled Release*, Vol. 244, pp. 247–256, 2016.

88. Guardia, P., A. Labarta and X. Batlle, "Tuning the size, the shape, and the magnetic properties of iron oxide nanoparticles", *The Journal of Physical Chemistry C*, Vol. 115, No. 2, pp. 390–396, 2011.

89. Woo, K., J. Hong, S. Choi, H.-W. Lee, J.-P. Ahn, C. S. Kim and S. W. Lee, "Easy synthesis and magnetic properties of iron oxide nanoparticles", *Chemistry of Materials*, Vol. 16, No. 14, pp. 2814–2818, 2004.

90. Patsula, V., M. Moskvin, S. Dutz and D. Horák, "Size-dependent magnetic properties of iron oxide nanoparticles", *Journal of Physics and Chemistry of Solids*, Vol. 88, pp. 24–30, 2016.

91. Vijayakumar, R., Y. Koltypin, I. Felner and A. Gedanken, "Sonochemical synthesis and characterization of pure nanometer-sized Fe3O4 particles", *Materials Science and Engineering: A*, Vol. 286, No. 1, pp. 101–105, 2000.

92. Guardia, P., N. Pérez, A. Labarta and X. Batlle, "Controlled synthesis of iron oxide nanoparticles over a wide size range", *Langmuir*, Vol. 26, No. 8, pp. 5843–5847, 2010.

93. Basuki, J. S., A. Jacquemin, L. Esser, Y. Li, C. Boyer and T. P. Davis, "A block copolymer-stabilized co-precipitation approach to magnetic iron oxide nanoparticles for potential use as MRI contrast agents", *Polymer Chemistry*, Vol. 5, No. 7, pp. 2611–2620, 2014.

94. Unni, M., A. M. Uhl, S. Savliwala, B. H. Savitzky, R. Dhavalikar, N. Garraud, D. P. Arnold, L. F. Kourkoutis, J. S. Andrew and C. Rinaldi, "Thermal decomposition synthesis of iron oxide nanoparticles with diminished magnetic dead layer by controlled addition of oxygen", *Acs Nano*, Vol. 11, No. 2, pp. 2284–2303, 2017.

95. Hufschmid, R., H. Arami, R. M. Ferguson, M. Gonzales, E. Teeman, L. N. Brush, N. D. Browning and K. M. Krishnan, "Synthesis of phase-pure and monodisperse iron oxide nanoparticles by thermal decomposition", *Nanoscale*, Vol. 7, No. 25, pp. 11142–11154, 2015.

96. Shultz, M. D., J. U. Reveles, S. N. Khanna and E. E. Carpenter, "Reactive nature of dopamine as a surface functionalization agent in iron oxide nanoparticles", *Journal of the American Chemical Society*, Vol. 129, No. 9, pp. 2482–2487, 2007.

97. Das, M., D. Mishra, P. Dhak, S. Gupta, T. K. Maiti, A. Basak and P. Pramanik, "Biofunctionalized, phosphonate-grafted, ultrasmall iron oxide nanoparticles for combined targeted cancer therapy and multimodal imaging", *Small*, Vol. 5, No. 24, pp. 2883–2893, 2009.

98. Thomas, L. A., L. Dekker, M. Kallumadil, P. Southern, M. Wilson, S. P. Nair, Q. A. Pankhurst and I. P. Parkin, "Carboxylic acid-stabilised iron oxide nanoparticles for use in magnetic hyperthermia", *Journal of Materials Chemistry*, Vol. 19, No. 36, pp. 6529–6535, 2009.

99. Aisida, S. O., P. A. Akpa, I. Ahmad, T.-k. Zhao, M. Maaza and F. I. Ezema, "Bio-inspired encapsulation and functionalization of iron oxide nanoparticles for biomedical applications", *European Polymer Journal*, Vol. 122, p. 109371, 2020.

100. Sundaresan, V., J. U. Menon, M. Rahimi, K. T. Nguyen and A. S. Wadajkar, "Dual-responsive polymer-coated iron oxide nanoparticles for drug delivery and imaging applications", *International Journal of Pharmaceutics*, Vol. 466, No. 1-2, pp. 1–7, 2014.

101. Lee, H., E. Lee, D. K. Kim, N. K. Jang, Y. Y. Jeong and S. Jon, "Antibiofouling polymer-coated superparamagnetic iron oxide nanoparticles as potential magnetic resonance contrast agents for in vivo cancer imaging", *Journal of the American Chemical Society*, Vol. 128, No. 22, pp. 7383–7389, 2006.

102. Wadajkar, A. S., J. U. Menon, Y.-S. Tsai, C. Gore, T. Dobin, L. Gandee, K. Kangasniemi, M. Takahashi, B. Manandhar, J.-M. Ahn *et al.*, "Prostate cancer-specific thermo-responsive polymer-coated iron oxide nanoparticles", *Biomaterials*, Vol. 34, No. 14, pp. 3618–3625, 2013.

103. Barrow, M., A. Taylor, P. Murray, M. J. Rosseinsky and D. J. Adams, "Design considerations for the synthesis of polymer coated iron oxide nanoparticles for stem cell labelling and tracking using MRI", *Chemical Society Reviews*, Vol. 44, No. 19, pp. 6733–6748, 2015.

104. Shamim, N., L. Hong, K. Hidajat and M. Uddin, "Thermosensitive-polymer-coated magnetic nanoparticles: adsorption and desorption of bovine serum albumin", *Journal of Colloid and Interface Science*, Vol. 304, No. 1, pp. 1–8, 2006.

105. Qiao, R., L. Esser, C. Fu, C. Zhang, J. Hu, P. Ramírez-Arcía, Y. Li, J. F. Quinn, M. R. Whittaker, A. K. Whittaker *et al.*, "Bioconjugation and fluorescence labeling of iron oxide nanoparticles grafted with bromomaleimide-terminal polymers", *Biomacromolecules*, Vol. 19, No. 11, pp. 4423–4429, 2018.

106. Novoselov, K. S., A. K. Geim, S. V. Morozov, D. Jiang, Y. Zhang, S. V. Dubonos, I. V. Grigorieva and A. A. Firsov, "Electric field effect in atomically thin carbon films", *Science*, Vol. 306, No. 5696, pp. 666–669, 2004.

107. Peng, C., W. Hu, Y. Zhou, C. Fan and Q. Huang, "Intracellular imaging with a graphene-based fluorescent probe", *Small*, Vol. 6, No. 15, pp. 1686–1692, 2010.

108. He, Q., H. G. Sudibya, Z. Yin, S. Wu, H. Li, F. Boey, W. Huang, P. Chen and H. Zhang, "Centimeter-long and large-scale micropatterns of reduced graphene oxide films: Fabrication and sensing applications", *Acs Nano*, Vol. 4, No. 6, pp. 3201–3208, 2010.

109. Zhang, W., Z. Guo, D. Huang, Z. Liu, X. Guo and H. Zhong, "Synergistic effect of chemo-photothermal therapy using PEGylated graphene oxide", *Biomaterials*, Vol. 32, No. 33, pp. 8555–8561, 2011.

110. Tian, B., C. Wang, S. Zhang, L. Feng and Z. Liu, "Photothermally enhanced photodynamic therapy delivered by nano-graphene oxide", *ACS Nano*, Vol. 5, No. 9, pp. 7000–7009, 2011.

111. He, S., B. Song, D. Li, C. Zhu, W. Qi, Y. Wen, L. Wang, S. Song, H. Fang and C. Fan, "A graphene nanoprobe for rapid, sensitive, and multicolor fluorescent DNA analysis", *Advanced Functional Materials*, Vol. 20, No. 3, pp. 453–459, 2010.

112. Wang, X.-Y., A. Narita and K. Müllen, "Precision synthesis versus bulk-scale fabrication of graphenes", *Nature Reviews Chemistry*, Vol. 2, No. 1, pp. 1–10, 2017.

113. Reina, G., J. M. González-Domínguez, A. Criado, E. Vázquez, A. Bianco and M. Prato, "Promises, facts and challenges for graphene in biomedical applications", *Chemical Society Reviews*, Vol. 46, No. 15, pp. 4400–4416, 2017.

114. Kurapati, R. and A. M. Raichur, "Near-infrared light-responsive graphene oxide

composite multilayer capsules: a novel route for remote controlled drug delivery", *Chemical Communications*, Vol. 49, No. 7, pp. 734–736, 2013.

115. Wang, C., J. Mallela, U. S. Garapati, S. Ravi, V. Chinnasamy, Y. Girard, M. Howell and S. Mohapatra, "A chitosan-modified graphene nanogel for noninvasive controlled drug release", *Nanomedicine: Nanotechnology, Biology and Medicine*, Vol. 9, No. 7, pp. 903–911, 2013.

116. Khoee, S. and A. Sadeghi, "An NIR-triggered drug release and highly efficient photodynamic therapy from PCL/PNIPAm/porphyrin modified graphene oxide nanoparticles with the Janus morphology", *RSC Advances*, Vol. 9, No. 68, pp. 39780–39792, 2019.

117. Liu, Z., J. T. Robinson, X. Sun and H. Dai, "PEGylated nanographene oxide for delivery of water-insoluble cancer drugs", *Journal of the American Chemical Society*, Vol. 130, No. 33, pp. 10876–10877, 2008.

118. Li, S.-D. and L. Huang, "Stealth nanoparticles: high density but sheddable PEG is a key for tumor targeting", *Journal of Controlled Release: Official Journal of the Controlled Release Society*, Vol. 145, No. 3, p. 178, 2010.

119. Hatakeyama, H., H. Akita and H. Harashima, "A multifunctional envelope type nano device (MEND) for gene delivery to tumours based on the EPR effect: A strategy for overcoming the PEG dilemma", *Advanced Drug Delivery Reviews*, Vol. 63, No. 3, pp. 152–160, 2011.

120. Wen, H., C. Dong, H. Dong, A. Shen, W. Xia, X. Cai, Y. Song, X. Li, Y. Li and D. Shi, "Engineered redox-responsive PEG detachment mechanism in PEGylated nano-graphene oxide for intracellular drug delivery", *Small*, Vol. 8, No. 5, pp. 760–769, 2012.

121. Teodorescu, F., Y. Oz, G. Queniat, A. Abderrahmani, C. Foulon, M. Lecoeur,

R. Sanyal, A. Sanyal, R. Boukherroub and S. Szunerits, "Photothermally triggered on-demand insulin release from reduced graphene oxide modified hydrogels", *Journal of Controlled Release*, Vol. 246, pp. 164–173, 2017.

122. Kost, J. and R. Langer, "Responsive polymeric delivery systems", *Advanced Drug Delivery Reviews*, Vol. 64, pp. 327–341, 2012.

123. Li, H., Y. Yu, S. Faraji Dana, B. Li, C.-Y. Lee and L. Kang, "Novel engineered systems for oral, mucosal and transdermal drug delivery", *Journal of Drug Targeting*, Vol. 21, No. 7, pp. 611–629, 2013.

124. Goenka, S., V. Sant and S. Sant, "Graphene-based nanomaterials for drug delivery and tissue engineering", *Journal of Controlled Release*, Vol. 173, pp. 75–88, 2014.

125. Blum, A. P., J. K. Kammeyer, A. M. Rush, C. E. Callmann, M. E. Hahn and N. C. Gianneschi, "Stimuli-responsive nanomaterials for biomedical applications", *Journal of the American Chemical Society*, Vol. 137, No. 6, pp. 2140–2154, 2015.

126. Mura, S., J. Nicolas and P. Couvreur, "Stimuli-responsive nanocarriers for drug delivery", *Nature Materials*, Vol. 12, No. 11, pp. 991–1003, 2013.

127. Turcheniuk, K., M. Khanal, A. Motorina, P. Subramanian, A. Barras, V. Zaitsev, V. Kuncser, A. Leca, A. Martoriati, K. Cailliau *et al.*, "Insulin loaded iron magnetic nanoparticle–graphene oxide composites: Synthesis, characterization and application for in vivo delivery of insulin", *Rsc Advances*, Vol. 4, No. 2, pp. 865–875, 2014.

128. Teodorescu, F., L. Rolland, V. Ramarao, A. Abderrahmani, D. Mandler, R. Boukherroub and S. Szunerits, "Electrochemically triggered release of human insulin from an insulin-impregnated reduced graphene oxide modified electrode", *Chemical Communications*, Vol. 51, No. 75, pp. 14167–14170, 2015.

129. Mac Kenna, N., P. Calvert, A. Morrin, G. G. Wallace and S. E. Moulton, "Electro-

stimulated release from a reduced graphene oxide composite hydrogel", *Journal of Materials Chemistry B*, Vol. 3, No. 12, pp. 2530–2537, 2015.

130. Lee, H., T. K. Choi, Y. B. Lee, H. R. Cho, R. Ghaffari, L. Wang, H. J. Choi, T. D. Chung, N. Lu, T. Hyeon *et al.*, "A graphene-based electrochemical device with thermoresponsive microneedles for diabetes monitoring and therapy", *Nature Nanotechnology*, Vol. 11, No. 6, p. 566, 2016.

131. Matteini, P., F. Tatini, L. Cavigli, S. Ottaviano, G. Ghini and R. Pini, "Graphene as a photothermal switch for controlled drug release", *Nanoscale*, Vol. 6, No. 14, pp. 7947–7953, 2014.

132. Hong, J., N. J. Shah, A. C. Drake, P. C. DeMuth, J. B. Lee, J. Chen and P. T. Hammond, "Graphene multilayers as gates for multi-week sequential release of proteins from surfaces", *Acs Nano*, Vol. 6, No. 1, pp. 81–88, 2011.

133. Park, S., J. An, I. Jung, R. D. Piner, S. J. An, X. Li, A. Velamakanni and R. S. Ruoff, "Colloidal suspensions of highly reduced graphene oxide in a wide variety of organic solvents", *Nano Letters*, Vol. 9, No. 4, pp. 1593–1597, 2009.

134. Xu, Y., Q. Wu, Y. Sun, H. Bai and G. Shi, "Three-dimensional self-assembly of graphene oxide and DNA into multifunctional hydrogels", *Acs Nano*, Vol. 4, No. 12, pp. 7358–7362, 2010.

135. Zhang, J., L. Song, Z. Zhang, N. Chen and L. Qu, "Environmentally responsive graphene systems", *Small*, Vol. 10, No. 11, pp. 2151–2164, 2014.

136. Sherlock, S. P., S. M. Tabakman, L. Xie and H. Dai, "Photothermally enhanced drug delivery by ultrasmall multifunctional FeCo/graphitic shell nanocrystals", *Acs Nano*, Vol. 5, No. 2, pp. 1505–1512, 2011.

137. Kim, H., D. Lee, J. Kim, T.-i. Kim and W. J. Kim, "Photothermally triggered cytosolic drug delivery via endosome disruption using a functionalized reduced

graphene oxide", *Acs Nano*, Vol. 7, No. 8, pp. 6735–6746, 2013.

138. Pan, Y., H. Bao, N. G. Sahoo, T. Wu and L. Li, "Water-soluble poly (N-isopropylacrylamide)–graphene sheets synthesized via click chemistry for drug delivery", *Advanced Functional Materials*, Vol. 21, No. 14, pp. 2754–2763, 2011.

139. Buysschaert, M. and A. Lambert, "The insulin pen", *The Lancet*, Vol. 333, No. 8644, p. 965, 1989.

140. Kim, H., Y. J. Kang, S. Kang and K. T. Kim, "Monosaccharide-responsive release of insulin from polymersomes of polyboroxole block copolymers at neutral pH", *Journal of the American Chemical Society*, Vol. 134, No. 9, pp. 4030–4033, 2012.

141. Matsumoto, A., T. Ishii, J. Nishida, H. Matsumoto, K. Kataoka and Y. Miyahara, "A synthetic approach toward a self-regulated insulin delivery system", *Angewandte Chemie International Edition*, Vol. 51, No. 9, pp. 2124–2128, 2012.

142. Kwon, I. C., Y. H. Bae and S. W. Kim, "Electrically erodible polymer gel for controlled release of drugs", *Nature*, Vol. 354, No. 6351, p. 291, 1991.

143. Tomar, L., C. Tyagi, M. Kumar, P. Kumar, H. Singh, Y. E. Choonara and V. Pillay, "In vivo evaluation of a conjugated poly (lactide-ethylene glycol) nanoparticle depot formulation for prolonged insulin delivery in the diabetic rabbit model", *International Journal of Nanomedicine*, Vol. 8, p. 505, 2013.

144. Hadebe, S. I., P. S. Ngubane, M. R. Serumula and C. T. Musabayane, "Transdermal delivery of insulin by amidated pectin hydrogel matrix patch in streptozotocin-induced diabetic rats: effects on some selected metabolic parameters", *Plos One*, Vol. 9, No. 7, p. e101461, 2014.

145. Nolan, C. M., M. J. Serpe and L. A. Lyon, "Thermally modulated insulin release from microgel thin films", *Biomacromolecules*, Vol. 5, No. 5, pp. 1940–1946, 2004.

146. Spizzirri, U. G., M. Curcio, G. Cirillo, T. Spataro, O. Vittorio, N. Picci, S. Hampel, F. Iemma and F. P. Nicoletta, "Recent advances in the synthesis and biomedical applications of nanocomposite hydrogels", *Pharmaceutics*, Vol. 7, No. 4, pp. 413–437, 2015.

147. Koenig, J. and A. Angood, "Raman spectra of poly (ethylene glycols) in solution", *Journal of Polymer Science Part A-2: Polymer Physics*, Vol. 8, No. 10, pp. 1787–1796, 1970.

148. Song, L., Z.-l. Zhi and J. C. Pickup, "Nanolayer encapsulation of insulin-chitosan complexes improves efficiency of oral insulin delivery", *International Journal of Nanomedicine*, Vol. 9, p. 2127, 2014.

149. Suckale, J. and M. Solimena, "Pancreas islets in metabolic signaling-focus on the beta-cell", *Front Biosci*, Vol. 13, No. 7156, p. 71, 2008.

150. Guth, K., M. Schäfer-Korting, E. Fabian, R. Landsiedel and B. Van Ravenzwaay, "Suitability of skin integrity tests for dermal absorption studies in vitro", *Toxicology in Vitro*, Vol. 29, No. 1, pp. 113–123, 2015.

151. Andrews, S. N., E. Jeong and M. R. Prausnitz, "Transdermal delivery of molecules is limited by full epidermis, not just stratum corneum", *Pharmaceutical Research*, Vol. 30, No. 4, pp. 1099–1109, 2013.

152. Oz, Y., A. Barras, R. Sanyal, R. Boukherroub, S. Szunerits and A. Sanyal, "Functionalization of reduced graphene oxide via thiol–maleimide "click" chemistry: Facile fabrication of targeted drug delivery vehicles", *ACS Applied Materials & Interfaces*, Vol. 9, No. 39, pp. 34194–34203, 2017.

153. Szunerits, S., F. Teodorescu and R. Boukherroub, "Electrochemically triggered release of drugs", *European Polymer Journal*, Vol. 83, pp. 467–477, 2016.

154. Boulahneche, S., R. Jijie, A. Barras, F. Chekin, S. K. Singh, J. Bouckaert, M. S.

Medjram, S. Kurungot, R. Boukherroub and S. Szunerits, "On demand electrochemical release of drugs from porous reduced graphene oxide modified flexible electrodes", *Journal of Materials Chemistry B*, Vol. 5, No. 32, pp. 6557–6565, 2017.

155. Hu, S.-H., R.-H. Fang, Y.-W. Chen, B.-J. Liao, I.-W. Chen and S.-Y. Chen, "Photoresponsive protein–graphene–protein hybrid capsules with dual targeted heat-triggered drug delivery approach for enhanced tumor therapy", *Advanced Functional Materials*, Vol. 24, No. 26, pp. 4144–4155, 2014.

156. Teodorescu, F., G. Queniat, C. Foulon, M. Lecoeur, A. Barras, S. Boulahneche, M. S. Medjram, T. Hubert, A. Abderrahmani, R. Boukherroub *et al.*, "Transdermal skin patch based on reduced graphene oxide: A new approach for photothermal triggered permeation of ondansetron across porcine skin", *Journal of Controlled Release*, Vol. 245, pp. 137–146, 2017.

157. Turcheniuk, K., T. Dumych, R. Bilyy, V. Turcheniuk, J. Bouckaert, V. Vovk, V. Chopyak, V. Zaitsev, P. Mariot, N. Prevarskaya *et al.*, "Plasmonic photothermal cancer therapy with gold nanorods/reduced graphene oxide core/shell nanocomposites", *RSC Advances*, Vol. 6, No. 2, pp. 1600–1610, 2016.

158. Guo, C. X., S. R. Ng, S. Y. Khoo, X. Zheng, P. Chen and C. M. Li, "RGD-peptide functionalized graphene biomimetic live-cell sensor for real-time detection of nitric oxide molecules", *Acs Nano*, Vol. 6, No. 8, pp. 6944–6951, 2012.

159. Xu, L. Q., L. Wang, B. Zhang, C. H. Lim, Y. Chen, K.-G. Neoh, E.-T. Kang and G. D. Fu, "Functionalization of reduced graphene oxide nanosheets via stacking interactions with the fluorescent and water-soluble perylene bisimide-containing polymers", *Polymer*, Vol. 52, No. 11, pp. 2376–2383, 2011.

160. Kaminska, I., M. R. Das, Y. Coffinier, J. Niedziolka-Jonsson, P. Woisel, M. Opallo, S. Szunerits and R. Boukherroub, "Preparation of graphene/tetrathiafulvalene

nanocomposite switchable surfaces", *Chemical Communications*, Vol. 48, No. 9, pp. 1221–1223, 2012.

161. Kaminska, I., M. R. Das, Y. Coffinier, J. Niedziolka-Jonsson, J. Sobczak, P. Woisel, J. Lyskawa, M. Opallo, R. Boukherroub and S. Szunerits, "Reduction and functionalization of graphene oxide sheets using biomimetic dopamine derivatives in one step", *ACS Applied Materials & Interfaces*, Vol. 4, No. 2, pp. 1016–1020, 2012.

162. Kaminska, I., A. Barras, Y. Coffinier, W. Lisowski, S. Roy, J. Niedziolka-Jonsson, P. Woisel, J. Lyskawa, M. Opallo, A. Siriwardena *et al.*, "Preparation of a responsive carbohydrate-coated biointerface based on graphene/azido-terminated tetrathiafulvalene nanohybrid material", *ACS Applied Materials & Interfaces*, Vol. 4, No. 10, pp. 5386–5393, 2012.

163. Kaminska, I., W. Qi, A. Barras, J. Sobczak, J. Niedziolka-Jonsson, P. Woisel, J. Lyskawa, W. Laure, M. Opallo, M. Li *et al.*, "Thiol–yne click reactions on alkynyl–dopamine-modified reduced graphene oxide", *Chemistry–A European Journal*, Vol. 19, No. 26, pp. 8673–8678, 2013.

164. Qu, S., M. Li, L. Xie, X. Huang, J. Yang, N. Wang and S. Yang, "Noncovalent functionalization of graphene attaching [6, 6]-phenyl-C61-butyric acid methyl ester (PCBM) and application as electron extraction layer of polymer solar cells", *Acs Nano*, Vol. 7, No. 5, pp. 4070–4081, 2013.

165. Manova, R. K., S. P. Pujari, C. A. Weijers, H. Zuilhof and T. A. van Beek, "Copper-free click biofunctionalization of silicon nitride surfaces via strain-promoted alkyne–azide cycloaddition reactions", *Langmuir*, Vol. 28, No. 23, pp. 8651–8663, 2012.

166. Zhang, L., N. Vila, T. Klein, G.-W. Kohring, I. Mazurenko, A. Walcarius and M. Etienne, "Immobilization of cysteine-tagged proteins on electrode surfaces by

thiol–ene click chemistry", *ACS Applied Materials & Interfaces*, Vol. 8, No. 27, pp. 17591–17598, 2016.

167. Escorihuela, J., A. T. Marcelis and H. Zuilhof, "Metal-free click chemistry reactions on surfaces", *Advanced Materials & Interfaces*, Vol. 2, No. 13, p. 1500135, 2015.

168. Mazur, M., A. Barras, V. Kuncser, A. Galatanu, V. Zaitzev, K. V. Turcheniuk, P. Woisel, J. Lyskawa, W. Laure, A. Siriwardena *et al.*, "Iron oxide magnetic nanoparticles with versatile surface functions based on dopamine anchors", *Nanoscale*, Vol. 5, No. 7, pp. 2692–2702, 2013.

169. Hoyle, C. E., A. B. Lowe and C. N. Bowman, "Thiol-click chemistry: A multifaceted toolbox for small molecule and polymer synthesis", *Chemical Society Reviews*, Vol. 39, No. 4, pp. 1355–1387, 2010.

170. Oz, Y., M. Arslan, T. N. Gevrek, R. Sanyal and A. Sanyal, "Modular fabrication of polymer brush coated magnetic nanoparticles: Engineering the interface for targeted cellular imaging", *ACS applied Materials & interfaces*, Vol. 8, No. 30, pp. 19813–19826, 2016.

171. Arslan, M., T. N. Gevrek, J. Lyskawa, S. Szunerits, R. Boukherroub, R. Sanyal, P. Woisel and A. Sanyal, "Bioinspired anchorable thiol-reactive polymers: Synthesis and applications toward surface functionalization of magnetic nanoparticles", *Macromolecules*, Vol. 47, No. 15, pp. 5124–5134, 2014.

172. Waite, C. L. and C. M. Roth, "PAMAM-RGD conjugates enhance siRNA delivery through a multicellular spheroid model of malignant glioma", *Bioconjugate Chemistry*, Vol. 20, No. 10, pp. 1908–1916, 2009.

173. Xiong, X.-B., Y. Huang, W.-l. Lu, X. Zhang, H. Zhang, T. Nagai and Q. Zhang, "Enhanced intracellular delivery and improved antitumor efficacy of doxorubicin

by sterically stabilized liposomes modified with a synthetic RGD mimetic", *Journal of Controlled Release*, Vol. 107, No. 2, pp. 262–275, 2005.

174. Zhu, S., L. Qian, M. Hong, L. Zhang, Y. Pei and Y. Jiang, "RGD-modified PEG-PAMAM-DOX conjugate: in vitro and in vivo targeting to both tumor neovascular endothelial cells and tumor cells", *Advanced Materials*, Vol. 23, No. 12, pp. H84–H89, 2011.

175. Zhang, L., S. Zhu, L. Qian, Y. Pei, Y. Qiu and Y. Jiang, "RGD-modified PEG–PAMAM–DOX conjugates: in vitro and in vivo studies for glioma", *European Journal of Pharmaceutics and Biopharmaceutics*, Vol. 79, No. 2, pp. 232–240, 2011.

176. Luo, D., K. A. Carter, D. Miranda and J. F. Lovell, "Chemophototherapy: An emerging treatment option for solid tumors", *Advanced Science*, Vol. 4, No. 1, 2017.

177. Maynard, H. D., S. Y. Okada and R. H. Grubbs, "Synthesis of norbornenyl polymers with bioactive oligopeptides by ring-opening metathesis polymerization", *Macromolecules*, Vol. 33, No. 17, pp. 6239–6248, 2000.

178. Das, M. R., M. Wang, S. Szunerits, L. Gengembre and R. Boukherroub, "Clicking ferrocene groups to boron-doped diamond electrodes", *Chemical Communications*, , No. 19, pp. 2753–2755, 2009.

179. Sneider, A., D. VanDyke, S. Paliwal and P. Rai, "Remotely triggered nanotheranostics for cancer applications", *Nanotheranostics*, Vol. 1, No. 1, p. 1, 2017.

180. Chen, Y.-W., Y.-L. Su, S.-H. Hu and S.-Y. Chen, "Functionalized graphene nanocomposites for enhancing photothermal therapy in tumor treatment", *Advanced Drug Delivery Reviews*, Vol. 105, pp. 190–204, 2016.

181. Wang, Y., K. Wang, J. Zhao, X. Liu, J. Bu, X. Yan and R. Huang, "Multifunc-

tional mesoporous silica-coated graphene nanosheet used for chemo-photothermal synergistic targeted therapy of glioma", *Journal of the American Chemical Society*, Vol. 135, No. 12, pp. 4799–4804, 2013.

182. Gao, J., H. Gu and B. Xu, "Multifunctional magnetic nanoparticles: Design, synthesis, and biomedical applications", *Accounts of Chemical Research*, Vol. 42, No. 8, pp. 1097–1107, 2009.

183. Laurent, S., D. Forge, M. Port, A. Roch, C. Robic, L. Vander Elst and R. N. Muller, "Magnetic iron oxide nanoparticles: Synthesis, stabilization, vectorization, physicochemical characterizations, and biological applications", *Chemical Reviews*, Vol. 108, No. 6, pp. 2064–2110, 2008.

184. Lee, N. and T. Hyeon, "Designed synthesis of uniformly sized iron oxide nanoparticles for efficient magnetic resonance imaging contrast agents", *Chemical Society Reviews*, Vol. 41, No. 7, pp. 2575–2589, 2012.

185. Zhang, L., W.-F. Dong and H.-B. Sun, "Multifunctional superparamagnetic iron oxide nanoparticles: design, synthesis and biomedical photonic applications", *Nanoscale*, Vol. 5, No. 17, pp. 7664–7684, 2013.

186. Ling, D., N. Lee and T. Hyeon, "Chemical synthesis and assembly of uniformly sized iron oxide nanoparticles for medical applications", *Accounts of Chemical Research*, Vol. 48, No. 5, pp. 1276–1285, 2015.

187. Na, H. B., G. Palui, J. T. Rosenberg, X. Ji, S. C. Grant and H. Mattoussi, "Multidentate catechol-based polyethylene glycol oligomers provide enhanced stability and biocompatibility to iron oxide nanoparticles", *Acs Nano*, Vol. 6, No. 1, pp. 389–399, 2012.

188. Turcheniuk, K., A. V. Tarasevych, V. P. Kukhar, R. Boukherroub and S. Szunerits, "Recent advances in surface chemistry strategies for the fabrication of func-

tional iron oxide based magnetic nanoparticles", *Nanoscale*, Vol. 5, No. 22, pp. 10729–10752, 2013.

189. Lee, G. Y., W. P. Qian, L. Wang, Y. A. Wang, C. A. Staley, M. Satpathy, S. Nie, H. Mao and L. Yang, "Theranostic nanoparticles with controlled release of gemcitabine for targeted therapy and MRI of pancreatic cancer", *Acs Nano*, Vol. 7, No. 3, pp. 2078–2089, 2013.

190. Huang, G., Z. Sun, H. Qin, L. Zhao, Z. Xiong, X. Peng, J. Ou and H. Zou, "Preparation of hydrazine functionalized polymer brushes hybrid magnetic nanoparticles for highly specific enrichment of glycopeptides", *Analyst*, Vol. 139, No. 9, pp. 2199–2206, 2014.

191. Shen, Y., W. Guo, L. Qi, J. Qiao, F. Wang and L. Mao, "Immobilization of trypsin via reactive polymer grafting from magnetic nanoparticles for microwave-assisted digestion", *Journal of Materials Chemistry B*, Vol. 1, No. 17, pp. 2260–2267, 2013.

192. Mu, X., J. Qiao, L. Qi, P. Dong and H. Ma, "Poly (2-vinyl-4, 4-dimethylazlactone)-functionalized magnetic nanoparticles as carriers for enzyme immobilization and its application", *ACS Applied Materials & Interfaces*, Vol. 6, No. 23, pp. 21346–21354, 2014.

193. Chan, N., M. Laprise-Pelletier, P. Chevallier, A. Bianchi, M.-A. Fortin and J. K. Oh, "Multidentate block-copolymer-stabilized ultrasmall superparamagnetic iron oxide nanoparticles with enhanced colloidal stability for magnetic resonance imaging", *Biomacromolecules*, Vol. 15, No. 6, pp. 2146–2156, 2014.

194. Lu, C., L. R. Bhatt, H. Y. Jun, S. H. Park and K. Y. Chai, "Carboxyl–polyethylene glycol–phosphoric acid: A ligand for highly stabilized iron oxide nanoparticles", *Journal of Materials Chemistry*, Vol. 22, No. 37, pp. 19806–19811, 2012.

195. Das, M., D. Bandyopadhyay, R. P. Singh, H. Harde, S. Kumar and S. Jain, "Orthogonal biofunctionalization of magnetic nanoparticles via "clickable" poly (ethylene glycol) silanes: A "universal ligand" strategy to design stealth and target-specific nanocarriers", *Journal of Materials Chemistry*, Vol. 22, No. 47, pp. 24652–24667, 2012.

196. Amstad, E., T. Gillich, I. Bilecka, M. Textor and E. Reimhult, "Ultrastable iron oxide nanoparticle colloidal suspensions using dispersants with catechol-derived anchor groups", *Nano Letters*, Vol. 9, No. 12, pp. 4042–4048, 2009.

197. Xu, C., K. Xu, H. Gu, R. Zheng, H. Liu, X. Zhang, Z. Guo and B. Xu, "Dopamine as a robust anchor to immobilize functional molecules on the iron oxide shell of magnetic nanoparticles", *Journal of the American Chemical Society*, Vol. 126, No. 32, pp. 9938–9939, 2004.

198. Stone, R., B. Qi, D. Trebatoski, R. Jetti, Y. Bandera, S. Foulger and O. Mefford, "A versatile stable platform for multifunctional applications: synthesis of a nitroDOPA–PEO–alkyne scaffold for iron oxide nanoparticles", *Journal of Materials Chemistry B*, Vol. 2, No. 30, pp. 4789–4793, 2014.

199. Kim, J. S., T. G. Kim, W. H. Kong, T. G. Park and Y. S. Nam, "Thermally controlled wettability of a nanoporous membrane grafted with catechol-tethered poly (N-isopropylacrylamide)", *Chemical Communications*, Vol. 48, No. 74, pp. 9227–9229, 2012.

200. Sandiford, L., A. Phinikaridou, A. Protti, L. K. Meszaros, X. Cui, Y. Yan, G. Frodsham, P. A. Williamson, N. Gaddum, R. M. Botnar *et al.*, "Bisphosphonate-anchored PEGylation and radiolabeling of superparamagnetic iron oxide: Long-circulating nanoparticles for in vivo multimodal (T1 MRI-SPECT) imaging", *Acs Nano*, Vol. 7, No. 1, pp. 500–512, 2013.

201. He, W., L. Zhang, B. Han, L. Cheng, N. Zhou, Z. Liu and Z. Cheng, "Re-

tracted article: Hydrophilic hybrid materials with magnetism & NIR fluorescence via surface-initiated RAFT polymerization", *Journal of Materials Chemistry B*, Vol. 1, No. 26, pp. 3257–3266, 2013.

202. Lu, X., R. Jiang, Q. Fan, L. Zhang, H. Zhang, M. Yang, Y. Ma, L. Wang and W. Huang, "Fluorescent-magnetic poly (poly (ethyleneglycol) monomethacrylate)-grafted Fe3O4 nanoparticles from post-atom-transfer-radical-polymerization modification: Synthesis, characterization, cellular uptake and imaging", *Journal of Materials Chemistry*, Vol. 22, No. 14, pp. 6965–6973, 2012.

203. Li, H., B. Yu, H. Matsushima, C. E. Hoyle and A. B. Lowe, "The thiol-isocyanate click reaction: Facile and quantitative access to ω-end-functional poly (N, N-diethylacrylamide) synthesized by RAFT radical polymerization", *Macromolecules*, Vol. 42, No. 17, pp. 6537–6542, 2009.

204. Scales, C. W., A. J. Convertine and C. L. McCormick, "Fluorescent labeling of RAFT-generated poly (N-isopropylacrylamide) via a facile maleimide- thiol coupling reaction", *Biomacromolecules*, Vol. 7, No. 5, pp. 1389–1392, 2006.

205. Thurecht, K. J., I. Blakey, H. Peng, O. Squires, S. Hsu, C. Alexander and A. K. Whittaker, "Functional hyperbranched polymers: Toward targeted in vivo 19F magnetic resonance imaging using designed macromolecules", *Journal of the American Chemical Society*, Vol. 132, No. 15, pp. 5336–5337, 2010.

206. Neubert, B. J. and B. B. Snider, "Synthesis of (±)-phloeodictine A1", *Organic Letters*, Vol. 5, No. 5, pp. 765–768, 2003.

207. Shepherd, J. L., A. Kell, E. Chung, C. W. Sinclar, M. S. Workentin and D. Bizzotto, "Selective reductive desorption of a SAM-coated gold electrode revealed using fluorescence microscopy", *Journal of the American Chemical Society*, Vol. 126, No. 26, pp. 8329–8335, 2004.

208. Verdoes, M., U. Hillaert, B. I. Florea, M. Sae-Heng, M. D. Risseeuw, D. V. Filippov, G. A. van der Marel and H. S. Overkleeft, "Acetylene functionalized BODIPY dyes and their application in the synthesis of activity based proteasome probes", *Bioorganic & Medicinal Chemistry Letters*, Vol. 17, No. 22, pp. 6169–6171, 2007.

209. Santi, D. V., E. L. Schneider, R. Reid, L. Robinson and G. W. Ashley, "Predictable and tunable half-life extension of therapeutic agents by controlled chemical release from macromolecular conjugates", *Proceedings of the National Academy of Sciences*, Vol. 109, No. 16, pp. 6211–6216, 2012.

210. Heredia, K. L., G. N. Grover, L. Tao and H. D. Maynard, "Synthesis of heterotelechelic polymers for conjugation of two different proteins", *Macromolecules*, Vol. 42, No. 7, pp. 2360–2367, 2009.

211. McCusker, C. F., P. J. Kocienski, F. T. Boyle and A. G. Schätzlein, "Solid-phase synthesis of c (RGDfK) derivatives: on-resin cyclisation and lysine functionalisation", *Bioorganic & Medicinal Chemistry Letters*, Vol. 12, No. 4, pp. 547–549, 2002.

212. Lai, J. T., D. Filla and R. Shea, "Functional polymers from novel carboxyl-terminated trithiocarbonates as highly efficient RAFT agents", *Macromolecules*, Vol. 35, No. 18, pp. 6754–6756, 2002.

213. Lv, W., L. Liu, Y. Luo, X. Wang and Y. Liu, "Biotinylated thermoresponsive core cross-linked nanoparticles via RAFT polymerization and "click" chemistry", *Journal of Colloid and Interface Science*, Vol. 356, No. 1, pp. 16–23, 2011.

214. Park, J., K. An, Y. Hwang, J.-G. Park, H.-J. Noh, J.-Y. Kim, J.-H. Park, N.-M. Hwang and T. Hyeon, "Ultra-large-scale syntheses of monodisperse nanocrystals", *Nature Materials*, Vol. 3, No. 12, p. 891, 2004.

215. Kwon, S. G., Y. Piao, J. Park, S. Angappane, Y. Jo, N.-M. Hwang, J.-G. Park and T. Hyeon, "Kinetics of monodisperse iron oxide nanocrystal formation by "heating-up" process", *Journal of the American Chemical Society*, Vol. 129, No. 41, pp. 12571–12584, 2007.

216. Zobrist, C., J. Sobocinski, J. Lyskawa, D. Fournier, V. Miri, M. Traisnel, M. Jimenez and P. Woisel, "Functionalization of titanium surfaces with polymer brushes prepared from a biomimetic RAFT agent", *Macromolecules*, Vol. 44, No. 15, pp. 5883–5892, 2011.

217. Watanabe, H., A. Fujimoto, R. Yamamoto, J. Nishida, M. Kobayashi and A. Takahara, "Scaffold for growing dense polymer brushes from a versatile substrate", *ACS Applied Materials & Interfaces*, Vol. 6, No. 5, pp. 3648–3653, 2014.

218. Nagase, K., J. Kobayashi, A. Kikuchi, Y. Akiyama, H. Kanazawa, M. Annaka and T. Okano, "Preparation of thermoresponsive anionic copolymer brush surfaces for separating basic biomolecules", *Biomacromolecules*, Vol. 11, No. 1, pp. 215–223, 2010.

219. Yuan, S., D. Wan, B. Liang, S. Pehkonen, Y. Ting, K. Neoh and E. Kang, "Lysozyme-coupled poly (poly (ethylene glycol) methacrylate)- stainless steel hybrids and their antifouling and antibacterial surfaces", *Langmuir*, Vol. 27, No. 6, pp. 2761–2774, 2011.

220. Oz, Y., Y. Abdouni, G. Yilmaz, C. R. Becer and A. Sanyal, "Magnetic glyconanoparticles for selective lectin separation and purification", *Polymer Chemistry*, Vol. 10, No. 24, pp. 3351–3361, 2019.

221. Nilsson, C. L., "Lectins: Proteins that interpret the sugar code", *Analytical Chemistry*, Vol. 75, No. 15, pp. 348 A–353 A, 2003.

222. Bojarová, P. and V. Křen, "Sugared biomaterial binding lectins: Achievements

and perspectives", *Biomaterials Science*, Vol. 4, No. 8, pp. 1142–1160, 2016.

223. Yang, Z. and W. S. Hancock, "Approach to the comprehensive analysis of glycoproteins isolated from human serum using a multi-lectin affinity column", *Journal of Chromatography A*, Vol. 1053, No. 1-2, pp. 79–88, 2004.

224. Yang, Z. and W. S. Hancock, "Monitoring glycosylation pattern changes of glycoproteins using multi-lectin affinity chromatography", *Journal of Chromatography A*, Vol. 1070, No. 1-2, pp. 57–64, 2005.

225. Qiu, R. and F. E. Regnier, "Use of multidimensional lectin affinity chromatography in differential glycoproteomics", *Analytical Chemistry*, Vol. 77, No. 9, pp. 2802–2809, 2005.

226. Li, J., Y. Hu, J. Yang, P. Wei, W. Sun, M. Shen, G. Zhang and X. Shi, "Hyaluronic acid-modified Fe3O4@ Au core/shell nanostars for multimodal imaging and photothermal therapy of tumors", *Biomaterials*, Vol. 38, pp. 10–21, 2015.

227. Sabale, S., P. Kandesar, V. Jadhav, R. Komorek, R. K. Motkuri and X.-Y. Yu, "Recent developments in the synthesis, properties, and biomedical applications of core/shell superparamagnetic iron oxide nanoparticles with gold", *Biomaterials Science*, Vol. 5, No. 11, pp. 2212–2225, 2017.

228. Grifantini, R., M. Taranta, L. Gherardini, I. Naldi, M. Parri, A. Grandi, A. Giannetti, S. Tombelli, G. Lucarini, L. Ricotti *et al.*, "Magnetically driven drug delivery systems improving targeted immunotherapy for colon-rectal cancer", *Journal of Controlled Release*, Vol. 280, pp. 76–86, 2018.

229. Nash, M. A., P. Yager, A. S. Hoffman and P. S. Stayton, "Mixed stimuli-responsive magnetic and gold nanoparticle system for rapid purification, enrichment, and detection of biomarkers", *Bioconjugate Chemistry*, Vol. 21, No. 12, pp. 2197–2204, 2010.

230. Hu, C., J. Wu, T. Wei, W. Zhan, Y. Qu, Y. Pan, Q. Yu and H. Chen, "A supramolecular approach for versatile biofunctionalization of magnetic nanoparticles", *Journal of Materials Chemistry B*, Vol. 6, No. 15, pp. 2198–2203, 2018.

231. Samanta, A. and B. J. Ravoo, "Magnetic separation of proteins by a self-assembled supramolecular ternary complex", *Angewandte Chemie International Edition*, Vol. 53, No. 47, pp. 12946–12950, 2014.

232. Cheng, G., Z.-G. Wang, Y.-L. Liu, J.-L. Zhang, D.-H. Sun and J.-Z. Ni, "Magnetic affinity microspheres with meso-/macroporous shells for selective enrichment and fast separation of phosphorylated biomolecules", *ACS Applied Materials & Interfaces*, Vol. 5, No. 8, pp. 3182–3190, 2013.

233. Ta, D. T., R. Vanella and M. A. Nash, "Magnetic separation of elastin-like polypeptide receptors for enrichment of cellular and molecular targets", *Nano Letters*, Vol. 17, No. 12, pp. 7932–7939, 2017.

234. Blin, T., A. Kakinen, E. H. Pilkington, A. Ivask, F. Ding, J. F. Quinn, M. R. Whittaker, P. C. Ke and T. P. Davis, "Synthesis and in vitro properties of iron oxide nanoparticles grafted with brushed phosphorylcholine and polyethylene glycol", *Polymer Chemistry*, Vol. 7, No. 10, pp. 1931–1944, 2016.

235. Hurley, K. R., H. L. Ring, M. Etheridge, J. Zhang, Z. Gao, Q. Shao, N. D. Klein, V. M. Szlag, C. Chung, T. M. Reineke *et al.*, "Predictable heating and positive MRI contrast from a mesoporous silica-coated iron oxide nanoparticle", *Molecular Pharmaceutics*, Vol. 13, No. 7, pp. 2172–2183, 2016.

236. Altan, C. L., B. Gurten, R. Sadza, E. Yenigul, N. A. Sommerdijk and S. Bucak, "Poly (acrylic acid)-directed synthesis of colloidally stable single domain magnetite nanoparticles via partial oxidation", *Journal of Magnetism and Magnetic Materials*, Vol. 416, pp. 366–372, 2016.

237. Zengin, A., U. Tamer and T. Caykara, "A sers-based sandwich assay for ultrasensitive and selective detection of alzheimer's tau protein", *Biomacromolecules*, Vol. 14, No. 9, pp. 3001–3009, 2013.

238. Chen, G. and M. Jiang, "Cyclodextrin-based inclusion complexation bridging supramolecular chemistry and macromolecular self-assembly", *Chemical Society Reviews*, Vol. 40, No. 5, pp. 2254–2266, 2011.

239. Willenbacher, J., B. V. Schmidt, D. Schulze-Suenninghausen, O. Altintas, B. Luy, G. Delaittre and C. Barner-Kowollik, "Reversible single-chain selective point folding via cyclodextrin driven host–guest chemistry in water", *Chemical Communications*, Vol. 50, No. 53, pp. 7056–7059, 2014.

240. Schmidt, B. V., M. Hetzer, H. Ritter and C. Barner-Kowollik, "Complex macromolecular architecture design via cyclodextrin host/guest complexes", *Progress in Polymer Science*, Vol. 39, No. 1, pp. 235–249, 2014.

241. Schmidt, B. V. and C. Barner-Kowollik, "Dynamic macromolecular material design the versatility of cyclodextrin-based host-guest chemistry", *Angewandte Chemie International Edition*, Vol. 56, No. 29, pp. 8350–8369, 2017.

242. Ma, X. and Y. Zhao, "Biomedical applications of supramolecular systems based on host–guest interactions", *Chemical Reviews*, Vol. 115, No. 15, pp. 7794–7839, 2014.

243. Cakir, N., G. Hizal and C. R. Becer, "Supramolecular glycopolymers with thermoresponsive self-assembly and lectin binding", *Polymer Chemistry*, Vol. 6, No. 37, pp. 6623–6631, 2015.

244. Zhang, Q., L. Su, J. Collins, G. Chen, R. Wallis, D. A. Mitchell, D. M. Haddleton and C. R. Becer, "Dendritic cell lectin-targeting sentinel-like unimolecular glycoconjugates to release an anti-HIV drug", *Journal of the American Chemical*

Society, Vol. 136, No. 11, pp. 4325–4332, 2014.

245. Li, X., M. Bao, Y. Weng, K. Yang, W. Zhang and G. Chen, "Glycopolymer-coated iron oxide nanoparticles: Shape-controlled synthesis and cellular uptake", *Journal of Materials Chemistry B*, Vol. 2, No. 34, pp. 5569–5575, 2014.

246. Shao, C., X. Li, Z. Pei, D. Liu, L. Wang, H. Dong and Y. Pei, "Facile fabrication of glycopolymer-based iron oxide nanoparticles and their applications in the carbohydrate–lectin interaction and targeted cell imaging", *Polymer Chemistry*, Vol. 7, No. 6, pp. 1337–1344, 2016.

247. Muñoz-Bonilla, A., G. Marcelo, C. Casado, F. J. Teran and M. Fernández-García, "Preparation of glycopolymer-coated magnetite nanoparticles for hyperthermia treatment", *Journal of Polymer Science Part A: Polymer Chemistry*, Vol. 50, No. 24, pp. 5087–5096, 2012.

248. Mulder, A., S. Onclin, M. Péter, J. P. Hoogenboom, H. Beijleveld, J. ter Maat, M. F. García-Parajó, B. J. Ravoo, J. Huskens, N. F. van Hulst *et al.*, "Molecular printboards on silicon oxide: Lithographic patterning of cyclodextrin monolayers with multivalent, fluorescent guest molecules", *Small*, Vol. 1, No. 2, pp. 242–253, 2005.

249. Zhang, Q., S. Slavin, M. W. Jones, A. J. Haddleton and D. M. Haddleton, "Terminal functional glycopolymers via a combination of catalytic chain transfer polymerisation (CCTP) followed by three consecutive click reactions", *Polymer Chemistry*, Vol. 3, No. 4, pp. 1016–1023, 2012.

250. Gu, H., K. Xu, C. Xu and B. Xu, "Biofunctional magnetic nanoparticles for protein separation and pathogen detection", *Chemical Communications*, , No. 9, pp. 941–949, 2006.

251. Bucak, S., D. A. Jones, P. E. Laibinis and T. A. Hatton, "Protein separations

using colloidal magnetic nanoparticles", *Biotechnology Progress*, Vol. 19, No. 2, pp. 477–484, 2003.

252. Liu, Z., M. Li, X. Yang, M. Yin, J. Ren and X. Qu, "The use of multifunctional magnetic mesoporous core/shell heteronanostructures in a biomolecule separation system", *Biomaterials*, Vol. 32, No. 21, pp. 4683–4690, 2011.

253. Zhang, Q., G. Nurumbetov, A. Simula, C. Zhu, M. Li, P. Wilson, K. Kempe, B. Yang, L. Tao and D. M. Haddleton, "Synthesis of well-defined catechol polymers for surface functionalization of magnetic nanoparticles", *Polymer Chemistry*, Vol. 7, No. 45, pp. 7002–7010, 2016.

254. Brubaker, C. E. and P. B. Messersmith, "The present and future of biologically inspired adhesive interfaces and materials", *Langmuir*, Vol. 28, No. 4, pp. 2200–2205, 2012.

255. Abdouni, Y., G. Yilmaz and C. R. Becer, "Sequence Controlled Polymers from a Novel β-Cyclodextrin Core", *Macromolecular Rapid Communications*, Vol. 38, No. 24, p. 1700501, 2017.

256. Boden, S., K. Wagner, M. Karg and L. Hartmann, "Presenting precision glycomacromolecules on gold nanoparticles for increased lectin binding", *Polymers*, Vol. 9, No. 12, p. 716, 2017.

257. Nikaido, H., "Multidrug resistance in bacteria", *Annual Review of Biochemistry*, Vol. 78, pp. 119–146, 2009.

258. O'Neil, J., "Review on antimicrobial resistance", *Antimicrobial Resistance: Tackling a Crisis for the Health and Wealth of Nations*, Vol. 2014, 2014.

259. Rabin, N., Y. Zheng, C. Opoku-Temeng, Y. Du, E. Bonsu and H. O. Sintim, "Biofilm formation mechanisms and targets for developing antibiofilm agents", *Future Medicinal Chemistry*, Vol. 7, No. 4, pp. 493–512, 2015.

260. Sanchez, C. J., K. Mende, M. L. Beckius, K. S. Akers, D. R. Romano, J. C. Wenke and C. K. Murray, "Biofilm formation by clinical isolates and the implications in chronic infections", *BMC Infectious Diseases*, Vol. 13, No. 1, p. 47, 2013.

261. Donlan, R. M., "Biofilms: Microbial life on surfaces", *Emerging Infectious Diseases*, Vol. 8, No. 9, p. 881, 2002.

262. Zhao, G., M. L. Usui, S. I. Lippman, G. A. James, P. S. Stewart, P. Fleckman and J. E. Olerud, "Biofilms and inflammation in chronic wounds", *Advances in Wound Care*, Vol. 2, No. 7, pp. 389–399, 2013.

263. Wu, H., C. Moser, H.-Z. Wang, N. Høiby and Z.-J. Song, "Strategies for combating bacterial biofilm infections", *International Journal of Oral Science*, Vol. 7, No. 1, p. 1, 2015.

264. Lebeaux, D., J.-M. Ghigo and C. Beloin, "Biofilm-related infections: Bridging the gap between clinical management and fundamental aspects of recalcitrance toward antibiotics", *Microbiol. Mol. Biol. Rev.*, Vol. 78, No. 3, pp. 510–543, 2014.

265. Römling, U. and C. Balsalobre, "Biofilm infections, their resilience to therapy and innovative treatment strategies", *Journal of Internal Medicine*, Vol. 272, No. 6, pp. 541–561, 2012.

266. Høiby, N., T. Bjarnsholt, M. Givskov, S. Molin and O. Ciofu, "Antibiotic resistance of bacterial biofilms", *International Journal of Antimicrobial Agents*, Vol. 35, No. 4, pp. 322–332, 2010.

267. Khatoon, Z., C. D. McTiernan, E. J. Suuronen, T.-F. Mah and E. I. Alarcon, "Bacterial biofilm formation on implantable devices and approaches to its treatment and prevention", *Heliyon*, Vol. 4, No. 12, p. e01067, 2018.

268. Kerekes, E. B., A. Vidács, M. Takó, T. Petkovits, C. Vágvölgyi, G. Horváth, V. L. Balázs and J. Krisch, "Anti-biofilm effect of selected essential oils and main com-

ponents on mono- and polymicrobic bacterial cultures", *Microorganisms*, Vol. 7, No. 9, p. 345, 2019.

269. Kalemba, D. and A. Kunicka, "Antibacterial and antifungal properties of essential oils", *Current Medicinal Chemistry*, Vol. 10, No. 10, pp. 813–829, 2003.

270. Nostro, A., A. S. Roccaro, G. Bisignano, A. Marino, M. A. Cannatelli, F. C. Pizzimenti, P. L. Cioni, F. Procopio and A. R. Blanco, "Effects of oregano, carvacrol and thymol on Staphylococcus aureus and Staphylococcus epidermidis biofilms", *Journal of Medical Microbiology*, Vol. 56, No. 4, pp. 519–523, 2007.

271. Swamy, M. K., M. S. Akhtar and U. R. Sinniah, "Antimicrobial properties of plant essential oils against human pathogens and their mode of action: An updated review", *Evidence-Based Complementary and Alternative Medicine*, Vol. 2016, 2016.

272. Chen, H., P. M. Davidson and Q. Zhong, "Impacts of sample preparation methods on solubility and antilisterial characteristics of essential oil components in milk", *Applied and Environmental Microbiology*, Vol. 80, No. 3, pp. 907–916, 2014.

273. Chang, Y., L. McLandsborough and D. J. McClements, "Physicochemical properties and antimicrobial efficacy of carvacrol nanoemulsions formed by spontaneous emulsification", *Journal of Agricultural and Food Chemistry*, Vol. 61, No. 37, pp. 8906–8913, 2013.

274. Zhu, D. Y., R. F. Landis, C.-H. Li, A. Gupta, L.-S. Wang, Y. Geng, S. Gopalakrishnan, J. W. Guo and V. M. Rotello, "Dynamically crosslinked polymer nanocomposites to treat multidrug-resistant bacterial biofilms", *Nanoscale*, Vol. 10, No. 39, pp. 18651–18656, 2018.

275. Duncan, B., X. Li, R. F. Landis, S. T. Kim, A. Gupta, L.-S. Wang, R. Ramanathan, R. Tang, J. A. Boerth and V. M. Rotello, "Nanoparticle-stabilized

capsules for the treatment of bacterial biofilms", *Acs Nano*, Vol. 9, No. 8, pp. 7775–7782, 2015.

276. Landis, R. F., C.-H. Li, A. Gupta, Y.-W. Lee, M. Yazdani, N. Ngernyuang, I. Altinbasak, S. Mansoor, M. A. Khichi, A. Sanyal *et al.*, "Biodegradable nanocomposite antimicrobials for the eradication of multidrug-resistant bacterial biofilms without accumulated resistance", *Journal of the American Chemical Society*, Vol. 140, No. 19, pp. 6176–6182, 2018.

277. Kamaly, N., B. Yameen, J. Wu and O. C. Farokhzad, "Degradable controlled-release polymers and polymeric nanoparticles: Mechanisms of controlling drug release", *Chemical Reviews*, Vol. 116, No. 4, pp. 2602–2663, 2016.

278. Liechty, W. B., D. R. Kryscio, B. V. Slaughter and N. A. Peppas, "Polymers for drug delivery systems", *Annual Review of Chemical and Biomolecular Engineering*, Vol. 1, pp. 149–173, 2010.

279. Singhvi, M., S. Zinjarde and D. Gokhale, "Polylactic acid: Synthesis and biomedical applications", *Journal of Applied Microbiology*, Vol. 127, No. 6, pp. 1612–1626, 2019.

280. Rancan, F., D. Papakostas, S. Hadam, S. Hackbarth, T. Delair, C. Primard, B. Verrier, W. Sterry, U. Blume-Peytavi and A. Vogt, "Investigation of polylactic acid (PLA) nanoparticles as drug delivery systems for local dermatotherapy", *Pharmaceutical Research*, Vol. 26, No. 8, pp. 2027–2036, 2009.

281. da Silva, D., M. Kaduri, M. Poley, O. Adir, N. Krinsky, J. Shainsky-Roitman and A. Schroeder, "Biocompatibility, biodegradation and excretion of polylactic acid (PLA) in medical implants and theranostic systems", *Chemical Engineering Journal*, Vol. 340, pp. 9–14, 2018.

282. de Tayrac, R., S. Chentouf, H. Garreau, C. Braud, I. Guiraud, P. Boudeville

and M. Vert, "In vitro degradation and in vivo biocompatibility of poly (lactic acid) mesh for soft tissue reinforcement in vaginal surgery", *Journal of Biomedical Materials Research Part B: Applied Biomaterials*, Vol. 85, No. 2, pp. 529–536, 2008.

283. Baldwin, A. D. and K. L. Kiick, "Tunable degradation of maleimide–thiol adducts in reducing environments", *Bioconjugate Chemistry*, Vol. 22, No. 10, pp. 1946–1953, 2011.

284. Oz, Y. and A. Sanyal, "The taming of the maleimide: Fabrication of maleimide-containing 'clickable' polymeric materials", *The Chemical Record*, Vol. 18, No. 6, pp. 570–586, 2018.

285. Yamashita, K., Y. Kikkawa, K. Kurokawa and Y. Doi, "Enzymatic degradation of poly (L-lactide) film by proteinase K: Quartz crystal microbalance and atomic force microscopy study", *Biomacromolecules*, Vol. 6, No. 2, pp. 850–857, 2005.

286. Miranda, O. R., H.-T. Chen, C.-C. You, D. E. Mortenson, X.-C. Yang, U. H. Bunz and V. M. Rotello, "Enzyme-amplified array sensing of proteins in solution and in biofluids", *Journal of the American Chemical Society*, Vol. 132, No. 14, pp. 5285–5289, 2010.

287. Onbulak, S., S. Tempelaar, R. J. Pounder, O. Gok, R. Sanyal, A. P. Dove and A. Sanyal, "Synthesis and functionalization of thiol-reactive biodegradable polymers", *Macromolecules*, Vol. 45, No. 3, pp. 1715–1722, 2012.

288. Li, X., Y.-C. Yeh, K. Giri, R. Mout, R. F. Landis, Y. Prakash and V. M. Rotello, "Control of nanoparticle penetration into biofilms through surface design", *Chemical Communications*, Vol. 51, No. 2, pp. 282–285, 2015.

289. Creran, B., X. Li, B. Duncan, C. S. Kim, D. F. Moyano and V. M. Rotello, "Detection of bacteria using inkjet-printed enzymatic test strips", *ACS Applied*

Materials & Interfaces, Vol. 6, No. 22, pp. 19525–19530, 2014.

290. Lazzari, S., D. Moscatelli, F. Codari, M. Salmona, M. Morbidelli and L. Diomede, "Colloidal stability of polymeric nanoparticles in biological fluids", *Journal of Nanoparticle Research*, Vol. 14, No. 6, p. 920, 2012.

291. Kataoka, K., A. Harada and Y. Nagasaki, "Block copolymer micelles for drug delivery: Design, characterization and biological significance", *Advanced Drug Delivery Reviews*, Vol. 64, pp. 37–48, 2012.

292. Samarajeewa, S., R. Shrestha, Y. Li and K. L. Wooley, "Degradability of poly (lactic acid)-containing nanoparticles: Enzymatic access through a cross-linked shell barrier", *Journal of the American Chemical Society*, Vol. 134, No. 2, pp. 1235–1242, 2012.

293. Stewart, P. S., "Antimicrobial tolerance in biofilms", *Microbial Biofilms*, pp. 269–285, 2015.

294. Samperio, C., R. Boyer, W. N. Eigel III, K. W. Holland, J. S. McKinney, S. F. O'Keefe, R. Smith and J. E. Marcy, "Enhancement of plant essential oils' aqueous solubility and stability using alpha and beta cyclodextrin", *Journal of Agricultural and Food Chemistry*, Vol. 58, No. 24, pp. 12950–12956, 2010.

295. Bilia, A. R., C. Guccione, B. Isacchi, C. Righeschi, F. Firenzuoli and M. C. Bergonzi, "Essential oils loaded in nanosystems: A developing strategy for a successful therapeutic approach", *Evidence-Based Complementary and Alternative Medicine*, Vol. 2014, 2014.

296. Sharma, G., S. Sharma, P. Sharma, D. Chandola, S. Dang, S. Gupta and R. Gabrani, "Escherichia coli biofilm: development and therapeutic strategies", *Journal of Applied Microbiology*, Vol. 121, No. 2, pp. 309–319, 2016.

297. Neopane, P., H. P. Nepal, R. Shrestha, O. Uehara and Y. Abiko, "In vitro biofilm

formation by Staphylococcus aureus isolated from wounds of hospital-admitted patients and their association with antimicrobial resistance", *International Journal of General Medicine*, Vol. 11, p. 25, 2018.

298. Dallo, S. F. and T. Weitao, "Insights into acinetobacter war-wound infections, biofilms, and control", *Advances in Skin & Wound Care*, Vol. 23, No. 4, pp. 169–174, 2010.

299. Metcalf, D. G. and P. G. Bowler, "Biofilm delays wound healing: A review of the evidence", *Burns & Trauma*, Vol. 1, No. 1, pp. 5–12, 2013.

300. Tracy, L. E., R. A. Minasian and E. Caterson, "Extracellular matrix and dermal fibroblast function in the healing wound", *Advances in Wound Care*, Vol. 5, No. 3, pp. 119–136, 2016.

APPENDIX A: SUPPLEMENTARY DATA

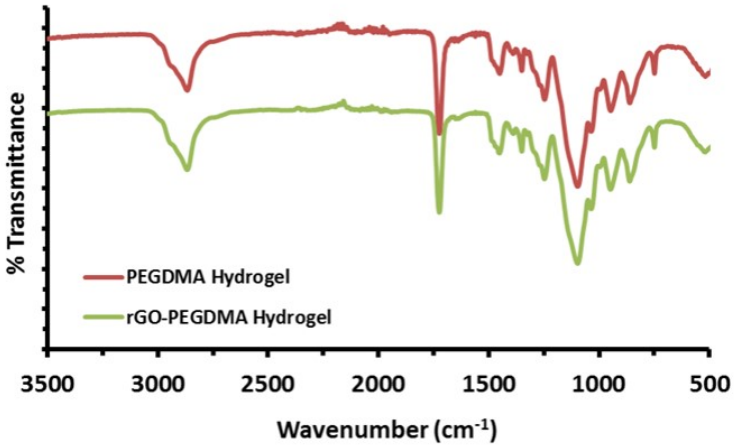

Figure A.1. FT-IR spectra of PEGDMA (red) and rGO-PEGDMA (green) hydrogels.

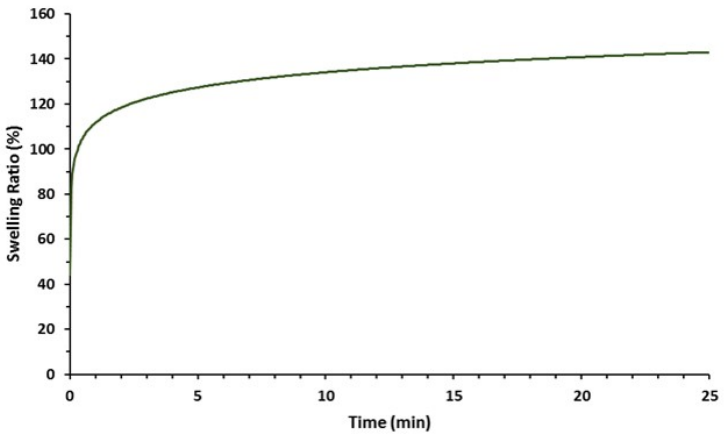

Figure A.2. Water uptake profile of rGO-PEGDMA hydrogel at pH 7.0.

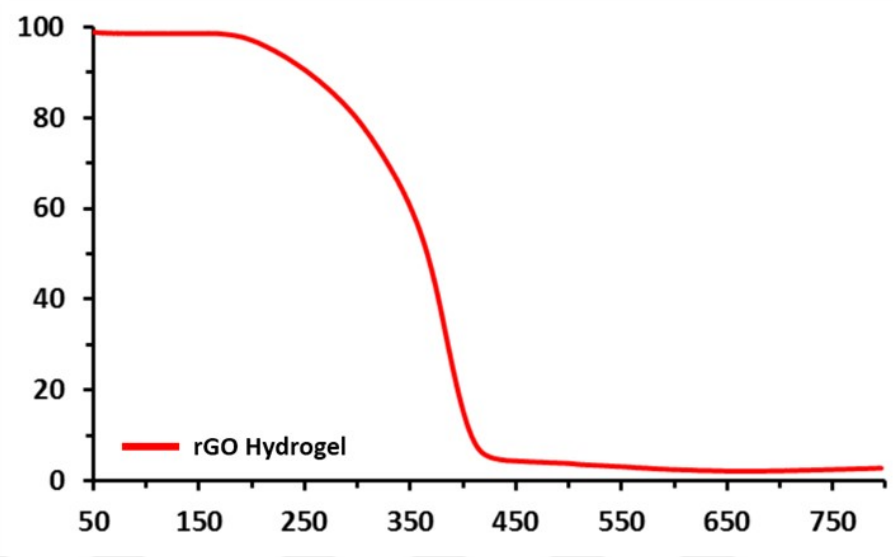

Figure A.3. TGA curve of PEGDMA-rGO (0.8 mg) based hydrogel.

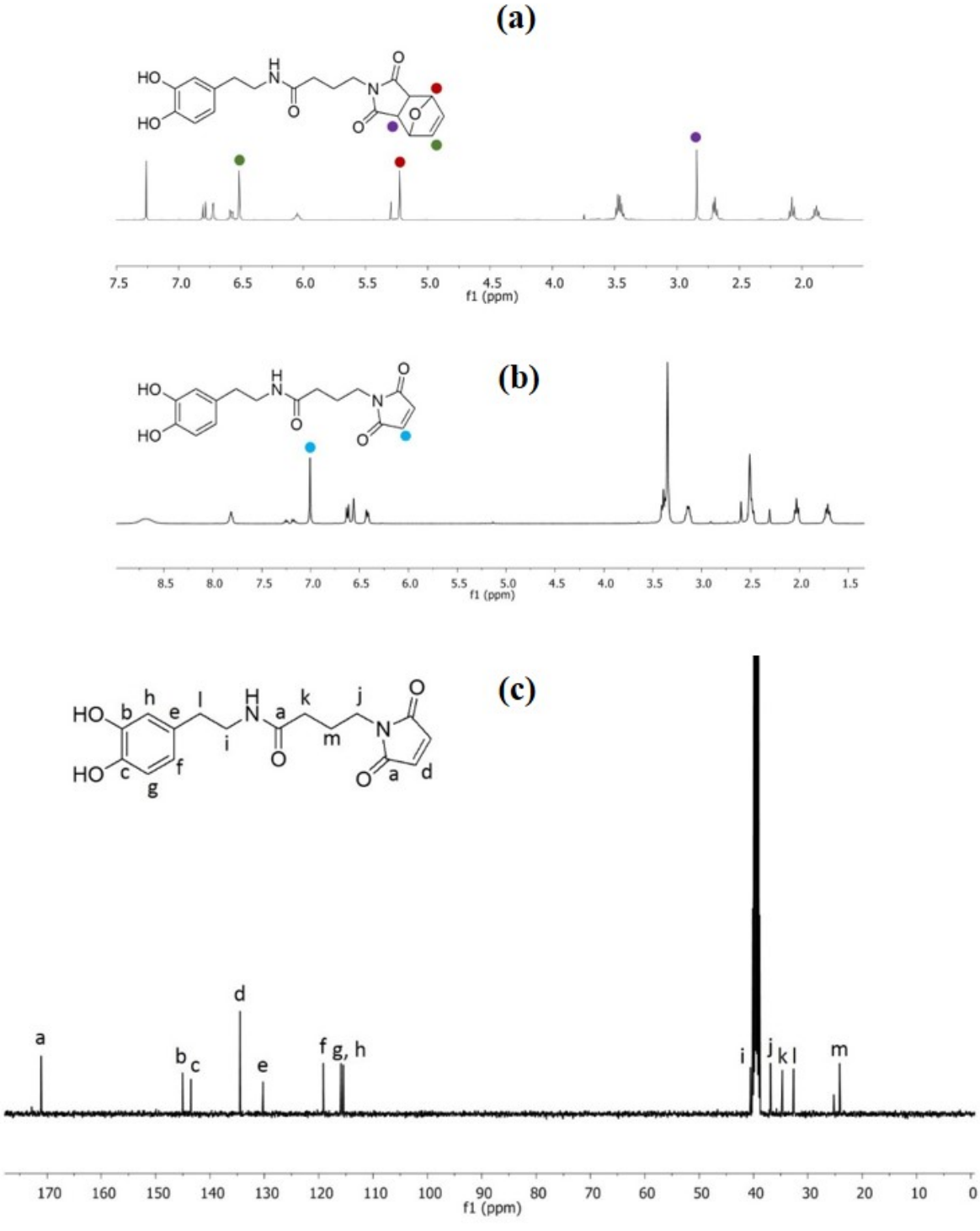

Figure A.4. (a) ^{1}H-NMR spectrum of Dopa-pMAL in $CDCl_3$, (b) ^{1}H-NMR spectrum of Dopa-MAL in $(CD_3)_2SO$ and (c) ^{13}C-NMR spectrum of Dopa-MAL in $(CD_3)_2SO$.

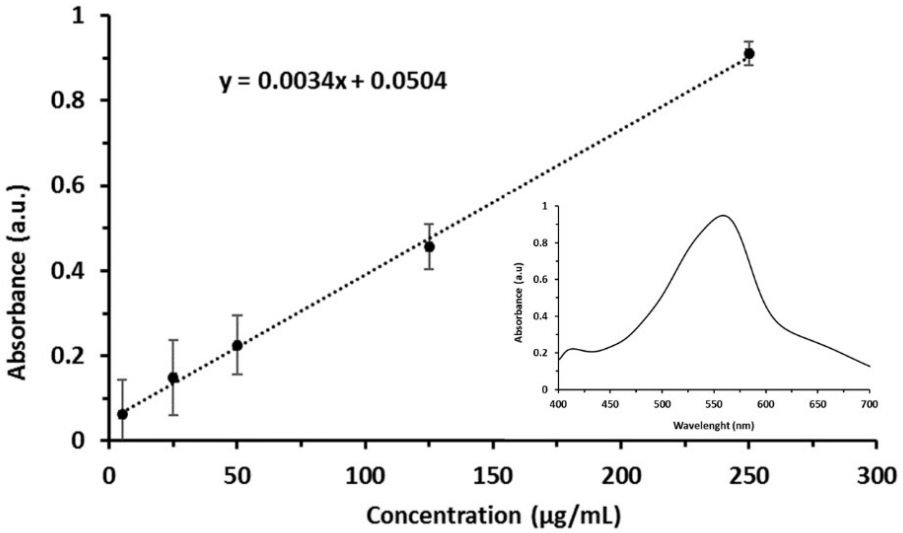

Figure A.5. Calibration curve of standard peptide solutions based on UV absorbance values at 562 nm and UV-Vis spectrum of rGO/dopa-MAL-c(RGDfC) (inset).

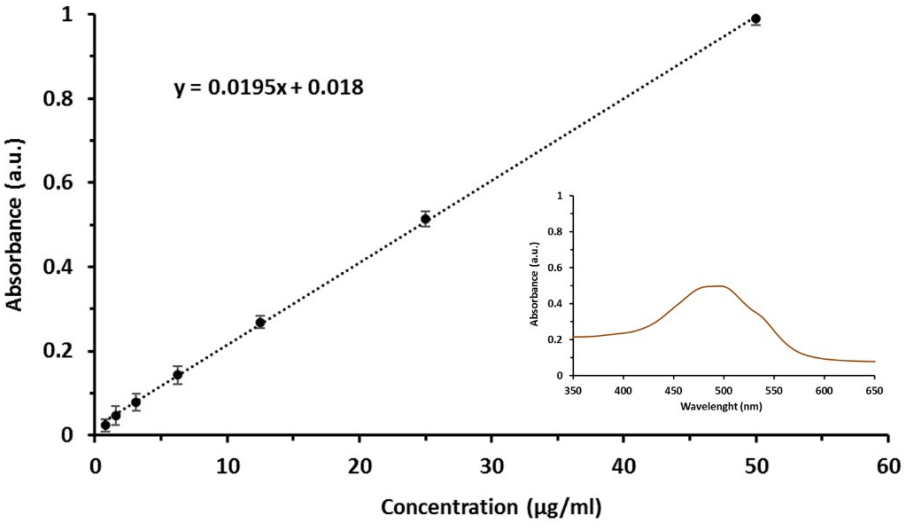

Figure A.6. Doxorubicin calibration curve and UV-Vis spectrum of diluted supernatant after doxorubicin loading onto rGO/dopa-MAL-c(RGDfC) (inset).

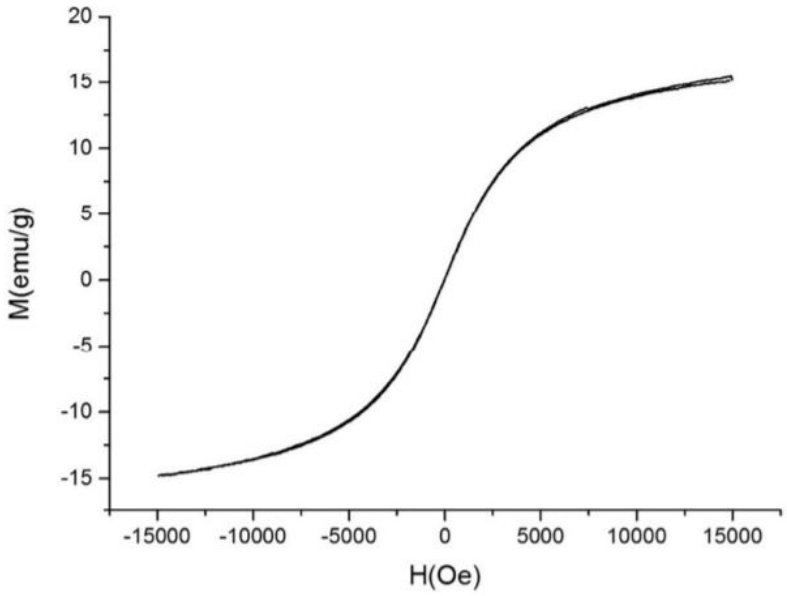

Figure A.7. Field dependent magnetization curve of Fe_3O_4@OA MNPs.

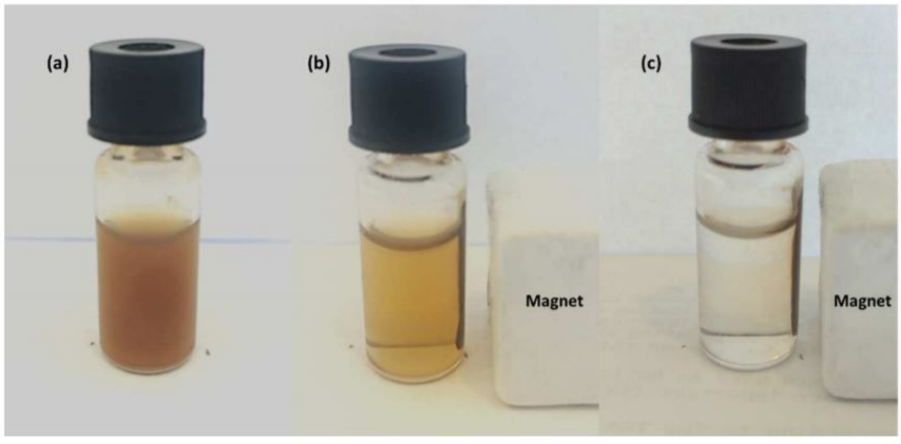

Figure A.8. Images of Fe_3O_4@PEGMEA MNPs in dilute water dispersion (a) without permanent magnet attraction, (b) with attraction <10 min and (c) 12 h magnet attraction.

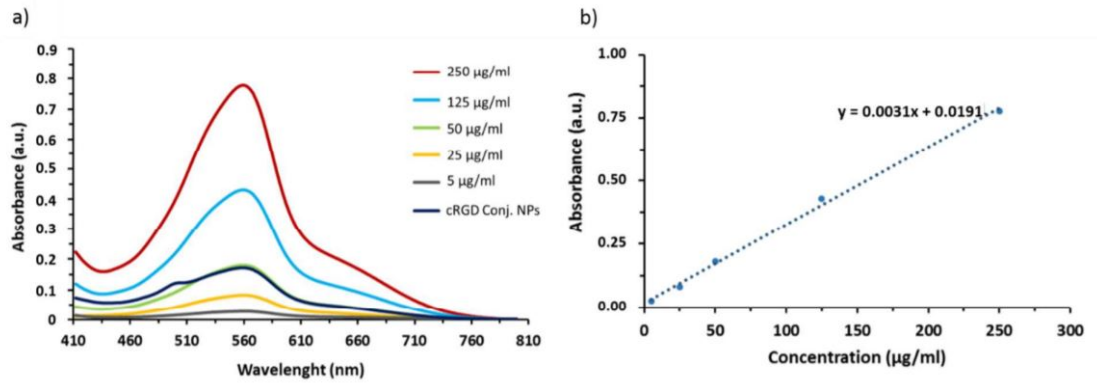

Figure A.9. (a) UV-vis spectrum of BCA assay standards and cRGD conjugated MNPs (b) BCA assay calibration curve.

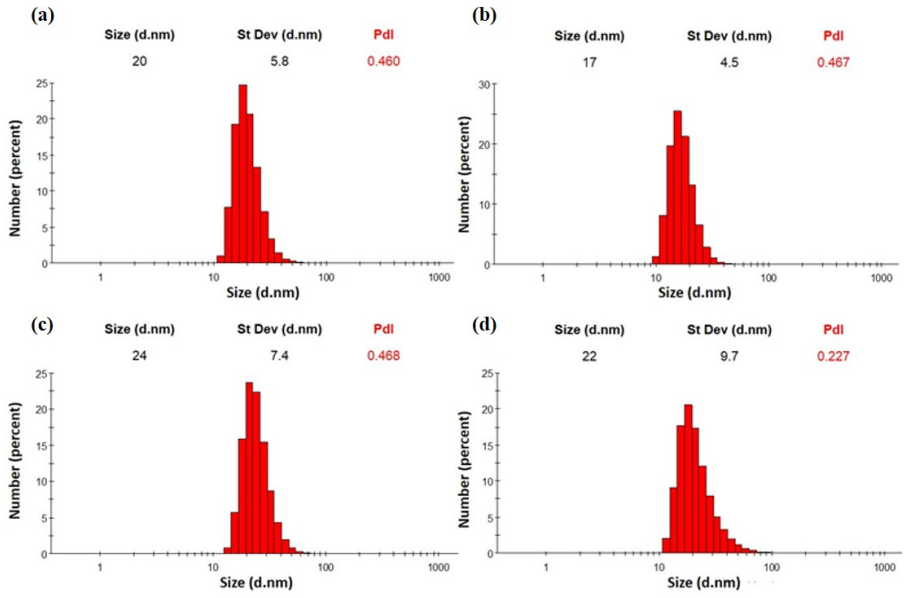

Figure A.10. DLS measurements of magnetic NPs (a) Fe_3O_4@OA, (b) Fe_3O_4@CTA, (c) Fe_3O_4@PEG and (d) Fe_3O_4@PEG@AD NPs.

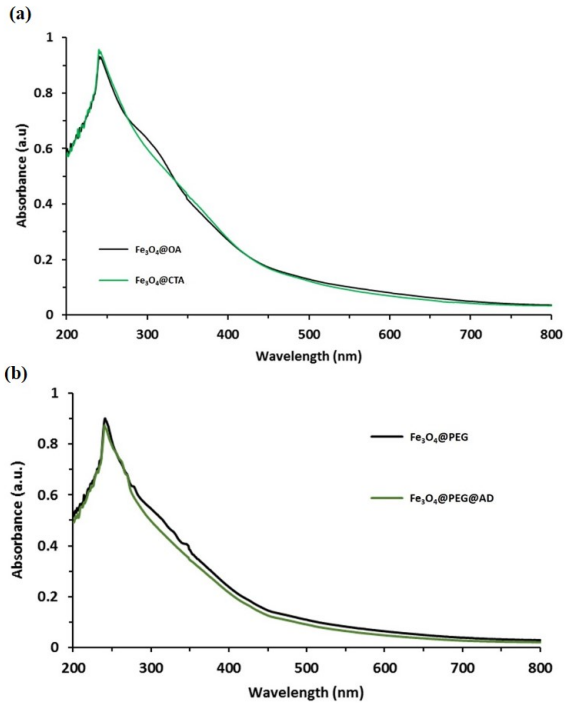

Figure A.11. UV visible spectra of (a) Fe_3O_4@OA and Fe_3O_4@CTA, (b) Fe_3O_4@PEG and Fe_3O_4@PEG@AD.

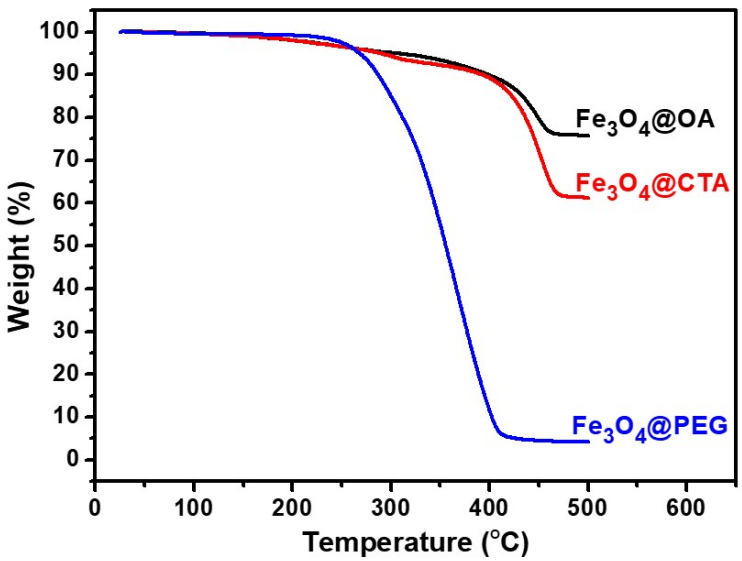

Figure A.12. TGA measuremants of OA, CTA and PEG polymer coated MNPs.

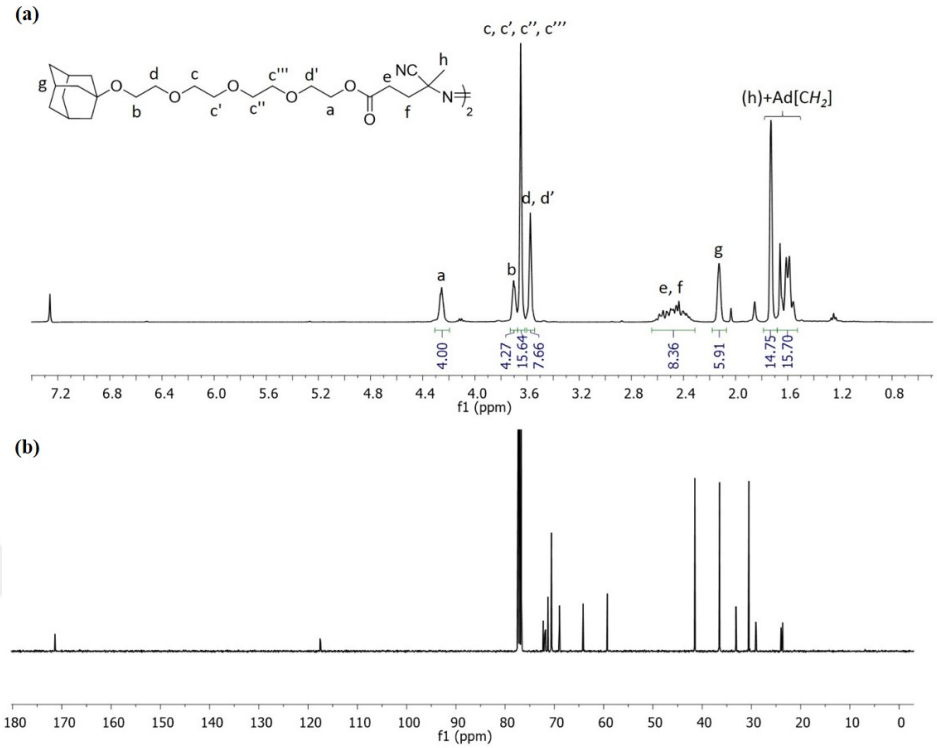

Figure A.13. (a) ^{1}H-NMR and (b) ^{13}C-NMR spectrum of azobis-ADA initiator.

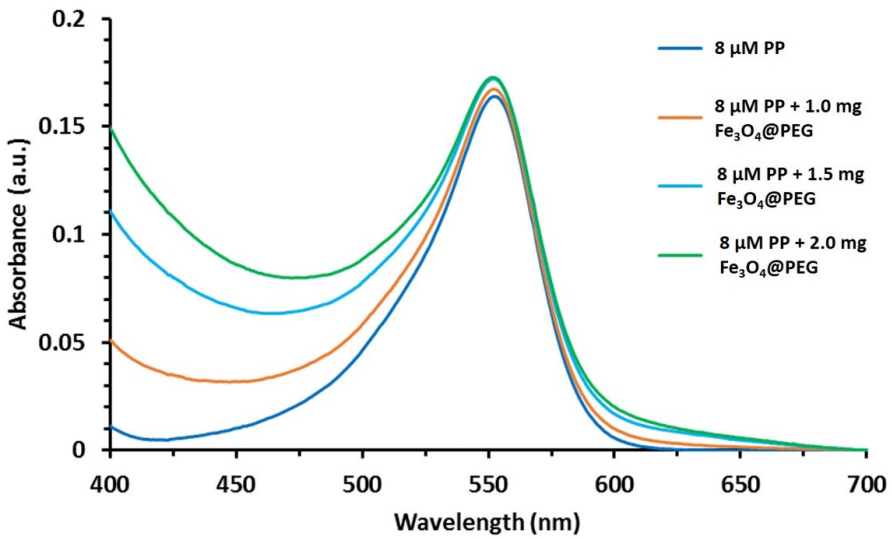

Figure A.14. UV-vis spectra of 8 μM PP solutions at pH = 10.2 after addition of varying amounts of Fe_3O_4@PEG MNPs.

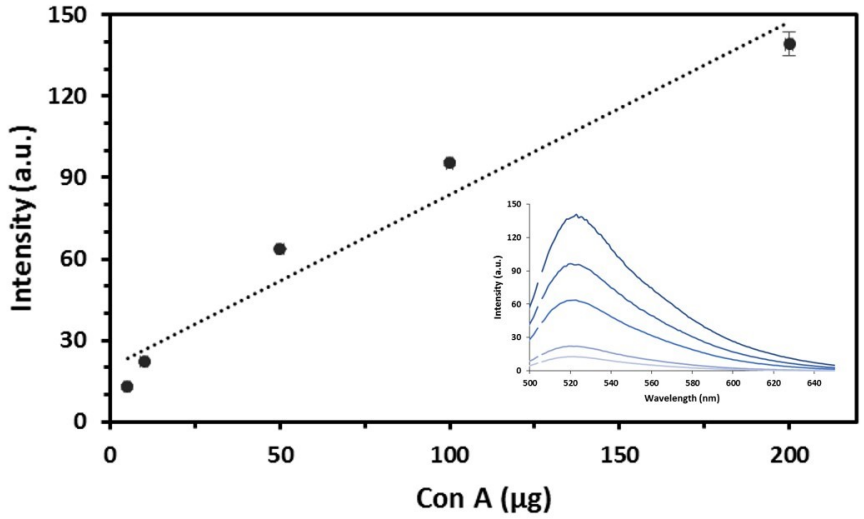

Figure A.15. Calibration curve of FITC-labelled ConA using fluorescence spectroscopy.

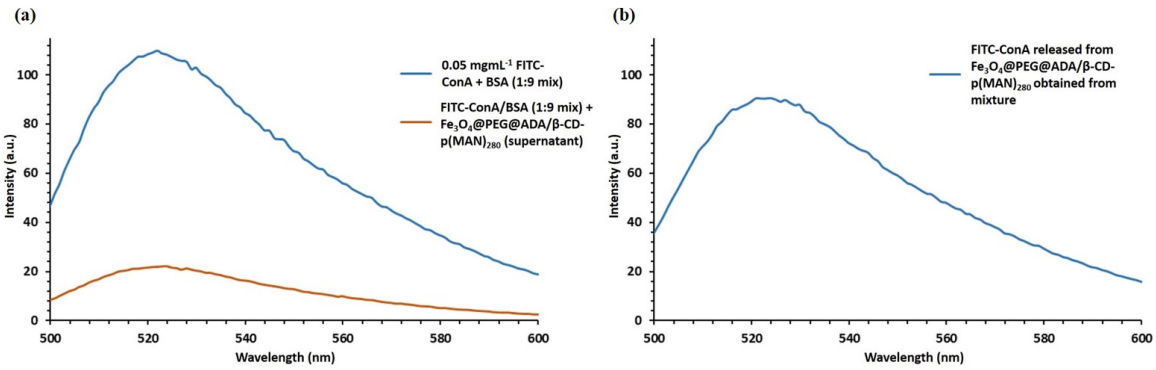

Figure A.16. Fluorescence spectra of (a) FITC-ConA/BSA mixture solution and supernatant after treatment with Fe_3O_4@PEG@ADA/β-CD-p$(MAN)_{280}$ MNPs, and (b) released ConA.

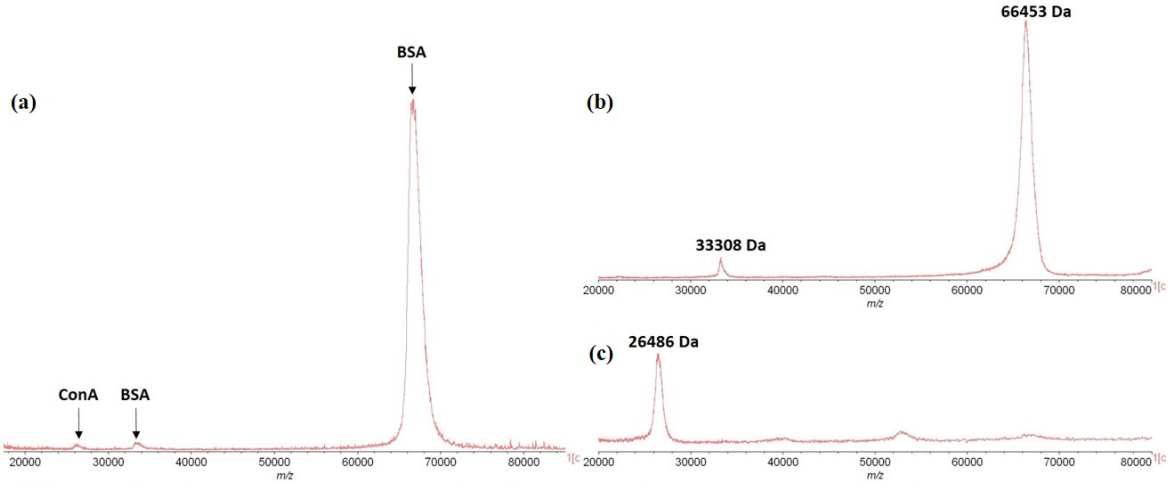

Figure A.17. MALDI-TOF mass spectra of (a) the BSA/ConA mixture (9 : 1), (b) residual BSA in the supernatant after magnetic separation and (c) ConA recovered from MNPs ConA-BSA mixture.

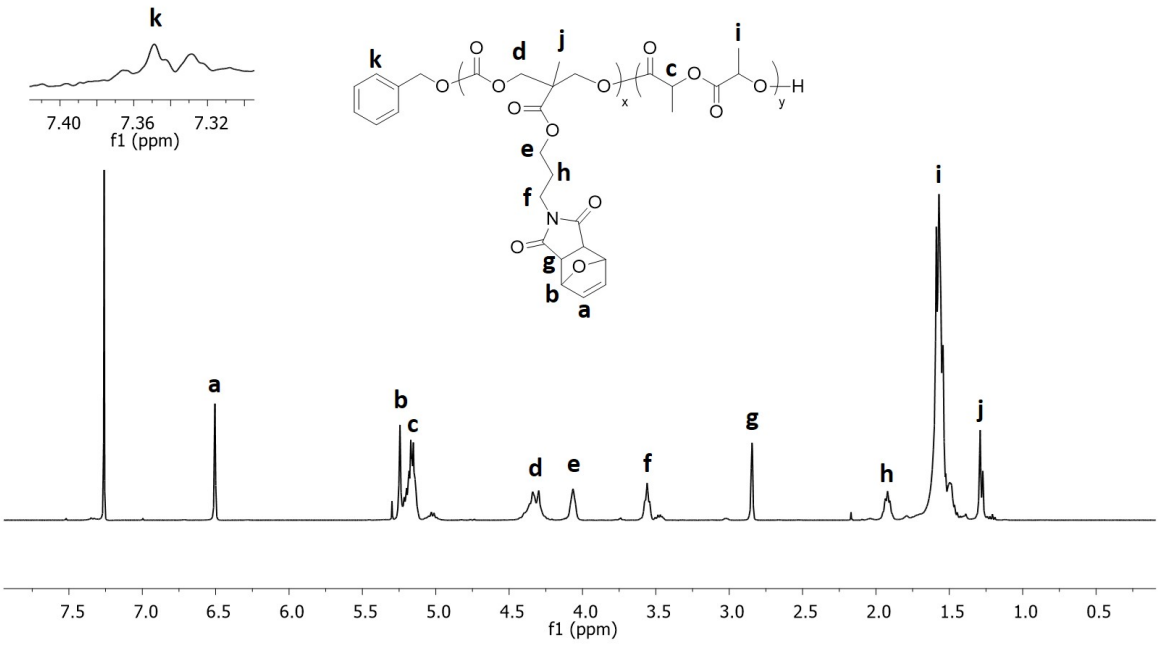

Figure A.18. ^{1}H-NMR spectrum of protected maleimide containing PLA polymer (pMA-PLA).

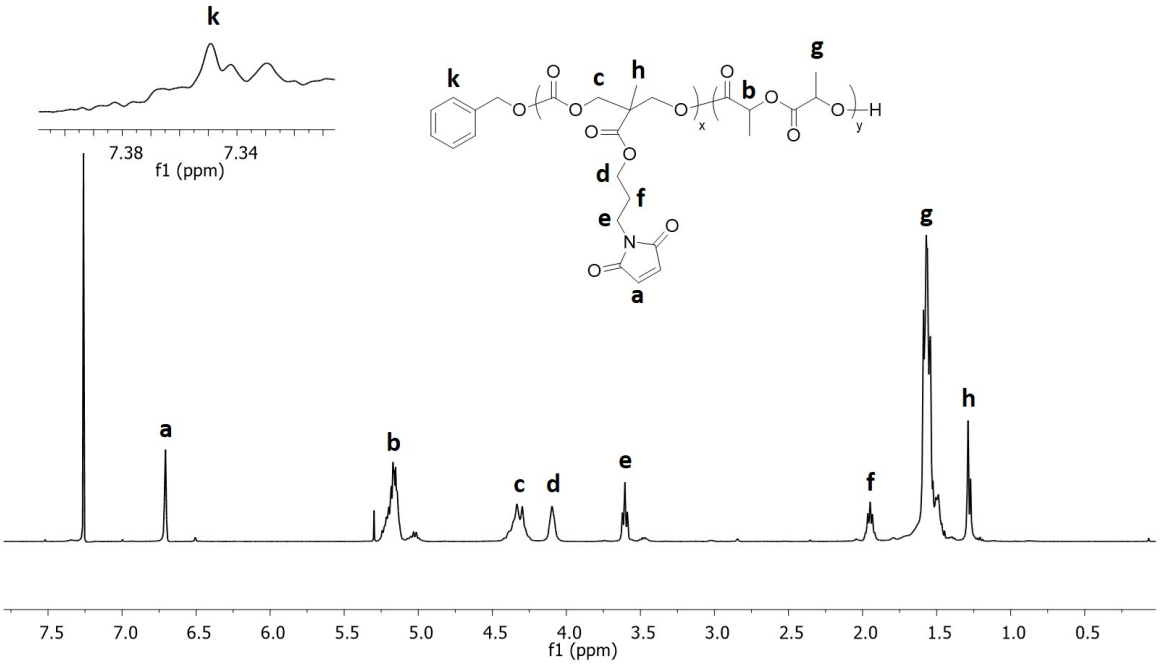

Figure A.19. ^{1}H-NMR spectrum of maleimide containing PLA polymer (MA-PLA).

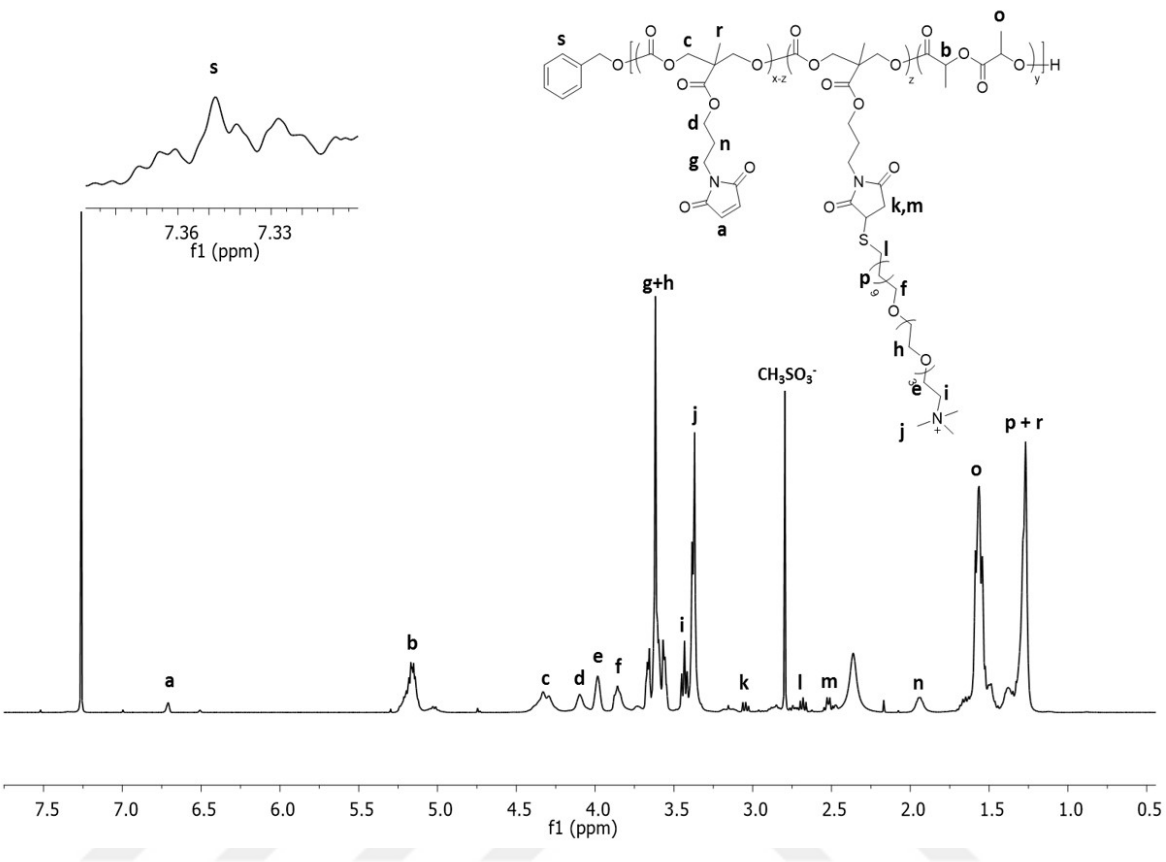

Figure A.20. ^{1}H-NMR spectrum of TTMA attached maleimide functional polymer (TT-MA-PLA).

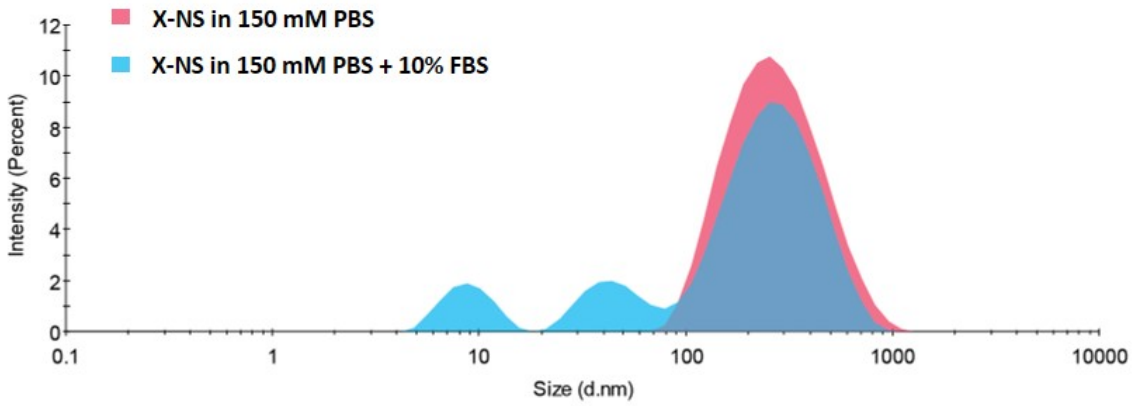

Figure A.21. Stability evaluation of X-NS in 10 % FBS solution for 24 h.

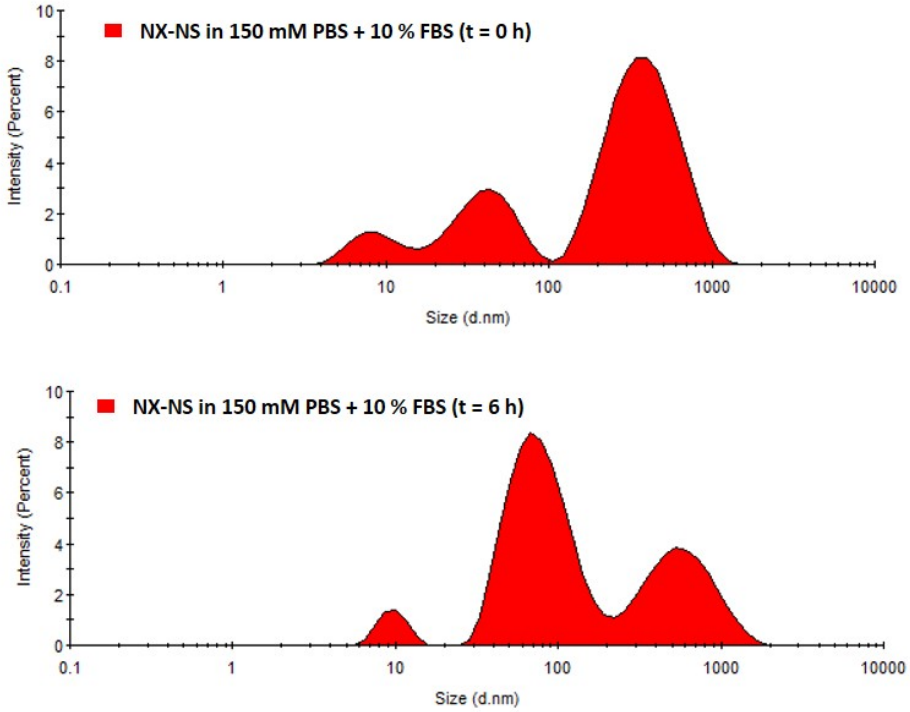

Figure A.22. Stability evaluation of NX-NS in 10 % FBS solution for 6 h.

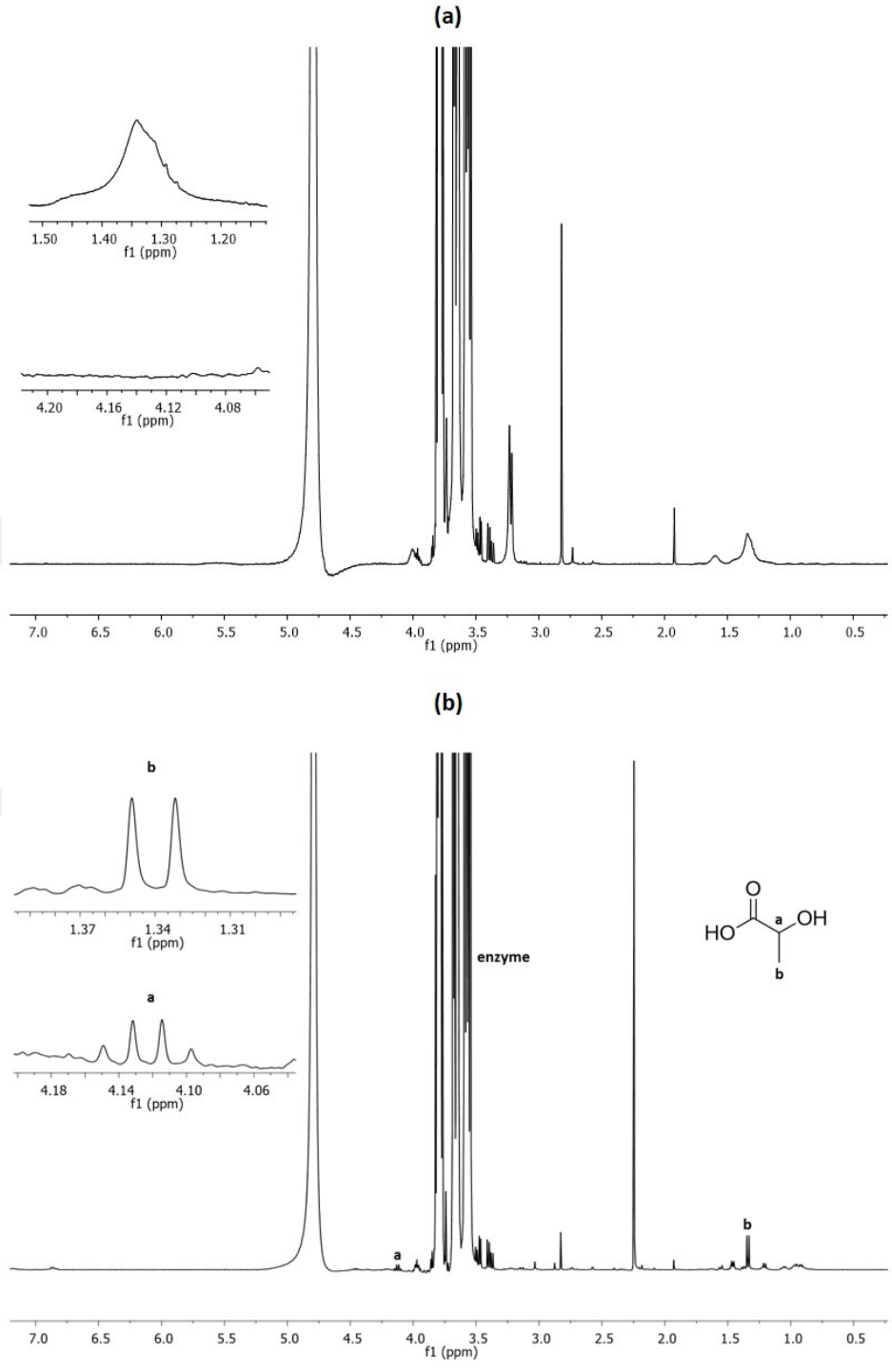

Figure A.23. ^{1}H-NMR spectra of (a) TT-MA-PLA polymer in deuterated PBS with proteinase K enzyme (t = 0 h) and (b) biodegraded X-NS in deuterated PBS after proteinase K addition (t = 48 h).

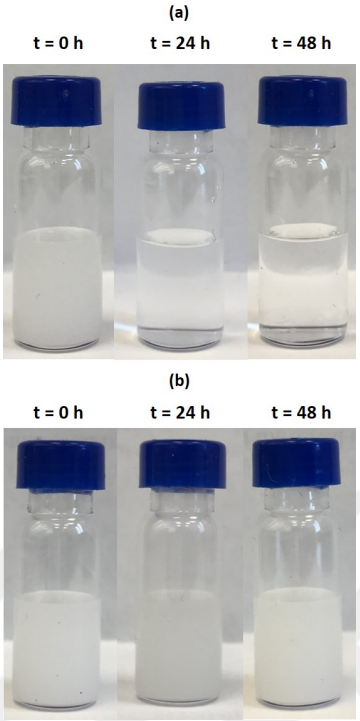

Figure A.24. (a) Degradation of X-NS with proteinase K enzyme (6.9 μM) in PBS solution (t = 0, 24 and 48 h) and (b) stability of X-NS in the absence of proteinase K enzyme (t = 0, 24 and 48 h) as a control.

APPENDIX B: COPYRIGHT NOTICES

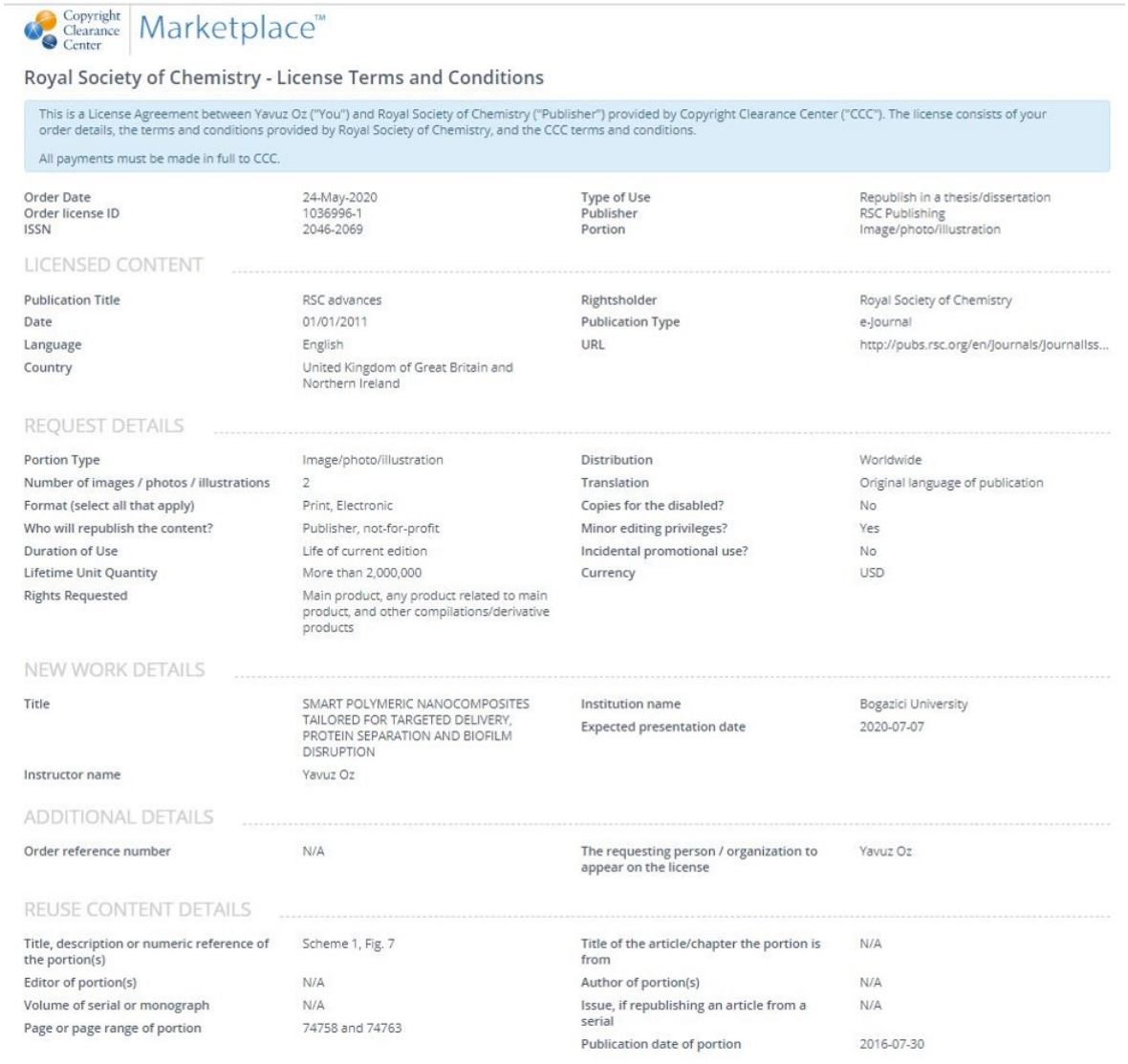

Copyright Clearance Center Marketplace™

Royal Society of Chemistry - License Terms and Conditions

This is a License Agreement between Yavuz Oz ("You") and Royal Society of Chemistry ("Publisher") provided by Copyright Clearance Center ("CCC"). The license consists of your order details, the terms and conditions provided by Royal Society of Chemistry, and the CCC terms and conditions.

All payments must be made in full to CCC.

Order Date	24-May-2020	Type of Use	Republish in a thesis/dissertation
Order license ID	1036996-1	Publisher	RSC Publishing
ISSN	2046-2069	Portion	Image/photo/illustration

LICENSED CONTENT

Publication Title	RSC advances	Rightsholder	Royal Society of Chemistry
Date	01/01/2011	Publication Type	e-Journal
Language	English	URL	http://pubs.rsc.org/en/Journals/JournalIss...
Country	United Kingdom of Great Britain and Northern Ireland		

REQUEST DETAILS

Portion Type	Image/photo/illustration	Distribution	Worldwide
Number of images / photos / illustrations	2	Translation	Original language of publication
Format (select all that apply)	Print, Electronic	Copies for the disabled?	No
Who will republish the content?	Publisher, not-for-profit	Minor editing privileges?	Yes
Duration of Use	Life of current edition	Incidental promotional use?	No
Lifetime Unit Quantity	More than 2,000,000	Currency	USD
Rights Requested	Main product, any product related to main product, and other compilations/derivative products		

NEW WORK DETAILS

Title	SMART POLYMERIC NANOCOMPOSITES TAILORED FOR TARGETED DELIVERY, PROTEIN SEPARATION AND BIOFILM DISRUPTION	Institution name	Bogazici University
		Expected presentation date	2020-07-07
Instructor name	Yavuz Oz		

ADDITIONAL DETAILS

Order reference number	N/A	The requesting person / organization to appear on the license	Yavuz Oz

REUSE CONTENT DETAILS

Title, description or numeric reference of the portion(s)	Scheme 1, Fig. 7	Title of the article/chapter the portion is from	N/A
Editor of portion(s)	N/A	Author of portion(s)	N/A
Volume of serial or monograph	N/A	Issue, if republishing an article from a serial	N/A
Page or page range of portion	74758 and 74763	Publication date of portion	2016-07-30

Figure B.1. Permission for Figure 1.2 from Ref. [24]

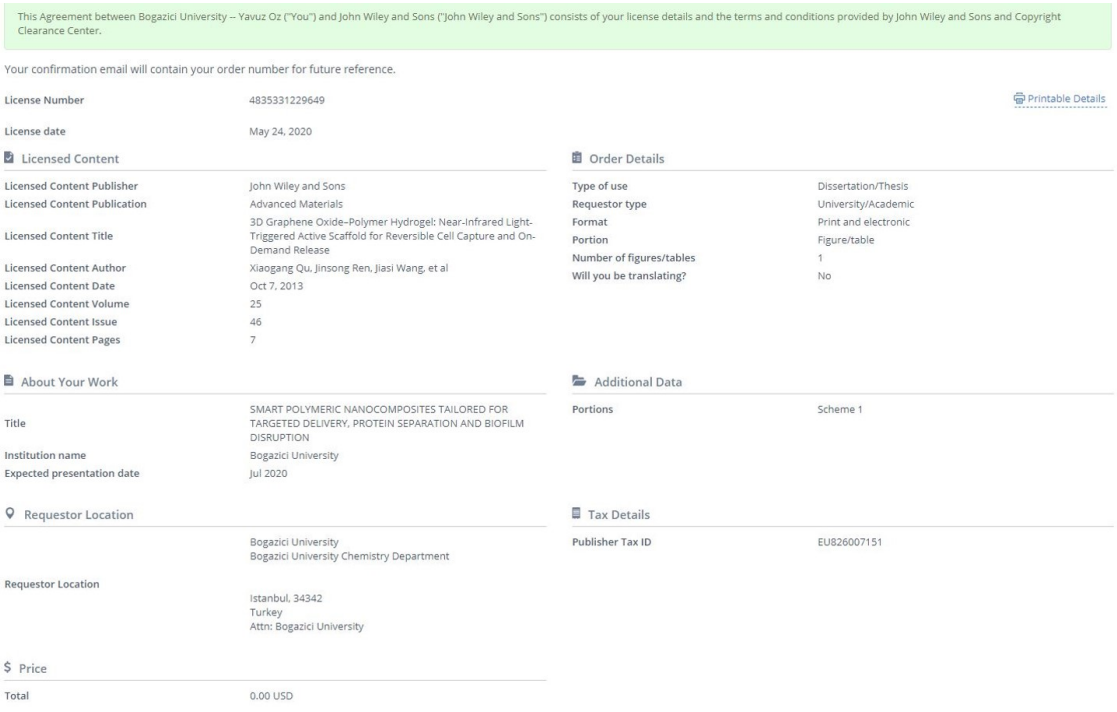

This Agreement between Bogazici University -- Yavuz Oz ("You") and John Wiley and Sons ("John Wiley and Sons") consists of your license details and the terms and conditions provided by John Wiley and Sons and Copyright Clearance Center.

Your confirmation email will contain your order number for future reference.

Printable Details

License Number	4835331229649
License date	May 24, 2020

Licensed Content

Licensed Content Publisher	John Wiley and Sons
Licensed Content Publication	Advanced Materials
Licensed Content Title	3D Graphene Oxide–Polymer Hydrogel: Near-Infrared Light-Triggered Active Scaffold for Reversible Cell Capture and On-Demand Release
Licensed Content Author	Xiaogang Qu, Jinsong Ren, Jiasi Wang, et al
Licensed Content Date	Oct 7, 2013
Licensed Content Volume	25
Licensed Content Issue	46
Licensed Content Pages	7

Order Details

Type of use	Dissertation/Thesis
Requestor type	University/Academic
Format	Print and electronic
Portion	Figure/table
Number of figures/tables	1
Will you be translating?	No

About Your Work

Title	SMART POLYMERIC NANOCOMPOSITES TAILORED FOR TARGETED DELIVERY, PROTEIN SEPARATION AND BIOFILM DISRUPTION
Institution name	Bogazici University
Expected presentation date	Jul 2020

Additional Data

Portions	Scheme 1

Requestor Location

Bogazici University
Bogazici University Chemistry Department

Requestor Location

Istanbul, 34342
Turkey
Attn: Bogazici University

Tax Details

Publisher Tax ID	EU826007151

Price

Total	0.00 USD

Figure B.2. Permission for Figure 1.3 from Ref. [33]



ACS Publications
Most Trusted. Most Cited. Most Read.

Interplay between Molecular Packing, Drug Loading, and Core Cross-Linking in Bottlebrush Copolymer Micelles

Author: Hande Unsal, Sebla Onbulak, Filiz Calik, et al

Publication: Macromolecules

Publisher: American Chemical Society

Date: Feb 1, 2017

Copyright © 2017, American Chemical Society

PERMISSION/LICENSE IS GRANTED FOR YOUR ORDER AT NO CHARGE

This type of permission/license, instead of the standard Terms & Conditions, is sent to you because no fee is being charged for your order. Please note the following:

- Permission is granted for your request in both print and electronic formats, and translations.
- If figures and/or tables were requested, they may be adapted or used in part.
- Please print this page for your records and send a copy of it to your publisher/graduate school.
- Appropriate credit for the requested material should be given as follows: "Reprinted (adapted) with permission from (COMPLETE REFERENCE CITATION). Copyright (YEAR) American Chemical Society." Insert appropriate information in place of the capitalized words.
- One-time permission is granted only for the use specified in your request. No additional uses are granted (such as derivative works or other editions). For any other uses, please submit a new request.

If credit is given to another source for the material you requested, permission must be obtained from that source.

BACK CLOSE WINDOW

Figure B.3. Permission for Figure 1.4 from Ref. [35]



Figure B.4. Permission for Figure 1.5 from Ref. [45]

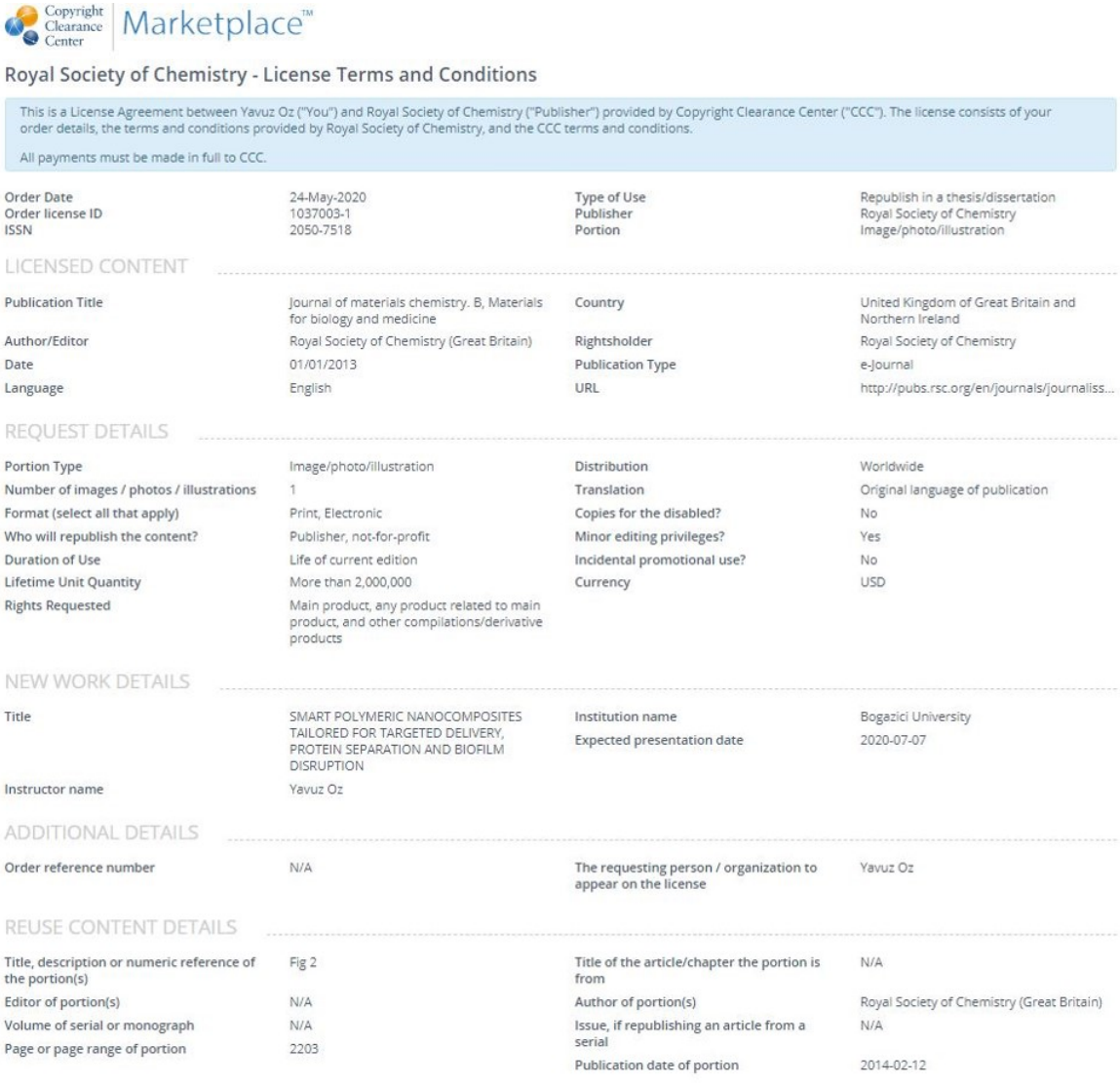

Copyright Clearance Center | Marketplace™

Royal Society of Chemistry - License Terms and Conditions

This is a License Agreement between Yavuz Oz ("You") and Royal Society of Chemistry ("Publisher") provided by Copyright Clearance Center ("CCC"). The license consists of your order details, the terms and conditions provided by Royal Society of Chemistry, and the CCC terms and conditions.

All payments must be made in full to CCC.

Order Date	24-May-2020	Type of Use	Republish in a thesis/dissertation
Order license ID	1037003-1	Publisher	Royal Society of Chemistry
ISSN	2050-7518	Portion	Image/photo/illustration

LICENSED CONTENT

Publication Title	Journal of materials chemistry. B, Materials for biology and medicine	Country	United Kingdom of Great Britain and Northern Ireland
Author/Editor	Royal Society of Chemistry (Great Britain)	Rightsholder	Royal Society of Chemistry
Date	01/01/2013	Publication Type	e-Journal
Language	English	URL	http://pubs.rsc.org/en/journals/journaliss...

REQUEST DETAILS

Portion Type	Image/photo/illustration	Distribution	Worldwide
Number of images / photos / illustrations	1	Translation	Original language of publication
Format (select all that apply)	Print, Electronic	Copies for the disabled?	No
Who will republish the content?	Publisher, not-for-profit	Minor editing privileges?	Yes
Duration of Use	Life of current edition	Incidental promotional use?	No
Lifetime Unit Quantity	More than 2,000,000	Currency	USD
Rights Requested	Main product, any product related to main product, and other compilations/derivative products		

NEW WORK DETAILS

Title	SMART POLYMERIC NANOCOMPOSITES TAILORED FOR TARGETED DELIVERY, PROTEIN SEPARATION AND BIOFILM DISRUPTION	Institution name	Bogazici University
		Expected presentation date	2020-07-07
Instructor name	Yavuz Oz		

ADDITIONAL DETAILS

Order reference number	N/A	The requesting person / organization to appear on the license	Yavuz Oz

REUSE CONTENT DETAILS

Title, description or numeric reference of the portion(s)	Fig 2	Title of the article/chapter the portion is from	N/A
Editor of portion(s)	N/A	Author of portion(s)	Royal Society of Chemistry (Great Britain)
Volume of serial or monograph	N/A	Issue, if republishing an article from a serial	N/A
Page or page range of portion	2203	Publication date of portion	2014-02-12

Figure B.5. Permission for Figure 1.6 from Ref. [48]

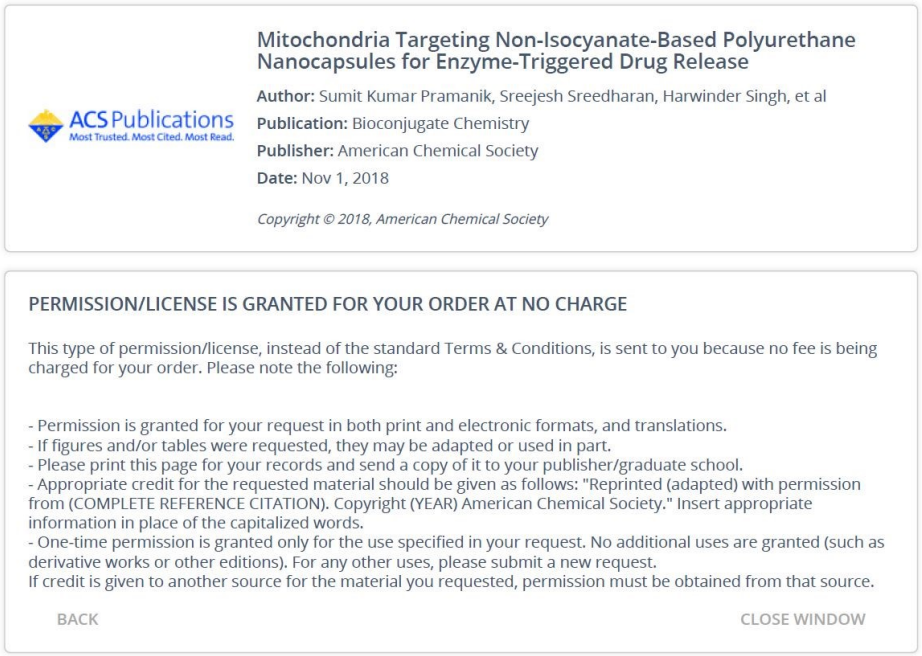

ACS Publications
Most Trusted. Most Cited. Most Read.

Mitochondria Targeting Non-Isocyanate-Based Polyurethane Nanocapsules for Enzyme-Triggered Drug Release

Author: Sumit Kumar Pramanik, Sreejesh Sreedharan, Harwinder Singh, et al
Publication: Bioconjugate Chemistry
Publisher: American Chemical Society
Date: Nov 1, 2018

Copyright © 2018, American Chemical Society

PERMISSION/LICENSE IS GRANTED FOR YOUR ORDER AT NO CHARGE

This type of permission/license, instead of the standard Terms & Conditions, is sent to you because no fee is being charged for your order. Please note the following:

- Permission is granted for your request in both print and electronic formats, and translations.
- If figures and/or tables were requested, they may be adapted or used in part.
- Please print this page for your records and send a copy of it to your publisher/graduate school.
- Appropriate credit for the requested material should be given as follows: "Reprinted (adapted) with permission from (COMPLETE REFERENCE CITATION). Copyright (YEAR) American Chemical Society." Insert appropriate information in place of the capitalized words.
- One-time permission is granted only for the use specified in your request. No additional uses are granted (such as derivative works or other editions). For any other uses, please submit a new request.

If credit is given to another source for the material you requested, permission must be obtained from that source.

BACK CLOSE WINDOW

Figure B.6. Permission for Figure 1.7 from Ref. [55]

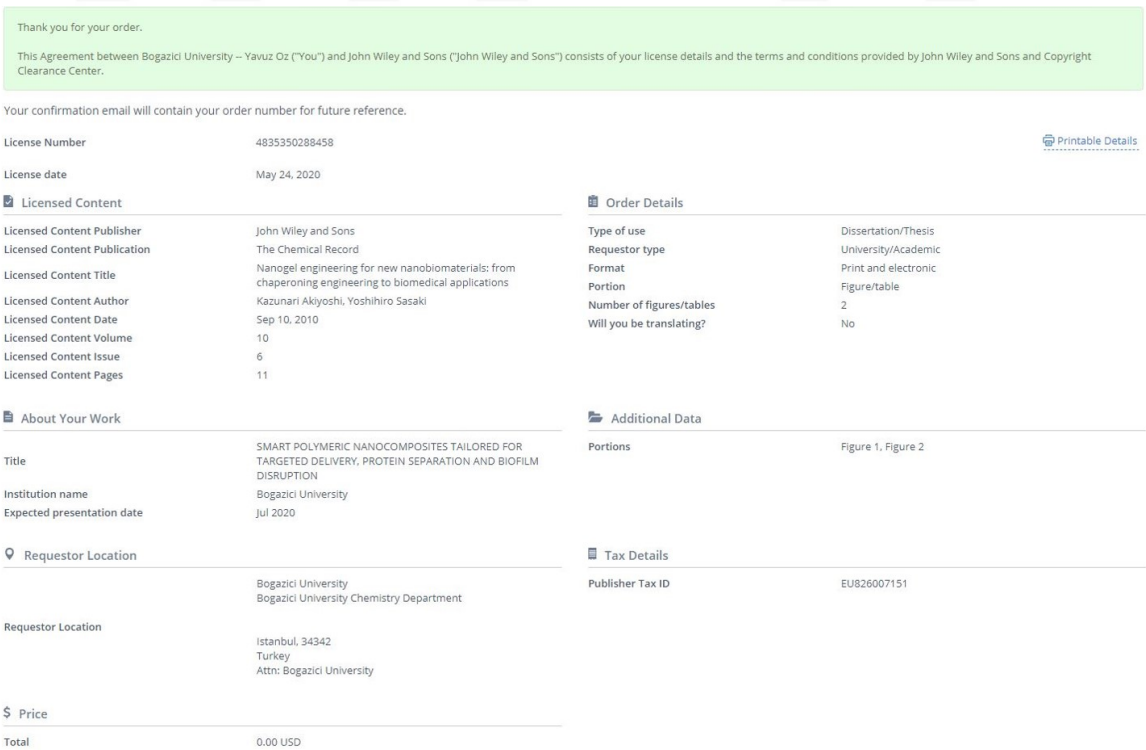

Thank you for your order.

This Agreement between Bogazici University -- Yavuz Oz ("You") and John Wiley and Sons ("John Wiley and Sons") consists of your license details and the terms and conditions provided by John Wiley and Sons and Copyright Clearance Center.

Your confirmation email will contain your order number for future reference.

Printable Details

License Number	4835350288458
License date	May 24, 2020

Licensed Content

Licensed Content Publisher	John Wiley and Sons
Licensed Content Publication	The Chemical Record
Licensed Content Title	Nanogel engineering for new nanobiomaterials: from chaperoning engineering to biomedical applications
Licensed Content Author	Kazunari Akiyoshi, Yoshihiro Sasaki
Licensed Content Date	Sep 10, 2010
Licensed Content Volume	10
Licensed Content Issue	6
Licensed Content Pages	11

Order Details

Type of use	Dissertation/Thesis
Requestor type	University/Academic
Format	Print and electronic
Portion	Figure/table
Number of figures/tables	2
Will you be translating?	No

About Your Work

Title	SMART POLYMERIC NANOCOMPOSITES TAILORED FOR TARGETED DELIVERY, PROTEIN SEPARATION AND BIOFILM DISRUPTION
Institution name	Bogazici University
Expected presentation date	Jul 2020

Additional Data

Portions	Figure 1, Figure 2

Requestor Location

	Bogazici University Bogazici University Chemistry Department
Requestor Location	Istanbul, 34342 Turkey Attn: Bogazici University

Tax Details

Publisher Tax ID	EU826007151

Price

Total	0.00 USD

Figure B.7. Permission for Figure 1.8 from Ref. [62]

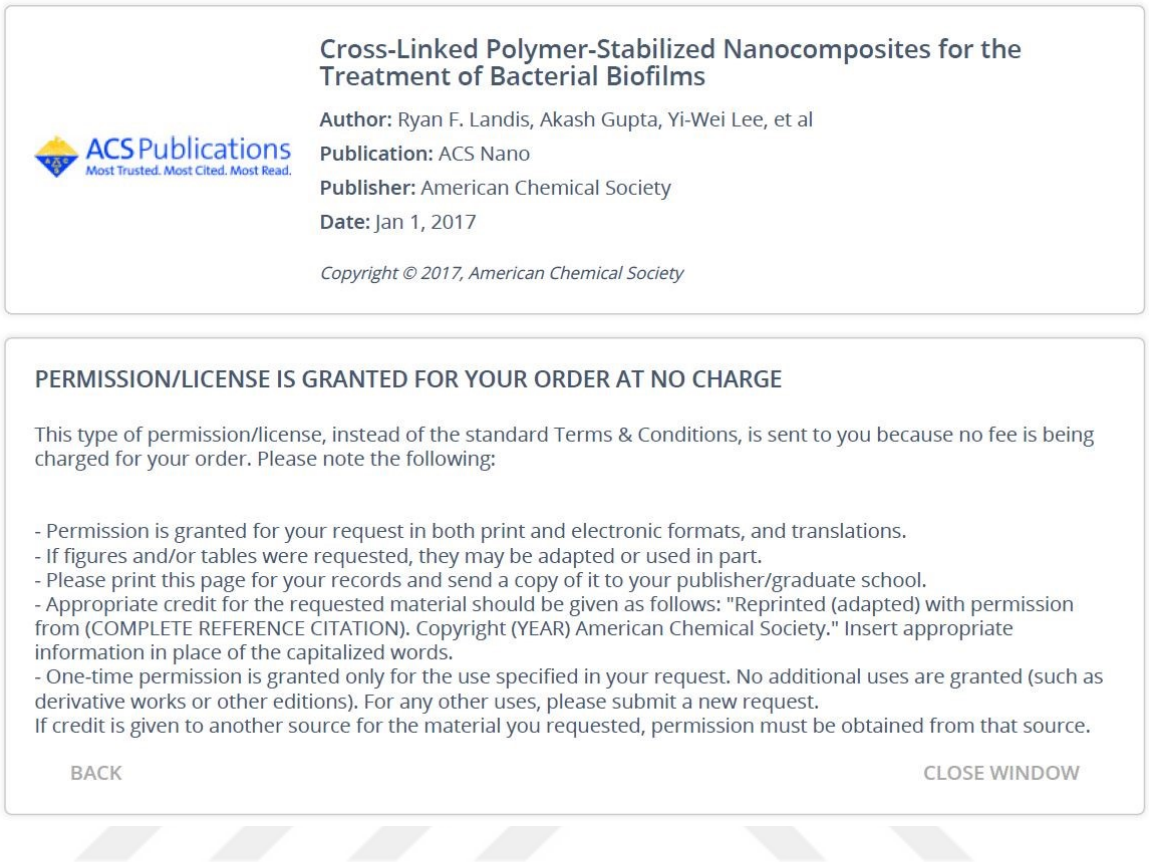

Figure B.8. Permission for Figure 1.10 from Ref. [75]

Thank you for your order.

This Agreement between Bogazici University -- Yavuz Oz ("You") and Elsevier ("Elsevier") consists of your license details and the terms and conditions provided by Elsevier and Copyright Clearance Center.

Your confirmation email will contain your order number for future reference.

Printable Details

License Number	4835351203187
License date	May 24, 2020

Licensed Content

Licensed Content Publisher	Elsevier
Licensed Content Publication	Journal of Controlled Release
Licensed Content Title	Targeted systemic delivery of siRNA to cervical cancer model using cyclic RGD-installed unimer polyion complex-assembled gold nanoparticles
Licensed Content Author	Yu Yi,Hyun Jin Kim,Peng Mi,Meng Zheng,Hiroyasu Takemoto,Kazuko Toh,Beob Soo Kim,Kotaro Hayashi,Mitsuru Naito,Yu Matsumoto,Kanjiro Miyata,Kazunori Kataoka
Licensed Content Date	Dec 28, 2016
Licensed Content Volume	244
Licensed Content Issue	n/a
Licensed Content Pages	10
Journal Type	S&T

Order Details

Type of Use	reuse in a thesis/dissertation
Portion	figures/tables/illustrations
Number of figures/tables/illustrations	1
Format	both print and electronic
Are you the author of this Elsevier article?	No
Will you be translating?	No

About Your Work

Title	SMART POLYMERIC NANOCOMPOSITES TAILORED FOR TARGETED DELIVERY, PROTEIN SEPARATION AND BIOFILM DISRUPTION
Institution name	Bogazici University
Expected presentation date	Jul 2020

Additional Data

Portions	Figure 1

Requestor Location

Bogazici University
Bogazici University Chemistry Department

Requestor Location

Istanbul, 34342
Turkey
Attn: Bogazici University

Tax Details

Publisher Tax ID	GB 494 6272 12

Figure B.9. Permission for Figure 1.11 from Ref. [87]

ACS Publications
Most Trusted. Most Cited. Most Read.

Bioconjugation and Fluorescence Labeling of Iron Oxide Nanoparticles Grafted with Bromomaleimide-Terminal Polymers

Author: Ruirui Qiao, Lars Esser, Changkui Fu, et al
Publication: Biomacromolecules
Publisher: American Chemical Society
Date: Nov 1, 2018

Copyright © 2018, American Chemical Society

PERMISSION/LICENSE IS GRANTED FOR YOUR ORDER AT NO CHARGE

This type of permission/license, instead of the standard Terms & Conditions, is sent to you because no fee is being charged for your order. Please note the following:

- Permission is granted for your request in both print and electronic formats, and translations.
- If figures and/or tables were requested, they may be adapted or used in part.
- Please print this page for your records and send a copy of it to your publisher/graduate school.
- Appropriate credit for the requested material should be given as follows: "Reprinted (adapted) with permission from (COMPLETE REFERENCE CITATION). Copyright (YEAR) American Chemical Society." Insert appropriate information in place of the capitalized words.
- One-time permission is granted only for the use specified in your request. No additional uses are granted (such as derivative works or other editions). For any other uses, please submit a new request.

If credit is given to another source for the material you requested, permission must be obtained from that source.

BACK CLOSE WINDOW

Figure B.10. Permission for Figure 1.13 from Ref. [105]

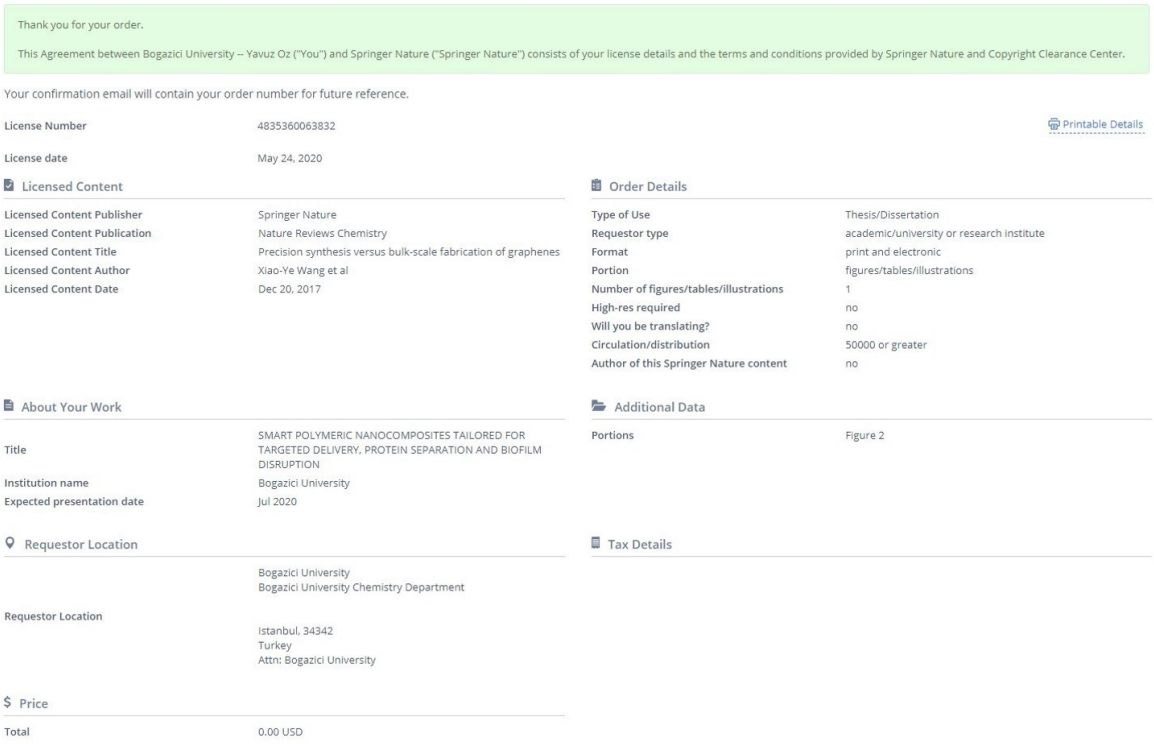

Thank you for your order.

This Agreement between Bogazici University -- Yavuz Oz ("You") and Springer Nature ("Springer Nature") consists of your license details and the terms and conditions provided by Springer Nature and Copyright Clearance Center.

Your confirmation email will contain your order number for future reference.

Printable Details

License Number	4835360063832
License date	May 24, 2020

Licensed Content

Licensed Content Publisher	Springer Nature
Licensed Content Publication	Nature Reviews Chemistry
Licensed Content Title	Precision synthesis versus bulk-scale fabrication of graphenes
Licensed Content Author	Xiao-Ye Wang et al
Licensed Content Date	Dec 20, 2017

Order Details

Type of Use	Thesis/Dissertation
Requestor type	academic/university or research institute
Format	print and electronic
Portion	figures/tables/illustrations
Number of figures/tables/illustrations	1
High-res required	no
Will you be translating?	no
Circulation/distribution	50000 or greater
Author of this Springer Nature content	no

About Your Work

Title	SMART POLYMERIC NANOCOMPOSITES TAILORED FOR TARGETED DELIVERY, PROTEIN SEPARATION AND BIOFILM DISRUPTION
Institution name	Bogazici University
Expected presentation date	Jul 2020

Additional Data

Portions	Figure 2

Requestor Location

Requestor Location	Bogazici University Bogazici University Chemistry Department Istanbul, 34342 Turkey Attn: Bogazici University

Tax Details

Price

Total	0.00 USD

Figure B.11. Permission for Figure 1.14 from Ref. [112]

Thank you for your order.

This Agreement between Bogazici University -- Yavuz Oz ("You") and John Wiley and Sons ("John Wiley and Sons") consists of your license details and the terms and conditions provided by John Wiley and Sons and Copyright Clearance Center.

Your confirmation email will contain your order number for future reference.

License Number	4835360357430
License date	May 24, 2020

Printable Details

Licensed Content

Licensed Content Publisher	John Wiley and Sons
Licensed Content Publication	Small
Licensed Content Title	Engineered Redox-Responsive PEG Detachment Mechanism in PEGylated Nano-Graphene Oxide for Intracellular Drug Delivery
Licensed Content Author	Donglu Shi, Yongyong Li, Xuequan Li, et al
Licensed Content Date	Jan 9, 2012
Licensed Content Volume	8
Licensed Content Issue	5
Licensed Content Pages	10

Order Details

Type of use	Dissertation/Thesis
Requestor type	University/Academic
Format	Print and electronic
Portion	Figure/table
Number of figures/tables	2
Will you be translating?	No

About Your Work

Title	SMART POLYMERIC NANOCOMPOSITES TAILORED FOR TARGETED DELIVERY, PROTEIN SEPARATION AND BIOFILM DISRUPTION
Institution name	Bogazici University
Expected presentation date	Jul 2020

Additional Data

Portions	Figure 1 and Figure 2

Requestor Location

Requestor Location	Bogazici University Bogazici University Chemistry Department Istanbul, 34342 Turkey Attn: Bogazici University

Tax Details

Publisher Tax ID	EU826007151

Figure B.12. Permission for Figure 1.16 from Ref. [120]



Photothermally triggered on-demand insulin release from reduced graphene oxide modified hydrogels

Author:
Florina Teodorescu,Yavuz Oz,Gurvan Quéniat,Amar Abderrahmani,Catherine Foulon,Marie Lecoeur,Rana Sanyal,Amitav Sanyal,Rabah Boukherroub,Sabine Szunerits

Publication: Journal of Controlled Release

Publisher: Elsevier

Date: 28 January 2017

© 2016 Elsevier B.V. All rights reserved.

Please note that, as the author of this Elsevier article, you retain the right to include it in a thesis or dissertation, provided it is not published commercially. Permission is not required, but please ensure that you reference the journal as the original source. For more information on this and on your other retained rights, please visit: https://www.elsevier.com/about/our-business/policies/copyright#Author-rights

BACK CLOSE WINDOW

Figure B.13. Permission for Chapter 3

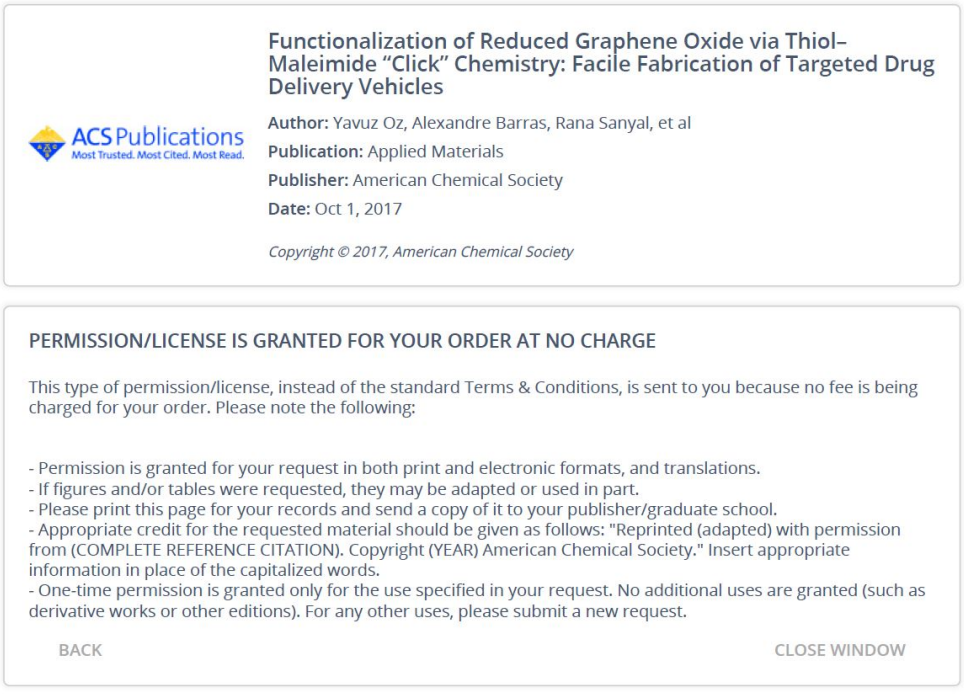

Figure B.14. Permission for Chapter 4

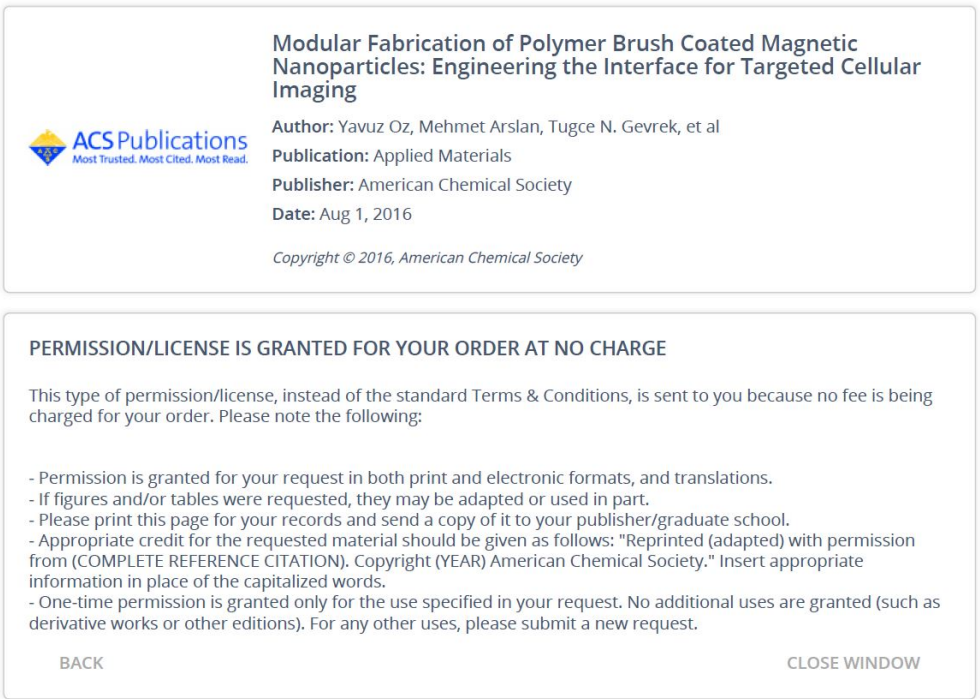

Figure B.15. Permission for Chapter 5